Investigation of the Role of Battery Resistance and Overpotential on Performance Models, Power Capability Prognostics, and Aging Behavior

by

Larry W. Juang

A dissertation submitted in partial fulfillment of
the requirements for the degree of

Doctor of Philosophy
(Electrical Engineering)

at the

University of Wisconsin – Madison

2014

Date of final oral examination: 12/11/2014

The dissertation is approved by the following members of the Final Oral Committee:
Thomas M. Jahns, Professor, Electrical & Computer Engineering
Robert D. Lorenz, Professor, Mechanical Engineering
Marc Anderson, Professor, Civil and Environmental Engineering
Bulent Sarlioglu, Assistant Professor, Electrical & Computer Engineering
Brian Sisk, Ph.D., Engineer, Johnson Controls Inc.

Abstract

This thesis investigates the behavior of battery resistance and overpotential for the purpose of modeling power capability prognostics and battery aging behavior. For a lead-acid battery, the traditional linear circuit model is inadequate to capture the battery electrode overpotential behavior described by the nonlinear Butler-Volmer equation. A discrete model that incorporates the Butler-Volmer nonlinear behavior is introduced, and its recursive form is developed for online battery monitoring in a Corbin Sparrow electric vehicle. For battery power capability prognostics, the commonly defined State-of-Power has been found to have a high variability within the context of recursive estimation. An equivalent State-of-Function metric, suitable even for nonlinear battery model forms, is proposed with the confidence interval provided by Kalman filter estimation. For lithium batteries, it has been found that, while the Butler-Volmer nonlinear behavior is approximately linear at room temperature, the nonlinear behavior manifests itself at lower temperatures. A discrete battery model with temperature explicitly built into it has been proposed. This discrete battery model with temperature as an input has been adopted in recursive form for online battery power prognostics and State-of-Charge estimation. In addition, an investigation has been conducted into the aging caused by superimposing an AC current signal onto the discharge current waveform, using measured resistance as the battery aging metric. It has been found that, by increasing the RMS value of the discharge waveform, the superimposed AC signal causes statistically significant aging acceleration.

Acknowledgement

This thesis is the outcome of more than seven years of work that began in the summer of 2007. This has been a great educational experience for me, both in and out of the technical field. However, without the assistance of many people, I would not have been able to accomplish the work. This thesis is, therefore, dedicated to all those who have helped me along the way.

I am indebted to my parents and my brother for their constant support. My advisers, Prof. Jahns and Lorenz, have guided me through the graduate program with firm and consistent hands and provided me with many invaluable advices, both technical and beyond. The Wisconsin Electric Machines and Power Electronics Consortium (WEMPEC) program has supported me financially, as well as Johnson Controls Inc. My two summer internships in the Ford Motor Company were instrumental in shaping my battery related work. I am thankful to my supervisors there, Dyche Anderson and James Swoish.

Many lifelong friends were made in the WEMPEC program. I am especially indebted to the colleagues I worked with in the battery related field. The foremost is Phillip Kollmeyer, who is a first-rate hands-on engineer and whose practical outlook on electric vehicle (EV) related issues always keeps me focusing on the important aspects. Without Phil's help, it is doubtful I could accomplish much of the works presented in this document. Other colleagues whose contributions I should not neglect include Adam Anders, Ruxiu Zhao, Kevin Frankforter, and Prof. Dawei Gao from Beijing Tsinghua University. Micah Erickson, who is always quick to seize any engineering

problem, shared many discussions with me on the battery technology. Other faculty members in the university have been generous to share with me their time and expertise, including Prof. Bill Sethares of the electrical & computer engineering department and Prof. Peter Zhenghao Qian of the statistics department.

Other friends in the WEMPEC program provided me with valuable discussions in technical areas outside the battery field. Among these friends are Wei Xu, Chen-yen Yu, Di Pan, Shih-Chin Yang, Yang Wang, Wenying Jiang, Chi-Ming Wang, James McFarland, Philip Hart, Yichao Zhang, Adam Shea, and Sheng-Chun Lee. The fond memories of technical discussions in the engineering hall student lounge flavored with sodas priced at 50 cent will always remain with me.

I have also made many friends outside of my technical field whose support was essential in helping me complete the thesis. Their friendships enhanced the experience in graduate school and are great resources at times of stress. I am thankful to Ting-Lan Ma and her family, Yu-Lien Chu and her family, Weija Cui, Li-Lin Cheng and Hiro Kobayashi, Hsun-Yu Chan, and Sheng-Yuan Cheng.

Madison, WI

Fall, 2014

Table of Contents

List of Figures

List of Tables

Table B 1 Specifications for the lab test equipment 261

Nomenclature

Abbreviations and Acronym

AC	Alternating Current
AGM	Absorbed Glass Mat
Ah	Amp-Hours
BMS	Battery Management System
CPE	Constant Phase Element
DC	Direct Current
EIS	Electrochemical Impedance Spectroscopy
HPPC	Hybrid Pulse Power Characterization
LPF	Low-Pass Filter
OCV	Open Circuit Voltage
RV	Random Variable
SEI	Solid-Electrolyte Interphase
SOC	State-of-Charge
SOF	State-of-Function
SOH	State-of-Health
SOP	State-of-Power

Symbols

A	Area of Electrode $\left[\frac{1}{cm^2}\right]$
C_1	Double Layer Capacitance [F]
C_i	Concentration of Species i $\left[\frac{mol}{cm^3}\right]$
D_i	Diffusion Coefficient $\left[\frac{cm^2}{s}\right]$
E_0	Electrode Standard Potential [V]
F	Faraday's Constant 96485.3 $\left[\frac{C}{mol}\right]$
ΔG	Gibbs Free Energy $\left[\frac{Joule}{mol}\right]$
i_0	Exchange Current [A]
i_{req}	Battery Current at Required Power [A]

J_i	Flux of Species i $\left[\frac{mol}{s\ cm^2}\right]$
n	Stoichiometric Number of Electrons [/]
P_{req}	Application Required Power [W]
r_0	Ohmic Resistance [Ohms]
r_1	Linearized Electrode Resistance [Ohms]
ΔS	Entropy Change $\left[\frac{J}{K}\right]$
T	Temperature [K]
v_{limit}	Battery Operating Voltage Limit [V]
v_{min}	Battery Minimum Voltage under Load [V]
v_{ocv}	Open Circuit Voltage [V]
α	Charge Transfer Coefficient [/]
η	Overpotential [V]

Chapter 1
Introduction

1.1 Background

The integration of electrochemical energy storage into an electrical system has been a field of rapid growth in recent years. The interest in sustainable, carbon-friendly mobility technology, in particular, has led to the commercialization of electric hybrid vehicles (HEV) and the push toward purely electric vehicles (EV). The most popular choice for the electrochemical energy storage components in these vehicles has been batteries due to their energy density advantages over ultracapacitors and their aging property advantages over fuel cells. As a result, battery modeling and monitoring have become important research topics. Additionally, the battery pack is, at present, one of the most limiting components in an EV in terms of aging. Factors influencing the battery aging properties have also become relevant research topics.

1.2 Problem Description

The use of electrochemical energy storage in new vehicular systems requires a multidisciplinary approach that combines understanding of the electrochemical devices themselves and the electric drive system. This thesis aims at broadening our understanding of the battery from the perspective of the electrical engineers who design the vehicles and the management systems that work with the battery packs. Typically, the battery management system (BMS) in a battery-powered vehicle is designed to

improve the perfomance of the batteries in several ways. The following is a list of the important tasks for the BMS:

1) Protection of battery cells against short-term catastrophic events such as thermal run-aways.
2) Protection of battery cells against undesirable conditions that could accelerate long-term aging, e.g., voltage unbalance between cells, thermal stress, over-charging, and over-discharging.
3) Monitoring the amount of charge stored.
4) Monitoring the battery power capability.
5) Monitoring the battery health.

In addition to the active management that a BMS provides, the electrical engineer also needs to take into account the battery properties and the intended application requirements during the design process for passive components, such as the sizing of the battery pack. The FreedomCAR consortium report provides a good example of battery pack sizing [1]. There is also evidence in the literature that the sizing of the DC-link capacitor in parallel with the battery pack can have an influence on battery aging [2].

To achieve the above-mentioned active and passive management features for vehicle battery packs, electrical engineers need to understand the battery's fundamental characteristics. These important characteristics include the basic information on battery operating voltage, current, and temperature range, as well as the battery capacity rating in amp-hours (Ah). This information is typically available in a battery datasheet and is sufficient for the basic protection functions for a BMS. More advanced knowledge is

required for other tasks such as estimating battery power capability, battery health, and the sizing of DC-link capacitors with respect to battery aging.

This thesis focuses on modeling of the battery voltage drop caused by current, i.e., resistive voltage drop and overpotential. The models are intended to facilitate online monitoring of battery power capability. Additionally, using battery resistance as an indicator for aging, this thesis includes an investigation of the aging impact of superimposed AC waveforms on the discharge current. Using statistical design of experiments and analyses, factors associated with superimposed AC waveforms, such as root-mean-square (RMS) values and frequency, are studied for their impacts on aging. The results of this study can provide guidelines for the system engineer to size the DC-link capacitor as a battery pack filter.

1.3 Proposed Technical Approach

With respect to the online monitoring of batteries, this thesis adopts the popular method of recursive estimation that has been adopted in many works in the literature such as [20], [23], and [45]. One innovation claimed in this thesis is the consideration of the model structure. Instead of applying the linear circuit model to all types of cells under all conditions, this thesis demonstrates that some types of cells, such as the lead-acid cell, exhibit behavior that warrants the inclusion of the non-linear Butler-Volmer relationship. Other chemistries, such as the lithium-based cell types, may still require the inclusion of Butler-Volmer relationship in the model under low temperature conditions.

With appropriate model structures, work has been done to implement online battery power capability prediction to provide power monitoring. Additionally, a

generic battery model that includes the temperature's influence on resistance and overpotential has been proposed in this thesis.

To answer the question of whether an additional AC component superimposed on the DC discharging current will cause accelerated aging, this thesis conducts a study that designed and analyzed an experiment based on statistical principles. A notable feature of the aging study in this thesis is its experiment design that facilitates inferential reasoning on a sound basis. The contribution is not only the particular results obtained during this study, but also the demonstration of the general methodology applied to the field of battery aging research.

1.4 Document Organization

As noted in the preceding section, electrical engineers need to have an understanding of the battery's fundamental electrochemical processes in order to converge quickly to practical designs related to battery pack management. These electrochemical processes are introduced in Chapter Two, the state-of-the-art review, as the background knowledge that is required. This state-of-the-art review chapter also presents information on the major BMS techniques discussed in the literature for the purpose of battery charge estimation, battery power estimation, and battery health monitoring. To provide the necessary background for the battery aging experiments presented in Chapter Six, basic principles of statistics, particularly for the design of experiments, is summarized in Chapter Two.

The rest of the thesis is organized as follows: Chapter Three introduces the mathematical model that incorporates the Butler-Volmer nonlinear behavior. The parameter identification methods are also introduced. Lead-acid battery data obtained

from test bench and actual EV drives have been used to illustrate the benefits of the nonlinear model over its linear counterpart. A recursive version of the Butler-Volmer relationship-based model is then introduced. This recursive version of the Butler-Volmer model is used in conjunction with real road data from the Corbin Sparrow electric vehicle, which performs significantly better compared with its linear model recursive estimator counterpart.

Chapter Four discusses the issues of state-of-function (SOF) and state-of-power (SOP). Specifically, it is pointed out that, using the recursive estimation scheme, the popular SOP suffers from volatility inherent in its definition. SOF with the purpose of determining whether battery power is above a set threshold is also introduced, along with the implementation of a confidence interval based on the Kalman filter used for the recursive estimation. Lithium-iron-phosphate battery data are then used to demonstrate the SOF and SOP prediction. The data are also used to compare FreedomCAR hybrid pulsed power characterization (HPPC) test results with the recursive estimator results, specifically their resistance and open-circuit voltage estimates that are important for power prediction.

Chapter Five provides a summary of all of the battery estimation work in this thesis. It focuses on the battery resistance and overpotential modeling at various temperatures. HPPC, electrochemical impedance spectroscopy (EIS), and drive cycle data are used to demonstrate the need for special consideration of modeling resistance and overpotential for lithium-based batteries at lower temperatures.

A generic cell model that includes the temperature influence on resistance and overpotential is also introduced. An adaptation of this generic cell model is proposed

for recursive estimation, and its outputs have been used for both power prognostics and remaining charge estimation. The generic cell model approach has been found to be suitable for a lithium-based batteries, but it is suitable for lead-acid batteries only without regenerative braking.

Chapter Six documents a study that addresses the question of whether a superimposed AC waveform causes accelerated aging in a lithium-ion battery. The motivation for the study, the adopted experimental method, and the subsequent data analysis are discussed. A second experiment designed to clarify questions after the first experiment was also performed, and its analysis method along with its conclusions are included in the chapter.

Chapter Seven presents the new contributions made in this PhD research program, as well as some suggestions for future research. The appendices at the end of the thesis contain documentation for the experimental equipment used in this thesis, the Corbin Sparrow electric vehicle, and the laboratory test bench.

Chapter 2
The State-of-the-Art Review

2.1 Historical Overview on Battery

The reference *Battery Management Systems* by Bergveld, et al has a good historic note on the development history of the electrochemical battery [3]. Based on the references [3-12], some important events of battery development are described here. The Italian scientist Alessandro Volta is credited with the invention of the first modern battery. The famous Volta pile consisted of alternating silver and zinc plates interleaved with paper and cloth, which had been soaked with an electrolyte. This structure was patented in 1800, while the derivation of electrochemical laws connecting chemistry and electricity is attributed to Michael Faraday, who published his results in 1834. A schematic of the Volta pile is shown in Figure 2.1.

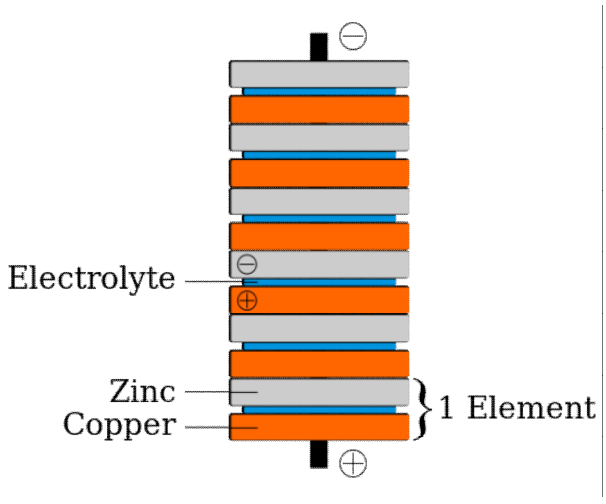

Figure 2.1 The Volta pile-first modern battery [6]

In the early days of battery development, gas formation, a parasitic reaction, at the electrodes plagued the devices' efficiency. The energy used to form gas could not be recovered [3]. The hydrogen bubble observed in these early cells could also cause a voltage drop and an increase in internal resistance [4]. Improving upon Volta's work, the British chemist John Frederic Daniell invented a new type of battery to address the hydrogen bubble problem in the Volta pile [4]. His battery is illustrated in Figure 2.2.

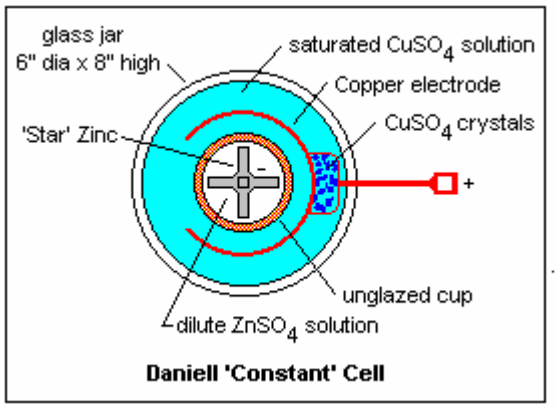

Figure 2.2 Daniell battery schematic [4]

The Daniell battery, like its predecessor the Volta pile, utilizes zinc and copper as electrode materials. The main improvement of the new battery is in the use of earthenware to physically separate the zinc sulfuric acid ($ZnSO_4$) and copper sulfuric acid ($CuSO_4$). The earthenware is however porous and allows the movement of ions during the electrochemical reaction. Instead of releasing hydrogen, the electrons from zinc are combined with copper ions in the $CuSO_4$ solution, plating copper in the glass jar wall or the earthenware. Before the advent of the Leclanche battery in the 1860's, the Daniell battery played an important role in the telegraphy industry.

Georges Leclanche patented his new battery in 1866 [5]. The new battery still employed zinc as the anode material but had a mixture of manganese dioxide (MnO_2) and

carbon as the cathode, packaged in earthenware. In addition, a carbon rod served as the current collector. The zinc rod electrode and the cathode package are then submerged in a glass jar filled with an ammonium chloride solution. The Leclanche batteries were widely used in the telegraphy and early telephone industries. Carl Gassner is credited for the zinc-carbon battery that, replacing the Leclanche battery's ammonium chloride solution electrolyte with a paste, became the world's first dry cell [5]. Figure 2.3 illustrates a Leclanche battery [7].

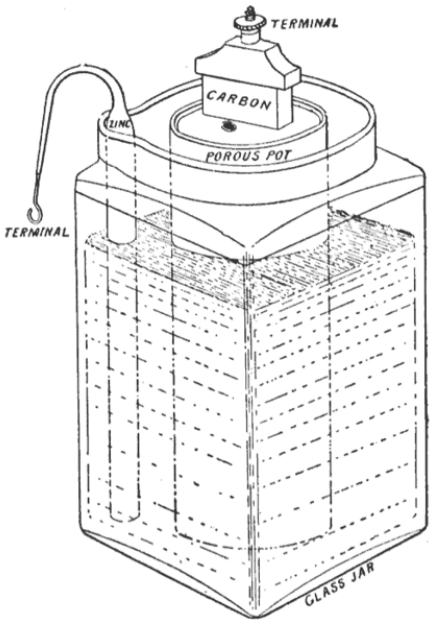

Figure 2.3 Leclanche battery illustration [7]

The above mentioned battery types were all primary batteries, which means they are only capable of converting chemical energy into electricity but not the other way around. To Gaston Plante the world's first rechargeable, or secondary, battery is attributed. In 1859, Plante presented a design that had a sandwich of thin layers of lead, separated by sheets of cloth in diluted sulphuric acid. The device is charged with a

voltage between the two lead electrodes and could then discharge the stored energy [3]. A discussion on the lead-acid battery electrochemical reaction is presented in 2.3.1.

The next important milestone in the development of battery technology is the invention of nickel-cadmium battery by the Swede Waldmar Jungner in 1899. Thomas Edison in the U.S., searching an alternative for the heavy lead-acid battery for electric vehicles, developed the nickel-iron alkaline battery [3].

The lithium-ion batteries were introduced in the 1970's and 1980's. In 1979, John Goodenough presented a lithium battery with a lithium cobalt oxide ($LiCoO_2$) cathode and a lithium metal anode. Rachid Yazami developed a system with graphite as the anode material in 1980. The lithium/graphite system is still the most used today. Since SONY's introduction of commercialization of lithium-ion batteries in 1991, lithium-ion battery has seen a rapid growth in market and is considered as a primary candidate for commercial electric vehicles energy storage [3].

2.2 Battery Basic Structure

An electrochemical cell most likely contains the following basic components: anode, cathode, electrolyte, and separator [3]. In electrochemical processes, an anode is the electrode where the oxidation reaction occurs, meaning that it releases electrons to the external circuit. A cathode is correspondingly the location where the reduction occurs, collecting the electrons from the anode through the external circuit. For a battery cell, the positive electrode is a cathode during discharge and an anode during charge, while the negative electrode is an anode during discharge and a cathode during charge. In the common literature, however, the convention is to adopt the terminal name designations that are appropriate during discharge operation. The electrolyte is the medium that

conducts the ions between the cathode and anode of a cell. The separator is a non-conductive layer that is permeable to ions, yet capable of preventing a galvanic short circuit between the cathode and anode terminals.

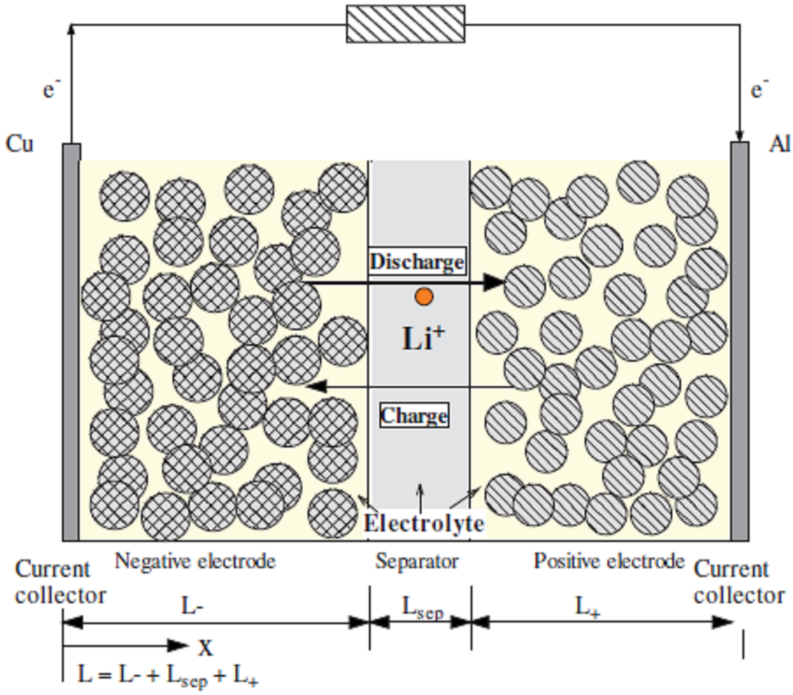

Figure 2.4 A Lithium-ion battery schematic [8]

2.3 Battery Chemistries

2.3.1 Lead-Acid Batteries

The lead-acid batteries' electrochemical reactions are the following (left to right for discharging) [9]:

Cathode: $PbO_2 + HSO4^- + 3H^+ + e^- \leftrightarrow PbSO_4 + 2\ H_2O$

Anode: $Pb + HSO_4^- \leftrightarrow PbSO_4 + H^+ + 2e^-$

Lead-acid batteries are based on a relatively old technology invented in the 19th century by the French physicist Gaston Plante [3]. The flooded, or wet, cells are very common

for industrial use. Since the flooded type of lead-acid batteries are usually not sealed, the user can replenish the electrolyte that is depleted during charging through venting [10].

In addition to the flooded type, two common variants exist for the sealed lead-acid batteries. Gel cells immobilize the electrolyte with a thickening agent such as fumed silica. The absorbed glass mat (AGM) batteries use a fiberglass-like separator to hold the electrolyte in place. The advantage of sealing is that the cells are more impact resistance and can function even when the container has been damaged. But the inability to replenish electrolyte means that overcharging can cause permanent damage to the cells. The lead-acid battery technology generally suffers little or no memory effect [3]. Memory effect refers to the restricted capacity that some batteries exhibit when they have been subjected to a particular limited range of capacity use. The lack of memory effect makes this technology a strong candidate for back-up power applications. Lead-acid batteries, however, suffer from a relatively low energy density and irreversible capacity loss during deep discharge [3].

2.3.2 Nickel-Cadmium Batteries

One version of the NiCd batteries' electrochemical reactions is the following (left to right for discharge) [11]:

Cathode: $NiOOH + H_2O + e^{1-} \leftrightarrows Ni(OH)_2 + OH^{1-}$

Anode: $Cd + 2OH^{1-} \leftrightarrows Cd(OH)_2 + 2e^{1-}$

The NiCd battery has a reputation for being robust and low cost. Due to its robustness, NiCd batteries can be charged at a higher rate and thus in a shorter time. However, NiCd batteries suffer from the memory effect. With a few complete charge/discharge cycles,

the memory effect can be overcome. Another drawback to NiCd batteries is that they have relatively low energy density [3].

2.3.3 Nickel-Metal Hydride Batteries

The electrochemical reaction can be the following (left to right for discharge) [11]:

Cathode: $NiOOH + H_2O + e^{1-} \leftrightarrow Ni(OH)_2 + OH^{1-}$

Anode: $Alloy[H] + OH^{1-} \leftrightarrow Alloy + H_2O + e^{1-}$

NiMH batteries represent an improvement over NiCd batteries in terms of energy density. They still suffer the memory effect despite the fact that some manufacturers claim otherwise. A drawback of the NiMH batteries is that it has a greater self-discharge rate compared with NiCd batteries. Also, since NiCd batteries absorb heat during charging while NiMH batteries generate heat during charging, NiMH batteries need to be more carefully regulated thermally during rapid charging [3].

2.3.4 Lithium-ion Batteries

One possibility for the Li-ion battery reaction, depending on the electrodes, is the following using cobalt oxide as the cathode material [12]:

Cathode: $Li_{1-x}CoO_2 + xLi^+ + xe^{1-} \leftrightarrow LiCoO_2$

Anode: $Li_xC \leftrightarrow xLi^+ + xe^{1-} + C$

A common anode material for Li-ion batteries is graphite, while the cathode material has many options of Li-based oxide. The electrolyte used in Li-ion batteries is an organic solvent, commonly ethlyene carbon (EC). The EC reduction with Li^+ forms a protective layer on the graphite anode surface that regulates the intercalaction of Li^+ and graphite during charging and increases the battery life [13]. One advantage of the Li-ion batteries

is that they have a considerably higher energy density than the preceding battery types. However, overcharging Li-ion batteries may lead in some cases to high dangerous conditions including explosions. As a result, careful control of the battery operating conditions must be implemented by the battery monitoring system [3].

2.4 Electrochemical Processes in a Battery

2.4.1 Thermodynamics and the Nernst Equation

Thermodynamics, strictly speaking, encompass only systems at equilibrium [14]. As such, the reversibility of a system is an important prerequisite. A thermodynamically reversible system is one such that an infinitesimal reversal in a driving force causes it to reverse direction. Of course, the concept of infinitesimal change in a driving force is ideal and the system needs to be in equilibrium to experience such a small force. A chemically reversible system is one that when the polarity of DC current changes, the reaction merely reverses its direction. A chemically irreversible system cannot be thermodynamically reversible, while a chemically reversible one may or may not be thermodynamically reversible [14].

For a thermodynamically reversible system, the linkage between electrode potential E and the concentrations of participants in the electrode process is usually described by the Nernst equation:

$$E = E^0 + \frac{RT}{nF} \ln \frac{C_O}{C_R} \tag{2.4.1}$$

In (2.4.1), E is the electrode potential in [V], E^0 is the standard potential of the electrode in [V], R is the universal gas constant 8.314 in $\left[\frac{J}{mol\ K}\right]$, T is temperature in [K], n is the

stoichiometric number of electrons involved in the reaction, F is the Faraday constant 96485.337 in $\left[\frac{C}{mol}\right]$, C_O is the concentration of the oxidant in $\left[\frac{mol}{cm^{-3}}\right]$, and C_R is the concentration of the reductant in $\left[\frac{mol}{cm^{-3}}\right]$. The electrode process for the Nernst equation in (2.4.1) is the following, where O is the oxidant and R the reductant.

$$O + ne \leftrightarrow R \tag{2.4.2}$$

The energy released in an electrochemical reaction can be separated into the external part, Q_R, and the internal part, Q_C [14]. The external part is what dissipates in the external circuit, e.g. a resistor or a light bulb, while the internal part is always thermal. One way to visualize the thermodynamically reversible process for the electrode is to assume the external resistance approach infinity. In such a limiting condition, Q_C is the same as the heat traversing a reversible path, Q_{rev}. The Gibbs free energy, ΔG, is defined as the maximum net work obtainable from the reaction, which occurs at the limiting condition $Q_C = Q_{rev}$. If the total work is defined as ΔH then the Gibbs free energy is:

$$\Delta G = \Delta H - Q_{rev} = \Delta H - T\Delta S \tag{2.4.3}$$

In (2.4.3), ΔS is the entropy change in $\left[\frac{J}{K}\right]$. At unit activity (2.4.3) is rewritten as:

$$\Delta G^0 = \Delta H^0 - T\Delta S^0 \tag{2.4.4}$$

The Gibbs free energy connects thermodynamics and electrostatics via the following relationship:

$$RT \ln K = -\Delta G^0 = nFE^0 \quad (2.4.5)$$

Now that the electrode potential as a function of temperature has been described by (2.4.5), the potential of a general cell, i.e. with two electrodes and electrolyte in between, is simply:

$$E_{cell} = E_{cathode} - E_{anode} \quad (2.4.6)$$

2.4.2 Kinetics of Electrodes

The reaction rate in an electrode is strongly dependent on the potential [14]. At some voltage the current does not flow while the current flows at various degrees at other voltage region. A potential dependent law is necessary for the description of the charge-transfer phenomenon.

The theory of interfacial dynamics for electrodes concerns itself with the case where the mass transport is not a limiting factor. This means the current rate is relatively low and the electrolyte is well stirred. In 1905, Tafel shows that the current is related exponentially with the potential. The famed Tafel equation has the following form:

$$\eta = a + b \log i \quad (2.4.7)$$

A more advanced form of the kinetics was named after John Alfred Valentine Butler and Max Volmer [15] [16]. The Butler-Volmer equation, in its simplest form that assumes the dominance of charge transfer, is the following.

$$i = i_0\left[\exp\left(-\alpha\frac{\eta F}{RT}\right) - \exp\left((1-\alpha)\frac{\eta F}{RT}\right)\right] \quad (2.4.8)$$

In (2.4.8), i_0 is called the exchange current. It is the limiting current to which the oxidation and reduction approaches at equilibrium. η is the overpotential driving the current. The symbol α is the charge transfer coefficient. The charge transfer coefficient is a measure of the symmetry of the energy barrier against which oxidation and reduction take place. When $\alpha = 0.5$, the reactions are symmetrical.

At small value of η, (2.4.8) can be simplified with first order Taylor series expansion. The voltage-current relationship becomes linear.

$$i = -i_0\frac{\eta F}{RT} \quad (2.4.9)$$

For a large value of η, one of the bracketed term in (2.4.8) can be neglected due to the exponential function. If $\exp(-\alpha\frac{\eta F}{RT}) >> \exp((1-\alpha)\frac{\eta F}{RT})$, (2.4.8) becomes:

$$i = i_0\left[\exp(-\alpha\frac{\eta F}{RT})\right] \quad (2.4.10)$$

Or

$$\eta = \frac{\eta F}{RT}\log i_0 - \frac{\eta F}{RT}\log i \quad (2.4.11)$$

It is clear that the empirically obtained Tafel relationship (2.4.7) can be derived from (2.4.8) using the large current assumption in (2.4.11). By assuming the symmetry of oxidation and reduction, α assumes the value of 0.5 and (2.4.8) can also be rewritten using the identity of hyperbolic sine function [17].

$$\eta = \frac{RT}{\alpha F}\sinh^{-1}\left(\frac{i}{2i_0}\right) \tag{2.4.12}$$

From the electrical engineering point of view, (2.4.8) presents a challenge when utilizing it for prediction. The engineer usually seeks to use battery current to predict voltage behavior because voltage across the electrode is not measurable while the terminal current is, whereas (2.4.8) has a form of using voltage to predict current. By making an assumption on symmetry, (2.4.12) provides an easier to use alternative.

It is noted here that all the discussion in 2.4.2 so far has been on the steady-state behavior of the electrode. In addition to the steady state Faradaic response, the voltage across an electrode is also governed by the transient response of the double-layer capacitance. A charge separation occurs at the electrode/electrolyte interface with electrode surface attracting ions of opposite charge sign in the electrolyte. This phenomenon is referred to as double-layer capacitance [3]. Such a response is responsible for a large portion of the transient response of the battery.

2.4.3 Mass Transfer of Ions

Mass transfer is the movement of material from one location in solution to another. Three modes of movement are commonly considered [14].

1. *Migration*. The movement of charged body caused by electric potential fields.
2. *Diffusion*. The movement of a species under influence of a gradient of chemical potential (concentration gradient).
3. *Convection*. Stirring of hydrodynamic transport.

The one dimensional version Nernst-Planck equation for mass transfer in an electrode is the following:

$$J_i(x) = -D_i\frac{\partial C_i(x)}{\partial x} - \frac{z_i F}{RT}D_i C_i\frac{\partial \varphi(x)}{\partial x} + C_i v(x) \qquad (2.4.13)$$

In (2.4.13), $J_i(x)$ is the flux of species i in $\left[\frac{mol}{s\ cm^2}\right]$ at distance x from the surface, D_i is the diffusion coefficient in $\left[\frac{cm^2}{s}\right]$, $\frac{\partial C_i(x)}{\partial x}$ is the concentration gradient at x, $\frac{\partial \varphi(x)}{\partial x}$ is the electric potential gradient, and z_i and C_i are the charge [/] and concentration $[\frac{mol}{cm^3}]$ of species. Finally, v(x) is the velocity $\left[\frac{cm}{s}\right]$ at which an element moves. It is noted that the three terms in (2.4.13) represent diffusion, migration, and convection, respectively.

If the electrolyte is plentiful and stirring at the electrode ineffective, (2.4.13) is reduced to only the diffusion term. The rate of mass transfer is then proportional to the diffusion term. Suppose further that at $x = \delta_0$ and beyond, the concentration of species is the same as the bulk solution C_i^*. For the case of a linear concentration gradient, the diffusion profile looks similar to Figure 2.5.

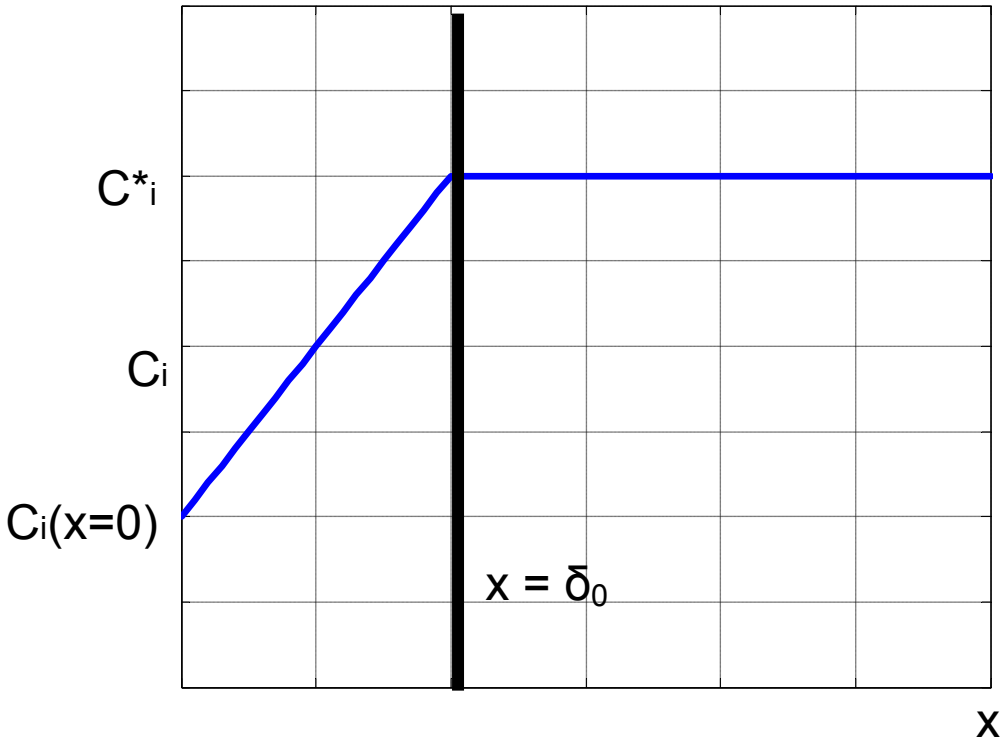

Figure 2.5 Example Diffusion Profile

In the linear gradient case, the current due to the diffusion profile is related as:

$$\frac{i}{nFA} = m_i\left(C_i^* - C_i(x=0)\right) \tag{2.4.14}$$

, where A is the area of electrode in $\left[\frac{1}{cm^2}\right]$ and m_i is the mass transfer coefficient in $\left[\frac{cm}{s}\right]$.

It is pointed out here that $\frac{i}{nFA}$ has the unit $\left[\frac{mol}{s\ cm^2}\right]$, which is the unit of reaction rate. The maximum rate of mass transfer of species i occurs when $C_i(x=0) = 0$. The value of the current under this condition is:

$$i_l = nFAm_iC_i^* \tag{2.4.15}$$

When current is at the rate of limited value, i_l, the reaction is occurring at the highest possible rate since the ions are being consumed completely at the electrode/electrolyte interface. Using (2.4.14) and (2.4.15), the ratio between C_i^* and $C_i(x = 0)$ can be found as:

$$\frac{C_i(x = 0)}{C_i^*} = 1 - \frac{i}{i_l} \tag{2.4.16}$$

Now consider a more realistic version of (2.4.8) where the Butler-Volmer equation takes into account the species concentration at the electrode/electrolyte interfaces of cathode and anode.

$$i = i_0\left[\frac{C_o(x = 0)}{C_o^*}\exp\left(-\alpha\frac{\eta F}{RT}\right) - \frac{C_R(x = 0)}{C_R^*}\exp\left((1-\alpha)\frac{\eta F}{RT}\right)\right] \tag{2.4.17}$$

The subscripts O and R represent oxidation and reduction, respectively. By first order Taylor series approximation, (2.4.17) can be written as:

$$\frac{i}{i_0} = \frac{C_o(x = 0)}{C_o^*} - \frac{C_R(x = 0)}{C_R^*} - \frac{\eta F}{RT} \tag{2.4.18}$$

By substituting with (2.4.16), (2.4.18) can be rewritten as:

$$\eta = i\frac{RT}{F}\left(\frac{1}{i_0} + \frac{1}{i_{lc}} - \frac{1}{i_{la}}\right) \tag{2.4.19}$$

, where subscripts lc and la mean the limiting value for cathodic and anodic reactions, respectively. Cathodic limiting current occurs when $C_o(x = 0) = 0$ and anodic limiting current occurs when $C_R(x = 0) = 0$. The linear relationship between voltage and current

in (2.4.19) is noted here. Such an approximation is the basis for modeling steady-state charge-transfer and ion distribution in electrolyte with resistors in battery models.

2.5 Battery Modeling Approaches

This section discusses the various types of battery models seen in the literature. In general the complexity of the model is constrained by the application. Specifically, if the battery model is intended for online, vehicular application, the model is required to be computationally manageable for the onboard computing unit. On the other hand, certain simulation works are for the development of battery materials, manufacturing process, etc. These would require more complex models that illuminate the various physical aspects concerning the battery's performance.

Three general categories of battery modeling approaches are:

1. *Electrical equivalent circuit models.* This genre of models usually captures the relationship between terminal voltage and current by the means of electrical circuit network.
2. *Curve-fitted behavioral models*. This school of approach relates the interested quantity, e.g. available Ah, with other measured quantities in non-physics based rules.
3. *Physics based models.* This set of models attempts to recreate the physical processes in a battery using first principle laws.

2.5.1 Electrical Equivalent Circuit Models and Various Parameter Estimation Methods

As discussed in 2.4.2 and 2.4.3, various processes relating voltage and current in a battery can be approximated as linear under certain assumptions. These linear approximations can be realized using resistors in the equivalent circuit models. In

addition, capacitors in equivalent circuit models offer a convenient means to mimic the transient behavior of the battery.

The electrical equivalent circuit approach has been applied to various battery chemistries, including lead-acid, NiMH, and lithium-ion [18], [19], [20]. An example of the equivalent circuit model is shown in Figure 2.6.

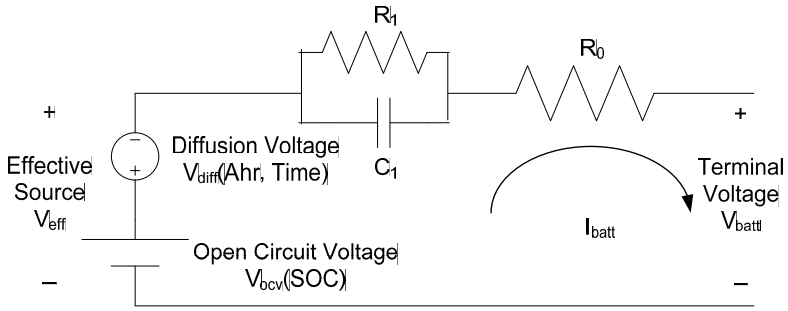

Figure 2.6 Example of a Battery Equivalent Circuit Model [21]

When the equivalent circuit model is to be used offline in a simulation environment, the parameters to the elements, i.e. resistors and capacitors, need to be identified using results from a standardized experiment. A common experimental procedure for such a purpose is the FreedomCAR consortium's hybrid pulsed power characterization (HPPC) test [1].

2.5.1.1 The FreedomCAR HPPC Method for Parameter Estimation

The HPPC test applies step currents both charging and discharging to the battery at various state-of-charge (SOC) levels. The difficulty in defining SOC on a practical basis is discussed in section 2.6. For now, SOC is considered as the ratio between the cell's available coulomb charge vs. maximum charge. Figure 2.7 shows the pulsed current profile used in the HPPC test.

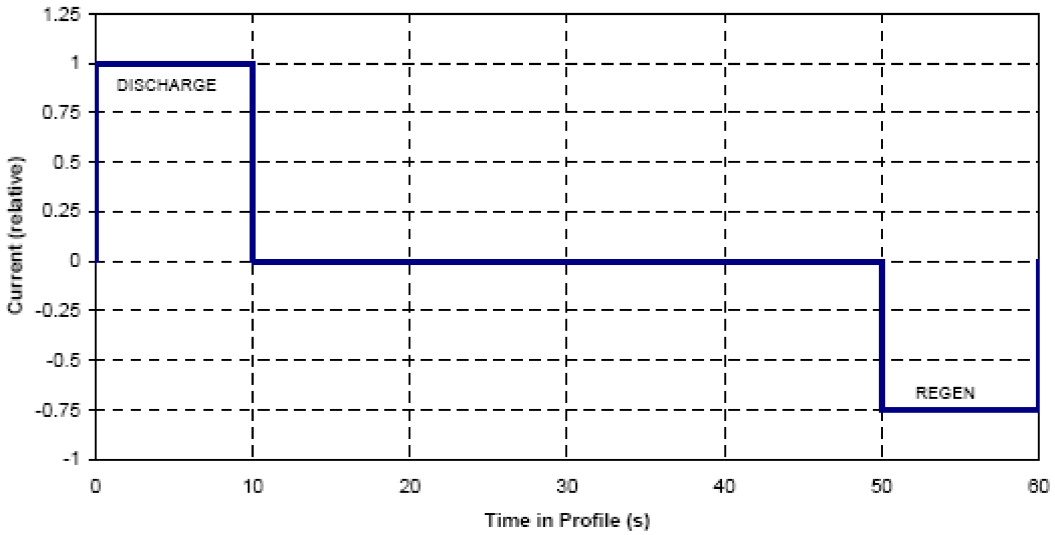

Figure 2.7 Example HPPC Pulsed Current Profile [1]

The complete HPPC test procedure consists of a repetition of a constant current to move the SOC by 10% decrement, one hour rest, and the HPPC test profile. The test will be performed from 90% to 10% SOC. Before the HPPC procedure begins, a complete discharge and a consequent recharge is also recommended to keep the test battery status consistent.

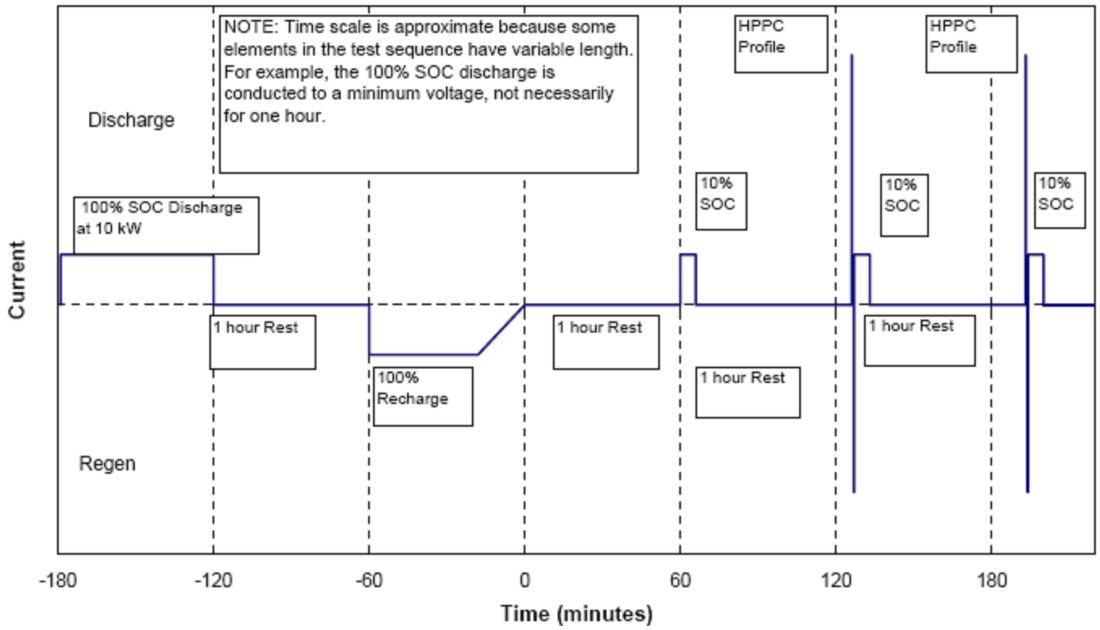

Figure 2.8 HPPC Test Procedure (Starting Sequence) [1]

Figure 2.8 shows the testing procedure for HPPC with the discharge/charge cycle that resets the battery status, a rest period before test that allows the temperature control to be effective, and the sequence of moving SOC, rest, and pulsed current profile. With the step current input and voltage response data, the battery's electric circuit model parameters can then be extracted. See for example [22].

In addition to the electrical element parameters, a simulation equivalent circuit model also requires the information relating SOC and the open-circuit voltage (OCV). Based on the thermodynamics discussed in 2.4.1, it is clear that OCV is a function of the concentrations of the ionic species in the electrolyte, thus the SOC. For a fixed temperature, this OCV vs. SOC relationship can be empirically obtained with a slow current discharge and recharge procedure. See for example [23].

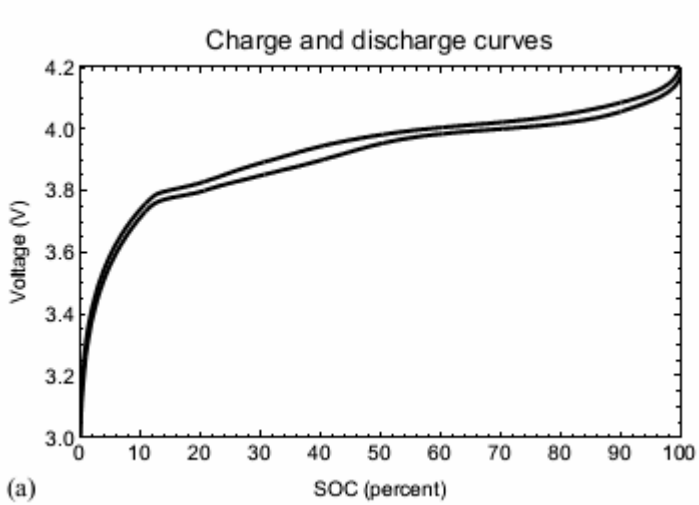

Figure 2.9 Low current charge and discharge curves for obtaining OCV vs. SOC information [23]

It is noted here that because of the thermodynamics involved the OCV vs. SOC relationship also depends on temperature. This caveat presents a challenge to the modeling effort. Figure 2.9 presents an illustration of the low current discharging and charging data for the estimation of OCV vs. SOC relationship for a Lithium-ion polymer battery [23].

2.5.1.2 The Electrochemical Impedance Spectroscopy (EIS) Method for Parameter Estimation

Another method for populating the equivalent circuit parameters is the electrochemical impedance spectroscopy (EIS). EIS is an established experimental technique in electrochemistry, usually used to differentiate material properties. For a comprehensive discussion on the EIS technique, the interested reader is referred to [24] and [25]. Here the basic principles for the technique are outlined.

By definition, an impedance of a system for a particular frequency is the division of its voltage phasor by its current phasor. To perform EIS on a battery, a small excitation signal, current or voltage, at a fixed frequency is injected to the test subject, and the resultant response, voltage or current respectively, is measured to find the impedance of the battery at the fixed frequency. The procedure is repeated for multiple frequencies and the impedance results are usually presented with the format in Figure 2.10.

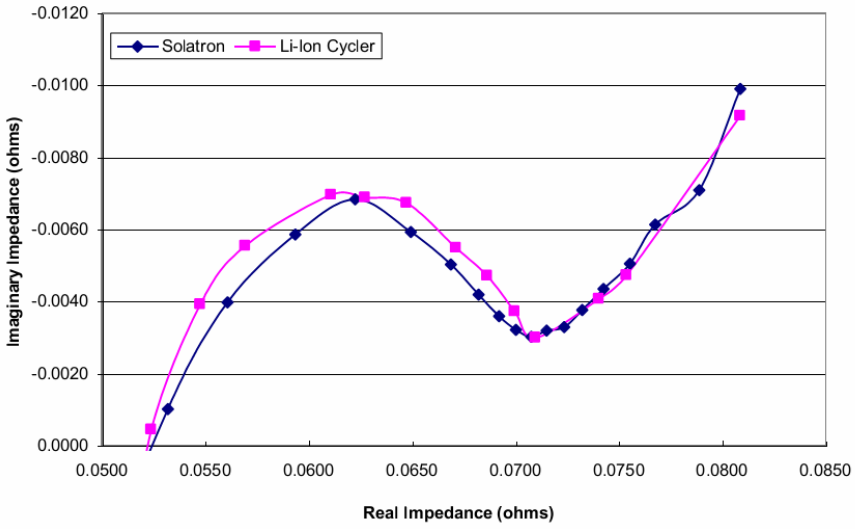

Figure 2.10 An example of a lithium ion battery impedance spectroscopy plot. The particular plot shows the agreement of the data obtained from two separate testing equipment [26]

In Figure 2.10, the y-axis is the impedance while the x-axis is the real impedance. Each data point represents the impedance for one single frequency. The choice of reversing the sign for imaginary impedance on the y-axis is due to the fact that most of the electrochemical systems display a capacitive behavior, i.e. negative imaginary impedance, at lower frequency range. The semicircle is thus more conveniently viewed with the reversing the imaginary impedance on the y-axis. The impedance data can also

be fitted to an equivalent circuit model. The choice of the model is somewhat arbitrary, but they usually involve RC structures for the lower frequency region. In order to take into account the positive imaginary behavior, a series inductance can also be added to the model. It is also pointed out here that the lower frequency data is generally on the right side of the figure.

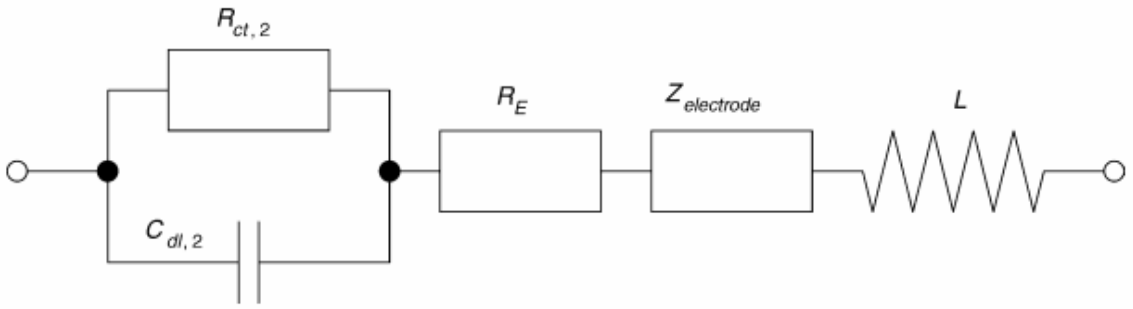

Figure 2.11 Example of equivalent circuit to be fitted by EIS data [27]

In Figure 2.11, an equivalent circuit to be fitted by EIS is shown. Notice the lack of OCV in the model; this is explained by the use of AC signals in EIS and the signals' inability to identify DC quantities. The $Z_{electrode}$ term represents a part with a constant phase element (CPE). This somewhat unusual model element aims to represent the diffusive response in the battery. The detailed derivation of CPE and its justification used in modeling can be found in [24]. Here it is briefly mentioned that the diffusion phenomenon observed in the electrolyte would in reality require an infinite number of elements to model, as the elements are distributed in space instead of being lumped within a local point. The diffusion behavior, in fact, is not unlike a transmission line, which can be modeled with an infinite series of RC circuits. Thus, battery equivalent circuit model can be represented in a ladder of RC circuits or utilizing the CPE. The main benefit of using the CPE vs. the RC ladder is the saving on model parameter terms.

As there are a finite number of data points in EIS, the saving of terms is important from the perspective of statistics.

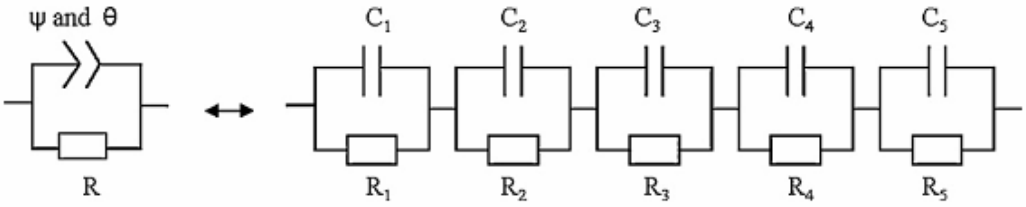

Figure 2.12 The interchange between CPE and ladder RC networks for battery modeling [29]

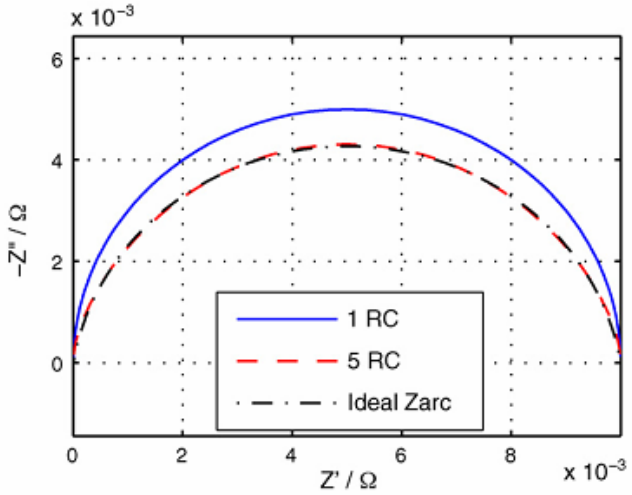

Figure 2.13 The ideal impedance plot of one RC, five RC's, and the circuit using CPE [29]

Figure 2.12 shows an example for interchanging five sets of RC circuits in series with a CPE parallel with a resistor. Figure 2.13 is their corresponding impedance plot, which shows the close agreement between the five RC's and the circuit utilizing a CPE. In reference [29], a methodology for converting the circuit with CPE to a series of RC's is mentioned.

The drawback of CPE is its unusual requirement for a fractional order (non-integer) derivative and is thus inconvenient for mathematical transform between frequency domain and time domain. The realization of CPE behavior in the time domain

would require the use of fractional calculus and its unique feature of using infinite memory. See [30] for the related mathematical treatment of fractional order system in time domain. For the readers who are interested in an example for system identification applied to a fractional order model in the application of an electrochemical system, they are referred to [31].

For the applications such as SOC, SOH prognostics, EIS has been applied to batteries under many different operating conditions. For a lithium nickel-cobalt-aluminum (NCA) battery, the effect of SOC on EIS results has been studied in [28], which shows that the lower frequency segment of the impedance trajectory is dependent on the SOC. EIS has also been used for studying the effect of temperature on a battery [80] [126]. For lithium NCA [28] and lithium iron-phosphate (LiFePO4) batteries (in this thesis), it has been shown that lower temperature has the effect of enlarging the capacitive semi-circles and increasing the series resistance R_0.

For a lead-acid battery, researchers have shown that the EIS impedance plots vary as a function of the battery dc bias current [141]. For a lithium-based battery, EIS was performed at a single non-zero value of dc-bias current in [142], but no published literature appears to have investigated the effects of a range of dc bias current values on the impedance spectrum of lithium batteries in conjunction with temperature variation. This is important because the ability to accurately model battery performance under a wide range of operating currents and temperatures has a major impact on the accuracy of battery condition estimators that depend on these models.

In the literature, batteries have often been modeled using linear equivalent circuits [20[28, [32[33[45]. While nonlinear capacitors in the form of CPE and multiple RC

circuits have been used to model the complex shapes of battery impedance spectra, it is important to note that these complex equivalent circuit models retain a linear relationship between the steady-state electrode voltage and current. This is a key point to understanding the contribution of this thesis, particularly for the contents in chapter three and chapter five.

2.5.1.3 The Recursive System Identification Method for Parameter Estimation

The third method by which an equivalent circuit model's parameters can be populated is using recursive system identification with the excitation from the load. This method assumes that there exists sufficient excitation during the use of the battery such that the battery parameters can be recursively updated. To the author's best knowledge, Wiegman was the first researcher to recognize the opportunity to apply recursive system identification for battery under load [20]. In 1999, Wiegman demonstrated a system by which he could track the varying parameters of the equivalent circuit model under dynamic load conditions, achieving online monitoring which the HPPC and EIS methods could not. Unfortunately, Wiegman's contribution has been largely overlooked; out of the large literature devoted to the same approach, only a few quoted Wiegman's original work, including [21] and [41].

Instead of quoting Wiegman's work, most of the authors in the field seem to agree that the work by Plett in [23] [32] [33] is the beginning of the recursive system identification approach for obtaining equivalent circuit parameters online. In a series of three papers published in 2004 [23] [32] [33], Plett introduced his methodology in good details, including a tutorial on the recursive system identification using the Kalman filter, battery model derivations, and experimental results. The result of Plett's work was an

explosion of the application of the recursive system identification approach in the field, including [34] and [46]. In this thesis, the basics for recursive system identification will be covered in 2.9.3.

2.5.2 Curve-Fitted Behavioral Models

In addition to the equivalent circuit model, a different approach has been offered in the literature, namely the curve-fitted behavioral model. The purpose of these models is usually to provide the user a prediction on a quantity of interest, e.g. SOC, based on a data driven approach. The origin of this methodology in the area of electrochemical modeling is perhaps Peukert's work in 1897. What Peukert discovered was that different magnitudes of discharging current led to different coulombs available for consumption at the load.

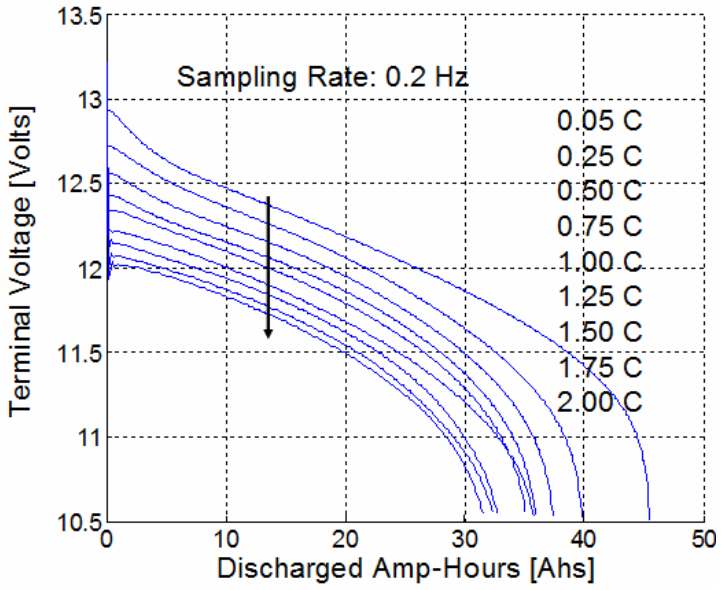

Figure 2.14 Voltage vs. extracted Ah for various constant current discharges for an Optima D34M lead-acid battery

Figure 2.14 shows experiment data for battery voltage against the extracted Ah for various constant current discharges for an Optima D34M lead-acid battery. As seen

in Figure 2.14, the battery's voltage collapses earlier under a higher current value, causing the extracted Ah considerably smaller then it would otherwise be.

This behavior is not explained by thermodynamics which assumes the equilibrium condition, i.e. an infinitesimal discharging current. However, when considering the necessarily present battery parasitic resistance and the Butler-Volmer relationship on the electrodes, the phenomenon is at least partially explained. Additionally, higher current can lead to an earlier depletion of ions in the electrolyte region close to the electrodes, causing a premature drop in voltage. Regardless of the underlying physical causes, the famous Peukert's law attempted to model such a phenomenon with the following [20]:

$$K\, I^{n-1} = \text{const.},\ n > 1 \qquad (2.5.1)$$

, where K is the available battery capacity in [Ah]. In (2.5.1), K is now a function of discharge current. A law such as this provides the user a more realistic expectation for the Ah available for extraction based on the discharge current value. However, the literature has shown that lithium-ion cells do not exhibit the same Peukert relationship as lead-acid batteries, as seen in Figure 2.15 [51]. This could be due to the different diffusion relationship lithium cells have.

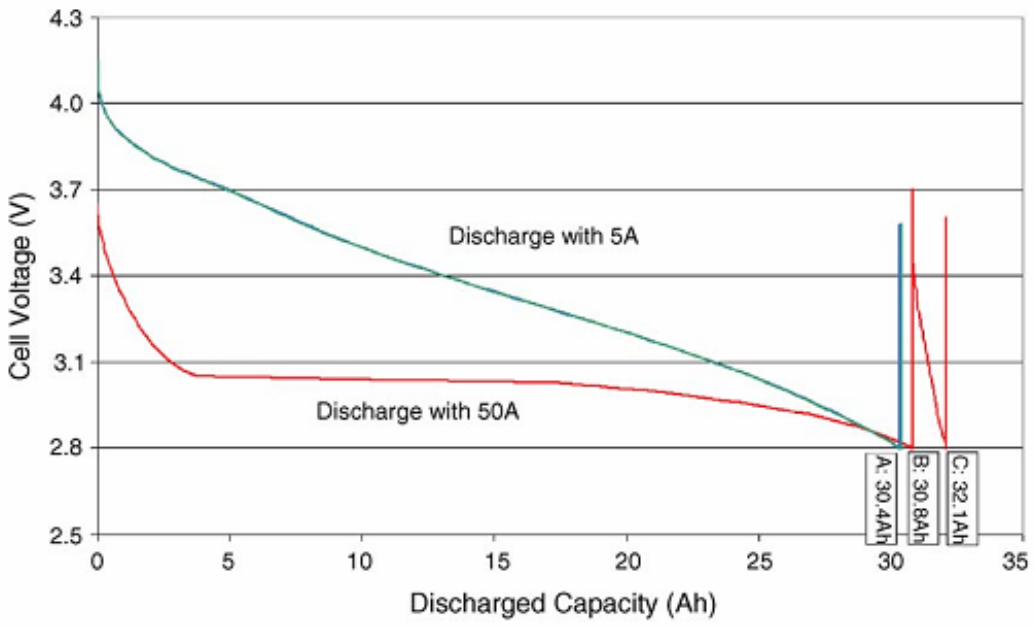

Figure 2.15 Voltage vs. extracted Ah for two constant current discharges for a lithium-ion cell [51]

Further advances were made using Peukert's discovery for the implementation of online battery SOC estimation on electric vehicles and other applications. Fuzzy logic or other sophisticated algorithms were used to formulize the relationship between available charge and other measurable quantities such as current magnitude [48] [52]. Other works adapt Peukert's discovery in their SOC estimation with more straightforward formulations; these normalize the Ah rating of their battery with respect to current magnitude and sometimes with temperature [53] [54]. When calibrated well for the intended application, these methods can demonstrate good results.

2.5.3 Physics-Based Models

This genre of models has attracted much research activity in the recent years due to its ability to relate theoretical electrochemical phenomena, such as diffusion and charge transfer, with measurable terminal characteristics, voltage and current. One of the

first papers published and frequently cited by subsequent literature is the 1993 Doyle, Fuller, and Newman paper [55]. In the following, the derivation of the Newman model is summarized using the original notations.

2.5.3.1 A Summary for the Physics-Based Model Proposed by Fuller et al

The Newman model considers the galvanostatic charging/discharging behavior of the cell structure in Figure 2.16.

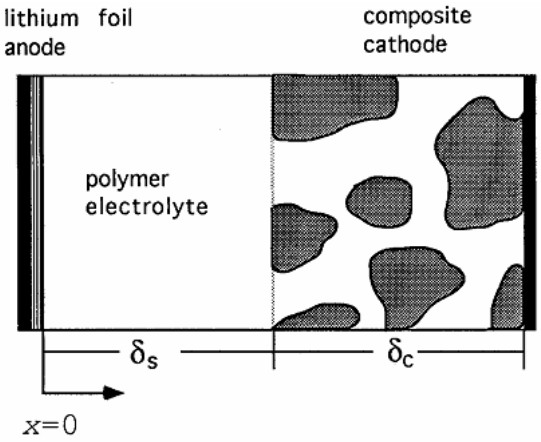

Figure 2.16 An one dimensional lithium/polymer cell sandwich in Newman model [55]

The following table lists the symbols, subscripts, and superscripts from the paper by Doyle et al [55].

Table 2.1 List of symbols, subscripts, and superscripts in [55]

Symbol	Interpretation	Unit
a	specific interfacial area	$\frac{m^2}{m^3}$
c	concentration of electrolyte	$\frac{mol}{m^3}$

c_0	concentration of polymer solvent	$\frac{mol}{m^3}$
c_i	concentration of species i	$\frac{mol}{m^3}$
c_T	maximum concentration in solid	$\frac{mol}{m^3}$
c_s	concentration in solid	$\frac{mol}{m^3}$
c_{max}	maximum concentration in polymer	$\frac{mol}{m^3}$
c^0	initial concentration in polymer	$\frac{mol}{m^3}$
D, D_s	diffusion coefficient of electrolyte in the polymer and of lithium in the solid matrix	$\frac{m^2}{s}$
f	activity coefficient	/
F	Faraday's constant = 96487	$\frac{C}{eq}$
i	current density	$\frac{A}{m^2}$
i_0	exchange current density	$\frac{A}{m^2}$
I	superficial current density	$\frac{A}{m^2}$
j_n	pore wall flux of lithium ions	$\frac{mol}{s\ m^2}$
k_2	reaction rate constant at cathode/polymer interface	$\frac{m^4}{mol\ s}$
k_{a1}	anodic reaction rate constant	$\frac{m^3}{s}$
k_{c1}	cathodic reaction rate constant	$\frac{m^3}{s}$
K_{ij}	frictional coefficient	$\frac{Js}{m^5}$

n	number of electrons transferred in electrode reaction	/
N_i	molar flux in x direction of species i	$\frac{mol}{s\ m^2}$
r	distance normal to surface of cathode material	M
R	universal gas constant = 8.3143	$\frac{J}{mol\ K}$
R_s	radius of cathode material	M
s_i	stochiometric coefficient of species i in electrode reaction	/
t	time	S
t_i^0	transference number (fraction of total electric current that anions and cations carry in passing through an electrolytic solution) of species i	/
T	temperature	K
u	utilization of intercalation material	/
U	open-circuit potential	V
v_i	velocity of species i	$\frac{m}{s}$
x	distance from the anode	m
z_i	charge number of species i	/
α	transfer coefficient between 0 to 1, as in the Butler-Volmer equation	/
β	activity coefficient correction	/
δ	dimensionless current density	/
δ_s	thickness of separator	m
δ_c	thickness of composite cathode	m
ε	porosity of electrode	/
ζ	activity coefficient correction	s
η	surface potential	V
Θ_p	site concentration in polymer	/
Θ_s	site concentration in solid matrix	/

κ	conductivity of electrolyte	$\frac{S}{m}$
ν	dimensionless exchange current density	/
ν_+, ν_-	number of cations and anions into which a mole of electrolyte dissociates	/
σ	conductivity of solid matrix	$\frac{S}{m}$
τ	dimensionless time	/
υ_i	electrochemical potential of species i	$\frac{J}{mol}$
Φ	electrical potential	V
Subscript	**Interpretation**	
c	cathode	
r	reference state	
s	solid state	
T	maximum concentration in intercalation material	
1	solid matrix	
2	solution phase	
Superscript	**Interpretation**	
0	solvent, or initial condition	
θ	standard cell potential	

It is noted in [55] that the presented model does not include the second order mechanisms such as film formation and volume change. As a result, this version of the model cannot be used for studying aging properties. The separator consists of a polymer material that serves as the solvent for a lithium salt. Using the polymer as the reference material and assume its velocity as zero, the mass transfer equation (2.5.2) is rewritten as (2.5.3).

$$c_i \nabla \mu_i = \sum_{i \neq j} K_{ij}\left(v_j - v_i \right) \tag{2.5.2}$$

$$N_+ = -\nu_+ D \nabla c + \frac{i t_1^0}{z_+ F} \tag{2.5.3}$$

$$N_- = -\nu_- D \nabla c + \frac{i t_1^0}{z_- F}$$

The material balance for the salt in the separator is enforced with:

$$\frac{\partial c}{\partial t} = \nabla \cdot \left(D(c) \left(1 - \frac{d(\ln c_0)}{d(\ln c)} \right) \nabla c \right) - \frac{i_2 \nabla t_+^0(c)}{z_+ \nu_+ F} \tag{2.5.4}$$

The current in the solution phase, i_2, is related to both the potential gradient and the electrochemical gradient and is given as:

$$i_2 = -\kappa(c) \nabla \Phi_2 - \frac{\kappa(c) RT}{F} \left(1 + \frac{\partial \ln f}{\partial \ln c} \right) \left(\frac{s_+}{n \nu_+} + \frac{t_+^0(c)}{z_+ \nu_+} \right) \nabla \ln c \tag{2.5.5}$$

At the lithium anode, x is set to be 0. The charge-transfer reaction that occurs at the electrode following the Butler-Volmer equation is given as:

$$I = i_{01} \left[\exp\left(\frac{\alpha_{a1} F \eta_{s1}}{RT} \right) - \exp\left(\frac{\alpha_{c1} F \eta_{s1}}{RT} \right) \right] \tag{2.5.6}$$
$$\eta_{s1} = \Phi_1 - \Phi_2 - U_1$$
$$i_{01} = F\left(k_{a1}\right)^{\alpha c1}\left(k_{c1}\right)^{\alpha a1}\left(c - c_{max}\right)^{\alpha c1}\left(c\right)^{\alpha a1}$$

The current model used here, the reaction stoichiometry, is intended for the polymer electrolyte. For the liquid electrolyte, the model can be further reduced as a simple charge-transfer process. The potential of the solid lithium phase is set to zero as the boundary condition at x = 0. The other boundary condition is equating the net transfer of current at the interface.

$$N_+ = \frac{I}{F} \text{ at } x = 0 \tag{2.5.7}$$

The flux and concentration of each species and the potential are assumed to be continuous at the other boundary, $x = \delta_s$. Because the composite cathode consists of both the solid active particles and the polymer/salt electrolyte, the model assumes the volume fraction of each component is known. The two phases are treated as superimposed continua, and the material balance on the lithium in the cathode gives:

$$\varepsilon\frac{\partial c}{\partial t} = \nabla\cdot\left(\varepsilon D(c)\nabla c\right) - \frac{i_2\nabla t_+^0(c)}{z_+\nu_+F} + \frac{aj_n(1-t_+^0)}{\nu_+} \tag{2.5.8}$$

The extra term j_n compared with (2.5.4) is the pore wall flux of lithium ions across the interface.

$$aj_n = \frac{-s_i}{nF}\nabla\cdot i_2 \tag{2.5.9}$$

Furthermore, the model takes into account of the composite nature of the cathode and the consequent lengthening of the ions' traveling path. The coefficients for the modification are also assumed known.

$$\begin{aligned}\kappa_{eff} &= \kappa\varepsilon^{1.5}\\ D_{eff} &= D\varepsilon^{0.5}\end{aligned} \tag{2.5.10}$$

The boundary condition at the solution phase is that the flux of each species is equal to zero at the end of the cathode where the current collector is connected.

$$N_i = 0 \text{ at } x = \delta_s + \delta_c \tag{2.5.11}$$

In addition, by assuming the active cathode particles are of spherical geometry with diffusion being the mechanism of transport of the lithium, the material balance is described by:

$$\frac{\partial c_s}{\partial t} = D_s\left[\frac{\partial^2 c_s}{\partial r^2} + \frac{2\partial c_s}{r\,\partial r}\right] \tag{2.5.12}$$

, where r is the direction normal to the spherical surface. The other boundary condition is the relationship between pore wall flux across the interface and the rate of diffusion of lithium ions into the surface of cathode active particle.

$$j_n = -D_s\frac{\partial c_s}{\partial r} \text{ at } r = R_s \tag{2.5.13}$$

A general expression for the OCV of the insertion material is given as the following:

$$U_2 = U_2^{\theta} - U_{ref}^{\theta} + \frac{RT}{F}\left(\ln\left(\frac{c_T - c_s}{c_s}\right) + \beta c_s + \zeta\right) \tag{2.5.14}$$

, where β and ζ are empirical values fitted to give more accurate results. By taking into account of the insertion process in the cathode, the kinetic expression for voltage and current relationship is given as:

$$\begin{aligned} i &= F\kappa_2\left(c_{max} - c\right)^{\alpha c} c^{\alpha a}\left[c_s \exp\left(\frac{\alpha_a F}{RT}(\eta - U')\right) - \left(c_T - c_s\right)\exp\left(-\frac{\alpha_c F}{RT}(\eta - U')\right)\right] \\ U' &= U_2^{\theta} - U_{ref}^{\theta} + \frac{RT}{F}\left(\beta c_s + \zeta\right) \\ \eta &= \Phi_1^{\theta} - \Phi_2^{\theta} \end{aligned} \tag{2.5.15}$$

Finally, the currents in both solid and solution phases are required to add up to the total current through the cathode:

$$I = i_1 + i_2 \tag{2.5.16}$$

The equations for simulating the physical phenomena in the example lithium anode, polymer electrolyte, and composite cathode system are now complete for the simulation of the system charging/discharging behavior.

2.5.3.2 Benefits and Disadvantages for the Physics based Modeling Approach

Since the publication of [55], many other works involving battery modeling has adopted the same physics based approach that's characterized by an emphasis in the interaction of the electrochemical domain and the electric domain using tools such as geometric assumptions, Fick's diffusion laws, and the Butler-Volmer kinetics equation [56] [70]. Additionally, finite element analysis software is now available for the physics based approach; for example, see [69].

An obvious benefit of the physics based approach is the explicit nature of the model. In fact, many researchers have proposed control schemes taking advantage of the explicitness of the model to achieve management and/or monitoring of aging [58] [59] [60] [61] [66]. In order for controls engineer to take advantage of the physics based model while maintaining the ease of implementation, modifications are also frequently made to the partial differential equations based physics models; see [60] and [61] for example.

It is also pointed out here that the physics based models usually involve certain assumptions that enable their derivation. [68], for example, compares the assumptions of

one-dimension vs. two-dimension for the sandwich cell structure. Additionally, "fudging" coefficients such as the effective traveling length in (2.5.10) is more likely selected based on curve fitting performance than actual measurements. In general, the physically meaningful parameters are not readily available except to the manufacturers of the cells, who usually guard their trade secrets and patents rigorously. One practice is to use values for parameters based on available literature, but the variety of cells and materials available far exceeds the ones that have published data.

From an electrical engineering perspective, it would be desirable to estimate the parameters of the physics based model based on the measurable terminal quantities, i.e. voltage, current, and temperature. However, given the complexity of the model and the sheer number of the parameters, it is unlikely that all the parameters of the model will be found statistically significant. The concept of statistically significance will be covered in 2.9.1. It suffices to point out here that a parameter's existence in the model is supported by the data only if the estimated parameter value is statistically significant. [63] studied the model structure proposed in [55] and found that many parameters are unidentifiable or statistically insignificant. As pointed out in [63], while the physics based model's parameters can be numerically fitted and the model with the fitted parameters can achieve good results in battery terminal response prediction, the internal states and insights are unreliable as a result of the lack of information in Fisher's sense. The interested reader is also directed to another example for studying the identifiability of the physics-based model in [64]. See 2.9.1 for an introduction of some concepts in statistics relevant to this work, including the Fisher information matrix.

2.6 State-of-Charge Estimation

One of the most studied metrics in a BMS is the SOC. The strong interest on the SOC metric is due to the perceived utility of the SOC in predicting the remaining battery use time/vehicle mileage until depletion. This perceived utility perhaps stems from the common experience with the fuel gauge in a gasoline vehicle which correlates well with the remaining mileage. A few difficulties exist for applying the same approach with battery.

First is that a direct measurement of the SOC is usually not available. Except for the flooded lead-acid batteries for which a hydrometer is available for monitoring the lead-acid battery electrolyte density, thus the make up of the electrolyte and subsequently the SOC [71], SOC usually cannot be measured directly.

The second difficulty is that the application's requirement for power delivery is not guaranteed to be met by the battery even if the stored charge has not been depleted. One example of this dilemma is the Peukert's law in (2.5.1), which shows the available charge decreases when the required discharge rate increases, i.e. voltage drop too significant for power delivery under high load. Another scenario in which stored charge does not guaranteed the delivery of required power is at lower temperature. At lower temperature, the reactions in a battery decrease their activity rates as described by the empirical Arrenius relationship [14]:

$$k = A \exp\left(-\frac{E_A}{RT}\right) \tag{2.6.1}$$

, where k is a rate constant and E_A has units of energy. A direct consequence of (2.6.1) is that battery has a higher impedance value at lower temperature [28], reducing its power

capability as a result. In addition from the discussion of thermodynamics in 2.4.1, the OCV of a battery drops as the temperature decreases, further reducing the battery power in the low temperature operating region.

Despite the difficulties, the SOC metric has remained an interest of the literature. The remaining of the section is devoted to a review of the SOC estimation methods proposed by researchers in the field.

2.6.1 Coulomb counting

The most straightforward method to estimate SOC is coulomb counting. The method assumes a fixed amount of charge, Q_{total}, is available after the battery is fully charged. The SOC is then normalized as:

$$SOC = \frac{Q_{total} - Q_{out}}{Q_{total}} \text{ x } 100\% \qquad (2.6.2)$$

As discussed in 2.5.2, different discharge current magnitudes would give the battery different available charge, Q_{total}. Some works adapt the Peukert modification for Q_{total} to, such as [53], [54], and [72].

The coulomb counting method is susceptible to current measurement noise. Due to the integration of current sensor error overtime, the coulomb counting method needs to be reset to ensure reasonable performance. The SOC value is usually reset at 100% after a full charge. This ensures the reliability of the coulomb counting method as long as the charging algorithm is consistent. Another issue with coulomb counting method is that not all the electrons are absorbed by the battery during charge, i.e. the coulomb efficiency is not 100% [73]. As a result, the coulomb counting method needs to have information

about the coulomb efficiency of the battery for estimation accuracy during regenerative charging.

2.6.2 Voltage-based methods

Another method to determine the SOC is by its terminal voltage, either in open circuit or connected to an external load. The open-circuit terminal voltage is correlated with the SOC based on thermodynamics. However, the open-circuit terminal voltage measurement needs to be taken after a rest period in order for the diffusion process inside the battery to be completed. This rest period requirement greatly reduces the opportunities for taking advantage of this correlation to accurately predict SOC in an online battery monitoring application. The terminal voltage with an external load can be measured online, but the voltage reading's correlation to SOC is reduced due to voltage fluctuations caused by load current variations and the diffusion process dynamics.

In order to overcome the lack of measurement for OCV during loaded condition, researchers have proposed variants of observer and Kalman filter to estimate the OCV and SOC. For this linear filter approach, the estimated states, usually including OCV and/or SOC, are estimated recursively and updated at every sample time. In some earlier versions, the battery electrical circuit model is assumed to have constant parameters and OCV or SOC is treated as a state to be estimated [42] [74]. Later versions of the filters proposed in literature include the estimation of parameters such as the resistance, as related in 2.5.1.3.

One difficulty in using estimated OCV for SOC estimation is that battery manufacturers have strived to maintain OCV stability even as the battery charge is being depleted. This characteristic of some lithium-ion cells makes the task of inferring SOC

from OCV even more challenging. For lithium-iron phosphate cells, the OCV vs. SOC curve is relatively flat, magnifying the error in SOC estimation due to error in OCV estimation, see Figure 2.18 for an example. The lead-acid battery, on the other hand, has a more pronounced drop of OCV as a function of decreasing SOC, as shown in Figure 2.17.

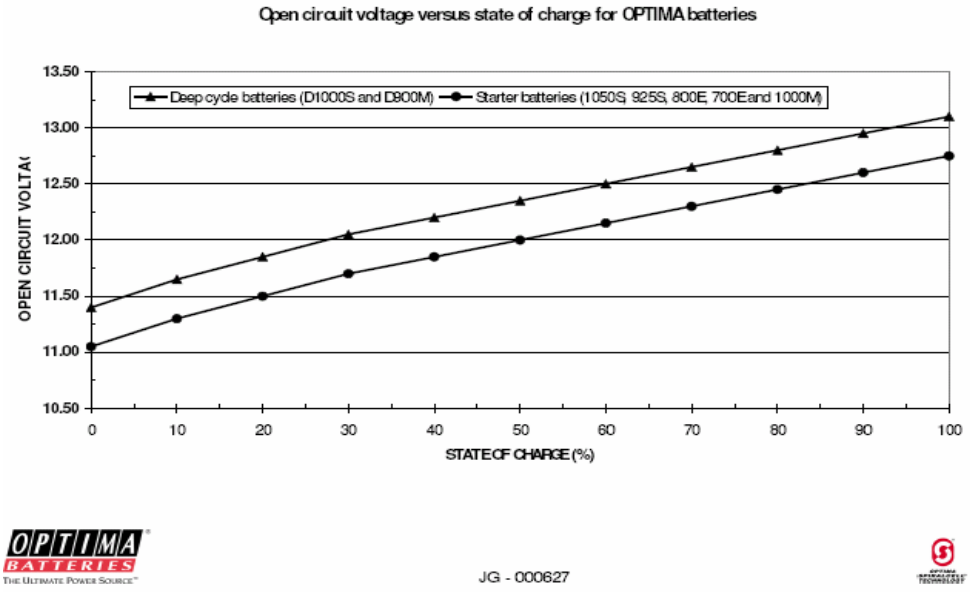

Figure 2.17 Optima lead-acid battery open-circuit voltage as a function of state-of-charge

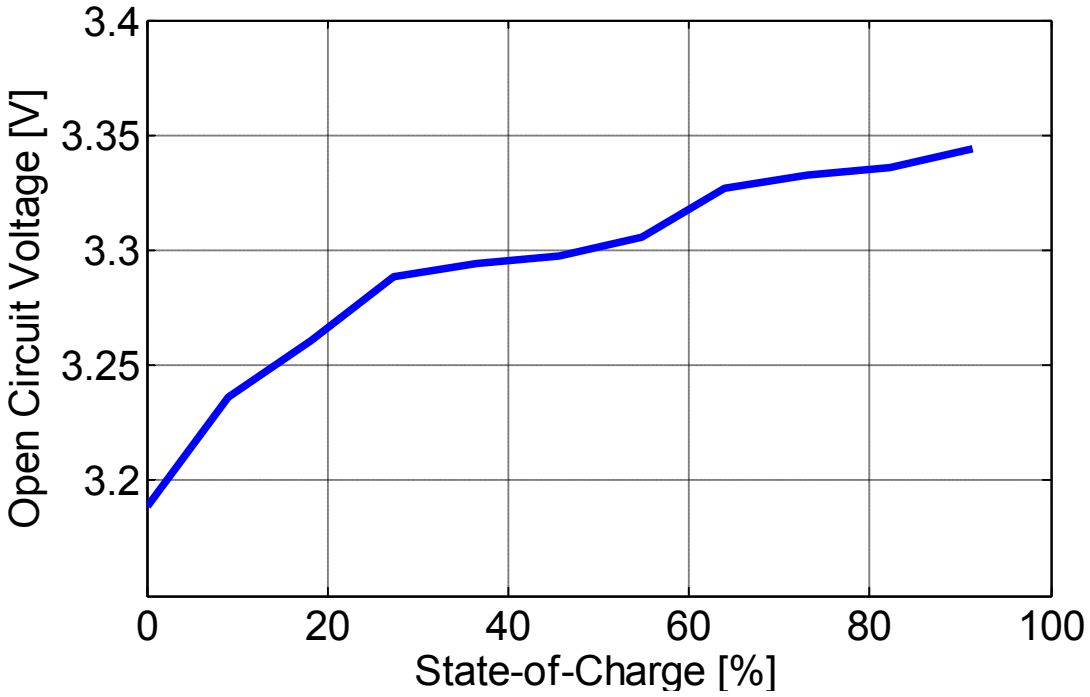

Figure 2.18 Experimental results for CALB Li-iron phosphate Cell open-circuit voltage vs. state-of-charge relationship

In addition, the relationship between OCV vs. SOC is usually obtained offline via procedures such as the HPPC test. When implemented to a recursive algorithm, the empirically obtained data is usually fitted into an equation to estimate SOC. The fitting process can also cause an error for the relationship of SOC as a function of OCV, which cannot be corrected by the recursive estimation; for an analysis tackling this source of inaccuracy, the interested reader is referred to [75].

2.6.3 Impedance-based methods

For various types of batteries, impedance-based methods have been proposed to estimate SOC. The basic idea is to measure the impedance spectra at different SOCs in an effort to correlate the measurements with the SOC values as determined by the coulomb counting method. Several parameters are proposed as possible candidates for

SOC indicators, including high frequency resistance, resonant frequency, and voltage relaxation time constant [76] [77] [78] [79].

As discussed in 2.5.1.2, EIS is an established technique for electrochemical system impedance measurement. For a review of using EIS and resistance measurement for SOC estimation, the interested reader is referred to [80]. For a lead-acid battery, Huet found that the series resistance value of the system is strongly dependent on SOC, providing a means for SOC estimation [80]. However, a later study by the same author and others cycled a lead-acid battery at both $\frac{C}{10}$ and $\frac{C}{100}$ rates found the resistance dependence on SOC is a function of the discharge rate, i.e. the dependency is found to be less strong at $\frac{C}{100}$ rate discharge cycling. Since the high-frequency resistance provides information on the $PbSO_4$ layer structure, it depends on the history of the previous cycling of the cell. For different discharge rates, different SOC values may correspond to the same value of high-frequency resistance [76].

Additionally, some researchers have found that the resonant frequency, i.e. the frequency at which the battery turns from capacitive to inductive, of a NiMH or NiCd battery is dependent on SOC [78]. Other researchers have pointed out the change in relaxation time constant as a function of SOC for lead-acid batteries [79]. The common characteristic of all these methods is the establishment of an empirical relationship between one measurable quantity and the SOC as determined by coulomb counting. This empirical relationship is then proposed as the substitute measurement for SOC. Two main drawbacks of this approach are briefly discussed here. The first is the required measurement may not be readily available. To perform EIS, specialized equipment is

needed, and the battery is required to be at no load condition. The second drawback is the potential confounding of the SOC and other factors on the measured metric. For example, the temperature effect on the value of battery impedance is a well established fact. Aged batteries also have more impedance in general. The change in impedance value is not easily attributed to either SOC or temperature or aging.

Finally, instead of relying on impedance of the whole frequency spectrum, some researchers have proposed using a single frequency injection. Coleman et al reported a SOC estimation scheme based on the high-frequency impedance (1 kHz) and the estimation of open-circuit voltage. The impedance is measured with an injected carrier frequency. The method essentially substitutes the EIS method with a single frequency to achieve the speed required for application. Based on the high-frequency impedance, the total impedance is inferred in a per unit fashion. The impedance information, along with some observation laws, deduces the OCV obtained through the Kirchoff voltage law. The claim is made that the internal resistance is not a reliable indicator of the SOC, having only little change for SOC > 50% and this approach helps mitigate that limitation.

2.6.4 Empirical data driven methods

This genre of methods is basically those curve-fitted behavioral models discussed in 2.5.2. The definition of SOC in these methods is usually more application focused. Instead of using a correlation between a measured metric and coulomb counting SOC to infer remaining charge, these methods set up data driven models that predict the end of discharge for their applications. The models can be based on neural networks or other types of data management techniques. The interested reader is referred to [49] and [50] for examples of this approach.

2.7 Battery Aging Processes, Methods for Aging Prediction, and State-of-Health Estimation

2.7.1 Battery Aging Processes

Another important metric a BMS may be required to provide is the SOH metric. SOH is a relative indicator for battery aging. Two important aging related metrics are commonly used. One is the battery full capacity under constant current discharge, and the other is the battery resistance. The two metrics are negatively correlated as aging increases the resistance and decreases the capacity; see [96] for experimental validation. Based on the discussion below, one of the main lithium-ion battery mechanisms involves the electrolyte decomposition and the subsequent increase in the solid electrolyte interhpase (SEI) layer. This provides a theoretical explanation to the correlation between resistance and capacity.

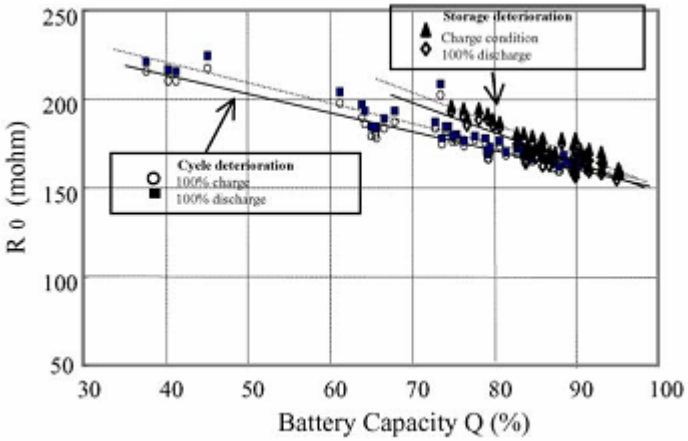

Figure 2.19 Battery resistance vs. capacity as aging progresses [96]

Different chemistries of battery have different physical mechanisms for aging. For lead-acid battery, grid corrosion, sulfation, change in pore structure in the electrode, and water loss have been cited for reasons leading to aging [84] [88]. For lithium-ion

batteries, the common mechanisms cited for aging include electrolyte decomposition leading to SEI layer buildup, solvent co-intercalation and subsequent cracking of formation in electrode, change in electrode volume and surface area due to SEI layer growth, and current collector corrosion [85] [86] [93] [95] [103] [104]. Figure 2.20 shows a schematic describing some aging mechanisms at the graphene layer/electrolyte interface.

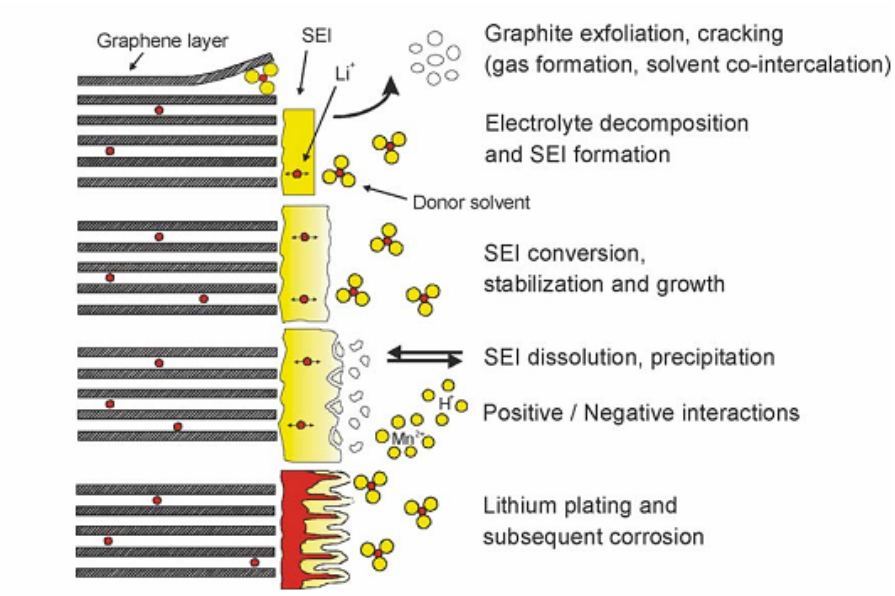

Figure 2.20 Changes at anode/electrolyte interface for a lithium ion battery [103]

For lithium-ion batteries, the storage time, storage temperature, and SOC during its storage are shown to be related to capacity loss [85] [93]. Additionally, temperature during operation has been identified as a major aging accelerator for batteries due to the facilitation of irreversible reactions [93]. Furthermore, the use history of the battery influences the battery aging; factors such as charging terminal voltage, depth of discharge, charging and discharging rates, have influence on battery's aging performance [90] [98].

One additional challenge for understanding battery aging process is that two modes of use, storage and cycling, can lead to different aging characteristics. The stored cells sometimes are used as baseline for comparing with data from cycling cells; see [2], [90], and [96] for example. Depending on cell chemistry, stored cells can sometimes show more aging in resistance; see [90] for instance.

2.7.2 Methods for Aging Prediction

For aging performance prediction of a battery, a few genres of methods are discussed in the literature. The first is to construct physics-based model that include secondary reactions responsible for aging [60] [61] [68] [88] [99]. This approach relies on detailed modeling effort discussed in 2.5.3; consequently, the disadvantages of the physics-based approach are inherent to this method of aging prediction. Furthermore, the aging mechanisms are usually secondary and smaller in their response magnitude compared with the primary reactions. This could make ascertaining their effects with experimental data more difficult. In addition, to implement these partial differential equations based models in control applications, further simplifications to the models are required. Works have been proposed to adapt complicated aging models into forms suitable for control application [60] [61], and the authors pointed out the reliability of their simplified models solely depends on the quality of the original work they adapted from.

The second method focuses on the empirical fitting of aging metrics based aging data. This approach usually involves the following steps [2] [85] [90] [91] [92] [95] [96] [97] [98] [105] [111] [112] [113].

(1) Placing batteries under specified test conditions. The test conditions are

determined by the questions interested by the experimenter, e.g. influence of temperature, SOC, etc on aging.

(2) Periodic measurement of battery characteristic metrics, i.e. capacity and resistance. For resistance, both HPPC and EIS can be used.

(3) Empirical fitting of data to the selected models. The fitted models can be used to guide expectation of battery performance in the field. Additionally, the effect of the test conditions on aging can be numerically evaluated for quantification. However, as pointed out in [98], many works present only experimental curves on capacity and resistance without fitting of data to equations.

Hochgraf et al presented a study on cycling dynamics' effect on lithium-ion cell degradation [2]. At 40^0C, six cells were prepared with two of the cells subjected to each of the three drive conditions: baseline dynamics, modified (reduced) dynamics, and storage (calendar). The results showed that the reduced dynamics drive cycle could have a reduced aging characteristic compared with the baseline dynamics.

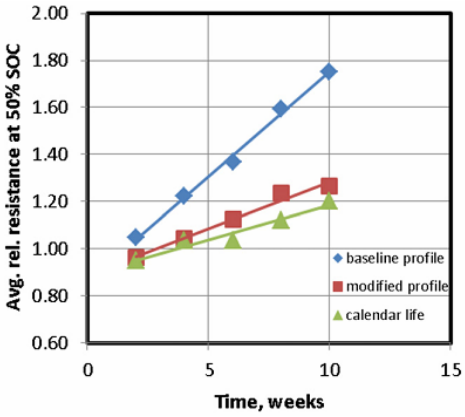

Figure 2.21 Average relative resistance at 50% SOC vs. time [2].

Broussely et al presented an experiment in which they subjected batteries under different float charge voltage and under different temperatures [85]. The cells were subjected to periodic capacity tests and the results were plotted against different test conditions. The data were used to infer on possible degradation mechanisms of the cells, such as the interactions of negative electrode with electrolyte.

Ecker et al presented a study where they considered both calendar and cycling conditions for aging [90]. They concluded for their cells the storage condition is more detrimental than the cycling condition, and they built a life prediction model based only on the storage condition. The model involves both statistical reasoning and electrochemical reasoning as presented in previous works. The change in impedance as a function of aging is then combined with thermal analysis for a more comprehensive lifetime modeling approach.

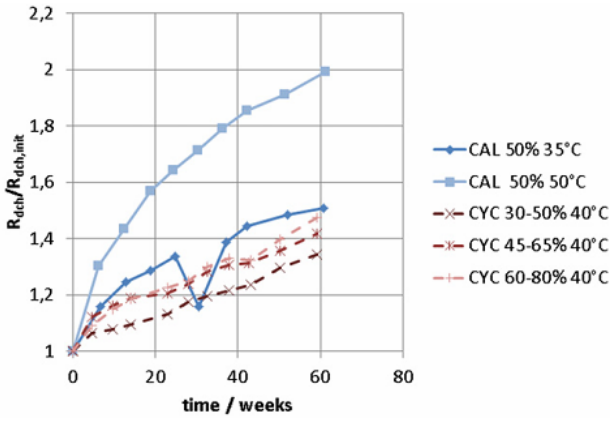

Figure 2.22 Overtime comparison between cycling and calendar conditions [90]

Dubarry et al presented work where they initially characterize 10 cells and found the consistency of the cells up to their satisfaction. Subsequently one of the cells was chosen as representative and was subjected to 2 C discharging cycles to induce aging. At fixed intervals, various magnitudes of current discharges were performed to characterize

the cycling cell. They identified two distinct stages of degradation: first the loss of lithium inventory and second the loss of active materials [91] [92].

Eom et al considered that the lifetime of cells under a set charge-discharge pattern originated from a statistical distribution. Failure time data from 12 cells under the same cycling condition were used to fit the distribution [97].

In [98], Li et al set up an experiment in which multiple stress factors on battery were examined, i.e. temperature, discharge rate, end of discharge voltage, charge rate, and end of charge voltage. Additional tests were done to examine the two-factor interactions between these factors. The results are fitted in an empirical model that predicts battery lifetime performance.

[110] by Thomas et al presented a method for accelerating aging the process with a statistical model. Temperature is found to heavily influence the aging process for stored cells. As a result, a statistical model is used to predict the cell's aging performance with both temperature and time as input variables. With the fitted model, the expected value of the cell's future resistance at room temperature can be determined.

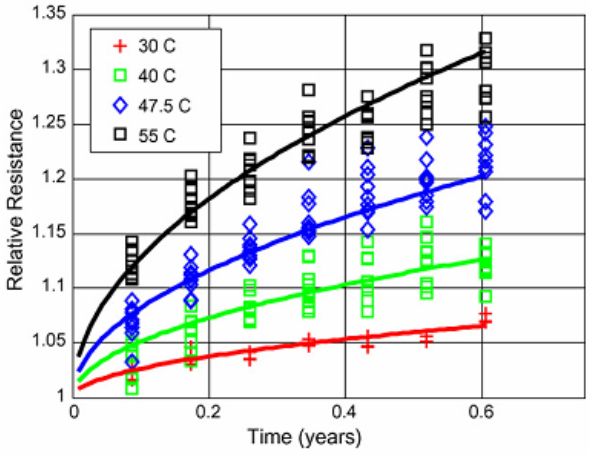

Figure 2.23 Aging data and fitted model [110]

Wang et al presented experimental work that considers Ah throughput, temperature, and discharge current rate as important aging factors [111]. They developed separate life models for different discharge current rates with Ah throughput as the main input. As some previous works, e.g. [90], they found aging is roughly a function of square root of time/Ah throughput.

The quality of statistical analysis in these works varies greatly. Some works could be improved by concepts such as design of experiment, statistical significance, and model checking. Based on the Monte Carlo method, [113] provides guidelines on building lifetime models with attention to prediction confidence interval. Additionally, [113] discusses on the optimal design concept.

A third category of methods to predict lifetime performance of the battery is based on the concept of accumulative stress/fatigue [106] [107]. The battery is assumed to be able to sustain a certain amount of accumulative stress in its life, and various operating conditions such as current magnitude and temperatures are assigned values for stress. The model then predicts the end of use time based on the remaining unused stress level. These methods rely heavily on the accurate assignment of stress value to different operating conditions.

2.7.3 State-of-Health Estimation

From the discussion in 2.7.1, the two metrics for determining the age of a battery cell are the capacity and the resistance. While in laboratory it is possible to perform a standard discharge in order to discover the cell's capacity, field application usually requires a more readily available solution. On the other hand, an estimate of the battery resistance is relatively quick to obtain on the measured voltage and current during drive

cycle or applied excitation. The recursive modeling approach discussed in 2.5.1.3 is particularly suitable for tracking the gradual change in resistance as battery ages, so long as other factors such as SOC and temperature are taken into consideration. While the convention for determining end of use for a rechargeable battery is when the battery can deliver only 80% of the original charge under the same charge-discharge procedure [115], tracking the change of battery resistance still informs the relative health of the battery. Furthermore, when considering battery power capability, the increase of resistance directly results in the power fade of the battery.

References that discuss the estimation or measurement of resistance as a means for SOH estimation include: [33], [77], [80], [83], [87], [116], and [117]. Whereas [77], [80], and [87] rely on impedance spectroscopy or random noise signal injection for impedance estimation, [33], [83], [117], and all other estimators that include resistance as a fitted variable rely on the drive cycle excitation. [116] implements specialized step signals to determine battery health.

Plett presented an interesting approach in which two versions of SOC, e.g. Ah counting and OCV inference, are compared to detect change battery health [118]. The key to this approach is that empirical evidence suggests OCV vs. SOC as defined by battery's present capacity is consistent throughout the aging process while OCV vs. discharged Ah varies. Figure 2.24 shows the empirical evidence on this claim.

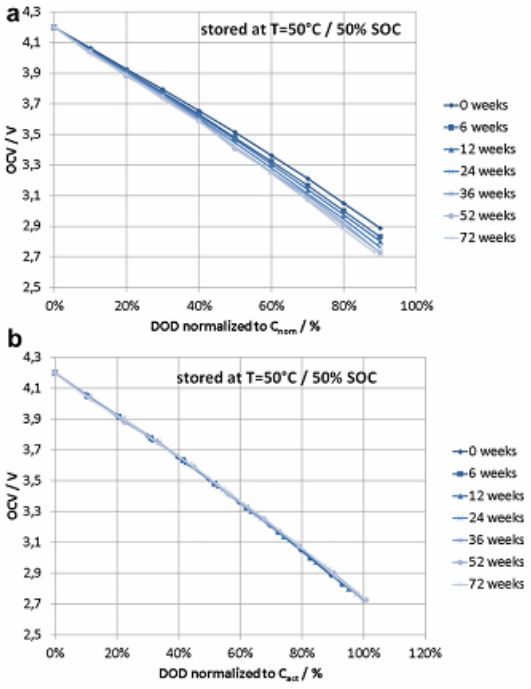

Figure 2.24 OCV curves over aging for cells stored at 500C and 50% SOC. Plot a shows the OCV curves vs. nominal DOD (depth-of-discharge) while plot b shows the OCV curves vs. actual DOD [90]

For the case that capacity information can be periodically obtained, researchers have proposed methods on predicting when capacity will drop below a threshold value [100] [101] [102]. So long as the decaying curvature of the capacity can be modeled, a probabilistic estimate on the time when the threshold is reached is possible. See Figure 2.25 and Figure 2.26 for illustration.

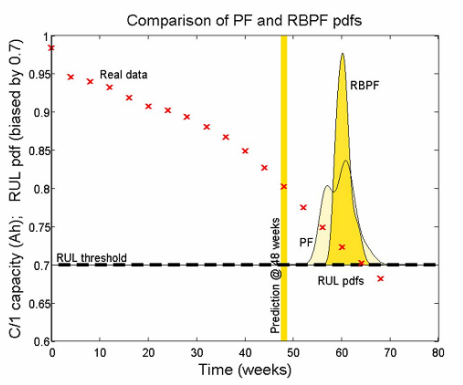

Figure 2.25 Particle Filter Probability Density for Predicting End of Use [100]

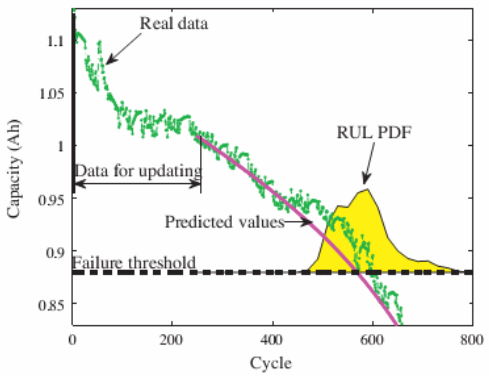

Figure 2.26 Particle Filter Probability Density for Predicting End of Use [101]

2.7.4 Lithium-Ion Cell Aging with a Superimposed AC waveform

In addition to prediction for battery aging performance, finding important factors for aging influence is also an important topic. An interesting factor in battery aging is the superimposed AC waveform. Bala et al demonstrated that with a superimposed AC waveform at 120 Hz [128], the tested $LiFePO_4$ cell was noticeably warmer under load, although the authors did not claim this warmer temperature necessarily leads to significantly faster aging. Electric vehicle power electronics DC bus filter design is another motivation for understanding whether a superimposed AC waveform leads to faster aging rate. In an electric vehicle design, the sizing of the DC bus capacitor, which filters the AC contents from the battery pack, requires engineering trade off. If superimposed AC waveforms are irrelevant to aging, the sizing of the capacitor may be reduced for cost benefits. If these AC waveforms were significant to aging, a quantitative metric for balancing between the right amount of filtering and cost would be important.

Hochgraf et al conducted an aging experiment in which three sets of $LiMn_2O_4$ cells were subjected to 1) normal drive cycles 2) reduced drive cycles mimicking the

effect of an ultracapacitor bank on the DC bus 3) storage condition [2]. They found that aging for the cells under reduced cycles is significantly less than that of those under normal cycles. In their study for cell aging under vehicle-to-grid condition, Peterson et al found that the amp-hours (Ah) throughput under drive condition causes significantly greater aging than those under the DC, grid connected condition [105]. While these two studies indicate the potential benefit for stronger filtering thus the aging impact of the superimposed AC waveforms, they do not provide a general understanding of the issue involved due to their use of arbitrary drive cycles. The experimental results of [2] are only good for illustrating the benefits achieved by one set of DC bus filtering for the particular drive cycle, while due to the focus on aging prediction Peterson et al merely commented on the need for an adjustment factor between two modes of use in [105].

Instead of using arbitrary cycles, Anders designed experiments testing differences in lithium-ion batteries' aging characteristics due to different shapes of discharge waveform, frequencies and temperatures [26]. The results were however only conclusive with respect to the temperature factor. Additionally, Okazaki et al conducted an aging experiment on lead-acid batteries to find out if superimposed AC waveform has an accelerating aging effect [129]. Their conclusion was negative.

2.8 State-of-Power and State-of-Function for Short-Term Power Estimation

The ability of a battery to fulfill its tasks involves more than having sufficient stored charge. The power capability of a battery depends on not only the charge remained in the battery but also temperature and its health. A key point is that the presence of charge remaining in the battery does not mean that the energy is accessible to

a particular application [20] [123]. Since battery manufacturers usually publish the operating voltage upper and lower limits, the BMS needs to insure that these limits are observed by preventing the sinking and sourcing of too much power during vehicle operation.

Two metrics have been proposed for battery power capability: state-of-function (SOF) and state-of-power (SOP). Since the introduction of the term in [123], various definitions of SOF have appeared in literature [119] [123] [124]. They are all related to the battery power capability. The work here follows the definition of SOF in [119] and that of SOP in [39]. The SOF represents a digital yes/no answer to the question whether battery is capable of fulfilling its task, while the SOP is a vernier signal indicating how much power is available. The SOF and SOP are defined as in (2.8.1) and (2.8.2).

$$\mathrm{SOF} = \begin{cases} 1 \text{ if } v_{min} \geq v_{limit} \\ 0 \text{ if } v_{min} < v_{limit} \end{cases} \tag{2.8.1}$$

$$\mathrm{SOP} = \frac{v_{limit}\left(v_{ocv} - v_{limit}\right)}{R} \tag{2.8.2}$$

v_{min} is the minimum voltage reached during load and v_{limit} is the low voltage limit specified by battery manufacturer. R is the steady state resistance of the battery, assuming the linear circuit model. The definitions in (2.8.1) and (2.8.2) are for discharging limit, whereas the charging version can be derived similarly.

The HPPC test proposed by the FreedomCAR consortium is perhaps the simplest short-term power capability tool [1]. By observing the voltage drop during the fixed-time current pulse at various SOC, the resistance and OCV for the associated condition can be used to help predict power performance.

Wiegman exercised his online-estimated models based on system identification techniques to predict the short-term voltage behavior of the battery under test [20]. Various modeling complexities are compared for prediction performance in Wiegman's work. Additionally, different current magnitudes are also used to check model performance. The presented results showed the prediction errors could be reduced by an increase in modeling complexity. The good performance of the model prediction allows the use of the model for short term power checking based on terminal voltage limitations.

For lead-acid batteries, van Bree et al presented a similar methodology involving a nonlinear equivalent circuit model [119]. The method to populate the equivalent circuit, however, was offline; van Bree et al gathered a batch of current and voltage data, and then perform an offline, nonlinear parameter estimation technique to populate the equivalent circuit parameters. In addition, the nonlinear characteristics of the lead-acid battery were modeled by including the Butler-Volmer equation in its original form instead of linearizing it as a resistor. The need for the nonlinear modeling is corroborated by the results in [121], where Buller et al used impedance spectroscopy to discover the change of electrode resistance as a function of current value for a lead-acid battery. Van Bree et al's results were promising as the agreement of the model prediction and the measurement data was strong. However, it should be noted that this method is only valid for the special case where the battery remains at a constant SOC. The method could be further improved if the identification process can be made recursive, thus allowing the adaptive estimation needed when SOC changes.

The Japanese company Hitachi introduced a smart car battery named "CYBOX" [120]. The idea is to measure, record, and compare terminal voltages during cold

cranking operation, while the open-circuit voltage is tracked for SOC indication. By pre-setting the criteria for recharging and replacing the batteries, the user will receive a SOF recommendation based on the performance of recent battery cold cranking events. A main advantage of this product is that it requires no current measurement for the algorithm. This simplification is based on the assumption that the power demand is relatively repeatable for a given cranking application, e.g. vehicle starting. Essentially, the impedance information is given by the transient response of the battery voltage during cranking, which keeps track of SOH. The SOC developed from the terminal voltage measurements is combined with the SOH information to provide an indicator of the SOF.

In [39], Wang et al presented a methodology in which the battery model is assumed to be an equivalent circuit depicted in Figure 2.27. With the drive cycle measured voltage and current, the model's parameters are recursively fitted, not unlike Wiegman's and Plett's works [20] [23]. After obtaining the model parameters, the battery was subjected to a voltage clamp at either upper or lower voltage limits and the resulting powers are measured. The model is also used to predict power based on the clamping voltages. The predicted and measured powers are then compared. They found that the two-second power prediction was more successful than 10-second prediction, while discharging at voltage limit causes more prediction error than charging. Wang et al concluded that the discrepancy is more due to the simplistic model structure than their recursive estimation algorithm. Plett also presented a work on using his recursively estimated model to predict battery power capability [124].

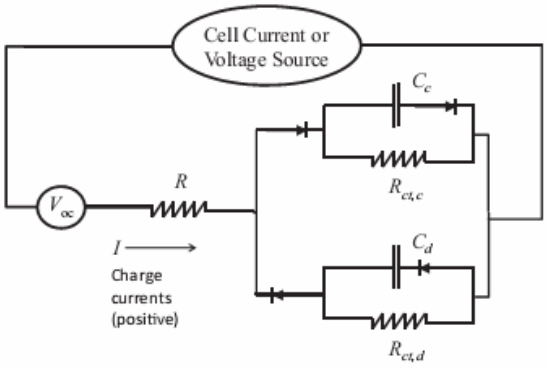

Figure 2.27 Equivalent circuit model used in [39]

Saha et al presented a work on using particle filter to predict the end of use, i.e. voltage collapse, for an unmanned aerial vehicle battery [122]. By assuming the flying pattern is consistent between different flights, the methodology is similar to what Saha proposed for battery life prognostics in [100]. The limitation of the method is obviously on the assumption of consistent flying pattern.

The discussion in this section so far have implicitly assumed that the battery is either working under a fixed temperature range or the recursive estimator can adapt to the change in model parameters due to temperature influence. To better model the battery power performance, explicit relationship between temperature and impedance may be important to consider. A few recent works have demonstrate that, for lithium ion batteries, the change in temperature can lead to change in impedance as observed in impedance spectroscopy data [125] [126]. In [127], Waag et al analyzed the impedance of lithium cells with nickel manganese cobalt oxide (NMC) with EIS and HPPC. The cells were under various conditions, including different temperatures. A set of representative results are shown in Figure 2.28.

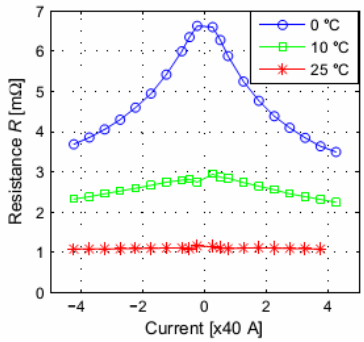

Figure 2.28 Current dependency of the cell total resistance for different temperatures [127]

The results shown in Figure 2.28 suggest that, for this particular type of cell, there may be benefits in including the Butler-Volmer relationship in the model for low temperature condition. Additionally, Waag et al have developed a nonlinear recursive estimation that's based on the Butler-Volmer equation overptential and robust under different temperatures [139]. However, the approach adopted in [139] does not allow for offline simulation since its adaptative scheme relies on data to adjust against temperatures.

2.9 Statistical Concepts and Methods

The work concerning electrical engineering applications for battery is statistical by nature. This statistical nature of the work is evident in the extensive use of equivalent circuits in the literature for modeling. While theoretical explanations exist for them, phenomenal equations such as the Arrenius form and Butler-Volmer equation were first derived from observations, hence statistical. Most of the works on battery lifetime have an empirical basis, and are also statistical in essence. Of course, extensive theories exist for deductively constructing battery models based on first principles such as diffusion; the discussion on the Newman battery model in 2.5.3 is an example. On the other hand, obtaining the parameters, e.g. diffusion coefficients, effective areas, etc, in the Newman

model can be challenging. The values are either provided from various sources, or an identification process is required. As discussed in 2.5.3, the interested reader is referred to [63] for the Newman model parameter identification issues. Even when the values of physical parameters are provided by prior knowledge, these were still obtained through measurements and should have associated uncertainties.

This statistical nature means much of the relevant knowledge has to be derived through a rigorous inductive process. The statistical concepts and methods are therefore important to the understanding of the work presented in the thesis.

2.9.1 Important Concepts in Statistics

2.9.1.1 Statistics

The British statistician Ronald A. Fisher considered three aspects of the science of statistics as important in his first book "Statistical Methods and Scientific Inference" [130]. These are 1) the study of populations 2) as the study of variation, and 3) as the study of methods of the reduction of data.

As a study of populations, statistics aims at understanding the aggregate of individuals. Some scientific theories such as kinetic theory of gases, theory of natural selection, and theory of chemical mass are essentially statistical. Once the statistical nature of these theories is lost, misinterpretation could arise [130]. The study of variation, or the study of error, can be understood best in the context of measurement uncertainty. Treating each measurement as an individual, the aim of statistics is to discover the aggregate properties such as the mean and variance. It is important to note that the objective of an experiment is rarely an individual result, but the population of results under similar circumstances, i.e. repeatability and generality.

The data reduction aspect of statistics is due to a practical necessity in the human thinking process. Given a batch of data, it is seldom that one can draw conclusions without the aid of models. The complexity of the models can vary from a simple mean value to all kinds of nonlinear mathematical functions. However, it is important to recognize the difference between models and "physical truth." The model as an aid for understanding can never truly represent a physical system in all of its details. As the famed statistician, George Box put it: "Essentially, all models are wrong, but some are useful" [131]. The recognition and treatment of modeling error are important for a data analyst.

2.9.1.2 Probability

While the concept of mathematical probability is well defined with Kolmogorov's axioms, its meaning in practical life is a contested subject. Two versions of probability's meaning have been proposed: statistical probability and inductive probability [132].

A statistical probability is the limiting value of the relative frequency with which some events happen. While it's possible a fair coin shows heads five straight times, the limiting value of the head's relative frequency is still 50%. This definition relies on important assumptions that the experiment is repeatable and can be repeated indefinitely. These assumptions are of course hypothetical as no resources would allow indefinite repetition of experiments and every experiment, despite the best controls, is unique.

The inductive probability is a gauge on individual personal belief regarding the occurrence of events. The main difference between statistical and inductive probability is that the former is empirical while the latter is logical. An example for inductive probability is a jury determining the probability of guilt based on given evidence.

Difficulties for inductive probability include quantification and its variation among rational minds despite the same access to evidence.

2.9.1.3 Continuous Random Variables and Probability Density Functions

The term random variable (RV) is defined as a numerical variable that takes different values with different probabilities [132]. In this work, we focus only on the continuous random variables that take on any value within a certain range. The probability density function (PDF) of a random variable is a mathematical function whose integral between an interval defines the probability of the RV taking a value within the integral. Let f(x) be the PDF, then the probability of an event occurring between x_1 and x_2 is:

$$\text{Prob}\,[x_1 < X \leq x_2] = \int_{x_1}^{x_2} f(x)dx \tag{2.9.1}$$

Many important PDFs have been proposed and utilized in applications. The most important one is arguably the Normal distribution defined as:

$$f(x) = \frac{1}{\sigma\sqrt{2\pi}}\exp\left(\frac{\frac{-1}{2}(x-\mu)^2}{\sigma^2}\right) \tag{2.9.2}$$

In (2.9.2), σ is the standard deviation and μ is the mean. The two parameters determine the shape of the PDF. This PDF, with zero mean and standard deviation at one, is shown below:

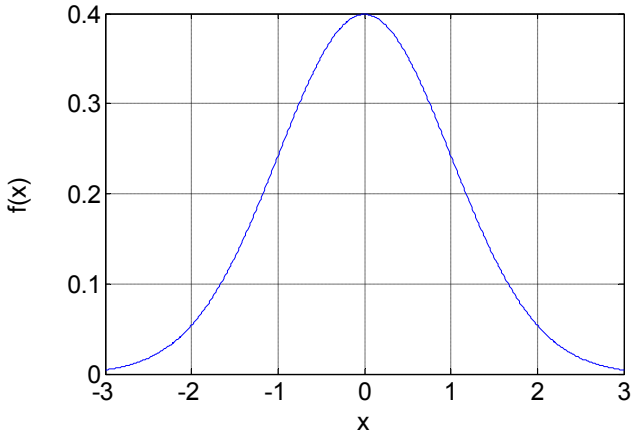

Figure 2.29 A normal distribution PDF with zero mean and standard deviation at one

An important distribution derived from the Normal distribution is the χ^2 distribution. Let Z's be independently and normally distributed with zero mean and unit standard deviation. The RV, Υ, with a χ^2 distribution with f degrees of freedom ($\chi^2(f)$) is:

$$\Upsilon = Z_1^2 + Z_2^2 + Z_3^2 + \ldots + Z_f^2 \qquad (2.9.3)$$

A $\chi^2(4)$ PDF is illustrated in Figure 2.30. The mean value of an RV Υ with $\chi^2(f)$ distribution is f and its variance is 2f [132].

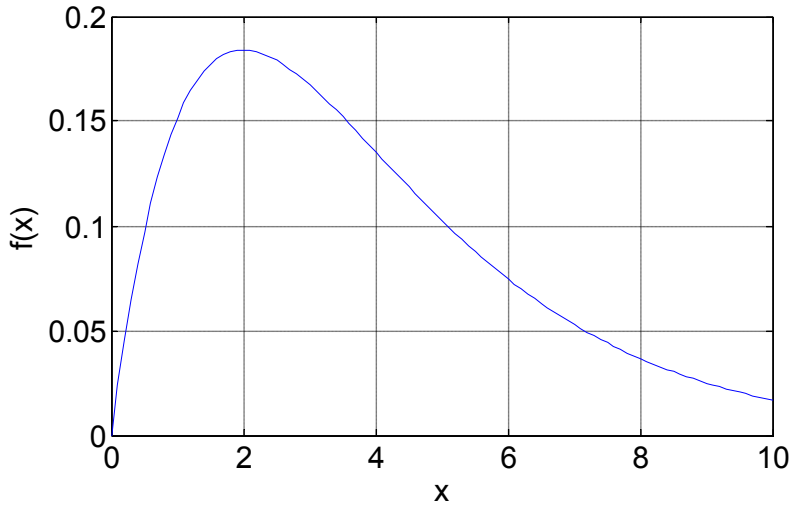

Figure 2.30 A $\chi^2(4)$ distribution PDF

Another important PDF is the t-distribution. The RV, T, follows a t-distribution of f degrees of freedom (t(f)):

$$T = \frac{Z}{\sqrt{\frac{\Upsilon}{f}}} \tag{2.9.4}$$

The statistic t for n samples of a normally distributed RV follows the t-distribution of n -1 degrees of freedom ($\mu \neq 0$, degrees of freedom = n if $\mu = 0$) and is given as:

$$t = \frac{\bar{x} - \mu}{s/\sqrt{n}}$$
$$s^2 = \frac{\sum_{i=1}^{n} \left(x_i - \bar{x}\right)^2}{n - 1} \tag{2.9.5}$$
$$\bar{x} = \frac{\sum_{i=1}^{n} x_i}{n}$$

, where s is the sample standard deviation and $\bar{x}$ is the sample mean.

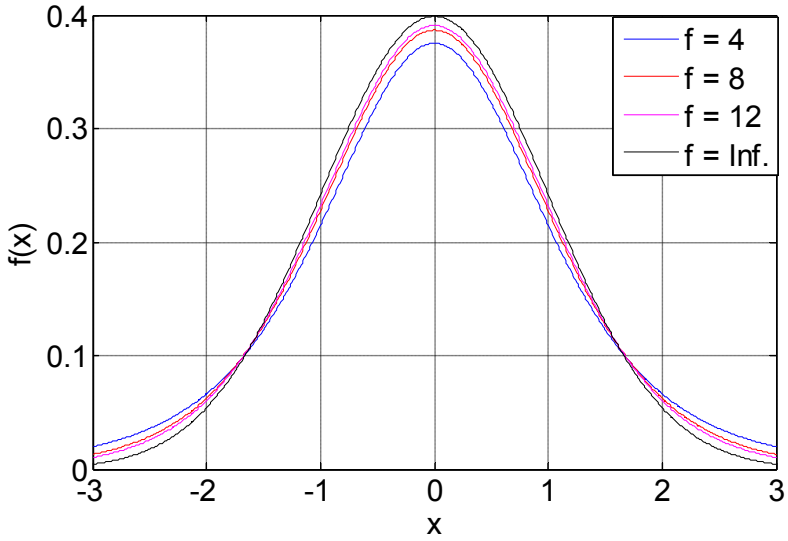

Figure 2.31 The PDF's of t-distribution with different degrees of freedom. The distribution asymptotically approaches the zero mean, unit variance normal distribution with greater degrees of freedom

Lastly, let Υ_1 and Υ_2 be independent χ^2 distributed RV's with degrees of freedom f_1 and f_2. The RV, V, is said to have an F distribution of degrees of freedom f_1 and f_2.

$$V = \frac{\Upsilon_1/f_1}{\Upsilon_2/f_2} \tag{2.9.6}$$

The use of the F-distribution arises in the significance testing of null hypothesis. In model checking, a null hypothesis is usually assumed and the data's conformity to the null hypothesis is checked with probability under the F-distribution, assuming the noise in the system is normally distributed and variance is stable between data points. The statistical technique is referred to as analysis of variance (ANOVA). The reader is referred to statistics literature such as [130] and [131] for more information.

2.9.1.4 Test of Significance

When an engineer or scientist attempts to describe a phenomenon with data, they usually present the data with the aid of a model. The soundness of the model is therefore of interest. For example, consider an experiment to compare two methods, denoted by MSI and SIB, that determine chlorine content in sewage effluents [133].

Table 2.2 Residual Chlorine Readings, Sewage Experiment [133]

Sample	MSI	SIB	d_i
1	0.39	0.36	-0.03
2	0.84	1.35	0.51
3	1.76	2.56	0.80
4	3.35	3.92	0.57
5	4.69	5.35	0.66
6	7.70	8.33	0.63
7	10.52	10.70	0.18
8	10.92	10.91	-0.01

If there was no significant difference between the two methods, then it is expected that sample difference, d_i, between MSI and SIB methods should have an average of zero. The t statistic for the d_i's based on (2.9.5) is calculated as 3.6454. The null hypothesis, that there is no difference between two methods, calls for an average of d_i's, thus the t statistic, to have a mean of zero. Assuming the null hypothesis, the probability (p-value) of the t-statistic taking the magnitude for the calculated value or a more extreme

one is 0.0082, less than 1 percent. The calculation of the probability can be visualized as finding the area of f(t) beyond the cutoff lines in Figure 2.32.

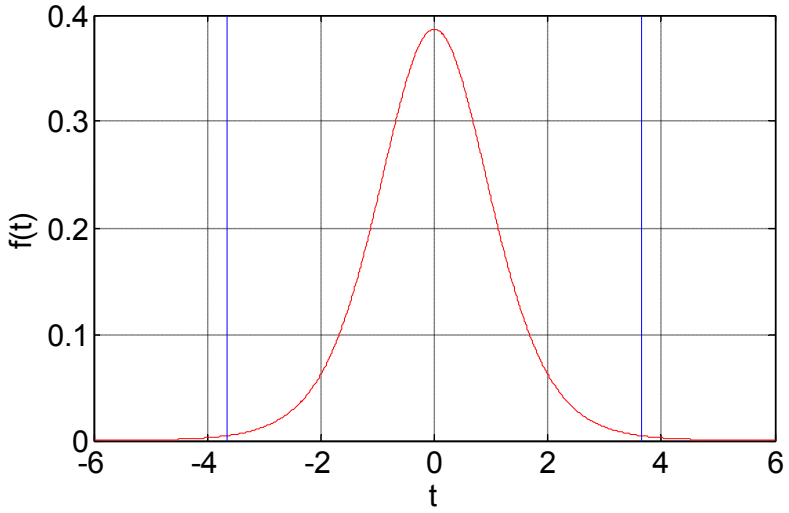

Figure 2.32 The PDF for t-distribution with 8 degrees of freedom and cut-off lines at t = 3.6454

While the interpretation of the test of significance is a contested subject, the inventor of the tool, Fisher, seemed to regard the test of significance as a guideline in reaching a conclusion based on the available evidence. When the p-value is somewhat ambiguous, e.g. in the range of 5% to 20%, Fisher would discuss how to improve the experiment to obtain better resolution. With a high p-value, Fisher would claim there's no statistical evidence to contradict the null-hypothesis, instead of accepting the null hypothesis as "correct." In the above example, the null-hypothesis is under strong suspicion with the given evidence and can be rejected if the significance probability is chosen as the customary 5%.

2.9.1.5 Covariance Matrix and Fisher Information

The covariance matrix arises when model parameters are estimated from data, using least squared error method. Specifically, the estimated parameters are RV's since

they are functions of the data. As such, estimated parameters have corresponding variances.

For the case of multiple linear regression, the generic model for N observations is [133]:

$$y_i = \beta_0 + \beta_1 x_{i1} + \beta_2 x_{i2} + \ldots + \beta_n x_{in} + \varepsilon_i \quad i = 1, 2, \ldots, N \tag{2.9.7}$$

where ε, the noise, is assumed to be normally distributed with zero mean and variance σ^2. It is possible to write (2.9.7) in a matrix form.

$$y = \mathbf{X\beta} + \varepsilon$$
$$\boldsymbol{\beta} = [\beta_0, \beta_1, \beta_2, \ldots, \beta_n]^T$$
$$\mathbf{X} = \begin{bmatrix} 1 & x_{11} & \ldots & x_{1k} \\ : & : & : & : \\ 1 & x_{N1} & \ldots & x_{Nk} \end{bmatrix} \tag{2.9.8}$$

By the pseudoinverse technique and least squares estimation, the estimated parameter vector $\hat{\boldsymbol{\beta}}$ is given as:

$$\hat{\boldsymbol{\beta}} = (\mathbf{X}^T\mathbf{X})^{-1}\mathbf{X}^T\mathbf{y} \tag{2.9.9}$$

The variance of $\hat{\boldsymbol{\beta}}$, i.e. the covariance matrix, is then derived as:

$$\mathrm{Var}(\hat{\boldsymbol{\beta}}) = (\mathbf{X}^T\mathbf{X})^{-1}\mathbf{X}^T\mathrm{Var}(y)((\mathbf{X}^T\mathbf{X})^{-1}\mathbf{X}^T)^T$$
$$\mathrm{Var}(y) = \sigma^2\mathbf{I} \tag{2.9.10}$$
$$\mathrm{Var}(\hat{\boldsymbol{\beta}}) = (X^TX)^{-1}\sigma^2$$

Since each estimated parameter $\hat{\beta}_i$ is an RV, a test of significance can be applied with the null hypothesis $\hat{\beta}_i = 0$. The purpose for the significance test is to ensure there is statistical evidence to support the term corresponding to $\hat{\beta}_i$ in the model.

Fisher introduced his concept of information in part as a tool for selecting number of samples in experiment design [130]. The issue at point is that given efficient statistical methods, whatever improvement to the precision of parameter estimates depends primarily on the data itself. When designing the experiment, it is worthwhile to investigate how much information is needed given a desired precision level. Additionally, Fisher would recommend the increase of precision by improvement of experimental techniques. On the other hand, for a given data set and a selected model structure, the information matrix can be obtained as the inverse of the covariance matrix, i.e. information is inversely proportional to variance. Hence, when the variance of a parameter estimate is so large relative to the estimate that the null hypothesis $\hat{\beta}_i = 0$ cannot be rejected, it is said that the data has not enough information/statistical evidence to support the parameter's existence.

The concept of Fisher information was later mathematically defined as the expected value of the negative Hessian matrix of the log likelihood function $f(X; \theta)$ at the true parameter value θ^*, where X is the observable data and θ is the parameter set. For a detailed treatment of the Fisher information as defined mathematically, the interested reader is referred to [134].

2.9.2 Design of Experiments

In the introduction of his second book "The Design of Experiments," Fisher remarked that there are two general lines of attack on which a critic argues against conclusions drawn from an experiment [130]. One is the deficiency of the interpretation/analysis of the experiment data, and the other is the logical structure of the experiment design. Fisher also argued that the two lines of criticism are two aspects of the same whole; if the experiment was not logically sound, then any interpretation that draws decisive conclusions is faulty. In these cases, the interpretation's failure lies in not recognizing the logical inability of the experiment to answer some/all of the questions of interest. It is also important to note that data analytical techniques usually cannot make up for the deficiency in the logical structure of the experiments.

Design of experiments thus seeks to maintain the logical integrity of the experiment for the purpose of answering specific questions. The rest of the subsection describes a tea tasting experiment used by Fisher in his book to illustrate some of the important concepts in design of experiments.

Fisher's tea tasting experiment aimed at determining whether a lady had the self-claimed ability to taste a cup of tea made with milk and discriminate whether the tea or milk was first added to the cup. Fisher's experiment consists in mixing eight cups of tea, four in one way and four in the other, and presenting them to the lady at a randomized order.

Table 2.3 An example of Fisher's tea tasting experiment

Order	1	2	3	4	5	6	7	8
Served first	Tea	Milk	Milk	Tea	Tea	Tea	Milk	Milk

The lady was told that two sets of four cups each was presented to her and she was to make a judgment on each of the eight cups. There are a total of 70 ways to separate eight cups into two groups of four; this is so because when choosing the first set of four cups consecutively, there are 8x7x5x6, or 1680, ways, and once the first set of four cups are selected the other set of four cups is also determined. However, that would be to count every possible set and every possible order. For each set, there can be 4x3x2x1, or 24 orders. Therefore there are 1680/24 = 70 ways to group the cups.

The inductive basis is the following: if the lady was guessing in random, she had an 1 in 70 chance of obtaining the completely correct grouping. The number 70 is important since it relates to the chance of getting the complete answer without the claimed ability. Notice the connection with the test of significance here: the null hypothesis is that the lady had not the claimed ability, and if she was to obtain the correct grouping under the null hypothesis, she'd be able to do so with an 1 in 70 chance.

The number of cups used thus determines the precision of the experiment. In this case, the precision is only up to 1 in 70. If the null hypothesis was to be declared invalid with a 1% probability, this experiment would never be able to achieve such a result. On the other hand, even with a tight requirement for rejecting the null hypothesis, "one in a million" could occur. Thus an isolated record itself is not sufficient for experimentally demonstrating a natural phenomenon; what is needed is a well established procedure that's repeated and rarely fails to give a statistically significant result.

Randomization is also an important aspect in safeguarding the results. The above inference reasoning is based on the assumption that absent of the claimed ability the lady's judgment is based on chance. This could easily not be the case; she could have

been differentiating the quality of tea and milk or the differences in the cups themselves. Perhaps the group that had milk added first also happened to have all their cups made by the same manufacturer. Randomization seeks to avoid confounding between the non-tested and tested hypotheses. Notice that it is not sufficient to claim that "all cups are made the same except for their order of adding tea and milk." This claim is simply impossible to enforce; there will always be certain uncontrollable differences, such as the temperature change during the serving of the teas. Only by randomization can the inference basis be protected.

A few steps could be taken to increase the precision of the experiment. The first one is to enlarge the number of cups involved in the experiment. This has the obvious effect of decreasing chance of obtaining correct grouping based on chance. The other two methods are 1) the reorganization of the experiment 2) the refinement of techniques.

With respect to the reorganization of the experiment, the experiment can increase precision by removing the restriction of grouping, i.e. randomly determine the order of adding milk and tea for each serving. In that case, the chance of obtaining the perfect result for the eight cups is 1 in $2^8 = 256$. The reorganization of the experiment can also decrease the precision of the experiment; for example if the two groups of servings are chosen to be 3 and 5 cups each, the chance of obtaining the perfect result under null hypothesis is 1 in 56.

The refinement of techniques may not be able to increase the precision of this particular test. But without certain precautions, the experiment may simply be impossible. The careful use of similar cups, tea, and water is implicitly assumed in this

tea tasting experiment. In other experiments, the refinement of techniques could involve the improvement of measurement that should decrease the noise level of the data.

2.9.3 Recursive Estimation and Kalman Filter

The classical linear regression technique involves least square estimation of parameters based on a given batch of data. The mathematical form for linear regression is shown from (2.9.7) to (2.9.9). A natural question arises with regard to this method of estimation: what should be done when data comes in sequentially? It is desired to monitor battery pack when the EV is operated, not when the operation terminates. Should the matrix operation from (2.9.7) to (2.9.9) be repeated as every new sample of data comes in, or is there a recursive method to achieve the parameter estimation? The least mean squares method (LMS) which allows for recursive estimation is described below.

Similar to (2.9.8), a linear function at sample time k can be written as:

$$\begin{aligned} &y(k) = X(k)\beta + \varepsilon \\ &\beta = [\beta_0, \beta_1, \beta_2, \ldots, \beta_n]^T \\ &X(k) = [1, x_1(k), x_1(k), \ldots, x_n(k)] \end{aligned} \tag{2.9.11}$$

Thus the predicted value at sample time k, $\hat{y}(k)$, and the corresponding error and squared error are:

$$\begin{aligned} &\hat{y}(k) = X(k)\hat{\beta} \\ &e(k) = y(k) - \hat{y}(k) \\ &e(k)^2 = \left(y(k) - \hat{y}(k)\right)^2 \end{aligned} \tag{2.9.12}$$

If the squared error function is to be minimized as a function of the parameters, the partial derivative of the squared error function should be zero.

$$\frac{\partial[y(k) - \hat{y}(k)]^2}{\partial \hat{\beta}} = -2(y(k) - \hat{y}(k))X(k) \tag{2.9.13}$$

The gradient for achieving zero for squared error function is shown in (2.9.13). To recursively estimate the parameter vector, $\hat{\beta}$, the previously obtained $\hat{\beta}(n-1)$ is updated along the gradient for minimizing squared error function.

$$\hat{\beta}(k) = \hat{\beta}(k-1) + cX^T(k)[y(k) - \hat{y}(k)] \tag{2.9.14}$$

In (2.9.14), the value c is the gain of the update. The theoretical upper bound for c is $\frac{2}{\lambda_{max}}$, where λ_{max} is the maximum eigenvalue of the autocorrelation matrix $E[x^Tx]$. For a more complete treatment of LMS method, the interested reader is referred to [135].

The famed Kalman filter has a similar structure to the LMS method discussed above. The main difference is that Kalman filter has an optimal gain that's determined based on the input and output variances. Specifically, the internal states/parameters in a Kalman filter are considered random variables perturbed by noise of a known variance. The perturbation and output prediction error provide the basis for estimating internal states' covariance matrix. Additionally, the output measurement also has noise of a known variance. These two variances are weighted to obtain the optimal gain for the update of states. For the application of system identification, the Kalman filter takes the following mathematical form. (2.9.15) is the state equation while (2.9.16) describes the recursive update of the terms. In (2.9.15), w and v are random noises with known covariance matrices of Q and R, respectively. In (2.9.16) the term P is the estimated

covariance matrix of the estimated parameters and K is the optimal gain based on the weighting of P and R.

$$\begin{aligned} \beta(k) &= \beta(k-1) + w(k) \\ y(k) &= X(k)\beta(k) + v(k) \end{aligned} \tag{2.9.15}$$

$$\begin{aligned} P^{-}(k) &= P^{+}(k-1) + Q \\ K(k) &= P^{-}(k)X^{T}(k)\left(X(k)P^{-}(k)X^{T}(k) + R(k)\right)^{-1} = P^{+}(k)X^{T}(k)R(k)^{-1} \\ \hat{\beta}(k) &= \hat{\beta}(k-1) + K(k)\left(y(k) - \hat{y}(k)\right) \\ P^{+}(k) &= \left(I - K(k)X(k)\right)P^{-}(k) \end{aligned} \tag{2.9.16}$$

2.9.4 Karl Pearson and Ronald A. Fisher

Statistical techniques have become pervasive in science. Fields such as biology, agriculture, and psychology have integrated statistics as a part of their disciplines. This development towards quantification in these previously qualitative fields is due to many researchers. However, two British personalities, Karl Pearson and R. A. Fisher, deserve to be recognized for their leading roles in introducing statistics into science. This subsection is devoted to their short biographies.

Karl Pearson was born in 1857 as Carl Pearson [136]. He later changed his name to Karl in tribute to Karl Marx. A man with keen interests in many fields, Pearson's studies included mathematics, political science, and linguistics. In the 1880's Pearson became involved with Francis Galton's work to bring mathematical rigor into biology. Galton's concept of correlation was refined by Pearson. Pearson is also credited with the discovery of skewed distributions and the chi-squared distribution. Aside from the useful statistical tools he developed, Pearson was more importantly a philosopher in the field of science. His book, the Grammar of Science (published in 1900), contains many interesting topics such as the relativity of motion, physics as geometry, and scientific laws as empirical formulations instead of rigid natural rules. Pearson was a writer with a

popular audience in mind, and his book is accessible to those with minimal background. Pearson's book is still highly relevant in the field of mathematical modeling and is recommended for anyone who is dissatisfied with the "clockwork" version of science taught in most secondary education curriculum [137].

Born in 1890, R. A. Fisher is noted not only for his contributions in statistics but also in biology. In biology, Fisher was known for his contributions related to the theory of natural selection. In statistics, his works were pioneering and included the analysis of variance, maximum likelihood estimation, statistical inference, design of experiment, etc. It would be no exaggeration to claim that Fisher has been the most influential character in the development of statistics as a scientific discipline. His works were quite different in many ways from his predecessors, including Pearson. As a result, a bitter controversy developed between the two men, and Fisher was correct on most of the contested issues with Pearson. Fisher was also a philosopher in the field of science. He devoted much space in his three books discussing the need for rigorous process to infer from data to conclusion, i.e. inferring from the particular to the general. These arguments require more technical background to comprehend compared with Pearson's Grammar of Science, and they can be found in [130].

2.10 Summary

From the discussion in the state-of-the-art review, several research opportunities can be identified. They are listed as follows:

1. *A statistical study on the effectiveness of the popular linear circuit model for different cell chemistries and different operating conditions, e.g. temperature.* The linear circuit model approximates the Butler-Volmer relationship as a

resistance. The need exists to investigate whether such an approximation is appropriate for particular cell chemistries and operating conditions. In Chapter three, a methodology is introduced to study the appropriateness of linear circuit model for lead-acid batteries, while an investigation of lithium-ion batteries at different temperatures is made for different temperatures in chapter five.

2. *The adaptation of Butler-Volmer based model for recursive system identification*. By recognizing the need to include the nonlinear behavior of Butler-Volmer relationship in the model, the need arises of adapting the new model for recursive system identification. The linear circuit model has been used in conjunction with system identification extensively in the literature. The recursive estimation scheme allows for model adaptation for aging, SOC changes, etc. Chapter three demonstrates a method by which the Butler-Volmer based model is adapted for recursive estimation.
3. *The incorporation of temperature as an explicit input that influences battery resistance and overpotential model.* The literature has illustrated that battery resistance and overpotential are functions dependent on operating temperature. Chapter five shows that for lithium-ion batteries, the overpotential resumes the Butler-Volmer relationship at lower temperatures, even though the linear circuit model appears adequate at room temperature. Additionally, the pure resistance of a lithium cell increases rapidly as temperature drops. Chapter five demonstrates these phenomena experimentally and offers a modeling approach that explicitly includes temperature as an input for both resistance and overpotential. Such a modeling approach can help better predict battery power performance.

4. *Better understanding of the use of recursive system identification for battery power prediction.* The recursive system identification allows for adaptive observation of battery model parameters online. This feature leads to the use of the adaptive model for power output prediction, SOP, in the literature. Chapter four illustrates a fundamental limitation of SOP within the context of recursive system identification. It then proceeds to propose an alternative approach, SOF, and shows SOF's theoretical probability limits for the prediction of battery power. The recursively obtained SOP results are also compared with the HPPC results on power prediction.
5. *A statistical design of experiment to investigate whether a superimposed AC waveform causes a different aging rate. If so, the quantification of such an effect can lead to better design guidelines for capacitor filter design.* The DC bus capacitor filter design involves an engineering trade off. If the aging of battery is not accelerated due to additional high frequency components, the DC bus capacitor can be downsized for cost benefits. Chapter six designs an experiment that first establishes the additional RMS value from superimposing an AC waveform on the discharging current can cause accelerated aging. The subsequent experiment then confirms RMS's influence in determining aging rate and demonstrates the statistically irrelevance of other factors such as frequency and waveform shapes. A methodology for quantifying the RMS effect on aging rate is also established in chapter six.

Chapter 3
Butler-Volmer Equation Based Battery System Identification

In this chapter, an improved nonlinear model for the electrode voltage-current relationship for online battery system identification is proposed. In contrast to the traditional linear-circuit model, the new approach employs a more accurate model of the battery electrode nonlinear steady-state voltage drop based on the Butler-Volmer equation. The new form uses an inverse hyperbolic sine approximation for the Butler-Volmer equation. Kalman filter-based system identification is proposed for determining the model parameters based on the measured voltage and current. Both the Butler-Volmer model and linear-circuit model have been implemented for lead-acid batteries and exercised using test data from a Corbin Sparrow electric vehicle. A comparison of predictions for the two models demonstrates the improvements that can be achieved using the new nonlinear model.

3.1 Linear Electric circuit and Butler-Volmer Battery Models

3.1.1 Introduction of linear-circuit and Butler-Volmer Battery Models

Figure 3.1 and Figure 3.2 illustrate the two battery models that are investigated in this work. The Butler-Volmer (BV) based model in Figure 3.1 is the proposed improved model while Figure 3.2 depicts the widely-used linear model. While differences exist among various battery modeling techniques found in the literature, linearization of the

BV equation is a feature common to most of them, usually accomplished using a resistor approximation, r_1.

Other than the electrode model, the remaining features in the battery models are shared in common: r_0 represents the ohmic voltage drops in the battery, the parallel r_1, C_1 circuit models the dynamic response of the electrode overpotential for the linear-circuit model while the LPF in Figure 3.1 stands for "low-pass filtering" and provides dynamic response modeling, and the v_{ocv} voltage source provides the battery open-circuit voltage.

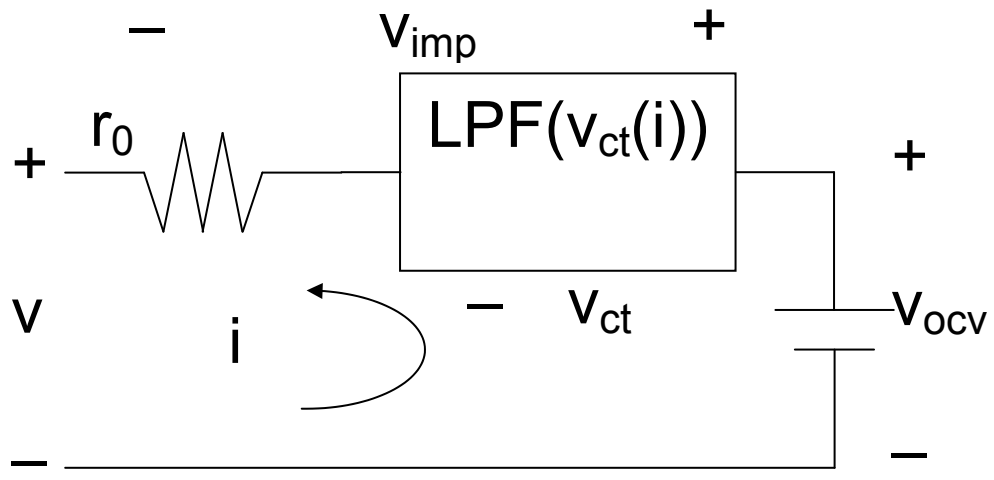

Figure 3.1 Nonlinear battery model incorporating Butler-Volmer electrode equation

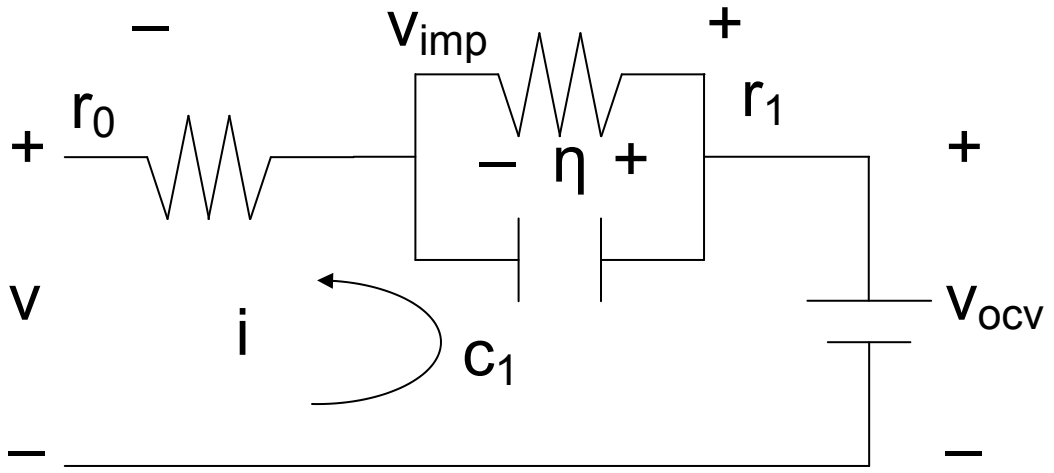

Figure 3.2 Conventional linear circuit-based battery model

It is recognized that adopting a first-order dynamic response for the battery model represents a significant simplification of the actual battery dynamics which are complicated, i.e. multiple-poles and dependent on battery operating conditions, including its SOC. The EIS results can be used to obtain a sense for the reduction in complexity. In Figure 3.3, the EIS graph shows positive imaginary impedance at high frequency, suggesting the presence of an inductive element. In addition, the RC circuit modeled in Figure 3.2 could have resulted in one semi-circle in the EIS graph, but Figure 3.3 suggests the presence of at least two such circles. However, since the focus of this work is on modeling the battery's steady-state terminal characteristics, the first-order dynamic model is satisfactory here.

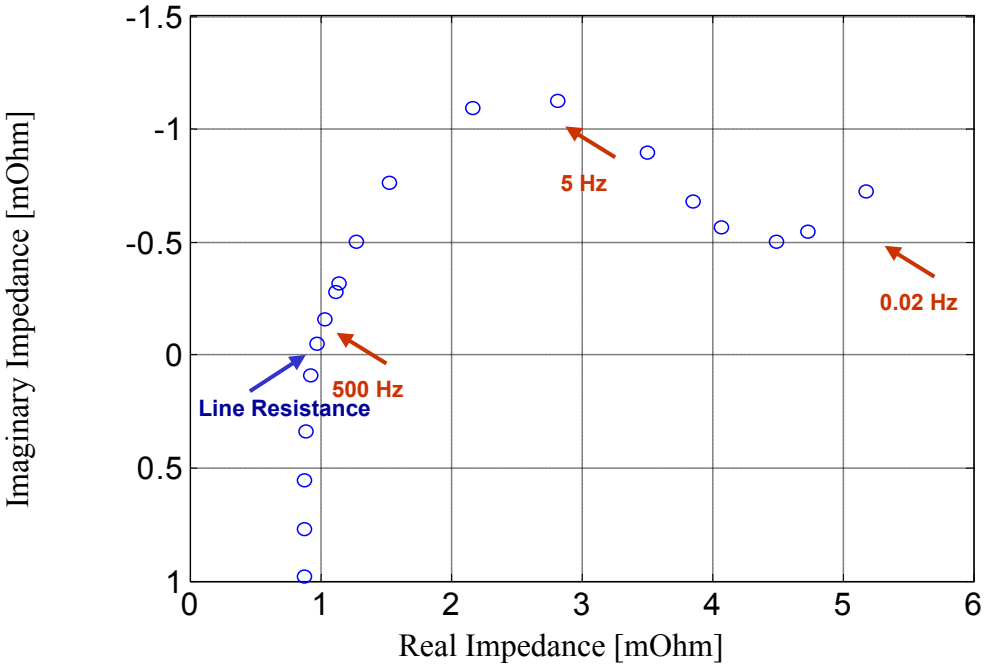

Figure 3.3 An EIS graph of a lithium iron phosphate battery

The Butler-Volmer equation in (3.1.1) describes the steady-state relationship between the charge transfer overpotential across an electrode, η, and the associated battery current magnitude, i [14].

$$i = i_0\left[\exp\left(-\alpha\frac{\eta F}{RT}\right) - \exp\left((1-\alpha)\frac{\eta F}{RT}\right)\right] \tag{3.1.1}$$

(3.1.1) shows the Butler-Volmer equation, where F is the Faraday's constant 96485 $\left[\frac{C}{mol}\right]$, R is the universal gas constant 8.314 $\left[\frac{J}{K\ mol}\right]$, T is the temperature in [K], i_0 is the equilibrium current density in $\left[\frac{A}{m^2}\right]$, and α and 1 - α are electrode transfer coefficients for reduction and oxidation, respectively.

3.1.2 Inverse Hyperbolic Sine Approximation for Butler-Volmer Equation and the Lumped-Electrode Assumption

As discussed in 2.4.2, the measurability of the battery current and the impossibility to measure the model component voltages makes it natural to use current as the predictor and battery terminal voltage as the output for modeling purpose. In (3.1.1), the situation is exactly the opposite with current being the output and overpotential being the input.

As in 2.4.2, the Butler-Volmer relationship can be simplified using the inverse hyperbolic sine function by assuming α = 0.5, as in (3.1.2).

$$\eta = \frac{RT}{\alpha F}\sinh^{-1}\left(\frac{i}{2i_0}\right) \tag{3.1.2}$$

In Figure 3.4, a Butler-Volmer relationship is plotted with parameters $i_0 = 1.62$, $\frac{RT}{\alpha F} = 0.0784$, and $\alpha = 0.5$, i.e. the condition for using the inverse hyperbolic sine approximation. The corresponding linear fit, which would be linear-circuit model's response, is also plotted for comparison. Figure 3.4 demonstrates the nonlinear behavior of the Butler-Volmer relationship and the potential issues for modeling battery with linear-circuit when the Butler-Volmer relationship is present.

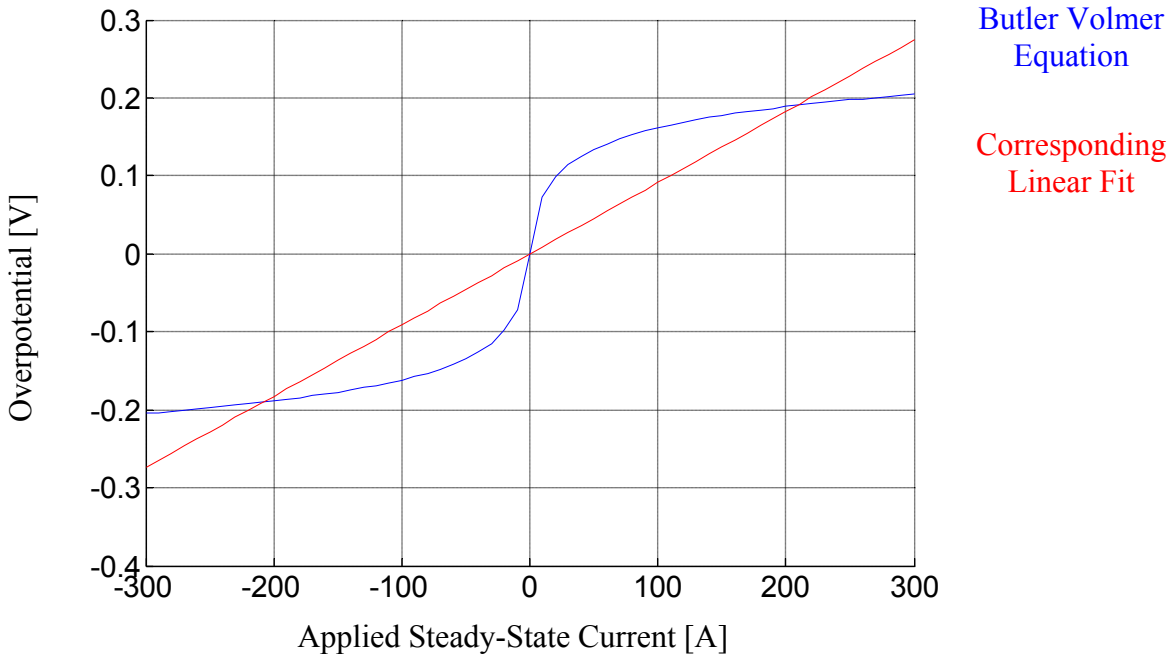

Figure 3.4 Butler-Volmer relationship with set parameters and the corresponding least square error linear fit

While (3.1.1) and (3.1.2) apply to both the battery cathode and anode individually, the two electrodes are typically combined in the model due to the impracticality of differentiating between the two electrodes on the basis of the battery voltage and current measurements. The following is a study on the impact of using lumped BV equations for the two electrodes in series.

As discussed before, a unique Butler-Volmer equation exists for the cathode and anode electrodes individually in a cell. Due to the series connection of the two electrodes, the model could be formed by adding the voltage responses of the two electrodes using two Butler-Volmer equations. Numerical simulations are carried out here to investigate whether the battery can be well represented using only one combined Butler-Volmer equation instead of two. Based on (3.1.2), the following equations were used for simulating the individual battery electrode responses:

$$\eta_{cathode} = k_1 \sinh^{-1}\left(\frac{i}{2i_0}\right) \tag{3.1.3}$$

$$\eta_{anode} = k_1 \sinh^{-1}\left(\frac{i}{2ni_0}\right) \tag{3.1.4}$$

$$\eta_{total} = \eta_{cathode} + \eta_{anode} \tag{3.1.5}$$

In (3.1.3), (3.1.4), and (3.1.5), the two electrodes' responses differ in their characteristic currents; i.e., the anode's characteristic current varies from that of the cathode by a factor of n. It is noted that if the two characteristic currents are identical (n = 1), the combined electrode response η_{total} is simply a scaled version of the individual electrode responses, making it convenient to represent the combined electrode response using a single Butler-Volmer expression.

In the simulations, a case with electrode characteristic current values that differ by a factor of 20 (i.e. n = 20) has been investigated. The values k_1 and i_0 in (3.1.3), (3.1.4), and (3.1.5) were chosen to be 0.0392 and 1.6235, respectively. Currents from -300 to 300 A with an interval of 20 A were applied to (3.1.3), (3.1.4), and (3.1.5) to obtain the data points for the terminal voltage η_{total} of the two electrodes connected in series. The predicted η_{total} has then been fitted with a single BV equation (3.1.2).

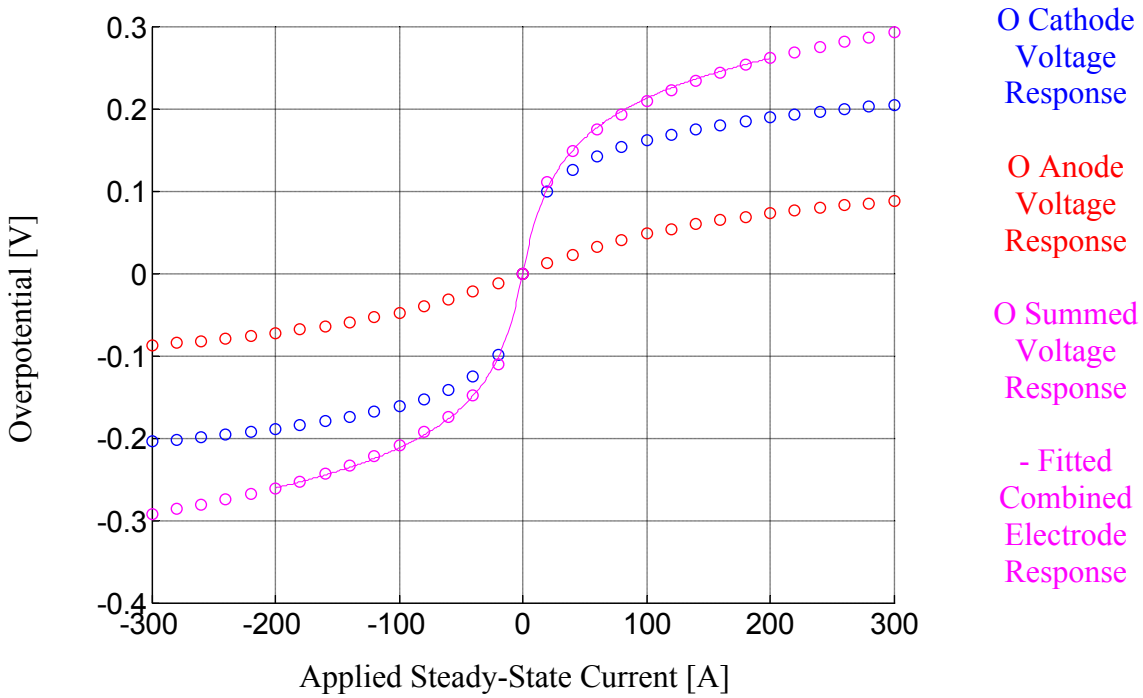

Figure 3.5 Simulated electrode voltage responses (individual and summed) and the fitted combined voltage response using a single BV hyperbolic sine equation for n = 20

Figure 3.5 shows the simulation results for η_{total} and the corresponding fitted curve using (3.1.2). These results show that the use of a single BV equation to represent the two combined electrodes closely matches the summed voltages of the two series electrodes despite the fact that the two electrode characteristic currents differ by more than an order of magnitude (20:1).

Table 3.1 summarizes the calculated sum of squared errors (SSE) values for five different cases of scaling factor n. These results indicate that the SSE value increases monotonically as n grows, but the SSE values remain very low over the full range, building confidence in the validity of the lumped response approach for the two electrodes.

Table 3.1 Calculated SSE as a function of scaling factor k

	n = 1	n = 5	n = 10	n = 20
SSE	8.0 e-15	2.0 e-7	2.0 e-6	7.6 e-6

3.1.3 Derivations of Discrete Form for Linear-Circuit and Butler-Volmer Based Models

In order to use the models in Figure 3.1 and Figure 3.2 in controls applications, the Butler-Volmer and linear-circuit based models for relating battery current and battery terminal voltage can be written in discrete form as in (3.1.6) and (3.1.7), respectively.

$$v(k) = v_{ocv} - r_0 i(k) - \frac{b_1}{1 + a_1 q^{-1}} \sinh^{-1}\left(\frac{i(k)}{2i_0}\right) \tag{3.1.6}$$

$$v(k) = v_{ocv} - \frac{b_0 + b_1 q^{-1}}{1 + a_1 q^{-1}} i(k) \tag{3.1.7}$$

In (3.1.6) and (3.1.7), the term q represents a shift operation. For example, $qi(k) = i(k + 1)$, and $q^{-1}i(k) = i(k - 1)$. These two models can be further manipulated into the following forms by multiplying the term $1 + a_1 q^{-1}$ and assuming v_{ocv} does not change during one sample.

$$\begin{aligned} v(k) = {} & (1 + a_1)v_{ocv} - a_1 v(k - 1) \\ & - (i(k) + a_1 i(k - 1))r_0 - \sinh^{-1}\left(\frac{i(k)}{2i_0}\right)b_1 \end{aligned} \tag{3.1.8}$$

$$\begin{aligned} v(k) = {} & (1 + a_1)v_{ocv} - a_1 v(k - 1) \\ & - i(k)b_0 + i(k - 1)b_1 \end{aligned} \tag{3.1.9}$$

A few remarks can be made based on (3.1.8) and (3.1.9). The first is the models have the same structure with respect to v_{ocv}, assumed as a constant in both cases. This assumption is of course contradictory to the general observation that v_{ocv} is dependent on SOC. However, when (3.1.8) and (3.1.9) are used either with short-term drive data or in the context of recursive estimation, this lack of modeling effort on v_{ocv} vs. SOC usually

has very limited effects. Under the short-term drive condition, the v_{ocv} may not change by much especially for certain types of battery such as lithium iron phosphate.

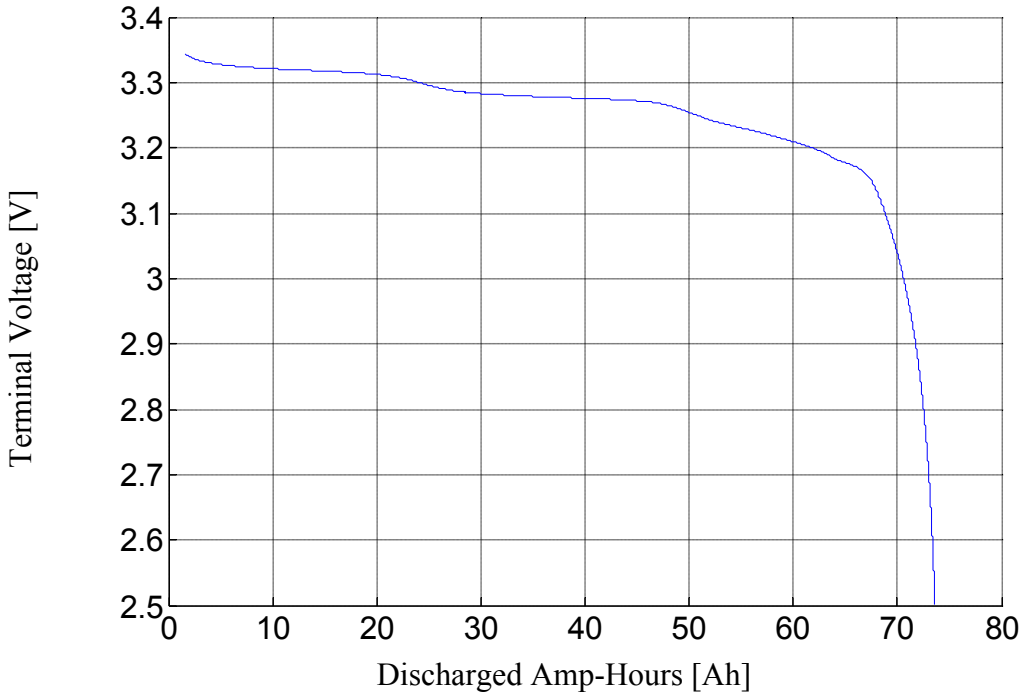

Figure 3.6 CALB lithium iron phosphate battery (rated at 60 Ah) $\frac{1}{20}$ C discharge curve at 25^0 C

Figure 3.6 shows the $\frac{1}{20}$ C discharge curve at 25^0 C for a CALB lithium iron phosphate battery rated at 60 Ah. Since $\frac{1}{20}$ C discharge rate causes a low voltage drop due to resistance and overpotential, this particular curve can be seen as approximately the v_{ocv} vs. SOC relationship for this battery. It can be observed that the derivative of the v_{ocv} vs. SOC relationship here is fairly small until the voltage collapse at the lower SOC region. In the context of recursive estimation, the constant modeling v_{ocv} is naturally updated recursively to reflect the change in SOC and the associated v_{ocv} change.

The second remark is that the term b_0 in (3.1.9) is essentially the same as the term r_0 in (3.1.8). This can be seen by the fact that both are multiplied by a –i(k) term in their respective models. The time constant parameter a_1 is also present in both models and represents the first order dynamic response assumed here. Thus both models are very similar in structure for their dynamic response, resistive drop, and $v_{ocv.}$

The final remark here concerns the term $\frac{b_1}{1 + a_1 q^{-1}}$ in (3.1.6). The presence of the operator q^{-1} provides the first order dynamic response in the model. However, when considering only the steady-state response, $\frac{b_1}{1 + a_1}$ in (3.1.6) corresponds to the $\frac{RT}{\alpha F}$ term in (3.1.2). This fact numerically connects (3.1.2) and (3.1.6).

3.2 Recursive Estimation and Associated Parameter Estimation for Time Constant and Exchange Current

3.2.1 Recursive Estimation with Kalman Filter

To achieve recursive estimation with the two models in (3.1.8) and (3.1.9), these two equations are further manipulated into the following forms respectively:

$$v(k) + a_1 v(k-1) = (1 + a_1)v_{ocv} - (i(k) + a_1 i(k-1))r_0 - \sinh^{-1}\left(\frac{i(k)}{2\, i_0}\right)b_1 \tag{3.2.1}$$

$$v(k) + a_1 v(k-1) = (1 + a_1)v_{ocv} - i(k)b_0 - i(k-1)b_1 \tag{3.2.2}$$

If the assumptions can be made such that the values of i_0 in (3.2.1) and a_1 in both (3.2.1) and (3.2.2) are known, (3.2.1) and (3.2.2) can be considered as a linear expression in the following forms.

$$z(k) = v(k) + a_1 v(k-1) = \varphi(k)\theta$$
$$\text{where } \theta = [v_{ocv}, r_0, b_1]^T \tag{3.2.3}$$
$$\varphi(k) = \left[(1 + a_1), -(i(k) + a_1 i(k-1)), -\sinh^{-1}\left(\frac{i(k)}{2\, i_0}\right)\right]$$

$$z(k) = v(k) + a_1 v(k-1) = \varphi(k)\theta \tag{3.2.4}$$
$$\text{where } \theta = [v_{ocv}, b_0, b_1]^T$$
$$\varphi(k) = [(1 + a_1), -i(k), -i(k-1)]$$

In (3.2.3) and (3.2.4), the output z(k) is linearly related to the input φ(k) with gains, i.e. parameters, θ. Since both the output z(k) and input φ(k) are directly obtained through the measurements, our task in recursive estimation is to obtain the parameter θ. A Kalman filter can be constructed for both battery models using (3.2.3) and (3.2.4). The purpose of this Kalman filter is to continually update the model parameters in order to minimize the error between the model estimates of the battery terminal voltages and their measured values. Figure 3.7 provides a block diagram of the Kalman filters used for both models' parameter identification.

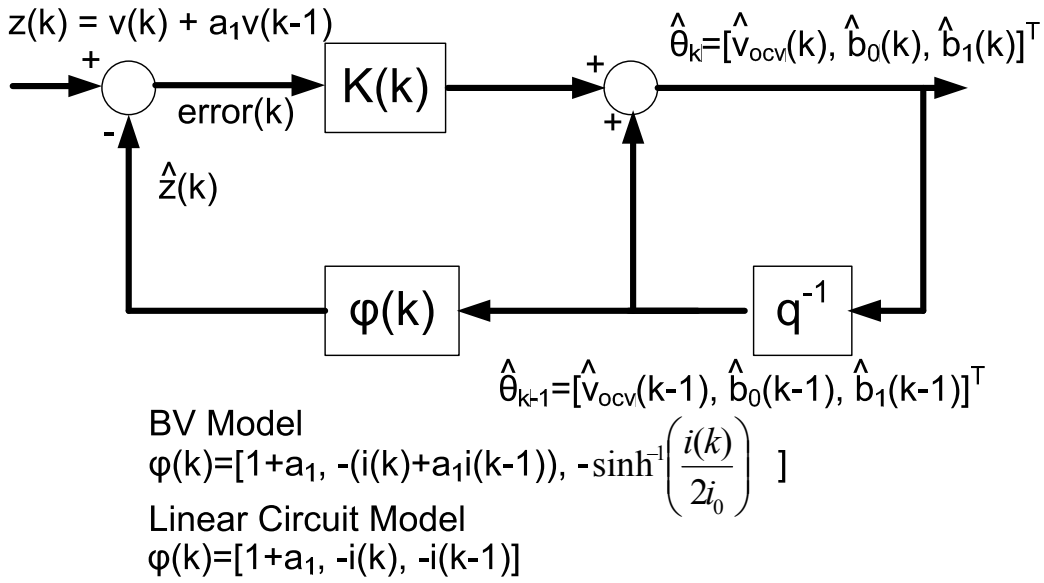

Figure 3.7 Block diagram of Kalman filter structure for both Butler-Volmer and linear-circuit models

The state equation and the measurement equation for the Kalman filter are shown in (3.2.5) and (3.2.6):

$$\theta(k+1) = \theta(k) + u \tag{3.2.5}$$

$$z(k) = \varphi(k)\theta(k) + w \tag{3.2.6}$$

where $\theta(k)$ is the state/parameter vector, $z(k)$ is a linear combination of the voltage measurements $v(k) + a_1 v(k-1)$, $\varphi(k)$ is the regressor vector or input, and u and w are zero-mean, uncorrelated white noise with covariance matrices Q and R, respectively. In this case, Q is a 3x3 diagonal matrix and R is a scalar. It should be noted that the state equation (3.2.5) assumes no systematic change in states/parameters $\theta(k)$ between time samples. The change in $\theta(k)$ between samples is modeled by the fictitious noise u.

(3.2.6) is simply a restatement of (3.2.3) and (3.2.4) with the addition of variable w to model the measurement noise.

Since Kalman filter is a recursive scheme, it requires an initial value θ(0) and the initial value for the covariance matrix. The initialization of the filter is done by selecting the best value available. Practically speaking, the parameters can be from those estimated in the last cycle, or those that have been observed for the same operating conditions, e.g. in temperature and SOC. Mathematically, the initialization is done by using the expected values.

$$\hat{\theta}(0) = E[\theta(0)] \tag{3.2.7}$$

$$P^{+}(0) = E[(\theta(0) - \hat{\theta}(0))(\theta(0) - \hat{\theta}(0))^{T}] \tag{3.2.8}$$

where P^{+} is the covariance matrix of the parameter estimates $\hat{\theta}$. As in the discussion in 2.9.3, the filter propagates at every time step according to the following expressions:

$$\begin{aligned} P^{-}(k) &= P^{+}(k-1) + Q \\ K(k) &= P^{-}(k)\varphi(k)T(\varphi(k)P^{-}(k)\varphi(k)T+R)-1 \\ P^{+}(k) &= (I - K(k)\varphi(k))P^{-}(k) \\ \hat{z}(k) &= \varphi(k)\hat{\theta}(k) \\ \hat{\theta}(k) &= \hat{\theta}(k-1) + K(k)[z(k) - \hat{z}(k)] \end{aligned} \tag{3.2.9}$$

where P^{-} is the covariance matrix from the previous sample updated by Q, and K(k) is the Kalman filter adaptive gain.

As indicated in (3.2.9) and Figure 3.7, the Kalman filter feeds back the measurement z(k) to the model and adjusts the model parameters θ to minimize the error between the prediction $\hat{z}(k)$ and measurement z(k). This feedback process guarantees the filter's tracking under most circumstances, similar to an observer. On the other hand, the

adaptive gain K(k) is calculated from the assumed statistical properties of v and w while an observer would have a fixed gain. The basis for the adaptive gain K(k) is that it minimizes the covariance matrix $P^+(k)$ according to Q, R, $P^+(k-1)$ and $\varphi(k)$ to ensure that the $\hat{\theta}$ is as close to the true parameters θ as possible in the least squares sense. Moreover, the addition of u in (3.2.6) has the effect of forcing the filter to rely on more recent data rather than the older data. In (3.2.9), this is accomplished by increasing $P^-(k)$ from $P^+(k-1)$ by Q, and the augmented $P^-(k)$ alters the updated gain K(k) in a manner that gives greater influence to more recent inputs.

It should be noted that both models can be used to successfully predict the terminal behavior of batteries, particularly when a Kalman filter or some other type of estimator is used to continually adjust the model parameters to minimize the prediction error. The Butler-Volmer model, however, incorporates nonlinear behavior that is exhibited quite strongly by some types of batteries, including lead-acid. As a result, the Butler-Volmer model is capable of predicting the terminal behavior of these types of batteries more accurately without as much need for parameter adjustments to minimize the prediction errors compared to a simpler linear-circuit model.

3.2.2 Offline Parameter Estimation for Exchange Current and Time Constant

As mentioned in 3.2.1, the derivation of the Kalman filter recursive estimation for both models depends on the assumption that both the exchange current and time constant terms are known, i.e. i_0 and a_1. Contrary to the methodology of offline parameter estimation that will be introduced in 5.3, the method discussed here can use a less sophisticated test stand that has a slower sampling rate and does not have the ability to

run simulated drive cycle. Specifically this subsection discusses a methodology to estimate these two parameters using only pulsed current response data.

In order to identify the two parameters i_0 and a_1 in (3.2.1) and (3.2.2) that are not recursively updated online, a test profile that consists of a repeating sequence of pulsed discharge currents was applied to the 55 Ah Optima™ lead-acid battery that was being investigated. As shown in Figure 3.8, the basic sequence consists of a series of five discharge current pulses with amplitudes that decrease consecutively from 165 to 55 Amps in intervals of 27.5 Amps. Each current pulse is applied for 40 seconds and the battery rests for 4 minutes between applied pulses. The basic sequence in Figure 3.8 is repeated until the battery is fully discharged. Figure 3.9 shows the battery voltage response to one discharge current pulse.

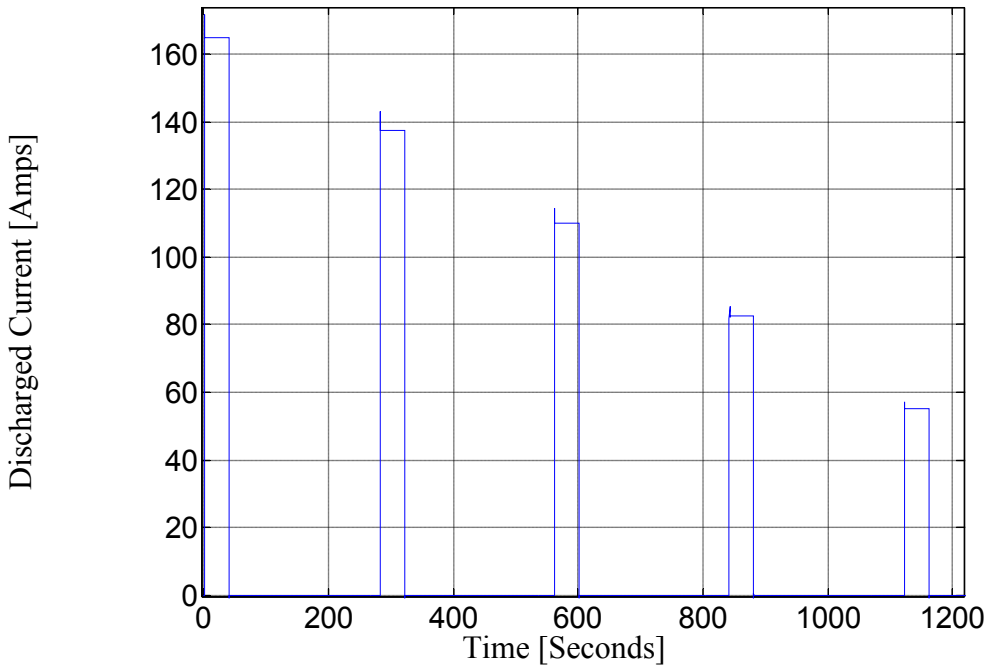

Figure 3.8 Pulsed current test sequence for estimating exchange current and time constant parameter

As seen in Figure 3.9, the voltage response can be segregated into the ohmic voltage response due to r_0 and the electrodes' dynamic voltage response. The sampling rate is 10 Hz. The first three samples of the voltage response following the current pulse application are assumed to be associated with the r_0 ohmic voltage drop and the rest with the electrodes.

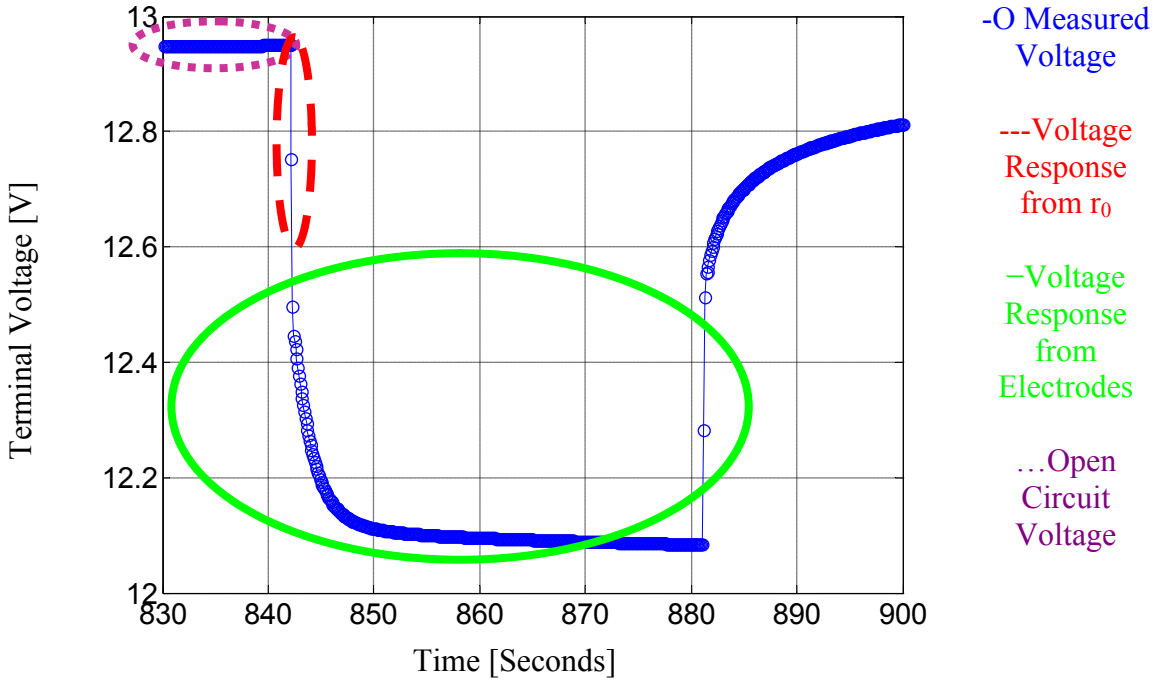

Figure 3.9 Sample measured response of Optima™ lead-acid battery terminal voltage to 40-second discharge current pulse with amplitude 82.5 A

The electrode voltage response magnitude can then be separated and plotted against the applied current magnitude, as shown in Figure 3.10. By fitting the data in Fig. 6 to the BV equation (2), the values $\frac{RT}{\alpha F}$ and i_0 can be estimated. The nonlinear curve-fitting is accomplished using the Gauss-Newton method.

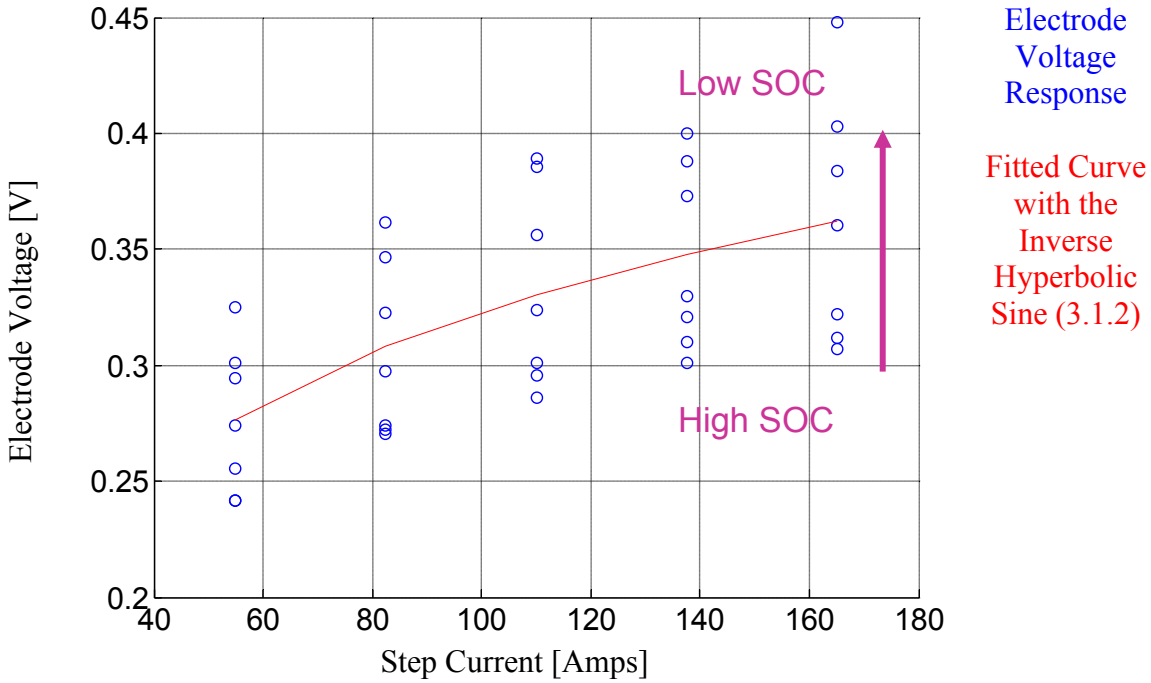

Figure 3.10 Measured electrode voltage drop vs. step current amplitude, with spread of data points at each current amplitude showing the effect of SOC

The spread of the data points at each current amplitude can be attributed to successive rounds of the five current amplitudes, indicating a strong relationship between the electrode voltage and the battery SOC. The recursive estimation scheme can compensate for some of this SOC influence by tuning the battery parameter b_1 in (3.2.1).

In addition to i_0, the offline system identification needs to determine the time constant of the electrodes' voltage response. For each current pulse, the data from the voltage response can be used to estimate the time constant parameter a_1. First, the voltage transient associated with the electrodes' charge transfer process and the double-layer capacitor, η, can be isolated from the terminal voltage v using Kirchoff's voltage equation:

$$\eta(k) = v_{ocv} - v(k) - r_0\, i_{step} \qquad (3.2.10)$$

where v(k) is the measured battery terminal voltage and voltages v_{ocv} and $r_0\ i_{step}$ are assumed to be constant during each current pulse's voltage response.

The discrete equation for the electrode voltage can be extracted from the Butler-Volmer based model voltage (3.2.1) as:

$$\eta(k) = \frac{b_1}{1 + a_1 q^{-1}} \sinh^{-1}\left(\frac{i_{step}}{2i_0}\right) \tag{3.2.11}$$

The electrode voltage approaches an asymptotic value $v_{asymptote}$ at the end of the 40-second current pulse that can be expressed as:

$$v_{asymptote} = \frac{b_1}{1 + a_1} \sinh^{-1}\left(\frac{i_{step}}{2i_0}\right) \tag{3.2.12}$$

Rearranging (3.2.11) and applying the expression for $v_{asymptote}$ in (3.2.12) leads to a new expression for the electrode voltage:

$$\begin{aligned} \eta(k) + a_1\eta(k\text{-}1) &= b_1 \sinh^{-1}\left(\frac{i_{step}}{2i_0}\right) \\ &= (1+ a_1)\, v_{asymptote} \end{aligned} \tag{3.2.13}$$

which can be rearranged as:

$$\eta(k) - v_{asymptote} = a_1(v_{asymptote} - \eta(k-1)) \tag{3.2.14}$$

(3.2.14) provides the basis for developing a linear least-squares estimate of a_1 using the $\eta(k)$ data from (3.2.10) and measurements of $v_{asymptote}$.

$$\begin{aligned} &\hat{a}_1 = (X^T X)^{-1} X^T Y \\ &\text{where} \\ &X = (v_{asymptote} - \eta(k-1)) \\ &Y = (\eta(k)) - v_{asymptote}) \end{aligned} \tag{3.2.15}$$

The mean of the 35 estimated $\hat{a}_1$ time constant parameter values is used in the recursive estimator in the next section. Figure 3.11 shows all 35 of the time constant parameter estimates plotted against the current pulse magnitude.

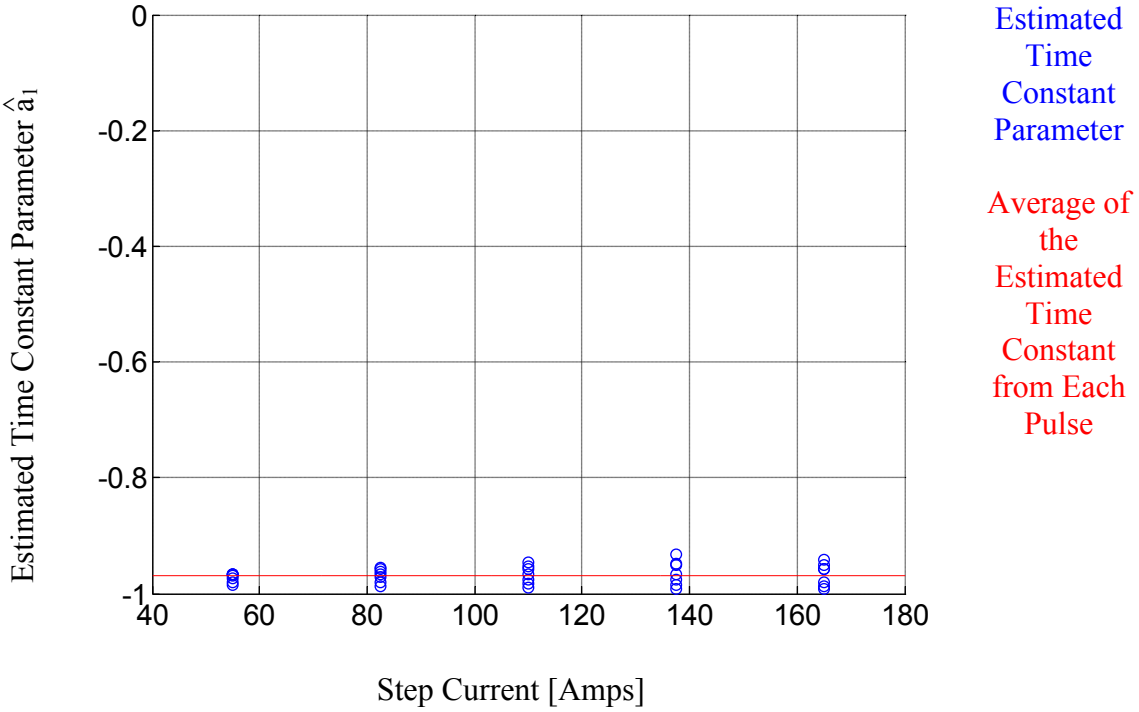

Figure 3.11 Estimated values of time constant parameter $\hat{a}_1$ vs. pulse current amplitude for 7 successive cycles of 5 increasing current step amplitudes

The mean of these estimates is also plotted in Figure 3.11. As noted before, the time constant in the Kalman filter is assumed fixed. For the linear-circuit model, the equations for estimating $\hat{a}_1$ are slightly different but the procedure is otherwise identical.

$$\eta(k) = \frac{-(-b_1 + b_0 a_1)}{1 + a_1 q^{-1}} i_{step} \tag{3.2.16}$$

$$v_{asymptote} = \frac{-(-b_1 + b_0 a_1)}{1 + a_1} i_{step} \tag{3.2.17}$$

$$\eta(k) + a_1 \eta(k-1) = -(-b_1 + b_0 a_1) i_{step} = (1 + a_1)\, v_{asymptote} \tag{3.2.18}$$

3.2.3 Discussion on Model Assumptions and Limitations

Some important assumptions made in this section and their implications will be discussed in this subsection. The first is the assumption of a fixed exchanged current i_0 in the recursive estimator formulation in the Butler-Volmer based model (3.2.3). As will be seen in 5.1.2, the exchanged current depends highly on temperature. From Figure 3.10 it can also be observed that the electrode voltage response, thus potentially i_0, depends heavily on SOC. The recursive estimator may alleviate the modeling deficiency by adapting the b_1 term. A more comprehensive modeling effort that explicitly includes temperature as an input to overpotential will be introduced in 5.4.

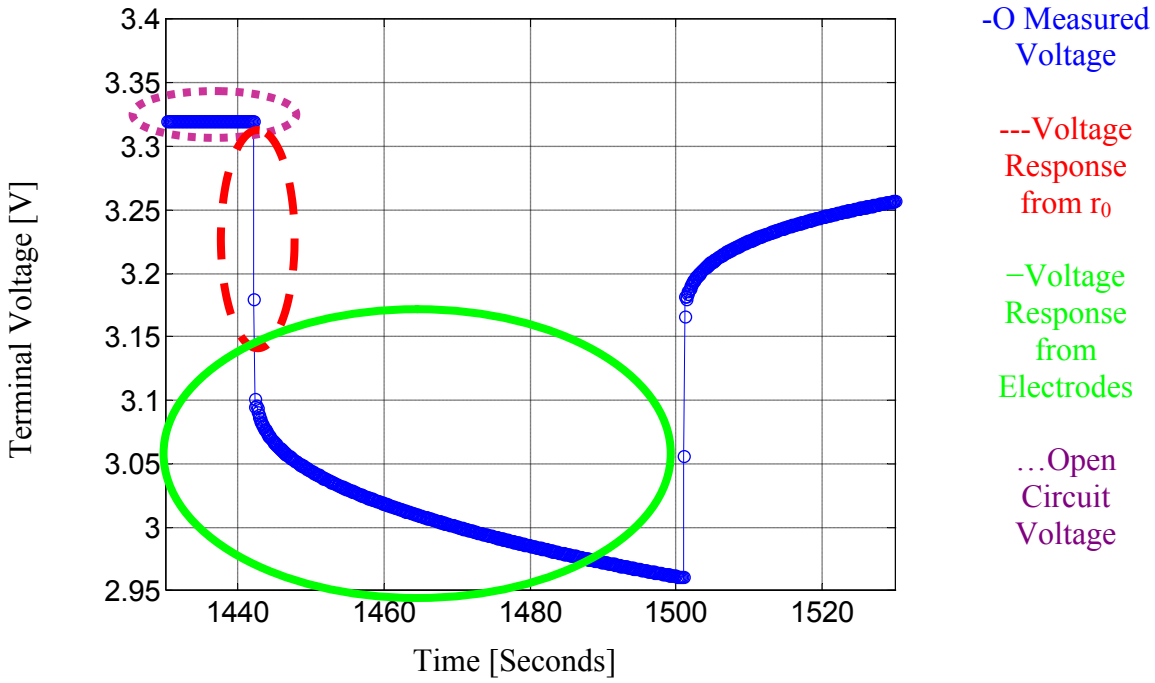

Figure 3.12 Sample measured response of CALB lithium iron phosphate battery terminal voltage to 40-second discharge current pulse with amplitude 180 A.

The methodology used in 3.2.2 to estimate both the time constant parameter and exchange current depends on the observation of the asymptote voltage response, $v_{asymptote}$. If the battery has a long time constant in its transient response, as many

lithium batteries do, this methodology is unsuitable. Of course, by applying a longer current step one can eventually observe $v_{asymptote}$ in theory; however, such a long current step could violate the assumption of stable v_{ocv} as the SOC changes. An example of battery having a longer time constant can be seen in Figure 3.12.

The simplified assumption of a fixed time constant enables adoption of a linear recursive estimator in the battery model described in (3.2.1) and (3.2.2) but it comes at the expense of not tracking the change of battery dynamics in different conditions, e.g. SOC. In addition, (3.2.10) ignores the drop in OCV resulting from decreases in SOC during the current pulse discharges, introducing another factor that degrades the accuracy of the $\hat{a}_1$ parameter estimates.

The aspect of modeling battery as a single time constant system while the real system is more complex has been touched upon in 3.1.1. One other important consideration is that from the least squares fitting perspective, the most suitable time constant value depends on the excitation current. In EV application, the excitation is typically below 5 Hz due to the limit of human response speed. This implies that if a single time constant is to be chosen for a battery model for the EV application, this time constant should be aligned with the dominant excitation frequency, i.e. around 1 Hz, for good least squares performance, even though the actual system has poles outside the excitation frequency range.

3.3 Experimental Results for Comparison between the Two Models

The performances of both the Butler-Volmer-based and linear circuit-based models have been evaluated using actual road driving cycle data from a Corbin Sparrow electric vehicle. The Sparrow EV used to gather the road data is powered by 13 Optima™

D34M lead-acid batteries in series, each of which is rated at 12 V and 55 Ah. The EV is not capable of regenerative braking, and the sample rate is 10 Hz. The maximum discharge current recorded during the drive cycle used to illustrate the models' performances is 235 A. Appendix A contains a thorough documentation of the Corbin Sparrow EV and the monitoring system implemented in WEMPEC (Wisconsin Electric Machines and Power Electronics Consortium).

Estimated battery voltage waveforms in Figure 3.13 and Figure 3.14 show the Kalman filter output voltages for the two models, Butler-Volmer (3.2.3) and linear circuit (3.2.4) respectively. Both models track the measured voltage quite well as seen in Figure 3.13 and Figure 3.14. Expanded time plots for short time periods are provided in the top right corner of both figures, confirming the close tracking of the terminal voltage waveforms.

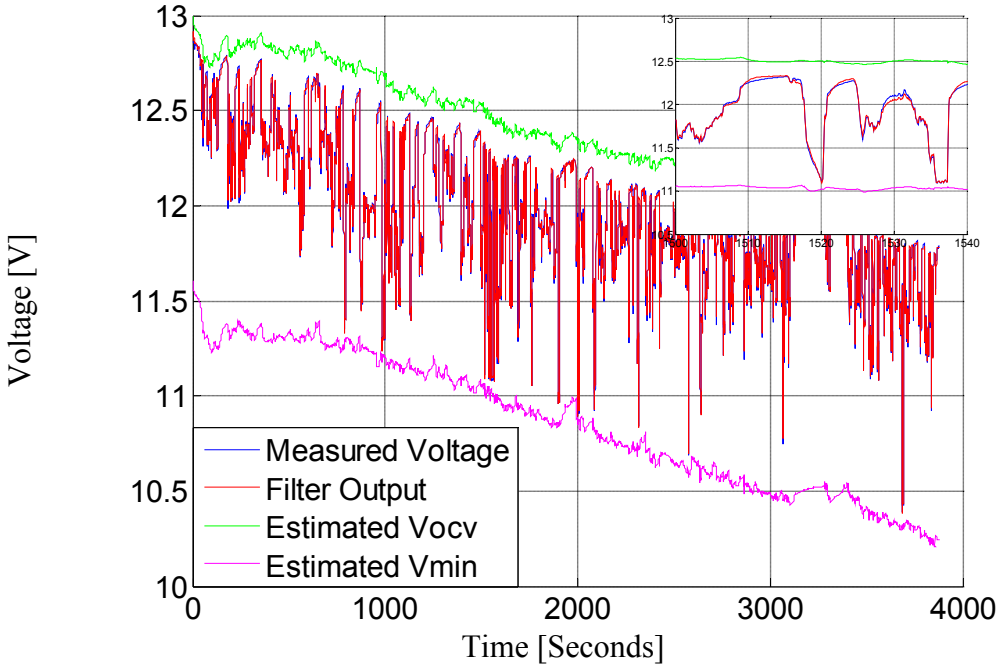

Figure 3.13 Butler-Volmer-based filter results for a lead-acid battery during an EV drive cycle, comparing measured and model-estimated voltages. The estimated OCV and predicted min. battery voltage for max. current are included

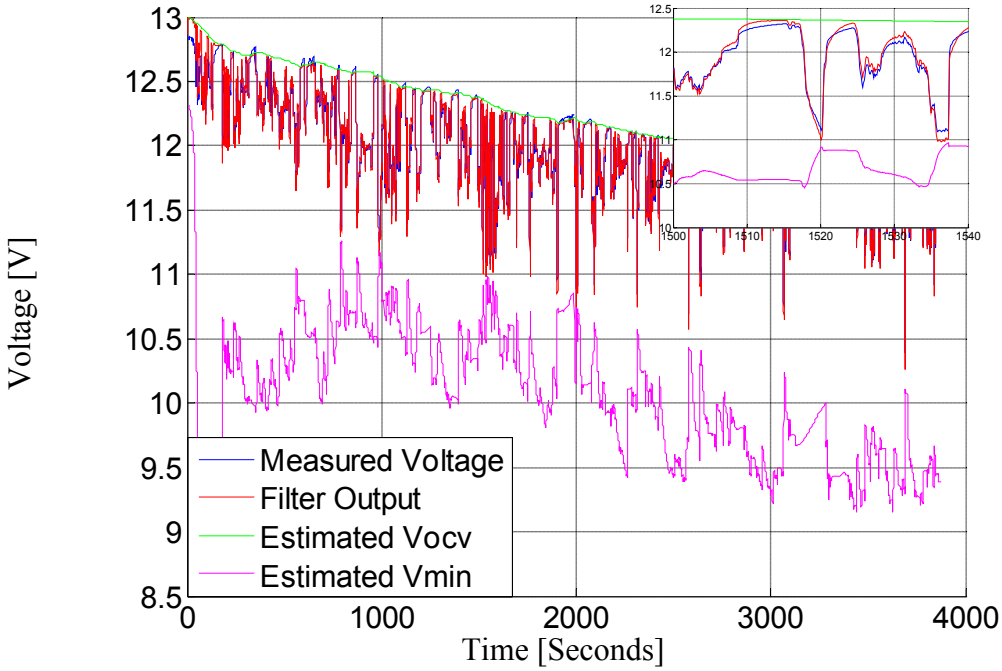

Figure 3.14 Linear circuit-based filter results for a lead-acid battery during an EV drive cycle, providing the same set of waveforms as in Figure 3.13

The estimated v_{ocv} waveforms for the two models are included in Figure 3.13 and Figure 3.14, exposing an offset voltage difference between the two estimates. Evaluation

indicates that the estimated v_{ocv} using the Butler-Volmer model in Figure 3.13 is more accurate since the EV and its accessories are completely powered by the battery bank and current is always being drawn from the battery bank even when the car is stationary. This ever-present discharge current means that the battery terminal voltage can never reach its v_{ocv} during operation, which is consistent with Figure 3.13 but not Figure 3.14.

Estimated v_{min} waveforms are also included in both figures, corresponding to the estimated steady-state minimum battery voltage, i.e. v_{ocv} subtracted by resistive and overpotential voltage drop, if maximum EV current (235 A) is drawn from the battery bank. The SOF is defined in (3.3.1) as a binary yes/no answer to whether the battery steady-state voltage would drop below a preset minimum voltage limit under maximum current load. A detailed treatment for SOF and SOP definition is given in 4.1. For now, it suffices to point out the v_{min} waveform can be derived the model structure and fitted parameter value, and v_{min} can be used to determine SOF.

$$\text{SOF} = \begin{cases} 1 \text{ if } v_{min} \geq v_{limit} \\ 0 \text{ if } v_{min} < v_{limit} \end{cases} \tag{3.3.1}$$

The v_{min} values are found by evaluating (3.1.6) and (3.1.7) with the recursively updated parameters θ using the maximum current value while ignoring the shift operator q. These minimum battery voltage estimates can be treated as a SOF indicator because battery operation is normally configured to shut down once a preset minimum voltage limit is reached. The benefits of introducing the nonlinear electrode model is particularly apparent by comparing the v_{min} waveforms in Figure 3.13 and Figure 3.14, suggesting that the nonlinear Butler-Volmer-based model will be a much better candidate than the

linear circuit-based model for delivering meaningful SOF readings for battery types such as lead-acid ones that exhibit large nonlinear electrode voltage drops.

The estimated voltage waveforms in Figure 3.14 indicate that the linear circuit-based model has greater difficulty determining the estimated v_{min}. This can be attributed to the fact that the model is adjusting its electrode resistor r_1 parameter value to linearly approximate the electrode voltage drop that is a function of current as seen in (3.1.2), i.e. the Butler-Volmer equation. The absence of an accurate nonlinear electrode model requires the linear model to continuously adjust its parameters as the operating point varies. As a result, the linear model estimates of v_{min} in Figure 3.14 coincide with those from the Butler-Volmer model for only a few points, most often when the terminal voltage is low due to high current loads. In summary, the linear circuit-based model is hindered by the fact that the approximation only performs well when operating in the vicinity of the test conditions, i.e. current, that were used to set the model parameters.

The performance of the linear model in Figure 3.14 raises concerns about the limitations of this model when combined with a Kalman filter. To further investigate this issue, both models were run open-loop for 50 seconds with the feedback deactivated. The model-estimated terminal voltages at the end of this interval are recorded for both models. These modified voltage estimates are plotted for both models in Figure 3.15 with the measured terminal voltages for comparison.

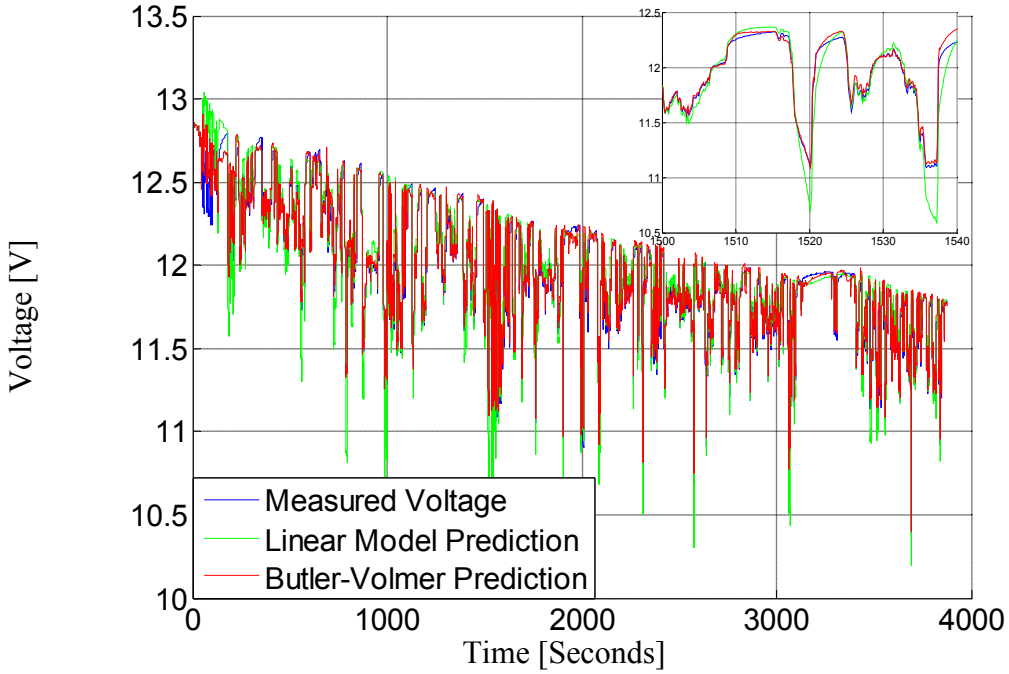

Figure 3.15 Butler-Volmer and linear circuit-based model terminal voltage predictions using 50 sec forecast results, including comparison with measured voltage

Figure 3.15 shows that the linear circuit-based model has difficulty forecasting the battery voltage output under high-current conditions if the battery parameters 50 seconds earlier were adapted for low-current conditions, while the Butler-Volmer-based model performs much better for these conditions. Figure 3.16 provides a histogram of the residuals for the two models from Figure 3.15, excluding data points for current values lower than 55 [A] in order to focus the comparison of the two models in the high-current region. The error histogram for the Butler-Volmer-based model in Figure 3.16 is narrower than the linear-circuit based model, indicating that Butler-Volmer-based model has better least squares prediction performance.

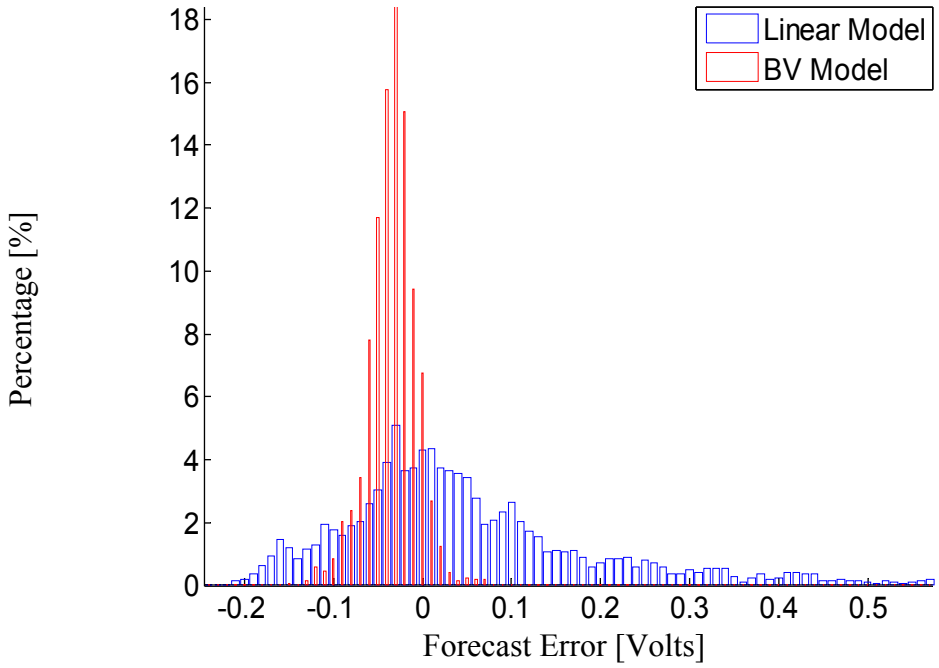

Figure 3.16 Residuals histogram for the two models from Figure 3.15, excluding data points where i < 55 A

It can be noted that the BV-based model error histogram in Figure 3.16 is biased with a negative average value, indicating that the model has a tendency to under-forecast the terminal voltage. This bias error can be attributed to the fact that v_{ocv} has dropped during the 50-second open-loop interval due to the change in SOC, but the forecast model treats v_{ocv} as a constant during this interval.

As a final step in this model evaluation, the autocorrelation of the residuals of the two models in Figure 3.13 and Figure 3.14 has been analyzed. As discussed, the feedback mechanism in the Kalman filter causes the sums of squares of the residuals for both models to be small. However, the value of the autocorrelation of the residuals should also be as close to zero as possible for a model to be high quality.

For the residuals *e*, autocorrelation is defined as the correlation between e(k) and its value e(k+j) separated by j intervals of time. Mathematically, the autocorrelation ρ at lag j is defined as:

$$\rho(j) = \frac{E[(e(k)-\bar{e})(e(k+j)-\bar{e})]}{\sqrt{E[(e(k)-\bar{e})]^2 E[(e(k+j)-\bar{e})]^2}} = \frac{E[(e(k)-\bar{e})(e(k+j)-\bar{e})]}{\sigma^2} \tag{3.3.2}$$

where E is the expected value operator, $\bar{e}$ is the mean value of the residuals, and σ^2 is the variance of e assuming stationarity. The residuals can be considered "whiter" with lower autocorrelation, and whiter residuals indicate that there are fewer systematic components in the actual battery that remain unmodeled. Figure 3.17 and Figure 3.18 show the calculated autocorrelation for the first 10 lags for the Butler-Volmer-based model and the linear circuit-based model residuals, respectively. The figures indicate that the autocorrelation of the linear circuit-based model's residuals is much greater than that of the Butler-Volmer-based model. This observation further strengthens the case for claiming that the Butler-Volmer-based model performs better than the linear circuit-based model in predicting the battery performance.

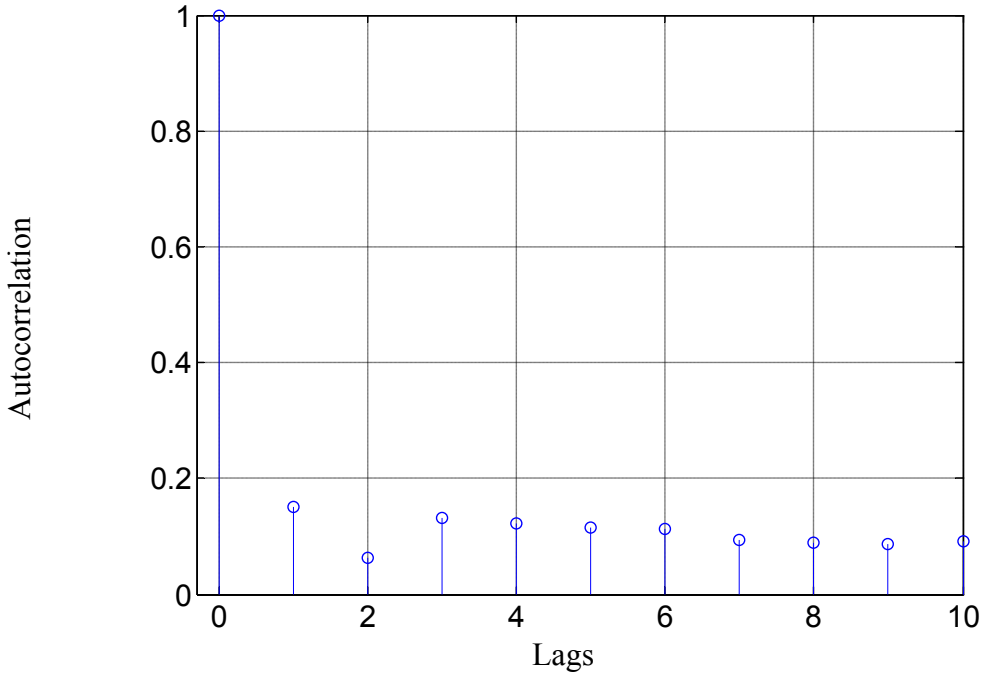

Figure 3.17 Calculated residual autocorrelation for the Butler-Volmer-based model at the first 10 lags

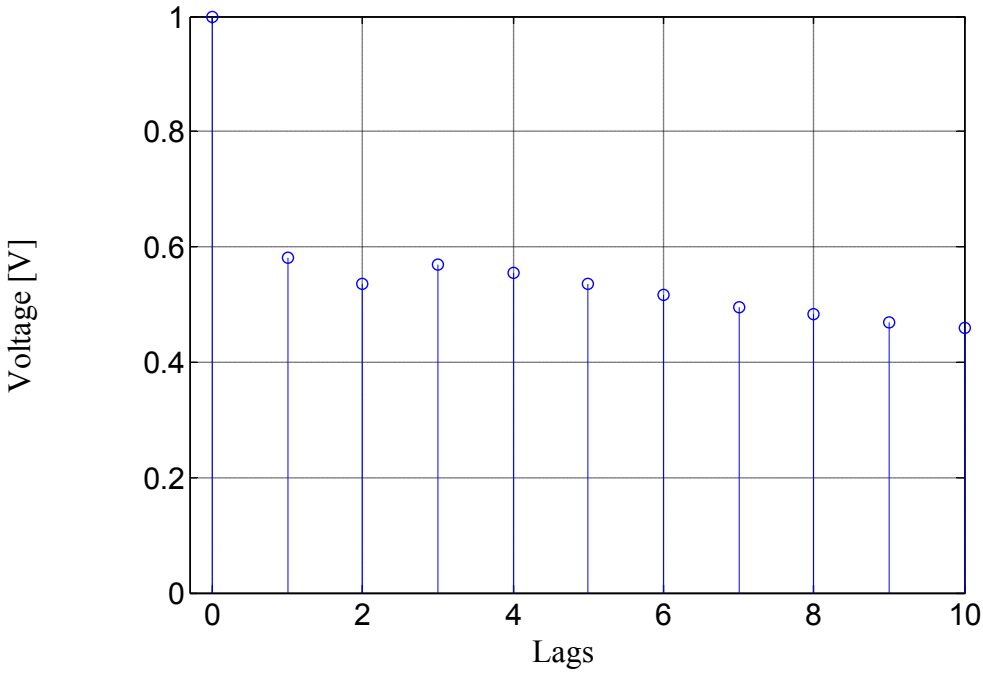

Figure 3.18 Calculated residual autocorrelation for the linear circuit-based model at the first 10 lags

3.4 Summary

This chapter presents a battery modeling technique that utilizes the Butler-Volmer equation in a battery equivalent circuit suitable for recursive online parameter identification. While incorporation of the Butler-Volmer equation into a battery model for vehicle applications has been reported previously [119], a new contribution of this work is the adoption of the hyperbolic sine approximation that is key to making the integration of this model into a recursive estimator possible.

Performance comparisons with the conventional linear circuit battery model indicate that the nonlinear model offers advantages for delivering meaningful SOF readings for lead-acid batteries and other battery types that exhibit large nonlinear electrode voltages. The proposed model has been verified for lead-acid batteries using measured road data collected from an EV drive.

Chapter 4
Battery Power Prognostics

A battery management system (BMS) for an EV is typically designed to provide, among other functions, a power capability estimate. In recent years, the technical literature has focused primarily on the estimation of battery SOC with the objective of providing reliable estimates of remaining range for EV applications. The constraints on a battery's capability to fulfill its required tasks include not only its remaining charge reflected in the SOC, but also the battery's power delivery capability. However as discussed in section 2.6, having enough SOC does not always mean the battery can fulfill the application's power requirement since power capability may be reduced by temperature or other factors.

Since battery manufacturers usually publish the operating voltage upper and lower limits, the BMS needs to insure that these limits are observed by preventing the sinking and sourcing of too much power during vehicle operation. The focus of this chapter is therefore on the battery power capability prognostics.

4.1 State-of-Function and State-of-Power

4.1.1 Definitions

Two metrics have been proposed for battery power capability: state-of-function (SOF) and state-of-power (SOP). Multiple definitions of SOF have appeared in literature, all of which related to the battery power capability. This paper will use definitions similar to the SOF in [119] and the SOP in [39]. It is important to note that

the SOF is a digital yes/no parameter stating whether the battery has sufficient power capability to carry out a specified function (e.g., engine starting), while SOP is a vernier signal indicating how much power is available. Both of these definitions use the battery equivalent circuit to predict the maximum power the battery can deliver within the specified voltage limits:

$$\text{SOF} = \begin{cases} 1 \text{ if } v_{min} \geq v_{limit} \\ 0 \text{ if } v_{min} < v_{limit} \end{cases} \tag{4.1.1}$$

$$\text{SOP} = \frac{v_{limit}\left(v_{ocv} - v_{limit}\right)}{r_0 + r_1} \tag{4.1.2}$$

where v_{limit} is the minimum battery voltage allowed by manufacturer specifications, and v_{min} is the minimum voltage reached by the battery during the discharge profile. The open-circuit voltage v_{ocv} and two resistances r_0 and r_1 are found in the familiar Randle battery equivalent circuit model provided in Figure 4.1. As discussed in chapter five, the linear circuit-based model is suitable for lithium cells in the room temperature, and this model will serve as the basis for the power capability prediction in this chapter. The SOP variable in (4.1.2) is derived from this equivalent circuit and corresponds, for discharge conditions, to the steady-state power delivered at the battery terminals when the battery terminal voltage drops to v_{limit}.

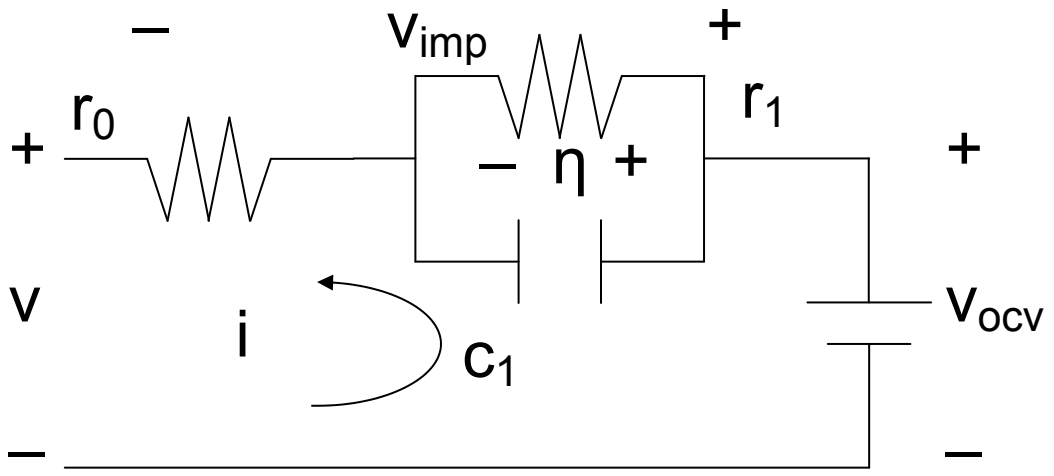

Figure 4.1 Conventional linear circuit-based battery model suitable for lithium batteries at room temperature

The definitions in (4.1.1) and (4.1.2) focus on the battery's discharge operation, but corresponding definitions can be adopted for the charging case. In addition, SOP is defined in (4.1.2) for steady-state operation as in [1], whereas [39] and [124] include transient behavior in their analysis. Specifically, the SOP defined in [1] assumes a rested start condition and captures the maximum power output within a fixed time period, while the SOP defined in [39] and [124] incorporate the battery time constant and can solve for any starting condition based on model assumptions. The simplified definition adopted here is not critical to this chapter's major focus and contribution. More will be provided on the justification for the simplification.

4.1.2 State-of-Power Volatility

As discussed before, one popular method for battery parameter estimation uses a recursive algorithm, often in the form of a Kalman filter that uses the measured battery voltage and current data as inputs. This recursive approach adapts the equivalent circuit

parameter values to reflect the effects of gradual SOC changes and aging. The SOP can then be estimated using the recursively-obtained parameters. An important benefit for this approach is the estimated parameters are updated continuously to provide real-time information.

Using the recursive estimation methodology introduced in chapter three, a CALB lithium-iron-phosphate battery's parameters are monitored online for a simulated drive cycle. The CALB battery specifications are given in Table 4.1.

Table 4.1 CALB 60AHA Li-iron-phosphate battery specifications

Nominal Capacity	60 [Ah]
Nominal Cell Voltage	3.2 [V]
1 kHz AC Impedance	≤ 1 [mOhms]
Cell Voltage Range	2.5 ~ 3.6 [V]

The SOP metric as defined in (4.1.2) has been found in the literature in many variants [39] [124]. Within the context of the recursive estimation algorithm defined in Chapter 3, v_{ocv} and the resistances are estimated using the same data, so their estimates are correlated. That is, an error in one parameter leads to errors in others. This correlation of the estimates, combined with the fact that v_{ocv} is divided by the sum of the resistances in the defining SOP equation in (4.1.2) mean that the SOP estimates generated by the recursive estimator are susceptible to having large fluctuations. This error sensitivity is aggravated by the fact that the resistances of lithium batteries are typically in the range of milli-Ohms.

When performing recursive estimation of parameters based on the linear circuit model in (3.2.4), the quality of the SOP estimate in (4.1.2) can be studied. Specifically, let assumptions be made about the convergence of $\hat{v}_{ocv}$ and $\hat{R} = \hat{r}_0 + \hat{r}_1$ as in (4.1.3).

$$\begin{aligned} &\hat{R} = \hat{r}_0 + \hat{r}_1 \\ &\hat{v}_{ocv} + E[i(t)]\,\hat{R} = E[v_{steady}(t)] \\ &\frac{d\hat{R}}{d\hat{v}_{ocv}} = \frac{-1}{E[i(t)]} \end{aligned} \tag{4.1.3}$$

In (4.1.3), it is assumed that the recursively estimated parameters $\hat{v}_{ocv}$ and $\hat{R} = \hat{r}_0 + \hat{r}_1$ have converged in a steady-state fashion and that this convergence is the strongest with respect to the average (expected) value of battery current E[i(t)]. The derivative of $\hat{R}$ with respect to $\hat{v}_{ocv}$ is thus a function of the average current.

$$\begin{aligned} &\frac{d\hat{P}_{limit}}{d\hat{v}_{ocv}} = v_{limit}\frac{\hat{R} + \left(\frac{1}{E[i(t)]}\left(\hat{v}_{ocv}-v_{limit}\right)\right)}{\hat{R}^2} \\ &\frac{d\hat{P}_{limit}}{d\hat{v}_{ocv}}\frac{\hat{v}_{ocv}}{\hat{P}_{limit}} = \hat{v}_{ocv}\frac{1 + \left(\frac{1}{E[i(t)]\,\hat{R}}\left(\hat{v}_{ocv}-v_{limit}\right)\right)}{\hat{v}_{ocv}-v_{limit}} \end{aligned} \tag{4.1.4}$$

From (4.1.2) and (4.1.3), the derivative of $\hat{P}_{limit}$ with respect to $\hat{v}_{ocv}$ is then found in (4.1.4) and this leads to the sensitivity of $\hat{P}_{limit}$ with respect to $\hat{v}_{ocv}$, defined as $\frac{d\hat{P}_{limit}}{d\hat{v}_{ocv}}\frac{\hat{v}_{ocv}}{\hat{P}_{limit}}$. A quick examination of the terms in this sensitivity expression reveals that it is expected to have a rather high numerical value for a typical lithium-ion battery. The CALB battery in Table 4.1 with internal resistance of 1 [mOhms], rated capacity of 60 Ah, and rated voltage of 3.6 [V] is adopted for an example. For small $\hat{R}$, $\frac{d\hat{P}_{limit}}{d\hat{v}_{ocv}}\frac{\hat{v}_{ocv}}{\hat{P}_{limit}}$ can

be approximated as $\frac{\hat{v}_{ocv}}{E[i(t)]\hat{R}}$. If the average current is chosen as the C-rate, i.e. 60 [A], $\frac{\hat{v}_{ocv}}{E[i(t)]\hat{R}}$ is then 60, a rather high value for sensitivity. Furthermore using the same set of parameters, the derivative $\frac{d\hat{P}_{limit}}{d\hat{v}_{ocv}}$ is found to be 40133, i.e. power is off by 40133 [W] for an error of 1 volt on $\hat{v}_{ocv}$.

4.1.3 State-of-Function with Confidence Interval

The high variability of estimated SOP raises concerns about the SOP's utility in applications when used in conjunction with recursive parameter estimation. On the other hand, it can be argued that an accurately estimated SOP is not really needed in some applications such as EV propulsion. During much of its operation, a vehicle's battery pack has a power delivery capability that significantly exceeds the power rating of its power conversion unit. However, low SOC, low temperature, and aging will reduce the battery pack's power capability below the electric drive's power rating. Under these conditions, the drive control strategy must adapt to the new constraint.

In many cases, the SOF metric can be as useful in EV applications as the SOP since the control strategy does not need to know the specific amount of power available, but only whether the battery power that is available exceeds a minimum threshold value required for the propulsion unit to accomplish its mission. For this more limited threshold comparison purpose, the battery SOF estimate can serve as a surrogate information source in place of the more detailed SOP estimate.

If the SOP estimate is available, one straightforward way to estimate the SOF is to simply compare the estimated SOP with the minimum required power, P_{req}. To enhance the robustness of the SOF estimate it is desired to take the variance of estimated SOP into account when comparing it with P_{req}.

At this point, it is worth noting that the Kalman filter inherently provides a probabilistic assessment of all its estimates, including each estimate's variance. In addition, any linear function of these estimates will also have a deterministic probability distribution and variance if the assumption can be justifiably made that the noise variables are of Gaussian distributions. Unfortunately, the form of SOP in (4.1.2) is not a linear combination of estimated quantities and no analytical solution for its variance is available. In its place, another power metric, P_{test}, is proposed for SOF estimation, defined as follows:

$$\begin{aligned} i_{req} &= \frac{P_{req}}{v_{limit}} \\ P_{test} &= i_{req}\left(v_{ocv} - (r_0+r_1)i_{req}\right) \\ \hat{P}_{test} &= i_{req}\left(\hat{v}_{ocv} - \frac{\hat{b}_0 + \hat{b}_1}{1 + a_1} i_{req}\right) \end{aligned} \tag{4.1.5}$$

The newly defined power metric P_{test} can be interpreted, for discharge conditions, as the power that the battery is delivering at its terminals when it is delivering current i_{req} . i_{req}, in turn, is the current that flows from the battery terminals when it is delivering the required power P_{req} at its minimum voltage limit v_{limit}. Note that i_{req} is a fixed value since both P_{req} and v_{limit} are determined values, so the estimate $\hat{P}_{test}$ qualifies as a linear

function of the correlated estimated variables, if the assumption of a known a_1 is made as in chapter three.

For purposes of evaluating the SOF, it can be shown that if SOP > P_{req}, then P_{test} > P_{req}. The derivation begins with a repeat of the SOP definition from (4.1.2):

$$\begin{aligned}
&\text{Let SOP} = \frac{v_{limit}\left(v_{ocv} - v_{limit}\right)}{r_0 + r_1} > P_{req} = i_{req}v_{limit} \\
&\text{Therefore:} \\
&\quad => (v_{ocv} - v_{limit}) > i_{req}(r_0 + r_1) \\
&\quad => (v_{ocv} - i_{req}\,(r_0+r_1)) > v_{limit} \\
&\quad => P_{test} = i_{req}(v_{ocv} - i_{req}\,(r_0+r_1)) > i_{req}v_{limit} = P_{req}
\end{aligned} \tag{4.1.6}$$

Conversely, a similar argument can be made that when SOP < P_{req}, then P_{test} < P_{req} and when SOP = P_{req}, P_{test} = P_{req}. As a result, it can be argued that, for the purpose of SOF estimation, P_{test} can serve as effectively as SOP.

As a consequence of being a linear variable, the estimated $\hat{P}_{test}$ has a probability density and variance when the parameters are estimated using the Kalman filter. The covariance matrix Λ for the Kalman filter is a 3x3 matrix populated by the variances and covariances of $[\hat{v}_{ocv}, \hat{b}_0, \hat{b}_1]$, as shown in (4.1.7).

$$\begin{aligned}
&\theta = [\hat{v}_{ocv}, \hat{b}_0, \hat{b}_1]^T \\
&\Lambda = \begin{bmatrix} \text{var}(\hat{v}_{ocv}) & \text{cov}(\hat{v}_{ocv}, \hat{b}_0) & \text{cov}(\hat{v}_{ocv}, \hat{b}_1) \\ \text{cov}(\hat{v}_{ocv}, \hat{b}_0) & \text{var}(\hat{b}_0) & \text{cov}(\hat{b}_0, \hat{b}_1) \\ \text{cov}(\hat{v}_{ocv}, \hat{b}_1) & \text{cov}(\hat{b}_0, \hat{b}_1) & \text{var}(\hat{b}_1) \end{bmatrix}
\end{aligned} \tag{4.1.7}$$

Using these results, the expression $\hat{P}_{test}$ has a variance that can be expressed as:

$$\begin{aligned}\operatorname{var}(\hat{P}_{test}) = i_{req}^2 \operatorname{var}(\hat{v}_{ocv}) + \left(\frac{i_{req}^2}{1+a_1}\right)^2 \operatorname{var}(\hat{b}_0) + \left(\frac{i_{req}^2}{1+a_1}\right)^2 \operatorname{var}(\hat{b}_1) \\ -2i_{req}\left(\frac{i_{req}^2}{1+a_1}\right)\operatorname{cov}(\hat{v}_{ocv},\hat{b}_0) - 2i_{req}\left(\frac{i_{req}^2}{1+a_1}\right)\operatorname{cov}(\hat{v}_{ocv},\hat{b}_1) \\ +2\left(\frac{i_{req}^2}{1+a_1}\right)^2 \operatorname{cov}(\hat{b}_0,\hat{b}_1)\end{aligned} \qquad (4.1.8)$$

With the expression of the variance for $\hat{P}_{test}$ and the inequality shown in (4.1.6), the SOF estimate can now be associated with a probabilistic statement with known theoretical confidence. This is a significant advantage for improving the quality of the SOF estimate.

4.2 Lithium-Iron-Phosphate Battery Estimation under UDDS Drive Cycle

The CALB 60AHA lithium-iron-phosphate battery with the characteristics presented in Table 4.1 has been used for the experimental verification tests. In [138], the authors described the details of an electric vehicle conversion project using a Ford F150 crew cab truck. In the conversion project, the battery pack uses the CALB 100AHA cells, a higher-current version of the 60AHA model cells that was tested in this project.

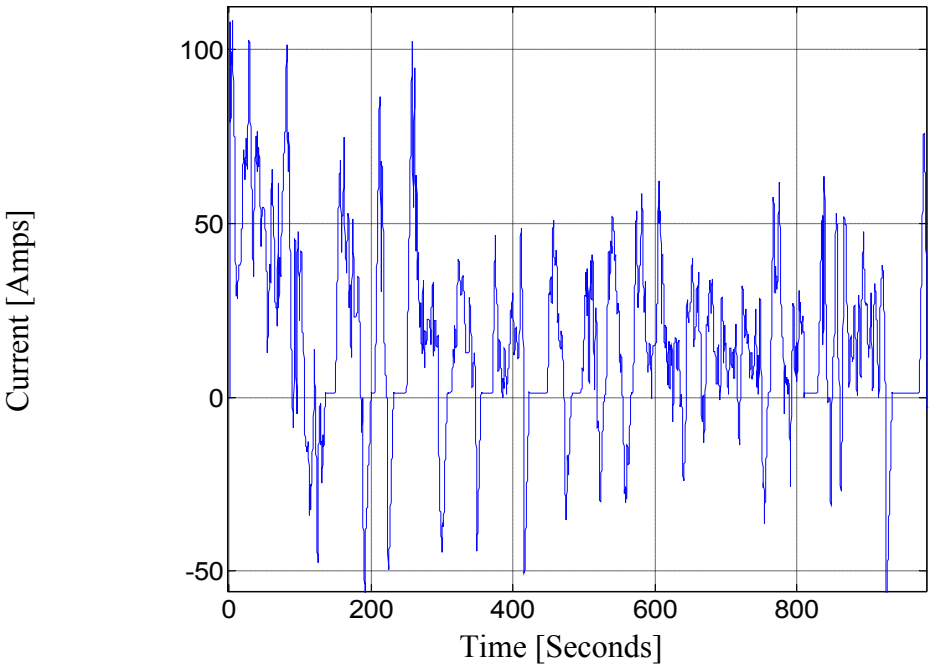

Figure 4.2 UDDS drive cycle current profile. The drive cycle repeats until battery is fully discharged

Figure 4.2 shows the current drive cycle used to excite the test battery on an experiment setup. The UDDS drive cycle current profile represents a conversion of the UDDS speed vs. time profile into an equivalent current vs. time schedule.

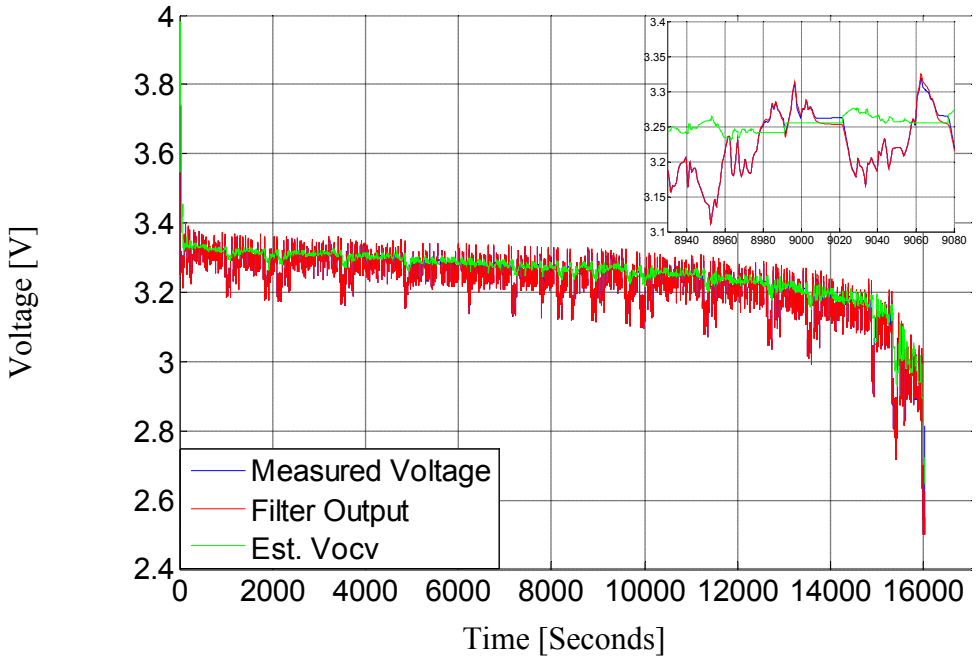

Figure 4.3 Kalman filter predictions of the open-circuit voltage $\hat{v}_{ocv}$ and terminal voltage compared to the measured terminal voltage for the UDDS cycle current profile

Based on the truck's physical parameters, e.g. inertia, etc, several standard drive cycles were scaled for single-cell, test bench experiments. The performance of the estimators was very similar for the different drive cycles. The experimental results presented here are for the UDDS (urban dynamometer driving schedule) cycle. More information about the battery test bench configuration used for these experimental test cycles can be found in Appendix B. Additionally, the minimum voltage per cell, i.e. v_{limit}, was set at 2.8 V in accordance with the specifications for the EV conversion project. The measured cell voltage, overlaid with the Kalman filter estimates for the battery terminal voltage and open-circuit voltage $\hat{v}_{ocv}$ are shown in Figure 4.3. In the expanded insert in the upper right corner of Figure 4.3, it can be observed that the estimated battery terminal voltage tracks the measured voltage very well. This good

agreement reflects the fact that the Kalman filter is designed to minimize the least-squared error of its estimates.

It should be noted that the UDDS drive cycle includes both motoring and regenerating modes, raising questions about the performance of the Kalman filter estimates in both modes. However, the motoring mode dominates the operating conditions for the EV drive cycles considered in this investigation. As a result, the model used for the results presented here assumes that the charging and discharging modes share the same model parameters.

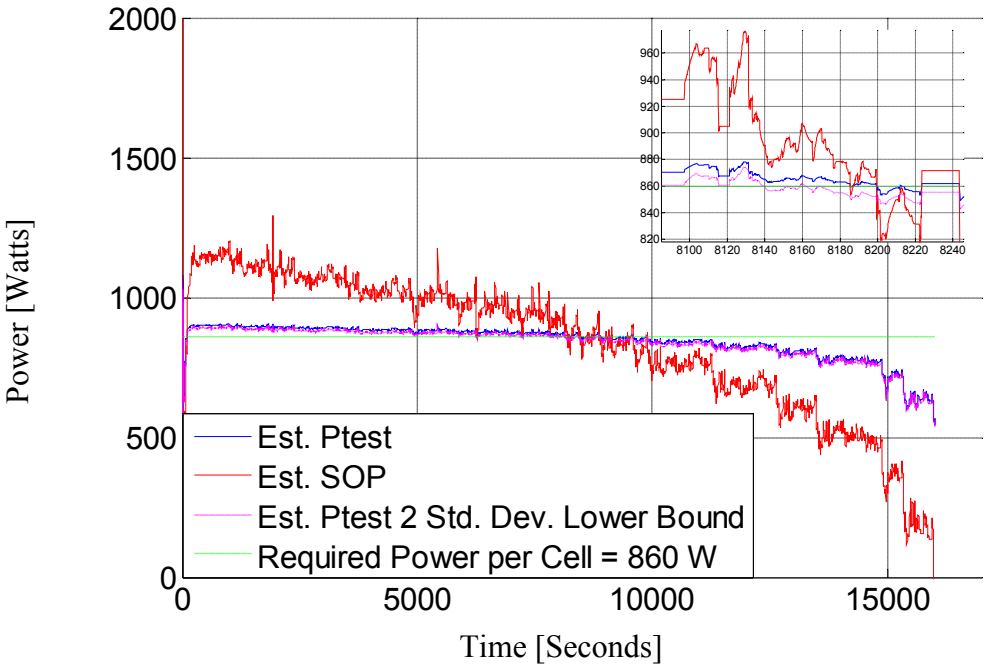

Figure 4.4 Estimated SOP and $\hat{P}_{test}$ metrics compared with required power calculated for the F150 truck [138] using the UDDS drive cycle

In Figure 4.4, the estimated SOP derived from the UDDS drive cycle test data is plotted for the full cycle duration. It can be observed that, consistent with expectations discussed in 4.1.2, the SOP estimate exhibits substantial fluctuations that raise questions about the quality of this battery condition metric. In contrast, the estimated $\hat{P}_{test}$, variable

defined in (4.1.5) is much better behaved than SOP, with significantly smaller variations during the cycle. As expected, the value of $\hat{P}_{test}$ dips below the line designating the minimum required power P_{req} (= 860 W for the CALB cell) at exactly the same time instants as the SOP power. The zoomed-in view in the upper right corner of Figure 4.4 shows the $\hat{P}_{test}$ lower-bound value (2 standard deviations) drops below the required power level during this interval while the $\hat{P}_{test}$ estimate stays above this threshold value. This suggests that the $\hat{P}_{test}$ lower-bound value could be used to serve as an early warning for the SOF function, indicating the battery is approaching its lower limit.

One additional benchmark for the filtering results is the first lag autocorrelation of the error that should ideally be zero. For the filter tuning used in these experiments, the value of this autocorrelation was determined to be 0.34. This value is considered to be good for purposes of this investigation, but it reflects some residual limitations of the model since the autocorrelation coefficient should ideally be zero.

4.3 Lithium-Iron-Phosphate Battery Estimation Results Comparison between Recursive Estimation under UDDS and HPPC Analysis

4.3.1 HPPC Test for the Lithium-Iron-Phosphate Battery

The accuracy of the SOP estimated during the drive cycle depends on the quality of estimates for two primary parameter/variable components in the battery model, $\hat{v}_{ocv}$ and $\hat{r}_0 + \hat{r}_1$. In this section, the predicted SOP obtained from the recursive estimator presented in this paper and its estimated components $\hat{v}_{ocv}$ and $\hat{r}_0 + \hat{r}_1$ are compared with

the SOP estimates delivered by the standardized hybrid pulse power characterization (HPPC) test. Performing two methods of estimation for the same physical system using separate sets of data is a respected approach to check the validity of both estimation methods.

The well-known HPPC test defined in [1] and applies a defined sequence of paired discharge/charge current pulses to the subject battery after one-hour rest periods. Each current pulse has the same fixed time duration, e.g., 12 seconds. The measured battery voltage and current waveforms are used to develop estimates of the battery equivalent resistance that is important for predicting the battery's power capability.

The estimated $\hat{v}_{ocv}$ at each tested SOC level is derived from the rested battery voltage before the pair of current pulses is applied. A fixed resting interval is also applied between the discharging and charging pulses (e.g., 40 sec) to give the battery some recovery time between the two pulses. The HPPC test is typically applied to a battery at a series of different SOC levels arranged at intervals of approx. 10% SOC. The adjustment between SOC levels is typically accomplished using a constant-current discharge. Figure 4.5 shows a portion of the HPPC test current profile applied to the CALB 60AHA battery cell.

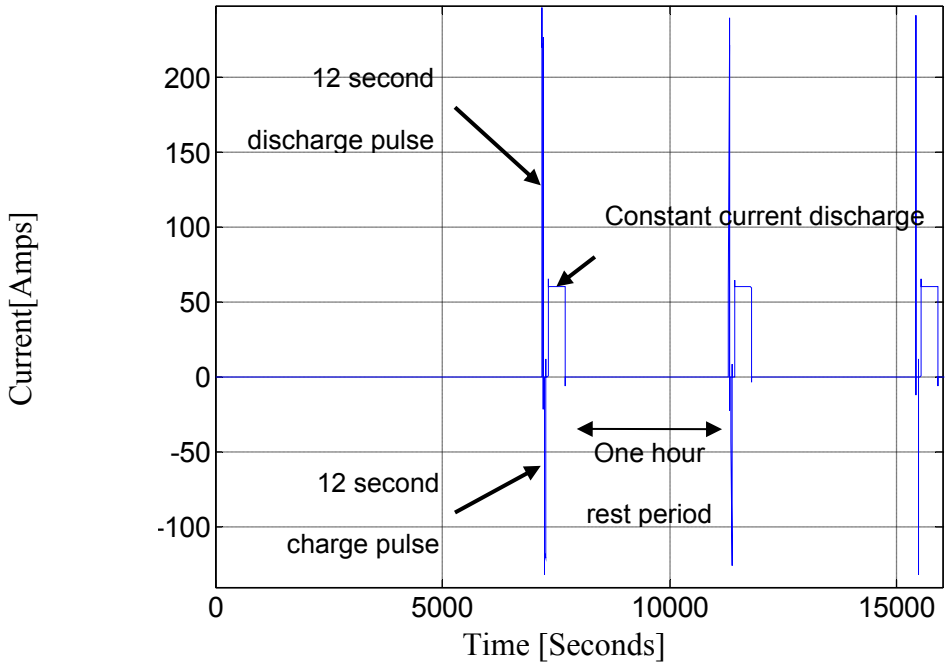

Figure 4.5 View of experimental HPPC test current pulses applied to the CALB 60AHA battery

When interpreting the results of the HPPC test, it is important to note that the power capability estimates extracted from the data are dependent on the selected pulse duration and initial conditions. That is, with the rested initial condition before each current pulse, the maximum voltage drop due to the stepped discharge current excitation occurs at the end of the current pulse. If the discharge current is allowed to extend beyond the 12-second interval chosen for this HPPC test, the resulting power capability estimate for the battery will decrease because of the dropping battery voltage during the pulse. As pointed out, the chosen SOP definition in (4.1.2) is the battery power capability at steady-state, which is different from the conditions associated with the HPPC test. In general, batteries in the lithium-ion family exhibit time constants to reach steady-state that are several tens of seconds. An example can be found in Figure 3.12.

4.3.2 Discussion on the Battery Time Constant Selection

An exercise has been conducted to compare: 1) the predicted SOP from the recursive estimator applied to the UDDS drive cycle test data; and 2) the estimated power capability from the HPPC test that is performed offline. As a first step, the time constant parameter a_1 is tuned according to the HPPC test procedure instead of using an offline test to estimate the time constant of the battery. Specifically, the HPPC test and its corresponding Thevenin circuit model assume that the battery is close to steady-state (within 0.1%) at the end of the current pulse. Hence, the implicit time constant τ assumed by the HPPC test with 12-second pulses can be calculated as:

$$0.001 = \exp\left(\frac{-12}{\tau}\right) \quad (4.3.1)$$
$$\Rightarrow \tau = 1.7372 \text{ seconds}$$

The value of the corresponding discrete time constant parameter a_1 for a sampling time of 0.1 seconds can then be evaluated for the time constant value in (4.3.1) as:

$$a_1 = -\exp\left(\frac{0.1}{-\tau}\right) \quad (4.3.2)$$
$$\Rightarrow a_1 = -0.944$$

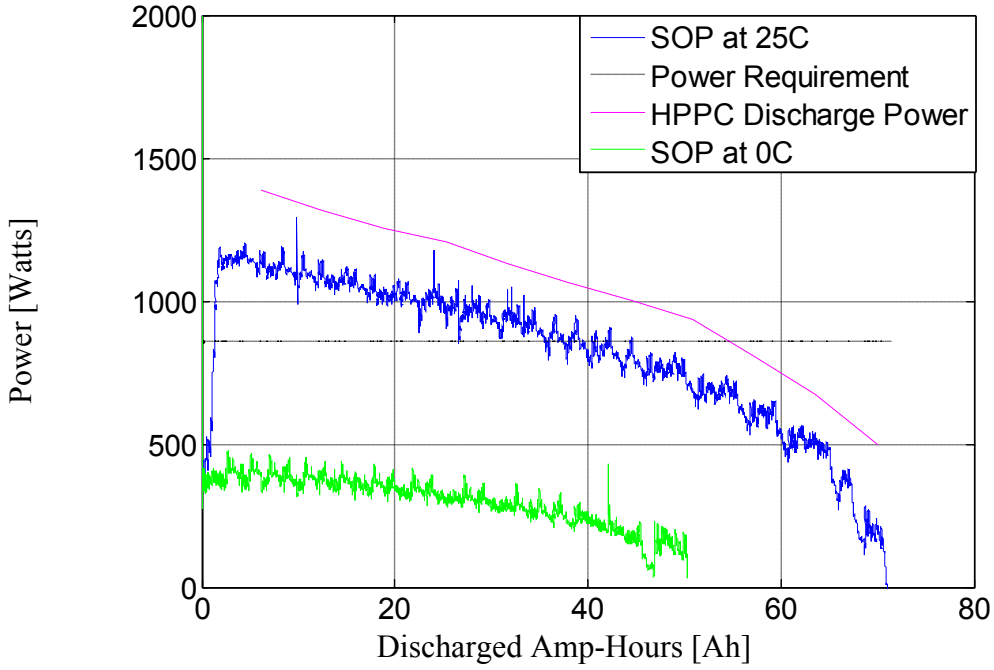

Figure 4.6 Estimated SOP curves provided by the recursive estimator using the UDDS drive cycle current profile for two battery temperatures (25°C and 0°C) compared with HPPC predicted power capability (25°C). τ = 1.74 sec

This value of a_1 has been adopted for all analysis in this paper except when noted otherwise.

Figure 4.6 shows two estimated SOP curves for different temperatures using the recursive estimator applied to the UDDS driving cycle current profile, together with the estimated discharge power capability curve derived from the HPPC test data. As expected, the SOP curve for data gathered at 0^0C shows a much lower power capability in Figure 4.6 compared to the other two curves associated with operation at 25^0C. This illustrates the important point that a simple SOC/Remaining-Amp-hour metric that does not consider temperature effects is insufficient to characterize the battery performance characteristics, especially with respect to its power capability.

It can be observed in Figure 4.6 that the estimated SOP curve at 25^0C is approximately 10% lower than the predicted HPPC discharge power curve. The

discrepancy can be traced back to differences between the estimated open-circuit voltage $\hat{v}_{ocv}$ delivered by the recursive estimator and the HPPC test, as shown in Figure 4.7. Although both curves have almost identical shapes, the average difference between the two $\hat{v}_{ocv}$ values is approximately 50 mV for every value of discharge Amp-hours. This difference is explained by the fact that HPPC test rests the battery for an hour such that the voltage has reached its steady-state value at the end of rest, leading to an elevated estimate for $\hat{v}_{ocv}$. In comparison, during a discharge-dominated load profile the unmodeled longer time constant resulting from the battery's complex electrode diffusion phenomena gets reflected in the recursive estimator battery model as a lower value of $\hat{v}_{ocv}$.

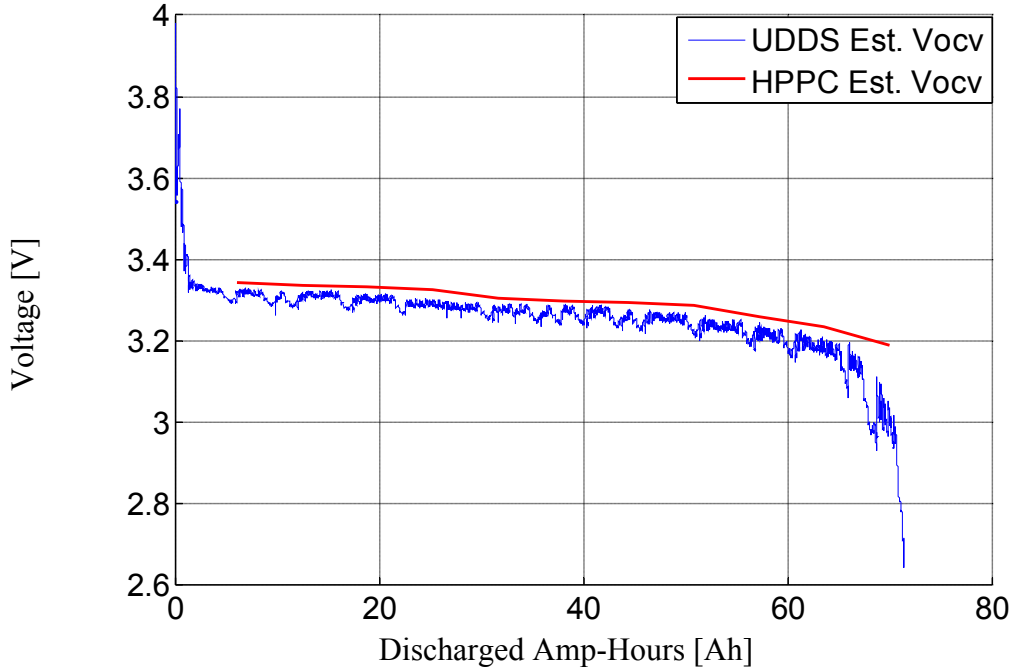

Figure 4.7 Comparison of $\hat{v}_{ocv}$ for the proposed recursive estimator using the UDDS cycle current profile and the HPPC test. $\tau = 1.74$ sec

For completeness, Figure 4.8 provides estimated values of the combined resistive impedance $\hat{r}_0 + \hat{r}_1$ in the battery model for the two estimation methods. As discussed earlier, the two estimators make similar assumptions about the battery system time constant. As a result, the curves in Figure 4.8 show that the estimated combined resistance values $\hat{r}_0 + \hat{r}_1$ track each other quite closely for the recursive estimator case using the UDDS drive cycle data with $\tau = 1.74$ sec.

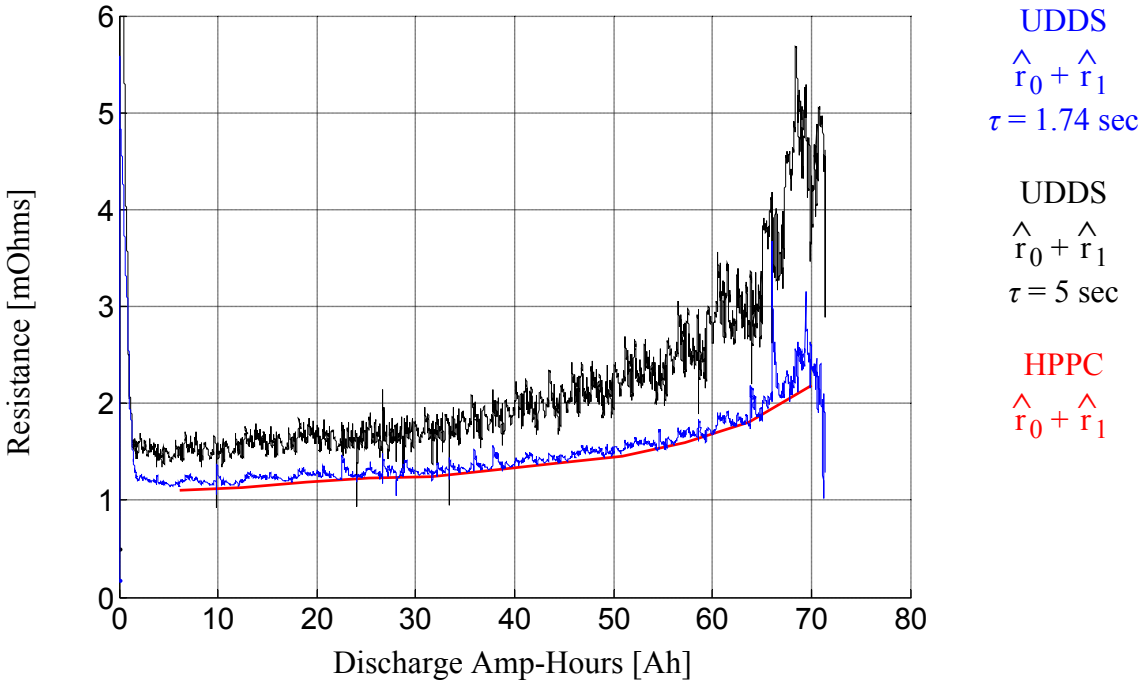

Figure 4.8 Comparison of $\hat{r}_0 + \hat{r}_1$ provided by the HPPC test results and the proposed recursive estimator using the UDDS drive cycle current profile with two time constant values ($\tau = 1.74$ sec and 5 sec)

As noted before, the adoption of a battery model with a single time constant is a simplification of the real battery system for many battery types, including lithium-based batteries. Recognizing that the single time constant model is an approximation, it can be shown that choosing the same value for this time constant τ is important in order to

achieve consistency between the HPPC test and recursive estimator models. This is demonstrated by showing the results of choosing a longer time constant $\tau = 5$ sec in the recursive estimator. The associated curve in Figure 4.8 shows that the estimated $\hat{r}_0 + \hat{r}_1$ for the case with $\tau = 5$ sec deviates significantly from the HPPC test results. The results for the case with $\tau = 5$ sec were achieved with the same filter tunings as the case with $\tau = 1.74$ sec.

Finally, the power prediction capability of the recursive estimator is evaluated by adding 250 [Amps] current pulses of duration of 12 seconds in the UDDS drive cycle. The modified current profile is in Figure 4.9.

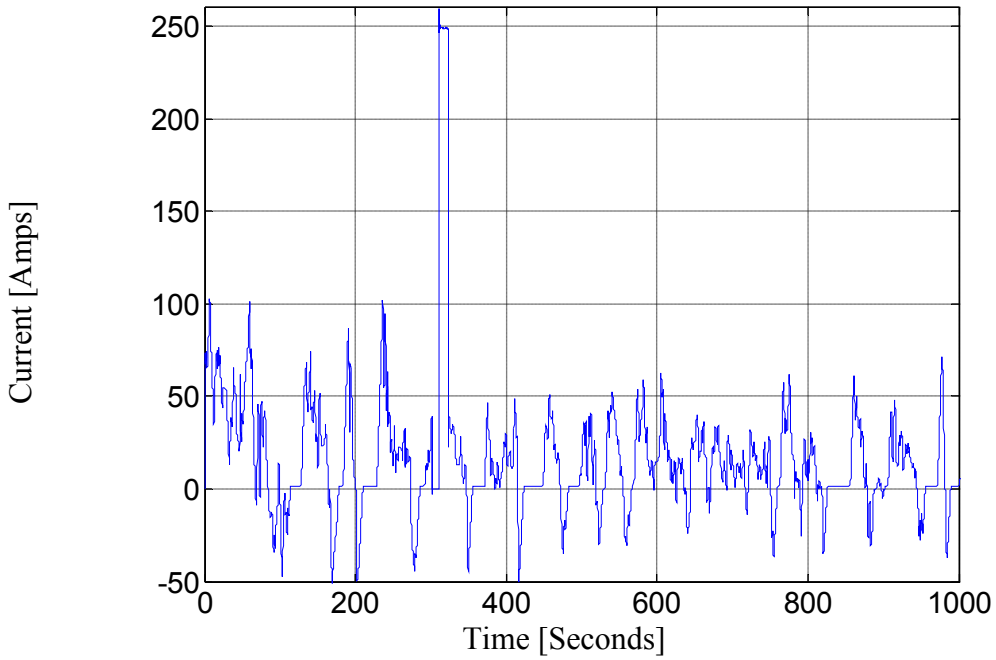

Figure 4.9 UDDS drive cycle current profile with injected 12-second current pulses of 250 Amps. The drive cycle repeats until battery is fully discharged

The resulted Kalman filter results are shown in Figure 4.10.

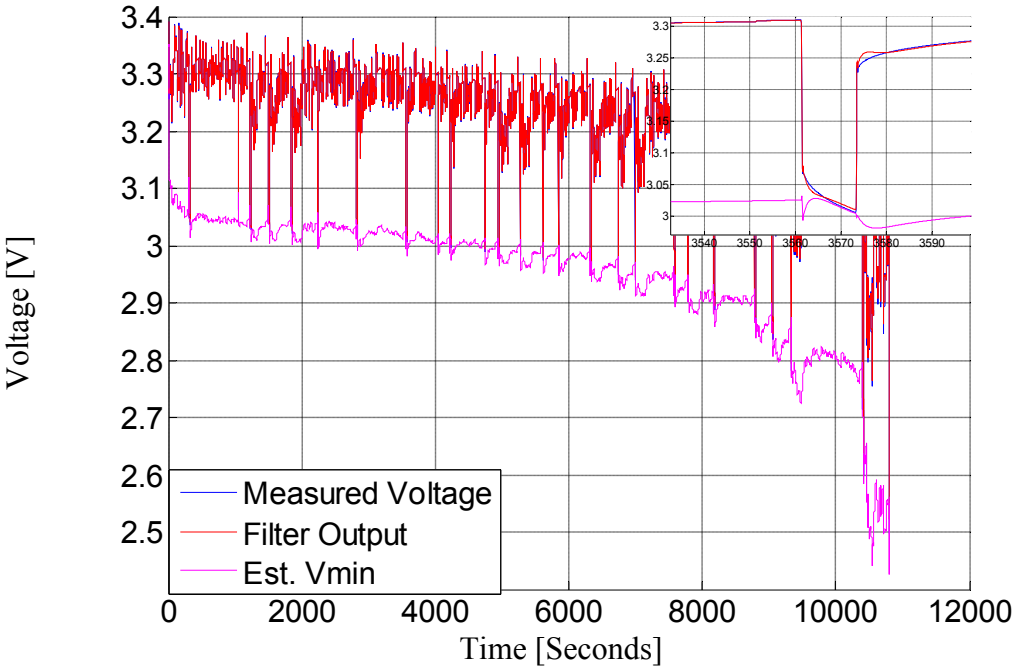

Figure 4.10 Kalman filter predictions for the current profile in Figure 4.9

From Figure 4.10, it can be seen that during the 12 second current pulse the voltage drops to the value quite close to the estimated $\hat{v}_{min}$. This result further strengthens the confidence in the power prediction by the recursive estimator. Thus when under electric drive condition, the battery pack's SOP can be obtained under the recursive estimation scheme. Due to the equivalence of SOP and SOF and availability of confidence interval for SOF, SOF can be implemented on an actual vehicle to provide power prognostics with margin of safety.

4.4 Summary

This chapter presents a methodology for online, recursive estimation for battery power capability. In contrast with conventional approaches, a method for calculating the SOF with deterministic mathematical probability under the context of a Kalman filter is introduced. The new statistic is equivalent to the traditional SOP in terms of SOF

determination using estimated parameters, but allows for a probabilistic statement on the SOF. This is considered to be a significant improvement in order to rigorously provide power prognostics with a margin of safety.

A comparison between the proposed power capability estimation using the recursive estimator and the results of the well-known standard HPPC test is also presented. The results demonstrate that by matching the key assumptions of the two model methods, the two estimators offer very similar power capability estimates, building confidence in the validity and usefulness of the proposed recursive estimator technique. Finally the power prediction capability of the recursive estimator is evaluated by adding current pulses and compare the estimated $\hat{v}_{min}$ with the actual voltage drop.

Chapter 5

Lithium-Ion and Lead-Acid Battery Temperature Dependent Modeling, Power Prognostics, and SOC Estimation

This chapter is a summary of all the battery monitoring work in this thesis. The temperature-dependent behavior of the resistance and overpotential of a CALB $LiFePO_4$ battery is first explored. Offline experimental results from HPPC tests and EIS methods for resistance and overpotential are explained using the Arrhenius equation. Using a nonlinear regression technique, simulated drive cycle data are used to confirm the experimental findings and construct a generic cell model that explicitly takes temperature effects of the resistance and overpotential into account.

This generic cell model is also adopted for Kalman filtering for online battery monitoring, i.e. SOF and SOC. In addition, a solution for SOC estimation that takes temperature, aging, and current dynamics into account is proposed for the $LiFePO_4$ battery. The same generic cell model is also applied to a lead-acid battery under discharge-only cycles. Finally the EIS experiment with DC current bias is adopted to verify the $LiFePO_4$ and lead-acid batteries' temperature-dependent behavior, in addition to time domain-based approaches such as the HPPC test and drive cycle tests.

5.1 Theory of Battery Resistance and Overpotential Behavior as a Function of Temperature

In this section, the theoretical forms of battery resistance and overpotential as functions of temperature are derived using the Arrhenius relationship that describes the rate of reaction based on temperature.

5.1.1 Battery Resistance in Arrhenius Form

The well-known Arrhenius equation empirically relates a rate constant k of chemical reactions to the temperature T in Kelvins.

$$k = A\exp\left(\frac{-E_a}{RT}\right) \tag{5.1.1}$$

In (5.1.1), A is a pre-exponential factor and E_a has units of energy per mole. To find a theoretical expression for pure ohmic resistance r_0 as a function of temperature, it is assumed that the resistance is inversely proportional to a rate constant, K. The rate constant is also assumed to follow the Arrhenius form, and r_0 is expressed as a function of temperature in (5.1.2).

$$r_0 = \frac{1}{k} = \frac{1}{A}\exp\left(\frac{E_a}{RT}\right) \tag{5.1.2}$$

It can be seen that (5.1.2) is simply the inverse of (5.1.1). The ohmic resistance (5.1.2) rapidly increases as the temperature drops, consistent with observations in the literature, e.g., [28].

5.1.2 Butler-Volmer Equation Exchange Current in Arrhenius Form

The Butler-Volmer equation had an important role in Chapter 3 where it was shown that lead-acid battery electrode overpotential has a significant Butler-Volmer behavior and the modeling of such a battery needs to take the nonlinear behavior into account. The Butler-Volmer equation is presented again in (5.1.3).

$$i = i_0\left[\exp\left(-\alpha\frac{\eta F}{RT}\right) - \exp\left((1-\alpha)\frac{\eta F}{RT}\right)\right] \tag{5.1.3}$$

The inverse hyperbolic sine approximation is also repeated.

$$\eta = \frac{RT}{\alpha F}\sinh^{-1}\left(\frac{i}{2i_0}\right) \tag{5.1.4}$$

Notice that the value of the exchange current i_0 determines the shape of the Butler-Volmer curve. This numerical phenomenon can be illustrated with an example.

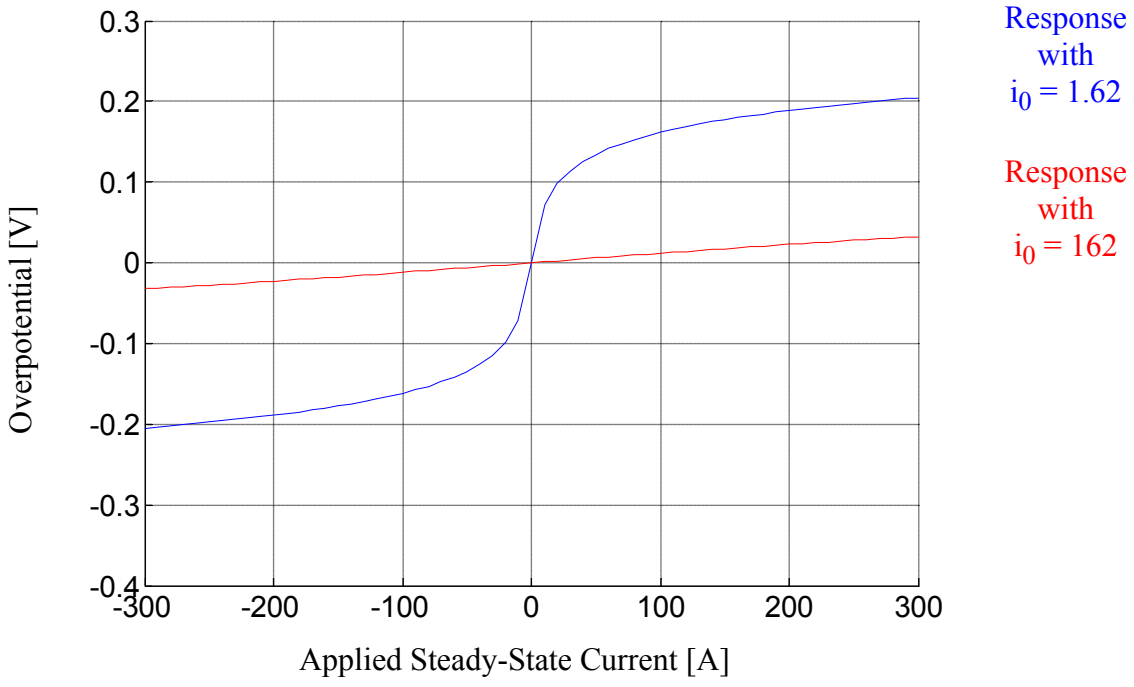

Figure 5.1 Simulated electrode voltage responses with the same $\frac{RT}{\alpha F}$ but different i_0

Figure 5.1 shows two simulated curves based on (5.1.4) and the same $\frac{RT}{\alpha F}$ value. The difference between the two curves is the value of i_0 adopted, one being 100 times the value of the other. It is observed that an increase in i_0 results in the straightening of the curve in the same current region. When dealing with a large i_0 value in (5.1.4), adopting a linear circuit model, i.e., ignoring the Butler-Volmer nonlinear effect, is a legitimate approach because the model complexity of the linear circuit model is lower and the two models are likely to produce similar results.

On the other hand, the exchange current may be temperature dependent and cause a more pronounced Butler-Volmer behavior in some temperature regions. Since the exchange current determines the rate of electron exchange between oxidation and reduction reactions in equilibrium, the exchange current may drop as the temperature decreases, i.e., the Arrhenius relationship. Therefore, the exchange current can be modeled as a function of temperature in the Arrhenius form.

$$i_0 = B\exp\left(\frac{-G}{RT}\right) \tag{5.1.5}$$

(5.1.4) and (5.1.5) together describe the overpotential as a function of temperature. It is important to note that the change in overpotential as a function of current cannot be captured by increasing the linear model complexity, i.e., adding more *RC* terms. Nor can the temperature influence be accurately captured by using a table of resistances for various temperatures. Recent publications show that the overpotential and the associated charge-transfer resistance for lithium nickel-manganese-cobalt oxide (NMC) cells become nonlinear functions of current at low temperatures, reflecting the BV relationship [127], [139]. While [139] relies on recursive estimation to adapt the

Butler-Volmer equation parameters with temperature, this chapter presents the derivation of the Bulter-Volmer equation temperature dependence based on the Arrhenius equation. This derivation is key to making it possible to develop an offline model that takes temperature into account.

5.2 HPPC and EIS Tests with Temperature as a Factor

In this section, the resistance and overpotential dependence on temperature is experimentally evaluated using HPPC and EIS tests. In this work, a CALB lithium iron phosphate cell rated at 60 Ah and 3.6 V was used in the experiments. The cell underwent HPPC tests at various temperatures as defined in [1]. The HPPC test employs 1 C discharge currents (i.e., 60 A in this case) to move from one SOC test point to another and the pulsed test currents are 0.5, 1, and 2 C. EIS was carried out during the rest periods in the HPPC sequence before the pulses were applied to provide additional information about the cell characteristics.

First, the CALB battery under test is shown in Figure 5.2. The temperature measurement is made on one of the terminals.

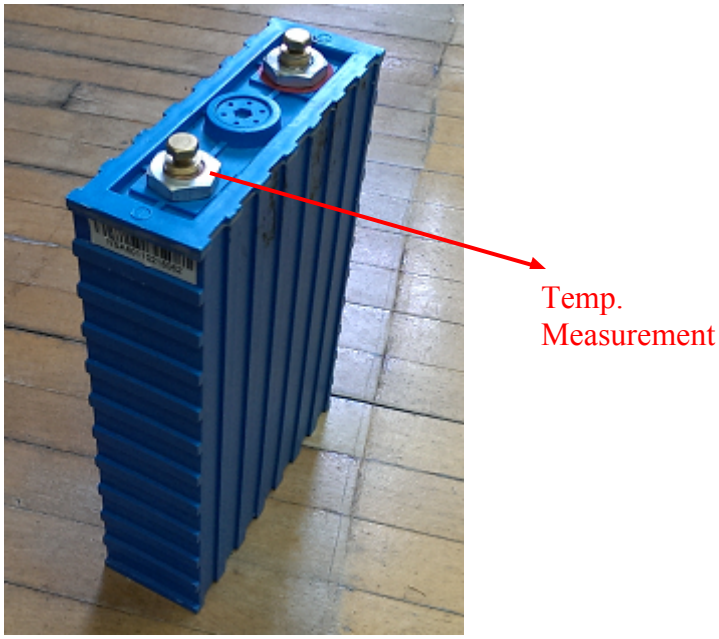

Figure 5.2 CALB $LiFePO_4$ battery rated at 60 Ah

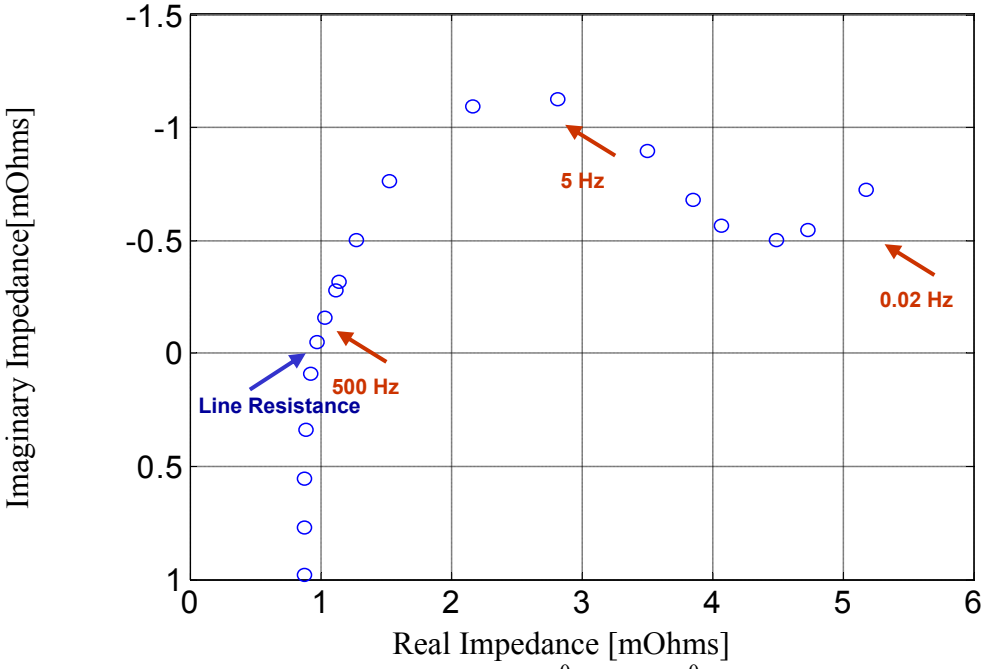

Figure 5.3 EIS data for 0^0C/273.15^{0}K

Figure 5.3 shows a typical measured EIS result at a fixed temperature, where each data point is the impedance for one excitation frequency plotted with real impedance along the x-axis and imaginary impedance along the y-axis. The ohmic resistance r_0 can be approximated as the real impedance at the resonant frequency where the measured

curve crosses the x-axis. This value is linearly extrapolated between the two nearest data points straddling the x-axis for each data set. For the 90% SOC condition, the measured r_0 is plotted as a function of temperature along with its fitted function using (5.1.2) in Figure 5.4. This figure shows that the value of r_0 drops exponentially as the cell temperature increases, and the match with the curve-fit waveform is excellent.

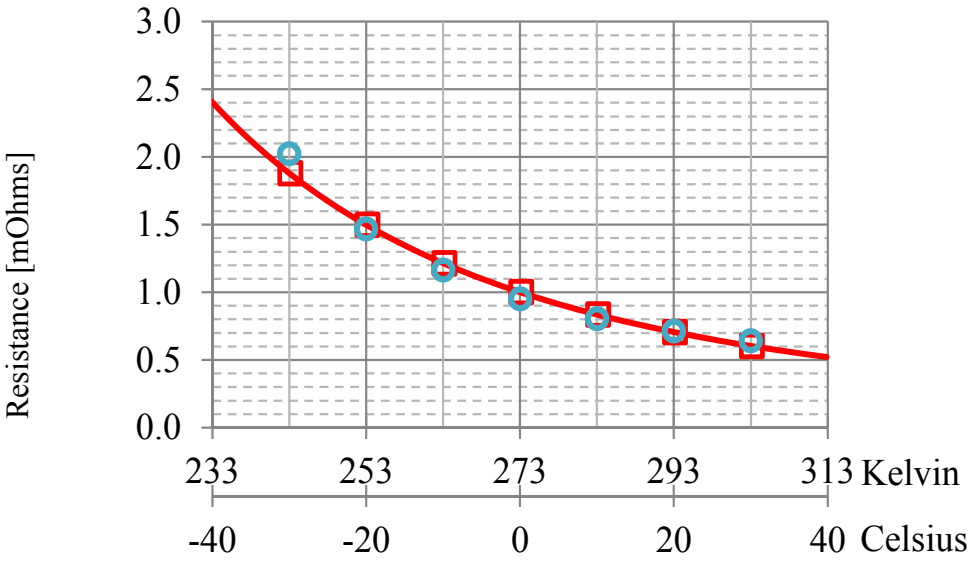

Figure 5.4 Pure resistance r_0 and its fitted function of temperature using (5.1.2) at 90% SOC

For the HPPC test data, resistance value r_0 for the battery model can be approximated by dividing the voltage drop during the pulse by the pulse current amplitude. This resistance is a combined effect of r_0 and the overpotential η, and due to the time constant, the duration of the pulse will affect the value of the resistance. Comparing Figure 5.5 and Figure 5.6, it can be seen that the HPPC-measured resistances are approximately the same for different pulse current amplitudes at 20^0C, but the resistances become more current-sensitive as the temperature drops. More specifically,

the HPPC resistance decreases for higher current at 0^0C, consistent with the Butler-Volmer relationship.

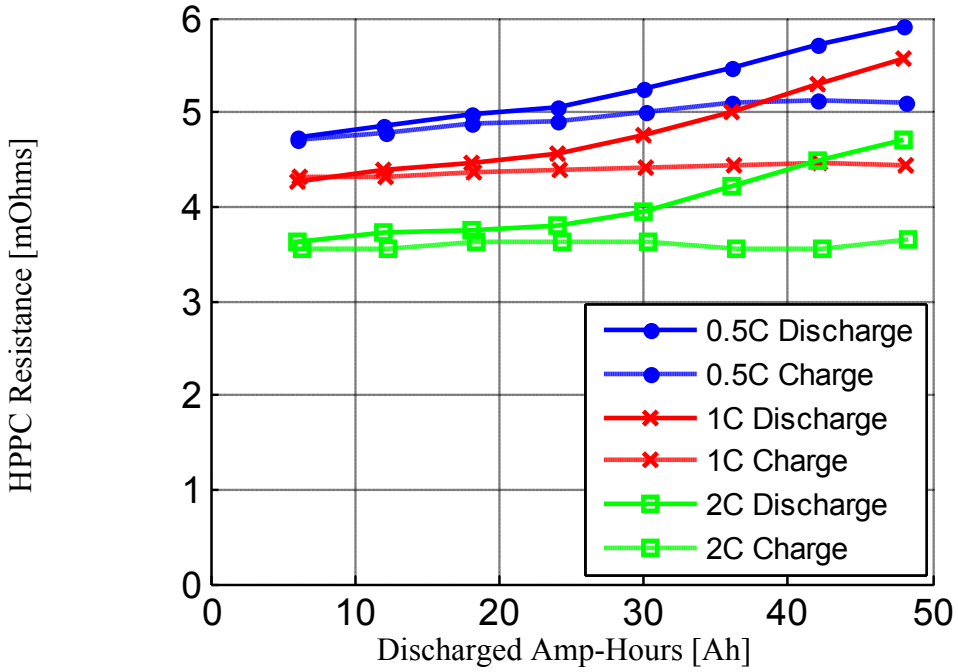

Figure 5.5 HPPC resistances at different SOC test conditions for different pulsed currents at 0^0C/273.15^{0}K

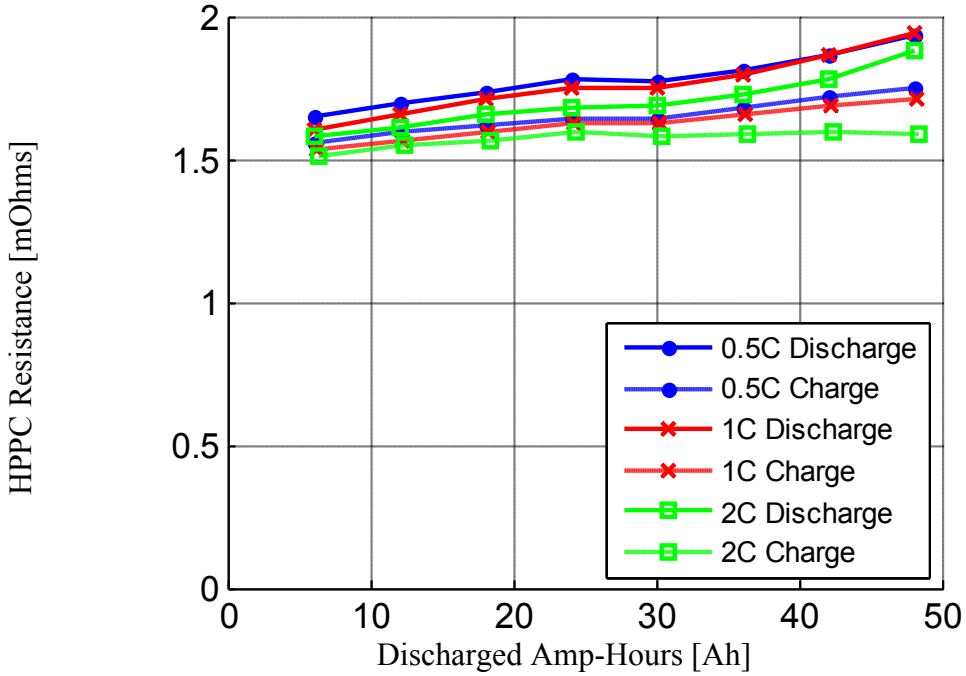

Figure 5.6 HPPC resistances at different SOC test conditions for different pulsed currents at 20^0C/293.15^{0}K

The fact that the HPPC resistances do not exhibit the Butler-Volmer relationship as much at 20^0C corroborates the wide use of the linear circuit model in the literature for lithium batteries when low temperatures are not encountered.

Qualitatively, the HPPC resistances show a more significant Butler-Volmer behavior at lower temperature. This observation is consistent with the modeling assumption made in (5.1.5) where a decrease in temperature causes a drop in the exchange current causing a more significant Butler-Volmer response as discussed in 5.1.2.

5.3 Parameter Fitting of Linear Electric Circuit Model and Butler-Volmer Model at Various Temperatures Using Short Term Drive Cycle

In this section an offline parameter estimation methodology, different from the one discussed in 3.2.2, is introduced. The methodology covered here requires battery data under an arbitrary drive cycle, either during an actual EV drive or a cycle on a test bench capable of the simulation. In order to further explore the features of the Butler-Volmer relationship at low temperatures, the $LiFePO_4$ cell was subjected to a simulated drive cycle at different temperatures in the lab, and the voltage, current, and temperatures were logged at 10 Hz.

The Butler-Volmer and linear circuit discrete time models are repeated in (5.3.1) and (5.3.2).

$$V(k) = v_{ocv} - r_0 i(k) - \frac{b_1}{1 + a_1 q^{-1}} \sinh^{-1}\left(\frac{i(k)}{2i_0}\right) \tag{5.3.1}$$

$$V(k) = v_{ocv} - \frac{b_0 + b_1 q^{-1}}{1 + a_1 q^{-1}} i(k) \tag{5.3.2}$$

As before, these models can be rewritten in the time domain by multiplying both sides of these equations by the term $(1 + a_1 q^{-1})$ and assuming v_{ocv} does not change during one sample.

$$v(k) = (1 + a_1)v_{ocv} - a_1 v(k-1) - (i(k) + a_1 i(k-1))r_0 - \sinh^{-1}\left(\frac{i(k)}{2i_0}\right)b_1 \quad (5.3.3)$$

$$v(k) = (1 + a_1)v_{ocv} - a_1 v(k-1) - i(k)b_0 + i(k-1)b_1 \quad (5.3.4)$$

Notice that given a batch of voltage and current data for a short duration of a drive cycle, (5.3.3) and (5.3.4)'s parameters can estimated. Specifically, in (5.3.3) the unknown parameters are $[v_{ocv}, a_1, r_0, i_0, b_1]^T$ and they are $[v_{ocv}, a_1, r_0, b_1]^T$ in (5.3.4). The predictor terms in both (5.3.3) and (5.3.4) consist of current and voltage data that are available in the drive data. The regression for (5.3.3) and (5.3.4), however, is nonlinear and requires an iterative method like the Gauss-Newton method. The following briefly introduces the Gauss-Newton method.

For the $LiFePO_4$ battery, the OCV vs. SOC curve is very flat and the drop in SOC during the drive cycle used for regression is usually less than 5%. Therefore, it makes sense to use a constant v_{ocv} for regression purposes. For chemistries whose OCV vs. SOC curves have a steeper slope, the v_{ocv} can be modeled as a line that has a different offset and slope when plotted against discharged Ah for each temperature.

$$v_{ocv} = v_a + v_b Ah \quad (5.3.5)$$

Consider m functions $r = (r_1, r_2, ..., r_m)$ of n variables $\beta = (\beta_1, \beta_2, ..., \beta_n)$. Usually r is interpreted as the residuals of the model, and β the parameters to be estimated. The Gauss-Newton method seeks to minimize the sum of squared errors.

$$S(\beta) = \sum_{i=1}^{m} r_i^2(\beta) \tag{5.3.6}$$

Starting with an initial guess β^0, the Gauss-Newton method iterates the following:

$$\beta^{(s+1)} = \beta^{(s)} + \left(J^T J\right)^{-1} J^T r \tag{5.3.7}$$

where J is the Jacobian matrix at the iteration step s, i.e., the partial derivatives of the residuals with respect to the individual parameters.

$$J = \frac{\partial r_i}{\partial \beta_j}\left(\beta^{(s)}\right) \tag{5.3.8}$$

(5.3.7) can also be modified with a fraction gain k to control the numerical stability, i.e.,

$$\beta^{(s+1)} = \beta^{(s)} + k\left(J^T J\right)^{-1} J^T r \tag{5.3.9}$$

Applying the Gauss-Newton method to both models in (5.3.3) and (5.3.4) with the same drive cycle data at 20^0C/293.15^0K, the results are shown in Figure 5.7 and Figure 5.8. The average squared errors are 9.25e-5 and 7.01e-5 respectively.

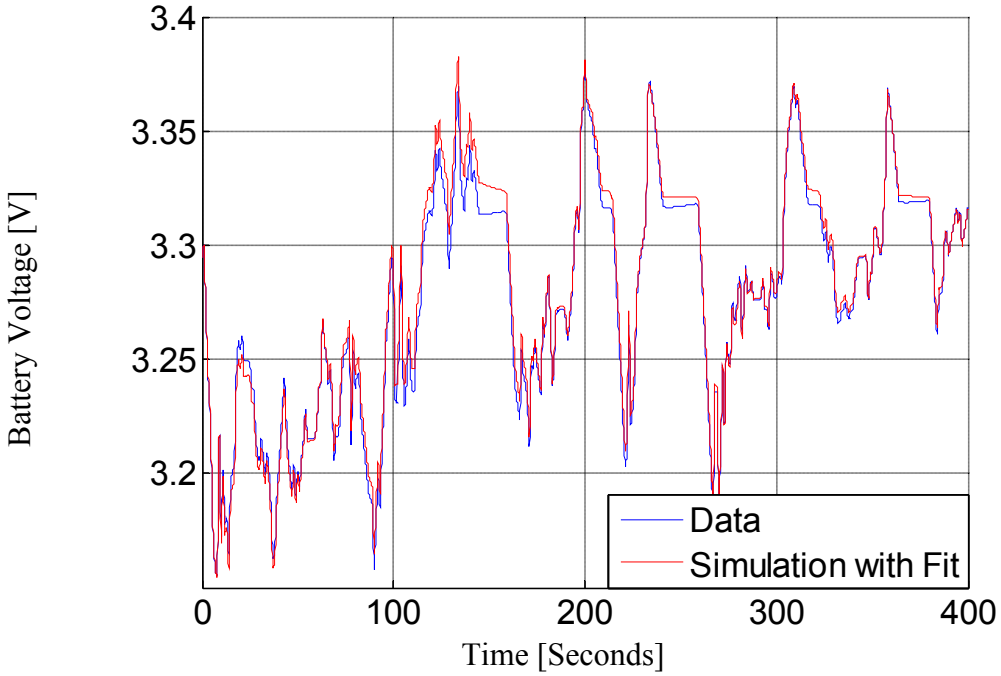

Figure 5.7 Drive cycle test data and Butler-Volmer model simulation with fitted parameters at ambient 20^0C/293.15^0K

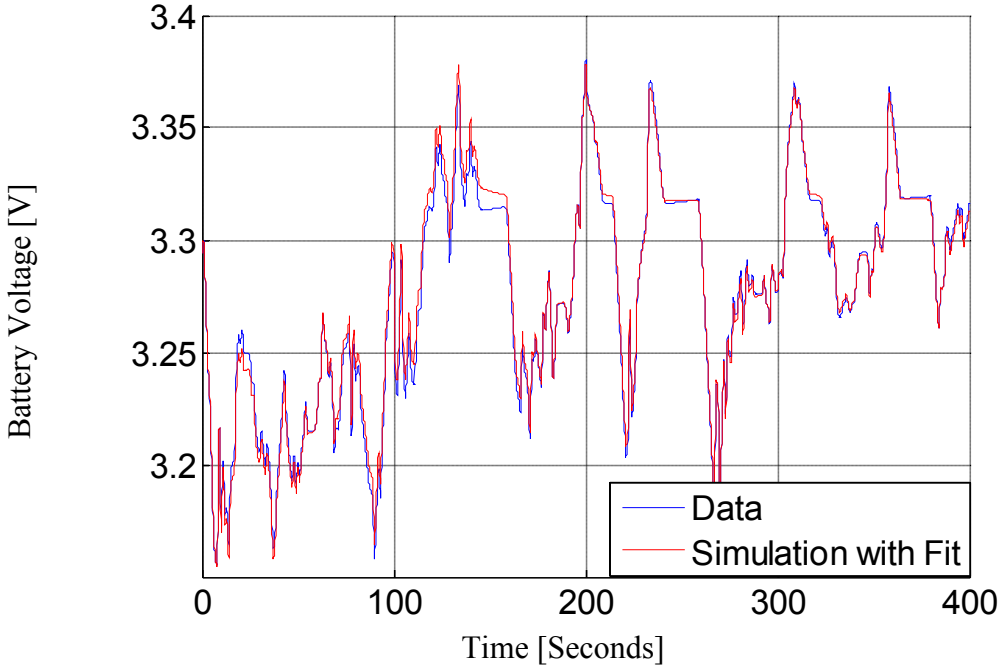

Figure 5.8 Drive cycle test data and linear circuit model simulation with fitted parameters at ambient 20^0C/293.15^0K

It can be seen that the predictions of both models are nearly the same so that the Butler-Volmer model offers no particular advantage over the linear model.

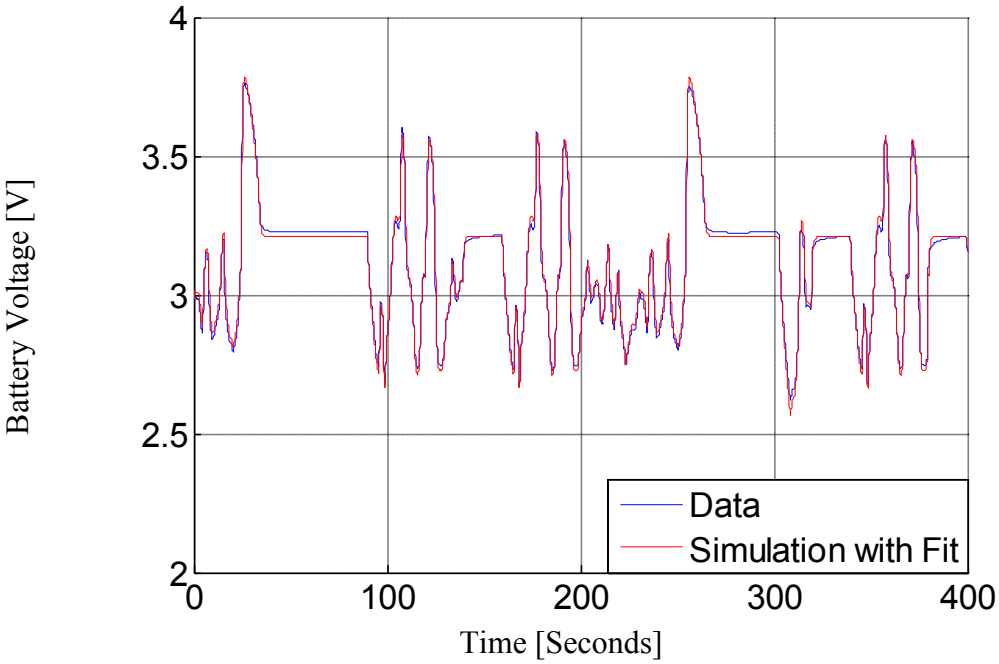

Figure 5.9 Drive cycle test data and Butler-Volmer model simulation with fitted parameters at ambient -20^{0}C/253.15^{0}K

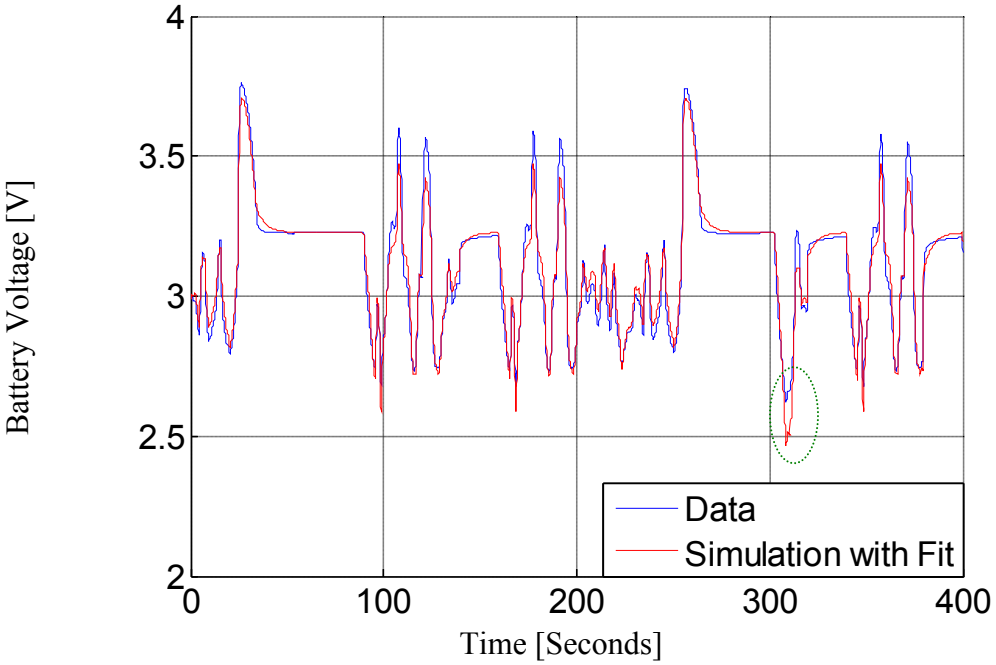

Figure 5.10 Drive cycle test data and linear circuit model simulation with fitted parameters at ambient -20^{0}C/253.15^{0}K

In contrast, the improved match achieved using the Butler-Volmer model for battery parameter data at -20^{0}C/253.15^{0}K is shown in Figure 5.9 and Figure 5.10. The average

error squares are 2.93e-4 and 7.32e-4, respectively. Notice in Figure 5.10 the dashed green circle points out a part of the data where a high discharge current is applied. The linear circuit model tends to overpredict the voltage drop at a high current, due to the lack of saturation effect at the high current region.

Since Figure 5.7 and Figure 5.8, Figure 5.9, and Figure 5.10 use the same data for estimation and simulation evaluation, it is desirable to see how the models fare when evaluation is performed on data from a different part of the drive cycle. Notice that due to the assumption of a fixed v_{ocv} in both models and v_{ocv} dependence on SOC, the data set used for prediction evaluation cannot be too far away in time and discharged Amp-hours from the data set used for parameter estimation. In this example, the second data set from the drive cycle at -20^0C/253.15^0K was separated from the first by 600 seconds and 1.7 Ah, counting both discharging and regenerating currents.

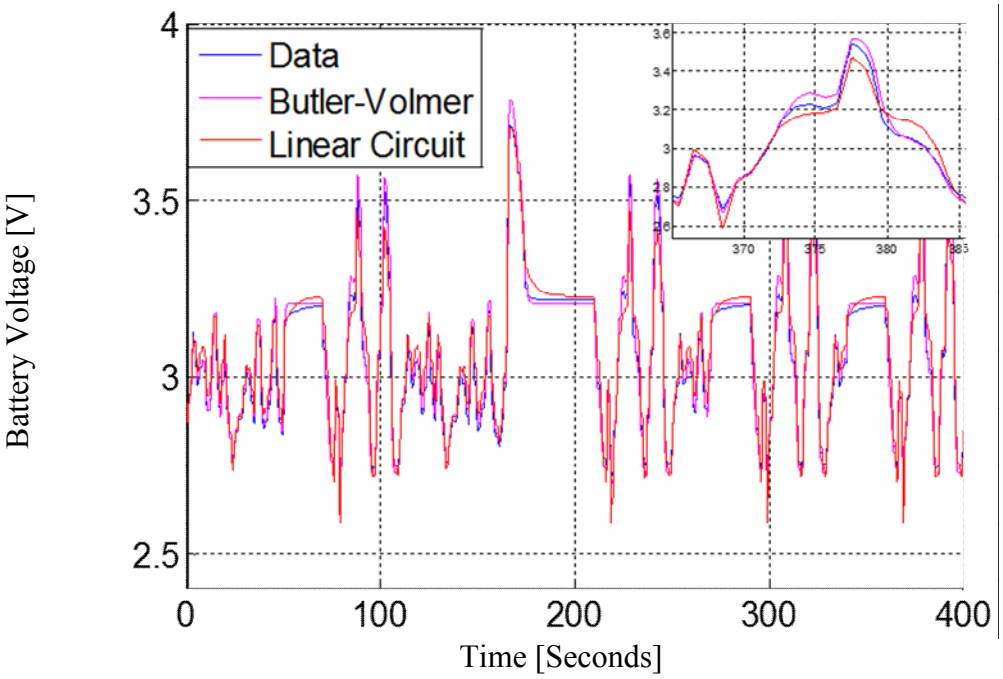

Figure 5.11 Drive cycle test data and both models' predictions using a different part of the drive cycle for evaluation at ambient -20^0C/253.15^0K

Figure 5.11, using average square errors, again demonstrates the advantages of the Butler-Volmer model at lower temperature compared with the linear circuit model. Figure 5.12 compares the prediction error histogram of the two models and visually confirms that linear-circuit model has a larger error variance.

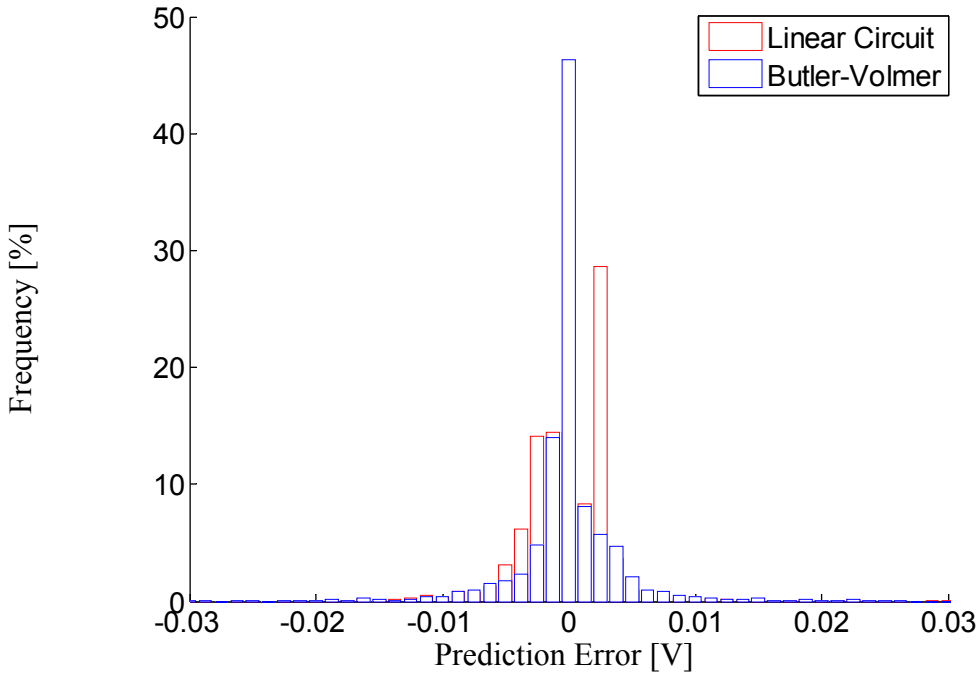

Figure 5.12 Prediction error histogram for the two models under the drive cycle in Figure 5.11

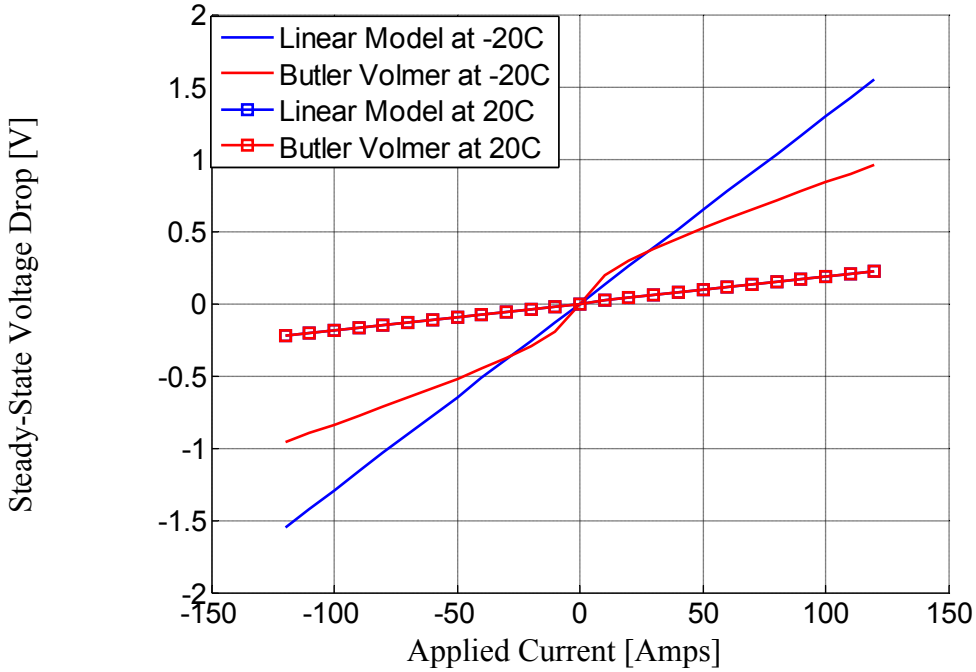

Figure 5.13 The predicted steady-state voltage drop based on fitted parameters at ambient -20^0C/253.15^{0}K and 20^0C/293.15^{0}K

Finally, to establish that Butler-Volmer behavior is indeed prominent at low temperature and the corresponding modeling effort is necessary, the models' predicted steady-steady voltage drops ($i*r_0 + \eta(i)$) vs. current based on fitted parameters are shown Figure 5.13. The effect of the Butler-Volmer relationship is clearly visible at the lower temperature (-20^0C), while at room temperature (20^0C) the two models yield voltage drop predictions that agree with each other quite closely. The linear circuit model is clearly incapable of modeling the Butler-Volmer relationship that is present during low-temperature conditions.

5.4 Offline Parameter Fitting of a Generic Battery Model with Resistance and Overpotential Dependence on Temperature

In this section, a generic battery model with resistance and overpotential that are dependent on the temperature is proposed. One benefit of this model is that it can adjust

to different temperature conditions quickly without relying on gradual convergence. The other benefit is that such an explicitly temperature-dependent form can lead to a recursive estimator that specifically takes temperature as an input, thus achieving online monitoring for vehicles expected to experience a large range of temperature.

Most importantly, the nonlinear feature of the Butler-Volmer equation is not possible for the linear-circuit model to mimic. The generic cell model offers a method to describe such a phenomenon at different temperature conditions. First the Butler-Volmer-based battery model in discrete from is repeated.

$$v(k) = v_{ocv} - r_0 i(k) - \frac{b_1}{1 + a_1 q^{-1}} \sinh^{-1}\left(\frac{i(k)}{2i_0}\right) \tag{5.4.1}$$

As discussed earlier in this chapter, the resistance r_0 and the overpotential η are modeled as functions of temperature in (5.4.2), (5.4.3), and (5.4.4).

$$r_0 = \frac{1}{k} = \frac{1}{A}\exp\left(\frac{E_a}{RT}\right) \tag{5.4.2}$$

$$\eta = \frac{RT}{\alpha F}\sinh\text{-}1\left(\frac{i}{2i_0}\right) = \frac{b_1 T}{1 + a_1} \sinh^{-1}\left(\frac{i(k)}{2i_0}\right) \tag{5.4.3}$$

$$i_0 = B\exp\left(\frac{-G}{RT}\right) \tag{5.4.4}$$

By substituting the appropriate terms in (5.4.1) with (5.4.2), (5.4.3), and (5.4.4), a discrete battery model with temperature as an input can be formed.

$$v(k) = v_{ocv} - \frac{1}{A}\exp\left(\frac{E_a}{RT}\right)i(k) - \frac{b_1 T}{1 + a_1 q^{-1}} \sinh^{-1}\left(\frac{i(k)}{2B\exp\left(\frac{-G}{RT}\right)}\right) \tag{5.4.5}$$

In order to perform parameter estimation for (5.4.5), it is necessary to combine, i.e. concatenate, the data from drive cycles under various temperatures. Without this

concatenation of data under various temperatures, it would be impossible to estimate parameters associated with temperature terms. The change of temperature within a cycle cannot realistically be sufficient for the estimation of parameters. Rearranging (5.4.5) and specifying the v_{ocv_i} for the open circuit voltage of each drive cycle of different temperatures to take into account the temperature effect on v_{ocv}, (5.4.6) is shown as follows:

$$\begin{aligned} v_n(k) = {} & (1 + a_1)v_{ocv\_i}\delta(i - n) - a_1 v_n(k - 1) \\ & - (i_n(k) + a_1 i_n(k - 1))\frac{1}{A}\exp\left(\frac{E_a}{RT_n(k)}\right) - \\ & b_1 T_n(k)\sinh^{-1}\frac{i_n(k)}{2B\exp\left(\frac{-G}{RT_n(k)}\right)} \end{aligned} \tag{5.4.6}$$

where the subscript n stands for n^{th} cycle, i for i^{th} cycle, and δ for the Kronecker delta function.

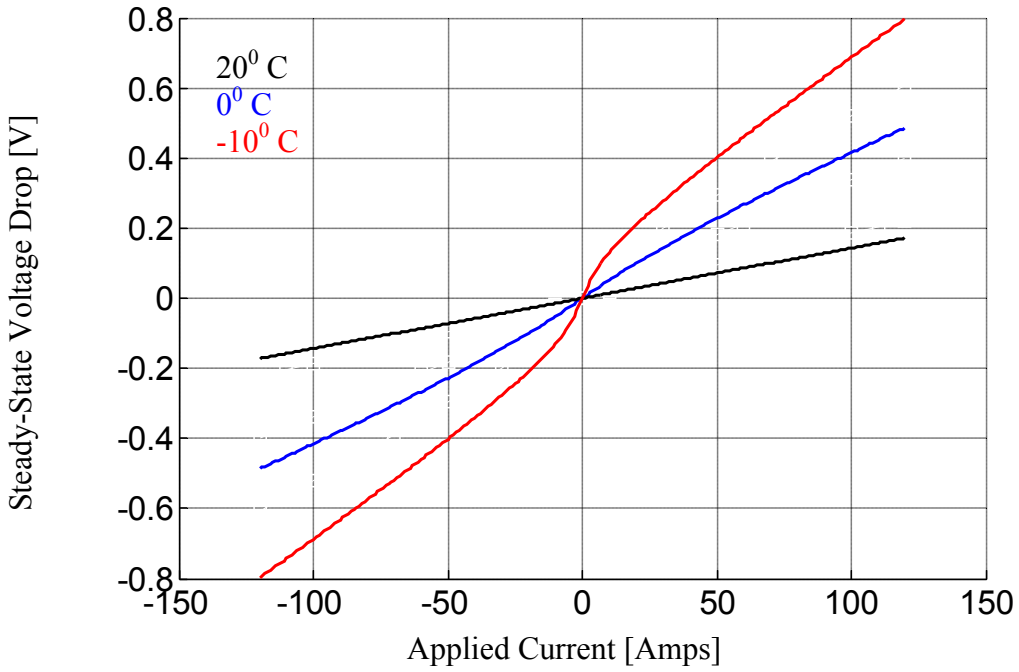

Figure 5.14 Steady-state voltage drop for the generic cell model at different temperatures

Figure 5.14 shows the steady-state voltage drops for different temperatures obtained from the generic cell model and visually displays the generic cell model's dependence on temperature.

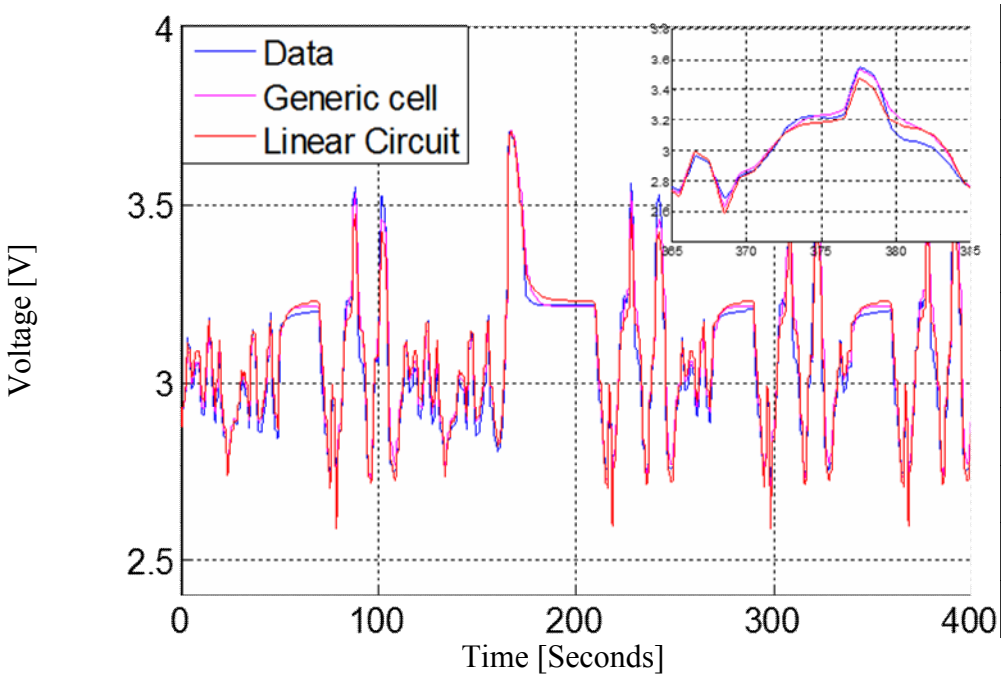

Figure 5.15 Drive cycle test data and generic cell and linear circuit predictions using a different part of the drive cycle for evaluation at ambient -20^0C/253.15^{0}K

In order to compare performance of the generic cell and the linear circuit models, the prediction methodology used in Figure 5.11 is repeated for the two models, i.e., using adjacent but different data points for prediction performance evaluation. One particular set of results, for -20^0C, is shown in Figure 5.15.

Table 5.1 The prediction average squared errors for the three modeling approaches

	-20^0C	-10^0C	-5^0C	0^0C	5^0C
Generic Cell	5.52e-4	2.64e-4	4.84e-4	3.11e-4	1.79e-4
Butler-Volmer	3.65e-4	3.00e-4	5.23e-4	2.68e-4	1.28e-4
Linear Circuit	6.60e-4	2.96e-4	5.30e-4	2.35e-4	9.03e-5

For five temperature conditions, the same prediction evaluation has been performed for the generic cell, simple Butler-Volmer that ignores temperature, and the linear circuit

models. The average squared errors for this particular data group are recorded in Table 5.1.

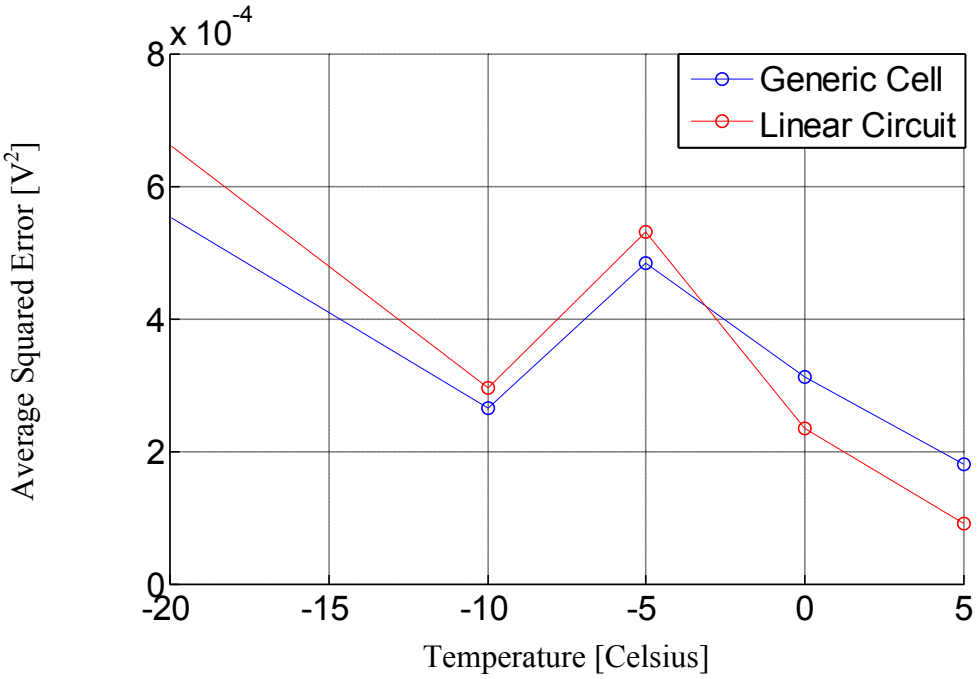

Figure 5.16 Comparsion of prediction performance for generic cell and linear circuit models based on Table 5.1

Figure 5.16 plots the results from Table 5.1 comparing the generic cell and linear circuit model. It can be seen that the generic cell model performs better in a comparative sense at lower temperatures. This result is not surprising since the Butler-Volmer phenomenon is more prominent at lower temperatures. Another point worth noting is that the prediction performance in the least-squares sense is subject to the drive cycle data. If the fitting and prediction data are drawn from the parts of the drive cycle that have a higher current load, the generic cell model is more likely to perform better since the Butler-Volmer behavior is more noticeable at higher current. For reference, the peak current for the data used in this chapter is 120 Amps or 2 C.

5.5 Adaptive Estimation Using Generic Cell Model

The generic cell model, with its explicit inclusion of temperature as an input, is suitable for offline simulation of $LiFePO_4$ batteries. However, some applications require online estimation and tracking of battery parameters, similar to those introduced in 3.2 and 4.2. Based on (5.4.6), this section introduces the process that adapts the generic cell model for online recursive estimatio, leading to the following expressions:

$$v(k) + a_1 v(k-1) = v_{ocv}(1 + a_1) - \frac{1}{A}(i(k) + a_1 i(k-1))\exp\left(\frac{E_a}{RT(k)}\right) - b_1 T(k)\sinh^{-1}\left(\frac{i(k)}{2B\exp\left(\frac{-G}{RT(k)}\right)}\right) \tag{5.5.1}$$

$$v(k) + a_1 v(k-1) = \theta\varphi(k) \tag{5.5.2}$$

$$\varphi(k) = \begin{bmatrix} 1 + a_1 \\ -(i(k) + a_1 i(k-1))\exp\left(\frac{E_a}{RT(k)}\right) \\ -T(k)\sinh^{-1}\left(\frac{i(k)}{2B\exp\left(\frac{-G}{RT(k)}\right)}\right) \end{bmatrix} \tag{5.5.3}$$

$$\theta = [v_{ocv}, \frac{1}{A}, b_1] \tag{5.5.4}$$

Closer examination reveals that (5.5.1) is a rearranged version of (5.4.6) with $v(k) + a_1 v(k-1)$ as the output on the left side of the equation. (5.5.2) expresses the right side of (5.5.1) as the product of the parameters to be fitted θ, and the regressor $\varphi(k)$. (5.5.3) defines the regressor $\varphi(k)$, while (5.5.4) identifies the parameters to be estimated. This estimator formulation for linear filtering is similar to the method introduced in 3.2, except the equations now include the temperature terms. The linear-circuit model can also be similarly set up for linear, recursive estimation, as presented in 3.2.

Once the estimator formulation is complete, the regressor $\varphi(k)$, parameter vector θ, and output $v(k) + a_1 v(k-1)$ are processed with Kalman filtering. The interested reader is referred to 3.2 for more details about the Kalman filtering. While (5.5.2) is formulated to accomplish the recursive estimation of v_{ocv}, $\frac{1}{A}$, and b_1, other parameters are obtained via the offline estimation of the generic cell model introduced in the previous section.

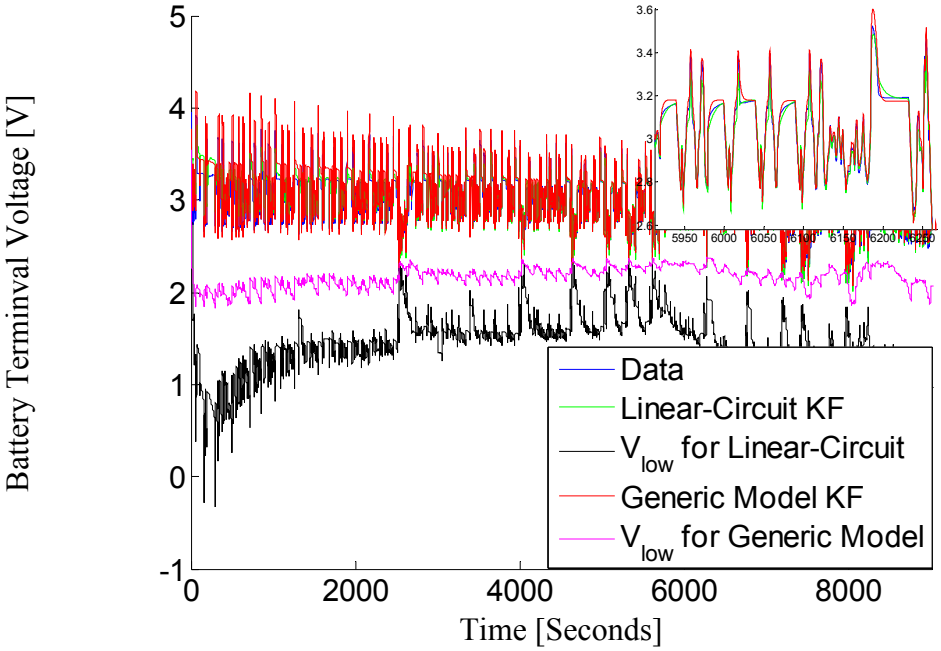

Figure 5.17 Comparison of Kalman filter v_{low} estimates for linear-circuit model and generic cell model for data at ambient 253.15^0K/-20^0C

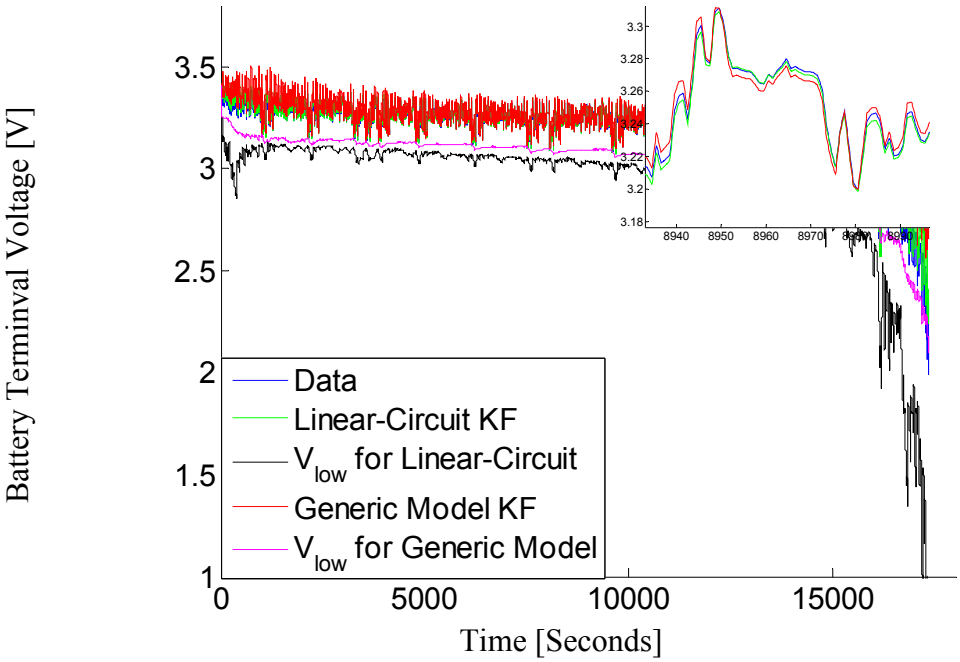

Figure 5.18 Comparison of Kalman filter v_{low} estimates for linear-circuit model and generic cell model for data at ambient 293.15^0K/20^0C

In Figure 5.17, both the linear-circuit and generic cell model Kalman filter results for the -20^0C condition are shown. In order to demonstrate the generic cell model's advantages for power prognostics, the predicted lowest battery voltage v_{low} is plotted for both models. As in 3.3 and 4.3, the derivation of v_{low} is simply the application of the maximum discharge current to the model, with the time shift operator q removed. For example, v_{low} for the linear-circuit model can be expressed as follows:

$$v_{low} = v_{ocv} - \frac{b_0 + b_1}{1 + a_1} i_{max} \tag{5.5.5}$$

Based on (5.4.5), the v_{low} for the generic cell model is expressed in (5.5.6):

$$v_{low} = v_{ocv} - \frac{1}{A}\exp\left(\frac{E_a}{RT}\right) i_{max} - \frac{b_1 T}{1 + a_1} \sinh^{-1}\left(\frac{i_{max}}{2B\exp\left(\frac{-G}{RT}\right)}\right) \tag{5.5.6}$$

v_{low} provides an estimate of the battery's output voltage capability at a given time instant for a predefined maximum current load. By comparing with the preset voltage limit for discharging, this estimated voltage can be the key to predicting whether the battery is capable of achieving a critical upcoming power delivery task, such as restarting the engine in a stop-start vehicle configuration.

The v_{low} waveforms that appear in Figure 5.17 indicate that the generic cell model offers performance advantages for accurate power prognostics for low battery temperature (-20^0C) due to its built-in Butler-Volmer relationship. The corresponding v_{low} waveforms in Figure 5.18 for 20^0C ambient temperature condition indicate that both models deliver approximately the same estimated v_{low} values as the battery temperature increases.

In Figure 5.17 and Figure 5.18, it is observed that v_{low} curves seem to have periodic noise associated with the driving cycle itself. To better understand this phenomenon, the measured temperature and the estimated R_0 are plotted alongside each other.

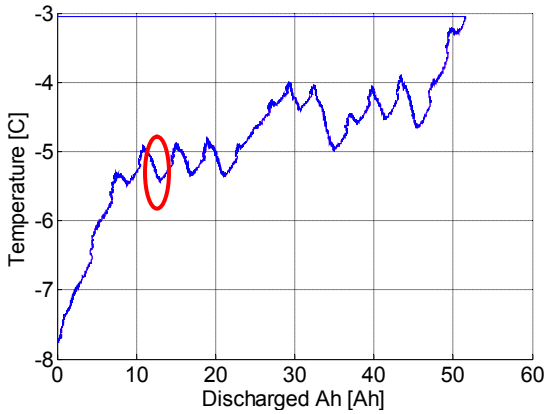

Figure 5.19 Temperature progression during UDDS drive cycle at ambient temperature -10^0C

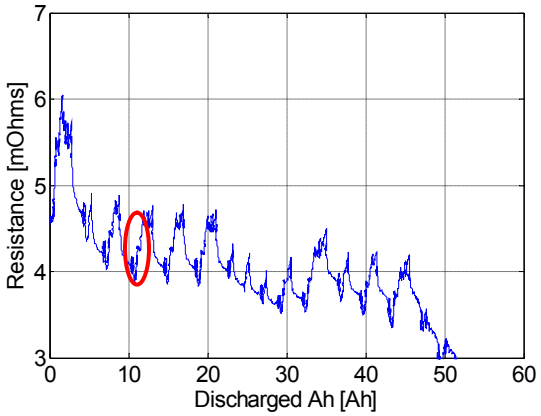

Figure 5.20 Estimated R_0 progression during UDDS drive cycle at ambient temperature -10^0C

From Figure 5.19 and Figure 5.20, it is observed that the estimated R_0 behavior is very much correlated with the measured temperature. The general trend of the resistance is decreasing as the battery heats up from the losses sustained during the drive cycle, even near the end of discharge the estimated R_0 is decreasing even though it would have increased due to the depleted charge had the temperature been constant. In addition, the red circles in Figure 5.19 show a part of the drive cycle where the temperature is dropping due to a lull in the current profile. Correspondingly Figure 5.20 shows an increase in resistance in the same part of the driving cycle.

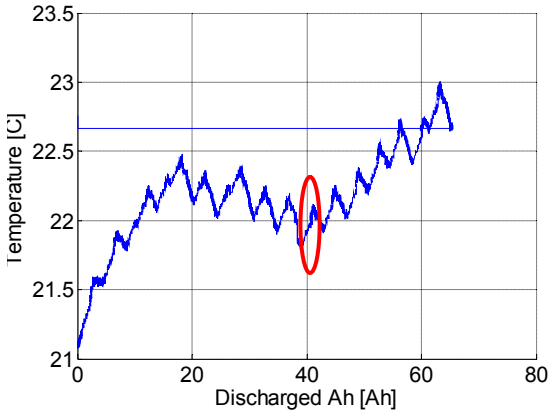

Figure 5.21 Temperature progression during UDDS drive cycle at ambient temperature 20^0C

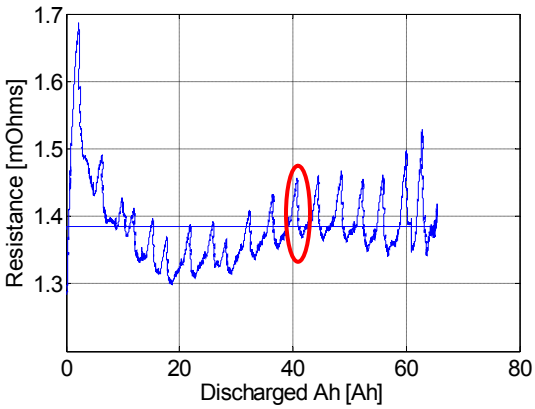

Figure 5.22 Estimated R_0 progression during UDDS drive cycle at ambient temperature 20^0C

A similar response can be seen in Figure 5.21 and Figure 5.22 for the UDDS drive cycle. It is noted that the range of resistance range for higher ambient temperature is smaller, consistent with the higher sensivity of resistance on temperature as seen in Figure 5.4. The temperature sensitivity of the estimated R_0 partially explains the v_{low} curve "noise."

5.6 Generic Cell Model for Offline Simulation

In [139], recursive estimation is implemented so that the value of i_0 in (5.4.3) can be estimated using a nonlinear estimation technique, along with the other key battery

parameters. This approach is designed to provide robustness against temperature and aging influences while maintaining the Butler-Volmer structure to provide an appropriate nonlinear response when the conditions require it. This method is also designed to work for both lead-acid and lithium chemistries.

On the other hand, this nonlinear recursive estimation approach proposed in [139] needs to be guided by the data as it comes in during the driving cycle. One potential drawback of this approach is that the recursive estimation algorithm, depending on the observer tuning gains, may not be able to adjust against a quick change in battery temperature; e.g., when the battery quickly heats up during initial start-up in cold weather.

Another drawback for the method in [139] is its inability to provide offline simulation modeling tools since its parameters are entirely dependent on drive cycle data excitation. In these two respects, the explicit modeling approach that includes temperature as an input as presented in this work seems to have an advantage. This section is therefore dedicated to an implementation for the offline simulation set up based on the generic cell model.

The equations for the temperature dependent model are repeated and augmented here for the offline simulation model. Notice that the v_{ocv} is modeled as a polynomial function of both temperature and Ah count.

$$r_0 = \frac{1}{k} = \frac{1}{A}\exp\left(\frac{E_a}{RT}\right) \tag{5.6.1}$$

$$\eta = \frac{RT}{\alpha F}\text{sinh-1}\left(\frac{i}{2i_0}\right) = \frac{b_1 T}{1 + a_1}\text{sinh}^{-1}\left(\frac{i(k)}{2i_0}\right) \tag{5.6.2}$$

$$i_0 = B\exp\left(\frac{-G}{RT}\right) \tag{5.6.3}$$

$$v(k) = v_{ocv}(Ah,T) - \frac{1}{A}\exp\left(\frac{E_a}{RT}\right)i(k) - \frac{b_1 T}{1 + a_1 q^{-1}} \sinh^{-1}\left(\frac{i(k)}{2B\exp\left(\frac{-G}{RT}\right)}\right) \qquad (5.6.4)$$

$$v_{ocv}(Ah,T) = f_0 + f_1 Ah + f_2 Ah^2 + f_3 Ah^3 + f_4 Ah^4 + f_5 Ah^5 + f_6 Ah*T + f_7 T + f_8 T^2 \qquad (5.6.5)$$

In (5.6.5) the first six terms gives the polynomial fit the ability to represent the battery v_{ocv} relationship with the Ah count. The seventh term, f_6Ah*T, provides fit for the interaction between the two factors, T and Ah. This interactive term was important in arriving a good fit. The rest is a second order fit for the temperature factor.

In order to fit to (5.6.5), the data from UDDS drive cycles under various ambient temperatures were used. Specifically, the estimated v_{ocv}, measured temperature, and Ah count were used to fit to (5.6.5). The results are shown in the surface plot in Figure 5.23.

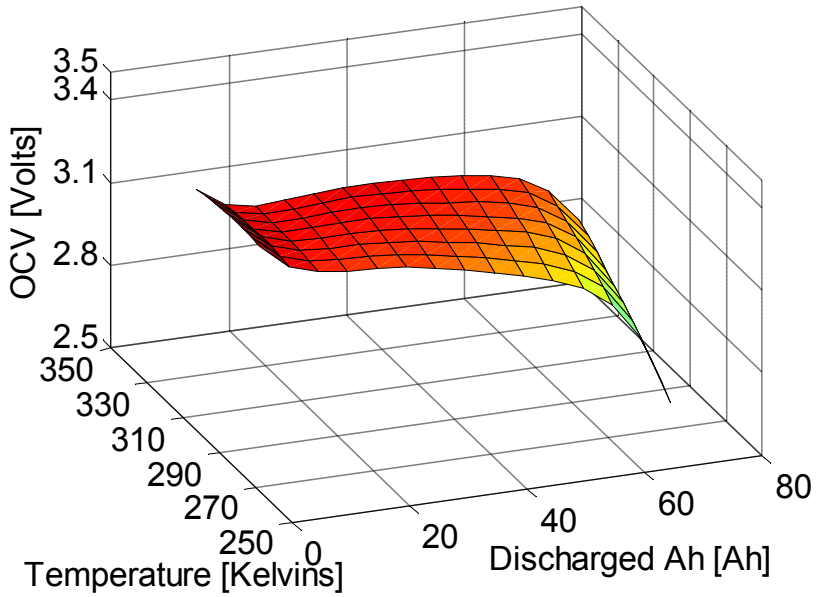

Figure 5.23 v_{ocv} estimation polynomial surface plot

The fitted polynomial function is used to check one drive cycle's estimated v_{ocv}. One such a check case is shown in Figure 5.24. The comparison between surface polynomial and the v_{ocv} shows the fit is quite good.

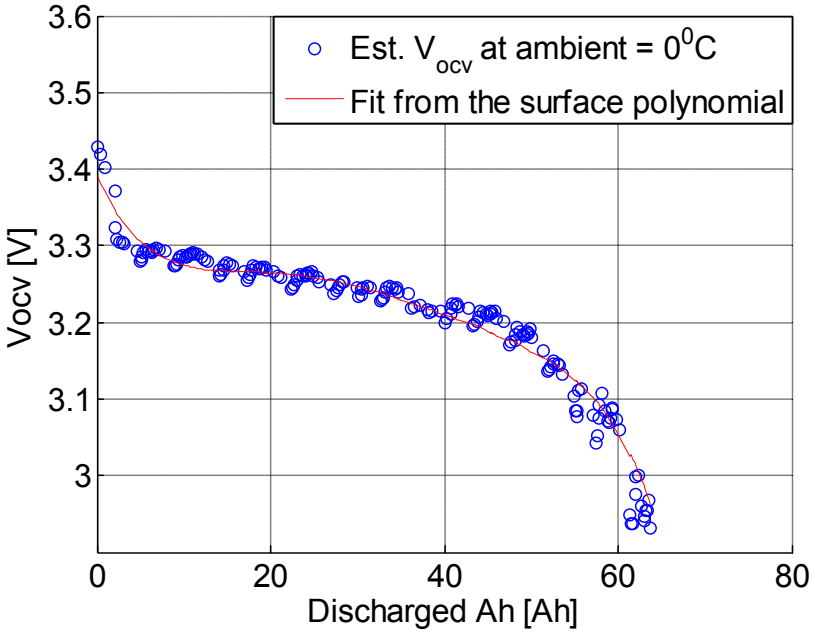

Figure 5.24 v_{ocv} estimation with UDDS drive cycle and polynomial fit at ambient = 0^0C

In addition to the electrical/electrochemical equations from (5.6.1) to (5.6.5), the simulated cell requires a thermal model for completion. The offline thermal model is a simple first order system with the asymptote set at the ambient temperature. The thermal model is shown in (5.6.6), where the temperature change is driven approximately by the electrical losses within the battery. A further addition to the model could be a modification of (5.6.6) based on the resistance of the simulated cell. However, this feature is not added in the simulation study.

$$T(k) = T_{ambient} + \frac{b}{1 + f_1 q^{-1}} i^2(k) \qquad (5.6.6)$$

With the equations from (5.6.1) to (5.6.6), the simulated cell is almost complete. One additional feature implemented is the increase of resistance R_0 at the end of discharge. This feature is an attempt to imitate the behavior of the real life battery, which exhibits an increase of resistance at the end of discharge. Further modifications are possible such as an increase in R_0 for charging near full charge; these can be implemented as needed but not included in the results in this section.

Figure 5.25 shows the voltage response of the simulated cell at ambient 25^0C under the UDDS cycle, where the "measured" voltage and current data were artificially corrupted with time correlated random noise. The measured voltage has a noise with standard deviation 0.1 mV, and the measured current has a noise with 0.1 mA. The temperature and R_0 response have also been plotted in Figure 5.26 and Figure 5.27.

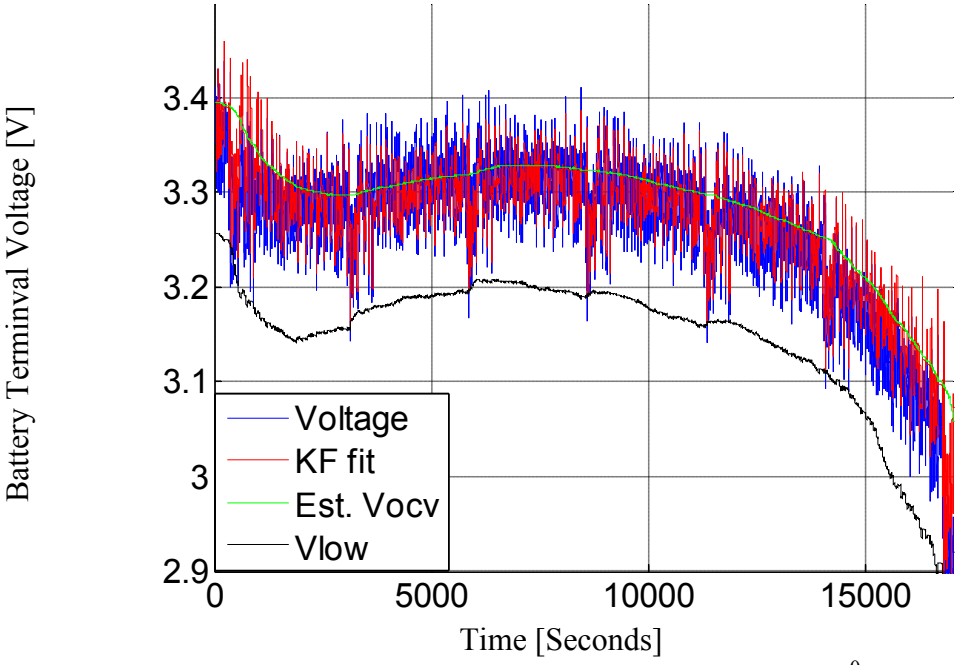

Figure 5.25 Simulated cell voltage and Kalman filtering results at 25^0C ambient

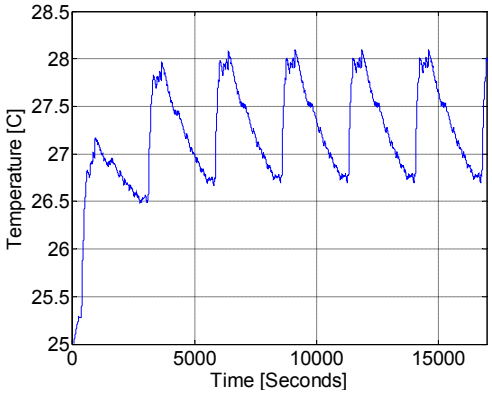

Figure 5.26 Temperature progression during UDDS drive cycle at ambient temperature 25^0C for simulated cell

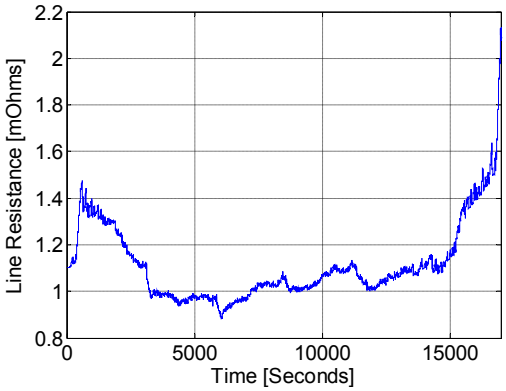

Figure 5.27 Estimated R_0 progression during UDDS drive cycle at ambient temperature 25^0C for simulated cell

In Figure 5.25, a few observations can be made. The estimated v_{low} shows a periodic variation as a function of the current profile, consistent with the experimental results. Such a phenomon, as explained in 5.5, is partly the results of the changing in resistance due to temperature change. The simulation captures this effect quite well, as seen in Figure 5.26 and Figure 5.27 where temperature and R_0 change are clearly inversely correlated.

Another benefit the simulated cell provides is to help the tuning of the Kalman filter. As explained in 3.2, the Kalman filter relies on a Q matrix to represent the assumed internal noise. Given that the variance of the measurement R is fixed, a higher the corresponding value in Q leads to faster tracking of the system parameter change. The estimated parameters in the generic cell recursive estimation set up are repeated in (5.6.7), while (5.6.8) shows the corresponding Q matrix.

$$\theta = [v_{ocv}, \frac{1}{A}, b_1] \tag{5.6.7}$$

$$Q = \begin{bmatrix} \mathrm{var}(v_{ocv}) & 0 & 0 \\ 0 & \mathrm{var}\left(\frac{1}{A}\right) & 0 \\ 0 & 0 & \mathrm{var}(b_1) \end{bmatrix} \tag{5.6.8}$$

In (5.6.8), a larger value for $\mathrm{var}(v_{ocv})$ leads to faster tracking of the v_{ocv} during the drive cycle. However, the trade off is the stability of the estimated v_{ocv}. Empirical experience indicates that one set of tuning is often good for a whole pack of cells at various aging conditions. On the other hand, the selection of appropriate values in the Q matrix is essential for balancing the stability of the estimated parameters and the tracking performance. In Figure 5.28 and Figure 5.29 the difference in $\mathrm{var}(v_{ocv})$ gain tuning is illustrated with the help of the true v_{ocv} from the simulated cell. It can be clearly seen that by increasing the $\mathrm{var}(v_{ocv})$ gain, the convergence of est. v_{ocv} towards the true v_{ocv} is accelerated but the noise on the est. v_{ocv} is also increased. Such noise can influence the results on the power prognostics estimation, specifically on v_{low}.

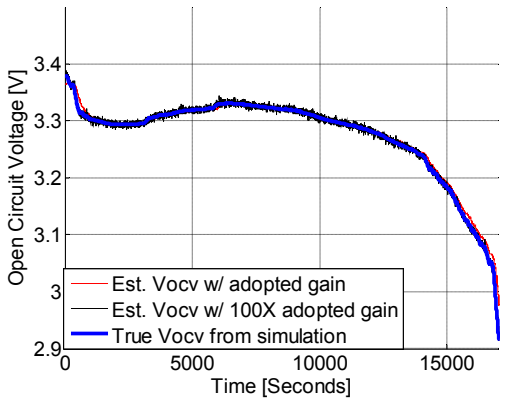

Figure 5.28 Est. v_{ocv} comparison with different values of the $\mathrm{var}(v_{ocv})$ gain

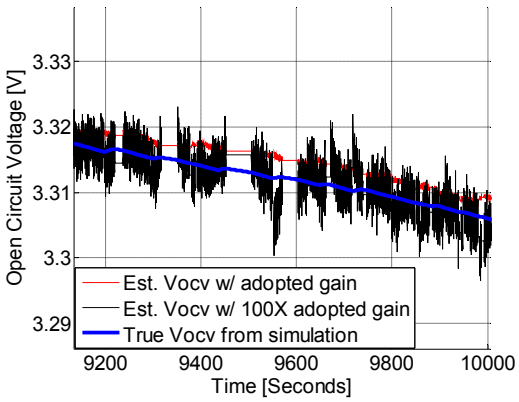

Figure 5.29 Est. v_{ocv} comparison with different values of the $\mathrm{var}(v_{ocv})$ gain, zoomed in from Figure 5.28

The simulated cell can thus be used for guiding the selection of tuning gains, which can be difficult using the experimental data since the actual values to the parameters are not known.

5.7 Lithium Battery State-of-Charge Estimation Based on V_{low} with Temperature, Aging, and Drive Cycle Dynamics Taken into Account

In 5.5, it is demonstrated that the temperature dependent generic cell recursive estimation scheme can provide a power prognostics metric v_{low}. This section discusses an approach to provide a practical SOC estimation for lithium cells for the EV application based on the power prognostics metric v_{low}.

From the discussion in 2.4.1, the Nernst equation describes the battery v_{ocv} as a function of both temperature and the ratio of oxidants and reductants, thus the SOC. Additionally, the resistance and overpotential of a battery are functions of the temperature and SOC, as seen in previous sections of this chapter.

$$E = E^0 + \frac{RT}{nF} \ln \frac{C_O}{C_R} \tag{5.7.1}$$

In addition to temperature and SOC, the drive cycle characteristics can also influence the timing of the end-of-discharge, if defined by a strict cut-off voltage measurement. For example, a large load current may result in a sudden voltage drop and take the cell voltage below the cut-off limit. However, if the est. v_{low} is adopted as the reference for determinging end-of-discharge, the influence of current dynamics can be greatly reduced. For lead-acid battery, the diffusion voltage drop is also a function of the

drive cycle average current. The Peukert's law discussed in 2.5.2 describes the early cut-off's due to higher average discharge currents. On the other hand, the literature shows lithum cells do not exhibit the same Peukert behavior as lead-acid batteries [51].

Therefore, this SOC estimation method proposes using the power prognostics metric v_{low} to decouple the drive cycle dynamics. The main factors that influence v_{low} estimation are temperature and SOC. It follows that v_{low} should be very similar for different drive cycles when temperature and SOC are taken into account. Meanwhile, it is well known that a battery at the end-of-discharge, i.e. low SOC, exhibits both an increased in resistance and rapid decrease in v_{ocv}. This phenomon will result in a rapid collapse in battery power capability as well as v_{low}. From a practical point of view, any SOC estimation scheme should have the end-of-discharge to correspond roughly where the rapid power collapse sets in. The failure to do so partially explains the defect of the naïve Coulomb counting approach. If both temperature and aging are relatively controlled, the expectation is that the battery can provide about the same amount of Ah before the power capability collapse, i.e. the end-of-discharge.

The summary of the proposed SOC estimation method is the following: it uses v_{low} estimate as the end-of-discharge reference to decouple the drive cycle dynamics. During the driving cycle, the v_{low} estimate is constantly compared with a cut-off limit in order to detect the power capability collapse. The Ah and temperature measured at the power capability collapse are recorded and contribute to a polynomial curve that describes the Ah count at which the end-of-discharge occurs as a function of temperature. This polynomial curve is then used to provide a guide for the Ah expected to be extracted

during any drive cycle. A flow chart depicting the information flows for the proposed SOC estimation method is shown in Figure 5.30.

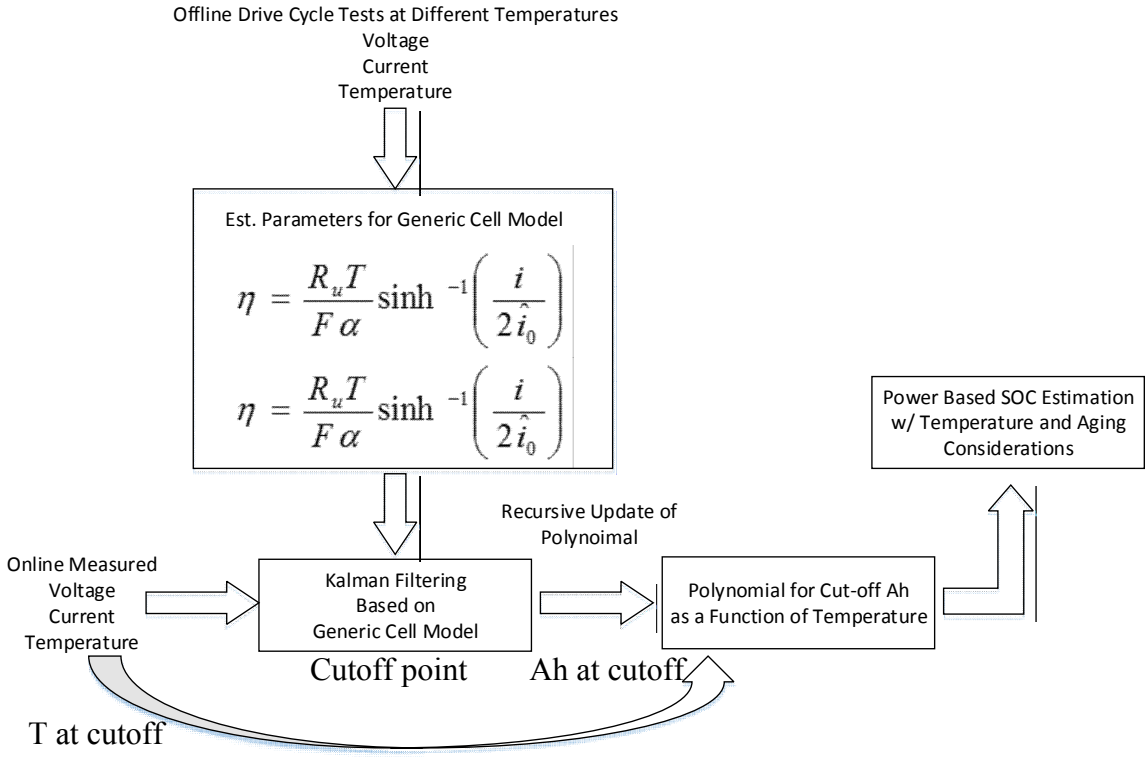

Figure 5.30 Information flow chart for SOC estimation scheme

Before the v_{low} estimation can be applied for SOC estimation, a further modification is needed for taking into account battery power loss due to resistance increase at low temperatures. For the CALB 60Ah cell, Figure 5.31 shows the line resistance R_0 relationship with temperature using fit information from the generic cell model.

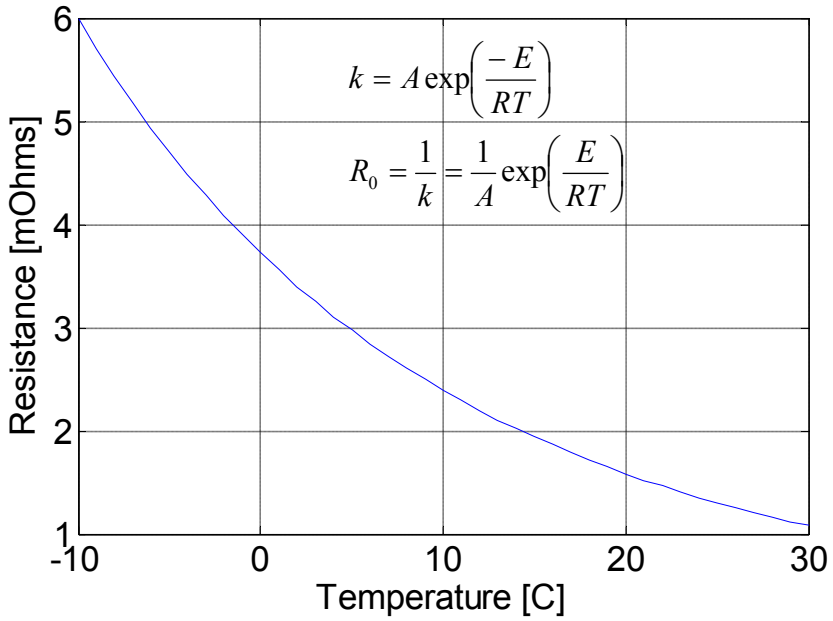

Figure 5.31 Fitted line resistance R_0 relationship with temperature for CALB 60 Ah cell

As seen in Figure 5.31, the resistance rapidly increases as temperature drops. Due to a higher resistive voltage drop v_{low} estimation may easily go below the cut-off before the power collapose sets in without i_{max} modification. In order to have consistent v_{low} estimation, the maximum current, i_{max}, is now scaled as a function of temperature. Specifically, using 25^0C as the reference temperature i_{max} is now given as:

$$i_{max}(T) = i_{max}\left(\frac{R(T = 25^0C)}{T}\right) \tag{5.7.2}$$

To examine different current dynamics' influence on the v_{low} estimation, four different driving cycles are applied to the CALB 60Ah cell at various temperatures. The v_{low} estimation, repeated in (5.7.3), under these different conditions are analyzed below.

$$v_{low} = v_{ocv} - \frac{1}{A}\exp\left(\frac{E_a}{RT}\right) i_{max}(T) - \frac{b_1 T}{1 + a_1}\sinh^{-1}\left(\frac{i_{max}(T)}{2B\exp\left(\frac{-G}{RT}\right)}\right) \tag{5.7.3}$$

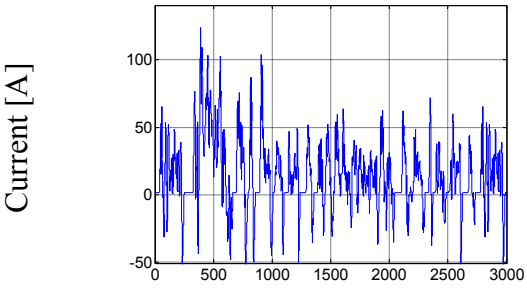

Figure 5.32 UDDS current profile

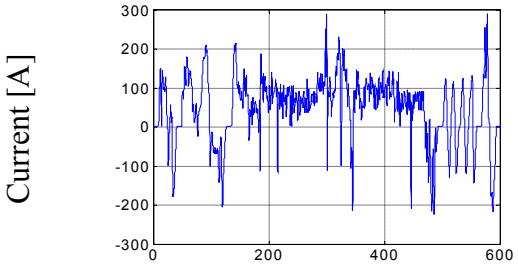

Figure 5.33 US06 current profile

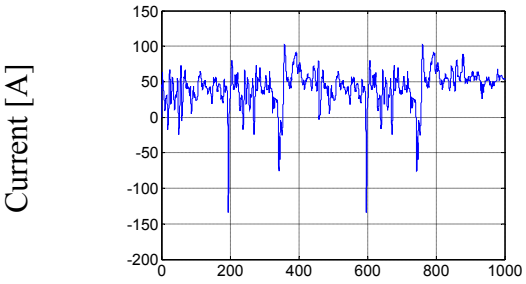

Figure 5.34 HWFET current profile

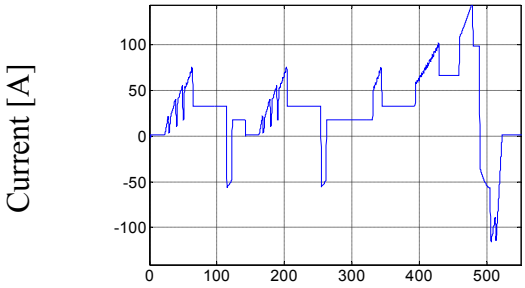

Figure 5.35 EUDC current profile

Figure 5.32 to Figure 5.35 show the four driving cycles used on CALB 60Ah in the lab experiment. It can be observed that they vary in their average current and dynamic components.

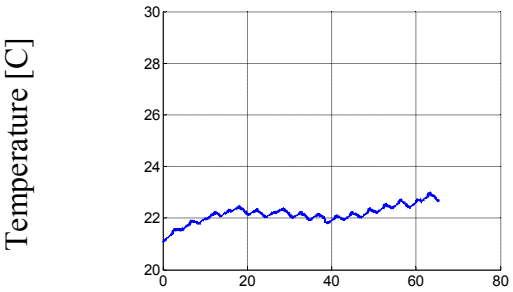

Figure 5.36 CALB battery temperature response at 20^0C for UDDS

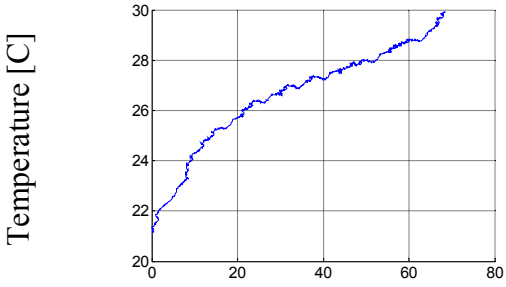

Figure 5.37 CALB battery temperature response at 20^0C for US06

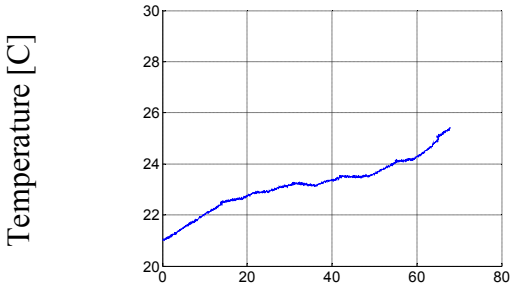

Figure 5.38 CALB battery temperature response at 20^0C for HWFET

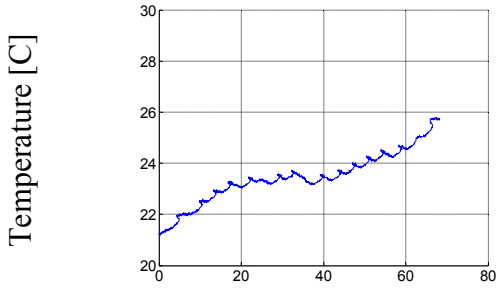

Figure 5.39 CALB battery temperature response at 20^0C for EUDC

The US06 cycle in particular is the most aggressive among the four drive cycles, and causes a significantly higher rise in temperature. The temperature response for the CALB battery at 20^0C ambient temperature for these four drive cycles can be seen from Figure 5.36 to Figure 5.39. Notice that at the same discharged Ah, the drive cycles have different temperature responses due to their different RMS value. The US06 cycle causes an almost 8^0C rise in temperature by the end-of-discharge, while the UDDS cycle causes a 2~3^0C rise only.

Figure 5.40 illustrates the v_{low} estimations during UDDS drive cycle under various ambient temperatures. Due to the noise on the v_{low} estimation from Kalman filtering, these v_{low}'s have been filtered with a moving medium filter that finds the medium value within 1 Ah of data. Thanks to the adjustment of i_{max} in (5.7.2) v_{low} estimations at different temperatures maintain the roughly the same level, although their collapse point is still a function of temperature as seen in the early rapid power loss for low temperature conditions.

In Figure 5.41, Figure 5.42, and Figure 5.43, the v_{low} estimations for other drive cycles show similar results as the UDDS cycle.

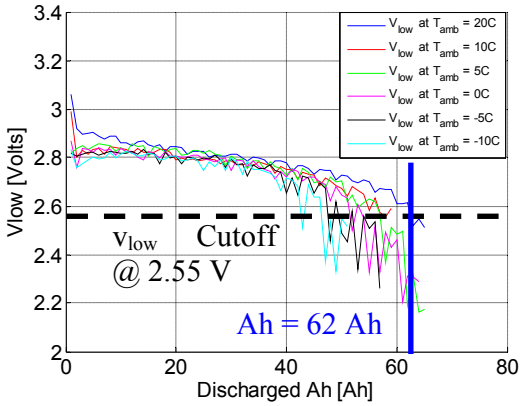

Figure 5.40 The v_{low} estimations for UDDS drive cycle under various ambient temperatures and illustration of cut-off Ah determination

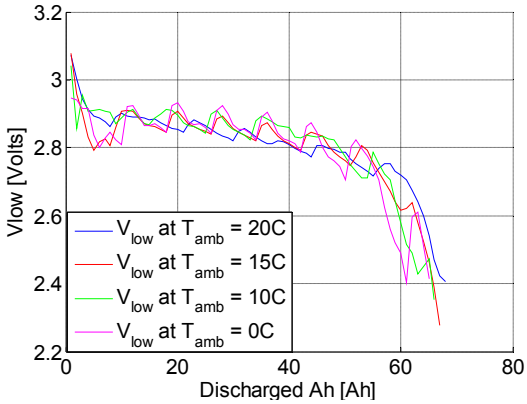

Figure 5.41 The v_{low} estimations for US06 drive cycle under various ambient temperatures

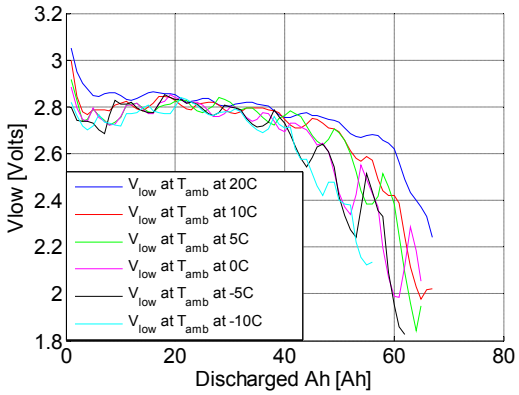

Figure 5.42 The v_{low} estimations for HWFET drive cycle under various ambient temperatures

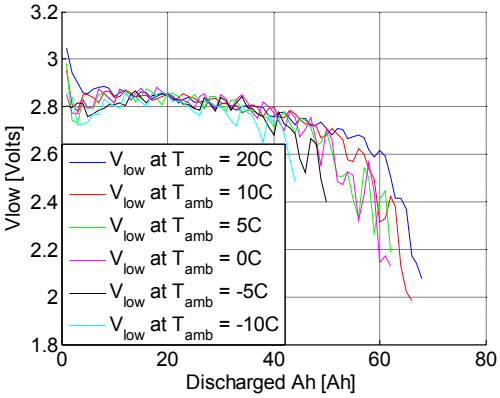

Figure 5.43 The v_{low} estimations for EUDC drive cycle under various ambient temperatures

In order to verify that these v_{low} estimations are similar across different drive cycles, the v_{low} estimation for ambient temperature at 20^0C is plotted together for comparison in Figure 5.44. Notice that at room temperature the temperature discrepancy between drive cycles is not as important as in low temperatures.

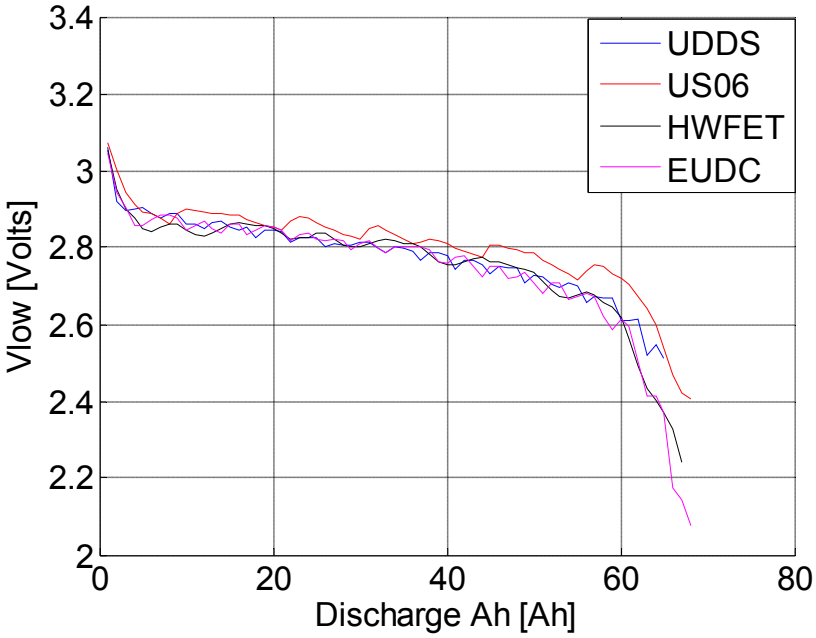

Figure 5.44 The v_{low} estimations for different drive cycles at ambient temperature 20^0C

In Figure 5.44, the v_{low} estimations for different drive cycles behave very similarly, thanks to the consistency of both the CALB battery and the generic cell Kalman filtering scheme. It can be noted that the v_{low} estimation for the US06 cycle is slightly higher than the rest, consistent with the fact that the CALB battery is hotter during the US06 cycle.

The experimental results so far demonstrate the the v_{low} estimation's consistency for different current profiles. The next step is to record the cut-off Ah's and the corresponding temperatures and provide a polynomial fit that predict the available Ah per drive cycle as a function of temperature. From all these different drive cycles at various ambient temperatures, the cut-off Ah's, the corresponding temperatures, and their polynomial (quadratic) fit are shown in Figure 5.45.

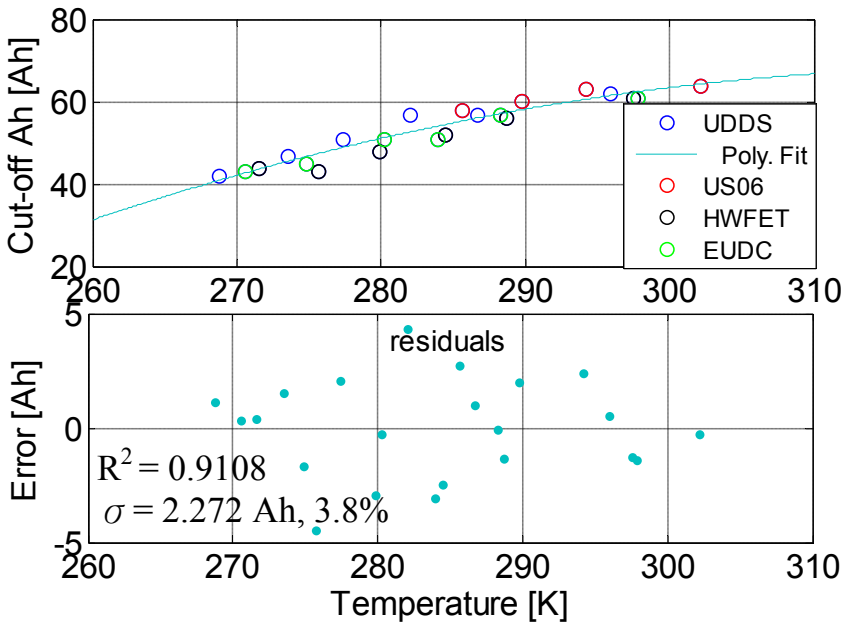

Figure 5.45 The cut-off Ah's as a function of temperature and the quadratic fit

In Figure 5.45, the data and their quadratic fit show the consistency of the cut-off Ah as a function of temperature. The fit has a standard error of 2.3 Ah, or roughly 3.8% of the rated 60 Ah capacity. In application, as the battery ages the cut-off Ah's are expected to move further down due to increased resistance and decreased capacity. As the new data of cut-off Ah's and temperatures are obtained, the new information can be used to recursively update the polynomial to reflect battery aging.

Finally, some data from the WEMPEC/Orchid electric truck are used to demonstrate the consistency of the v_{low} estimation. The detailed information for the truck can be found in [138]. The truck has a battery bank consisting of 108 CALB 100 Ah cells. The cells are distributed into three blocks, one in the front engine compartment and two in the cab space. The consistency of the v_{low} estimation is demonstrated by using two drive cycle data, one full drive cycle depleting the battery and one short drive

starting near the end-of-discharge. For one particular cell 35, both the v_{low} estimations and the nearest temperature measurement are plotted below for the two drive cycles.

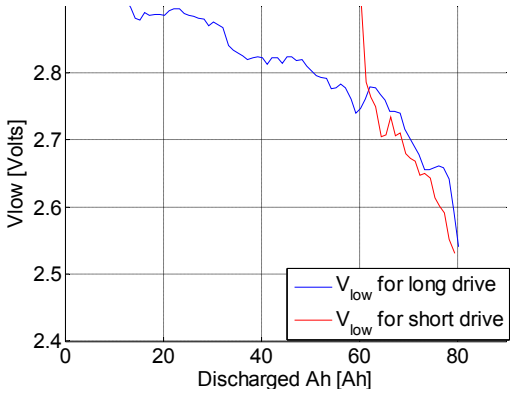

Figure 5.46 The v_{low} estimation comparison for cell 35 in WEMPEC truck

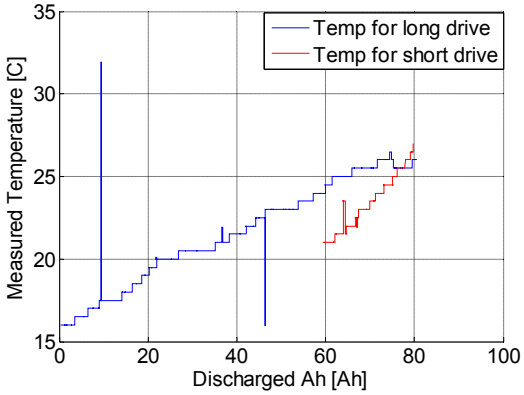

Figure 5.47 The temperature measurement comparison for cell 35 in WEMPEC truck

In Figure 5.46 the v_{low} estimations for both drive cycle show very similar behavior, despite the huge difference in their respecitve starting conditions. Since both drive cycles were under relatively high temperature, the difference in temperature does not cause a significant discrepancy between the v_{low} estimations. However, in Figure 5.47 the short drive cycle temperature is slightly below the long drive cycle, and correspondingly the short drive cycle v_{low} estimation is also below that of the long drive cycle.

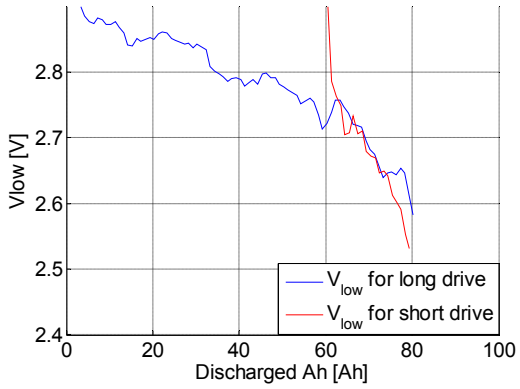

Figure 5.48 The v_{low} estimation comparison for cell 17 in WEMPEC truck

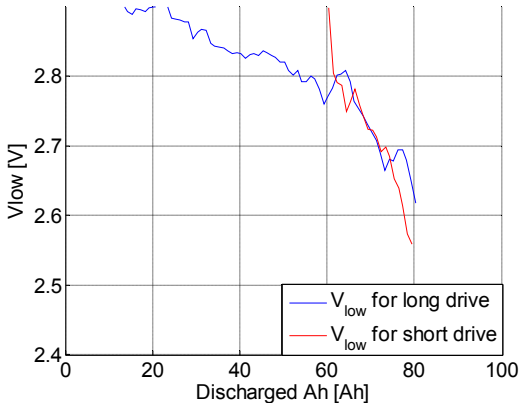

Figure 5.49 The v_{low} estimation comparison for cell 26 in WEMPEC truck

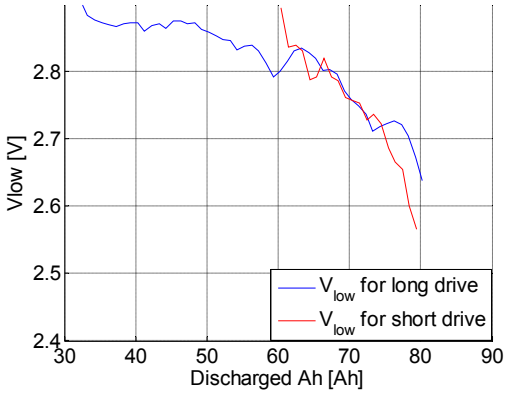

Figure 5.50 The v_{low} estimation comparison for cell 46 in WEMPEC truck

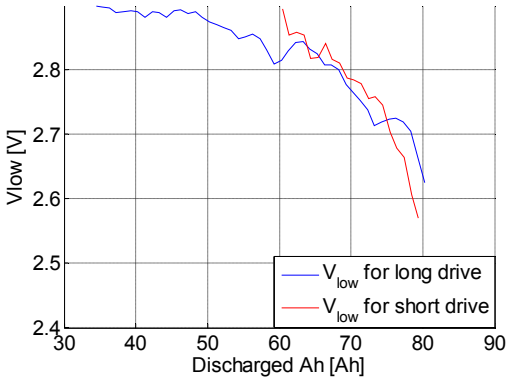

Figure 5.51 The v_{low} estimation comparison for cell 66 in WEMPEC truck

Figure 5.48 to Figure 5.51 show other cells' v_{low} estimation comparisons for the two drive cycles. The consistency of the v_{low}'s is again noted.

5.8 Generic Cell Model Applied to Lead-Acid Battery

The generic cell model approach introduced in 5.4 and 5.5 can also be applied to a lead-acid battery in order to provide a comprehensive temperature dependent modeling approach. In chapter three, the Butler-Volmer equation was used to provide a lead-acid battery model for online recursive estimation. The generic cell model approach can be seen as the extension to the Butler-Volmer method introduced in chapter three with temperature as an explicit input to the model.

In this section, the generic cell modeling approach is applied to the lead-acid battery drive cycles without regenerative events. Some EV's do not have regenerative capability, e.g. the Corbin Sparrow. In addition, the charging process for the lead-acid battery involves highly complex electrochemical reactions and is difficult to model. As an example, Figure 5.52 shows the lead-acid OPTIMA D34M battery's voltage response to a step charging current at 82.5 A.

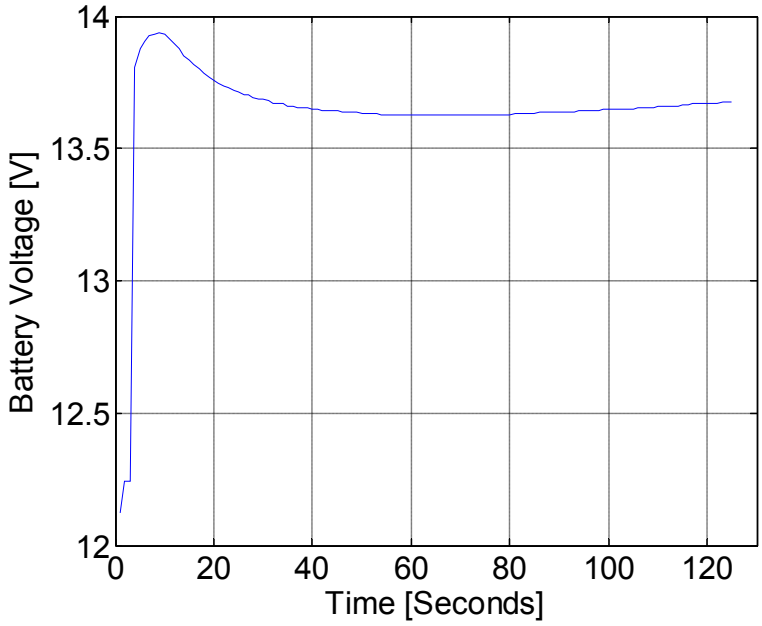

Figure 5.52 Lead-acid OPTIMA D34M battery's voltage response to a step charging current at 82.5 A

As seen in Figure 5.52, the voltage initially rises quickly, falls down, and then continues its gradual rise. One possible explanation for this behavior is the gassing, or water splitting, reaction mentioned in [20], [143]. Neither circuit elements nor Butler-Volmer type equations can adequately mimic such a complex behavior. As a result, the preliminary investigation in this section will focus on discharge only drive cycles.

$$r_0 = \frac{1}{k} = \frac{1}{A}\exp\left(\frac{E_a}{RT}\right) \tag{5.8.1}$$

$$\eta = \frac{RT}{\alpha F}\sinh\text{-}1\left(\frac{i}{2i_0}\right) = \frac{b_1 T}{1 + a_1}\sinh^{-1}\left(\frac{i(k)}{2i_0}\right) \tag{5.8.2}$$

$$i_0 = B\exp\left(\frac{-G}{RT}\right) \tag{5.8.3}$$

$$v(k) = v_{ocv} - \frac{1}{A}\exp\left(\frac{E_a}{RT}\right)i(k) - \frac{b_1 T}{1 + a_1 q^{-1}}\sinh\text{-}1\left(\frac{i(k)}{2B\exp\left(\frac{-G}{RT}\right)}\right) \tag{5.8.4}$$

$$v_{ocv} = a + bAh \tag{5.8.5}$$

As in 5.4, the generic cell model equations are provided from (5.8.1) to (5.8.5). In 5.4, the offline generic cell model parameter estimation obtained a small portion of data from drive cycles under various ambient temperatures, and concatenated all the data into a full matrix for parameter fitting. In addition, the assumption was made in 5.4 that the CALB $LiFePO_4$ battery's v_{ocv} does not change significantly during this small portion of data. However, the lead-acid battery is known to have a much sharper v_{ocv} fall off as a function of discharged Ah compared with $LiFePO_4$ battery. To prevent this discrepancy from interfering with parameter fitting, the v_{ocv} is assumed to be a linear function of Ah count, as seen in (5.8.5). The comparison between the generic cell model fit and the data are shown in Figure 5.53 and Figure 5.54 for ambient temperature at 20^0C and -20^0C respectively.

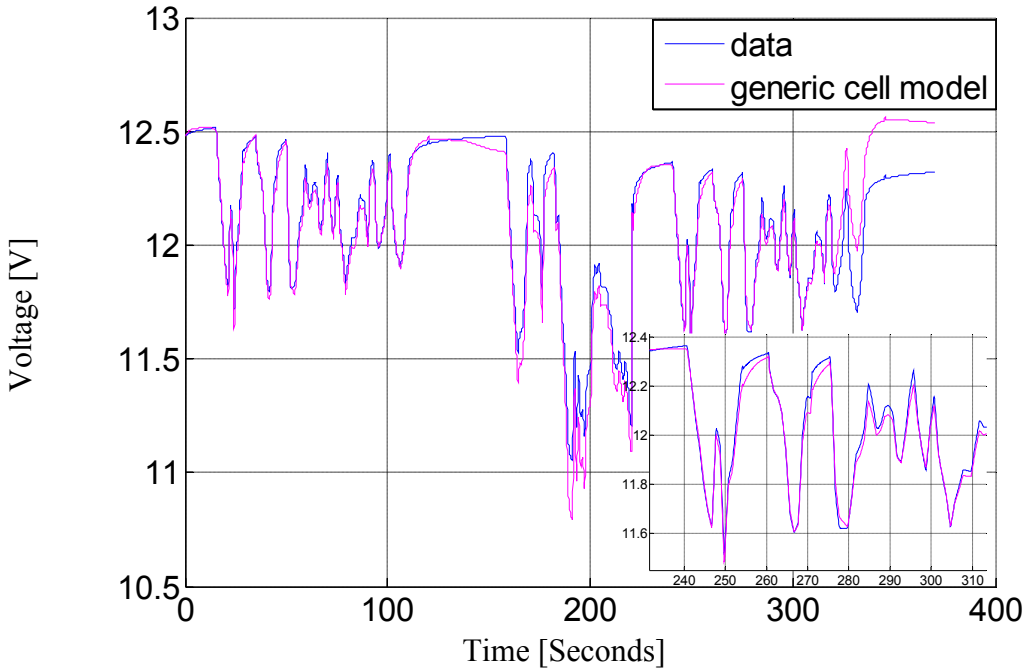

Figure 5.53 Drive cycle test data and generic cell predictions at ambient temperature 20^0C/293.15^0K

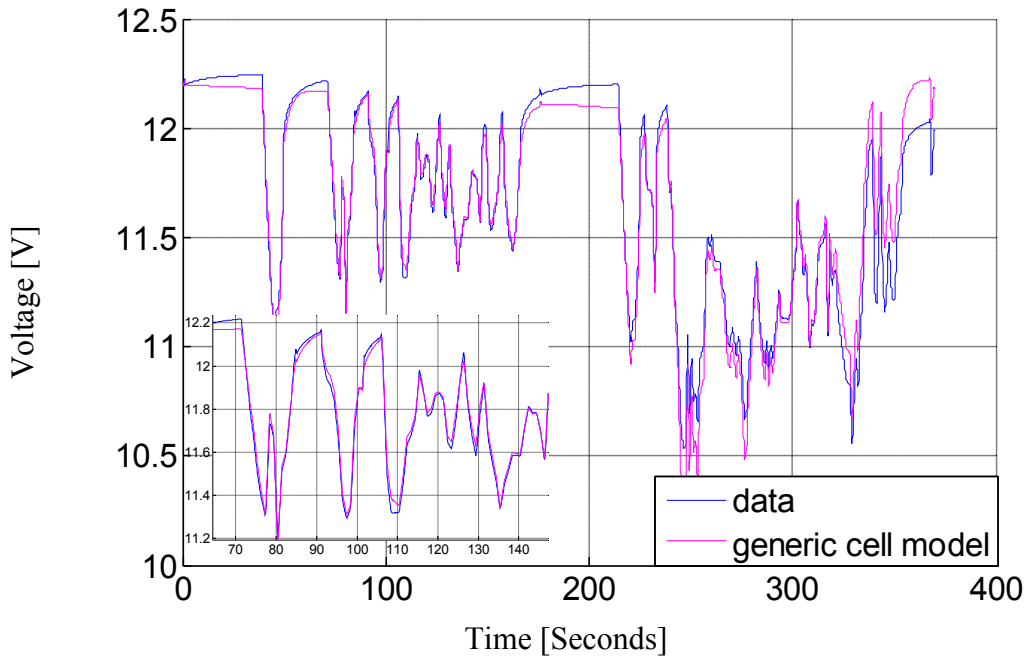

Figure 5.54 Drive cycle test data and generic cell predictions at ambient temperature - 20^0C/253.15^0K

Figure 5.53 and Figure 5.54 show the generic cell model, with the v_{ocv} as a linear function of Ah count modification, tracks data very well in both room and low temperatures. With the obtained parameters, the generic cell model can then be modified for online Kalman filtering, as done in 5.5 for the CALB $LiFePO_4$ battery. The formulation for the Kalman filtering is repeated here for reference.

$$v(k) + a_1 v(k-1) = v_{ocv}(1 + a_1) - \frac{1}{A}(i(k) + a_1 i(k-1))\exp\left(\frac{E_a}{RT(k)}\right) \qquad (5.8.6)$$

$$- b_1 T(k)\sinh^{-1}\left(\frac{i(k)}{2B\exp\left(\frac{-G}{RT(k)}\right)}\right)$$

$$v(k) + a_1 v(k-1) = \theta\varphi(k) \qquad (5.8.7)$$

$$\varphi(k) = \begin{bmatrix} 1 + a_1 \\ -(i(k) + a_1 i(k-1))\exp\left(\frac{E_a}{RT(k)}\right) \\ -T(k)\sinh^{-1}\left(\frac{i(k)}{2B\exp\left(\frac{-G}{RT(k)}\right)}\right) \end{bmatrix} \tag{5.8.8}$$

$$\theta = [v_{ocv}, \frac{1}{A}, b_1] \tag{5.8.9}$$

As in 5.5, the parameters estimated in this recursive set up are v_{ocv} and the gains to the R_0 and overpotential Butler-Volmer relationship. The aging effects can be captured by the recursive scheme, while the temperature effect is captured by making it an explicit input to the model.

Figure 5.55 and Figure 5.57 show the results for the recursive estimation for the Optima D34M lead-acid battery under UDDS based drive cycles at ambient temperature 30^0C and 0^0C. The v_{low} estimations in Figure 5.55 and Figure 5.57 are both calculated with a simple i_{max} at the maximum current value during the drive cycle. Figure 5.56 and Figure 5.58 show the respective current profiles for Figure 5.55 and Figure 5.57.

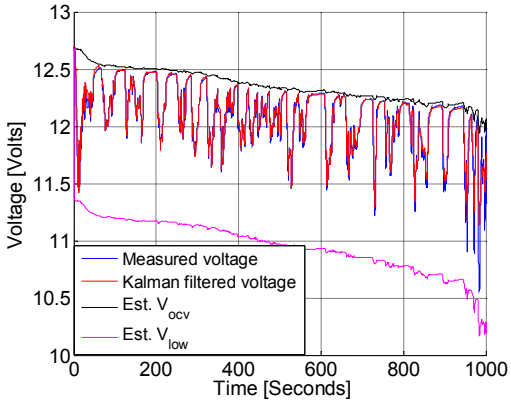

Figure 5.55 Optima D34M battery voltage under UDDS cycle and generic cell based Kalman filtering with its estimated v_{ocv} and v_{low} at ambient temperature 30^0C

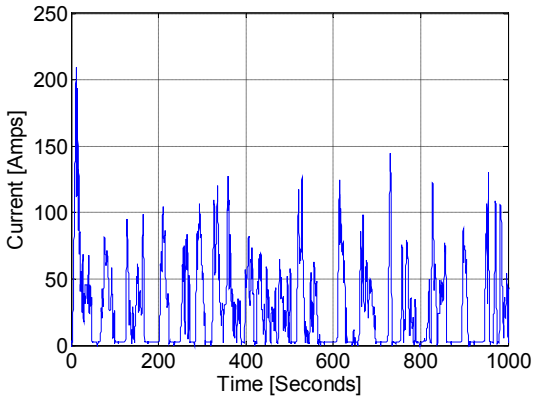

Figure 5.56 The current profile corresponding to Figure 5.55

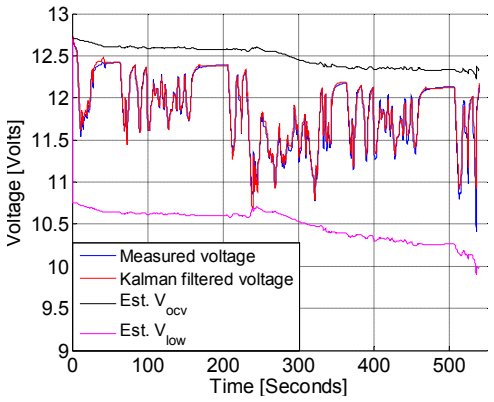

Figure 5.57 Optima D34M battery voltage under UDDS cycle and generic cell based Kalman filtering with its estimated v_{ocv} and v_{low} at ambient temperature 0^0C

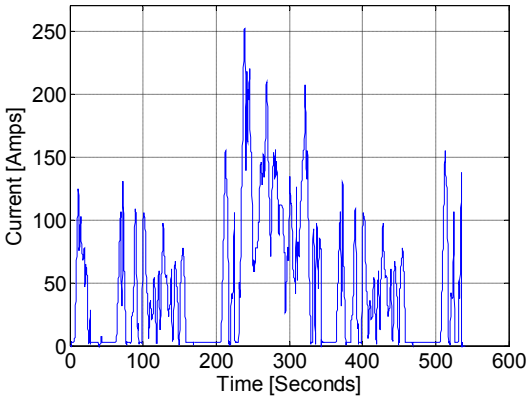

Figure 5.58 The current profile corresponding to Figure 5.57

In Figure 5.57 the estimated v_{ocv} is seen to be somewhat higher than the plateauing voltage measurement. It is pointed out that the drive cycle does not have actually go down to zero at the resting intervals. The minimum current is at 1.6 A. The temperature effect explains this difference between estimated v_{ocv} and the plateauing voltage measurement is more significant at 0^0C ambient than 30^0C ambient.

This section applies the generic cell modeling approach to a lead-acid battery and adopted the model for the recursive estimation scheme for power prognostics. The lead-acid battery regenerative behavior is too complex to be covered in this investigation, but the Butler-Volmer and Arrhenius equations based approach is still capable of modeling the lead-acid battery well under discharge only cycles.

5.9 Investigation of Lithium and Lead-Acid Battery Resistance and Overpotential Behavior under Various Temperatures Using Electrochemical Impedance Spectroscopy

This section deploys EIS to investigate the impact of temperature and dc bias current on battery impedance characteristics. Measured test results are used to demonstrate that, under conditions where the nonlinear Butler-Volmer equation is necessary to model the electrode charge transfer characteristics, the semicircular trajectory that typically appears in the EIS results shrinks in diameter as the battery's dc bias current increases. For a lithium-based battery, the nonlinearity introduced by the Butler-Volmer relationship is more pronounced at low temperature, while lead-acid batteries typically exhibit this nonlinearity even at room temperature. The impact of dc bias current on the battery model and EIS characteristics are thoroughly investigated using a combination of experimental tests combined with theoretical justification based on the Arrhenius equation. The results obtained in this section are consistent with the results in other parts of the thesis using time domain signals, namely that lithium based batteries show Butler-Volmer behavior at low temperatures while the lead-acid battery demonstrates the Butler-Volmer behavior at both normal and low temperatures. The nonlinearity in the electrode voltage/current relationship described by the Butler-Volmer equation (3.1.1) requires that the impact of changing dc bias currents must be accurately reflected in the battery model in order to insure the model's usefulness.

Figure 5.59 illustrates a battery equivalent circuit model using RC circuits. The measured EIS impedance plot in Figure 5.60 has been obtained from the CALB battery at 90% SOC.

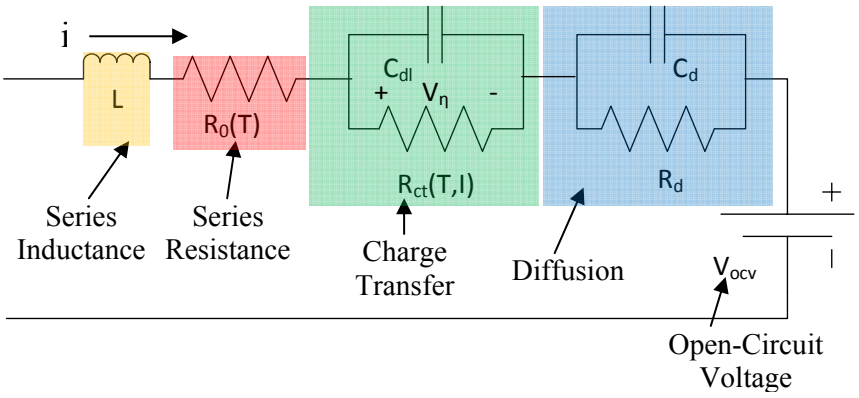

Figure 5.59 Battery linear equivalent circuit model

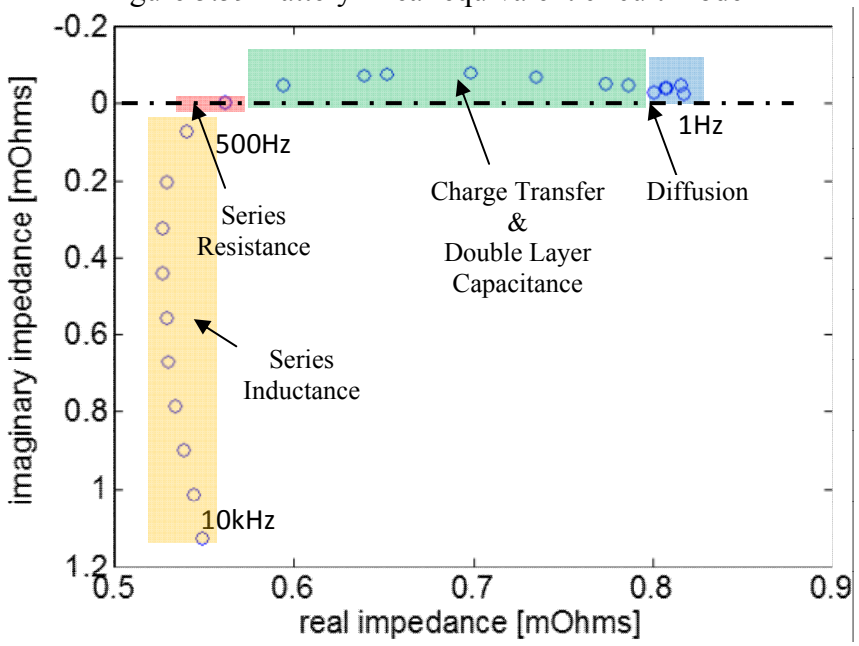

Figure 5.60 EIS results with identification of the key frequency regions

The battery model in Figure 5.59 can be partitioned into 5 sections that influence different frequency ranges. The series inductor L is responsible for determining the model's high-frequency characteristics. The value of R_0 can be determined from the EIS results as the resistance value where the impedance trajectory crosses the x-axis (i.e., zero imaginary impedance), corresponding to the resonant frequency of the equivalent circuit.

The next feature in the EIS trajectory is the semi-circle to the right of the R_0 value associated with very low frequencies that is generated by the interaction of the electrode

charge transfer resistance R_{ct} and the double-layer capacitance C_{dl}. This capacitance C_{dl} has often been modeled as a nonlinear CPE component. This investigation is not concerned with the details of this capacitor model and focuses instead on analyzing the resistive components.

The second parallel RC combination in the model represents the ion diffusion phenomenon that is responsible for the portion of EIS trajectory to the right of the charge transfer semicircle in Figure 5.60, often producing a tail-like feature in the impedance plot. The final model component is the open-circuit voltage source v_{ocv}. The value of v_{ocv} cannot be obtained via EIS but is dependent on SOC and strongly affects the low-frequency impedance when dc bias currents are applied. Sub-hertz frequency data points have been avoided in this investigation because the SOC changes too much for large dc bias currents during the time it takes to make such low frequency measurements.

In 5.1.1, the pure resistance R_0 was modeled as a function of temperature by the Arrhenius equation and showed an increase in value as the temperature drops. Correspondingly, as the temperature drops the EIS results are expected to shift towards right to reflect this increase in resistance. The charge transfer resistance R_{ct} is modeled as a function of temperature and current, i.e. as in the generic cell model. These temperature dependent functions of resistance and overpotential are repeated here for reference.

$$r_0 = \frac{1}{k} = \frac{1}{A}\exp\left(\frac{E_a}{RT}\right) \tag{5.9.1}$$

$$\eta = \frac{RT}{\alpha F}\text{sinh-1}\left(\frac{i}{2i_0}\right) = \frac{b_1 T}{1 + a_1}\,\text{sinh}^{-1}\left(\frac{i(k)}{2i_0}\right) \tag{5.9.2}$$

$$i_0 = B\exp\left(\frac{-G}{RT}\right) \tag{5.9.3}$$

From (5.9.2), the charge transfer resistance R_{ct} can be derived by using Ohm's law.

$$R_{ct} = \frac{\eta}{i} = \frac{R_u T}{iF\alpha} \sinh^{-1}\left(\frac{i}{2i_0}\right) \tag{5.9.4}$$

The 100Ah CALB $LiFePO_4$ cell and a 55Ah, 12V Optima D34M lead-acid battery were used in the experiments in this section. All EIS results have been obtained at frequencies from 1 Hz to 10 kHz at 90% SOC with an hour of rest preceding each EIS frequency sweep measurement.

EIS tests without a dc bias current were first performed on the lead-acid battery for various temperatures. The measured results are shown in Figure 5.61, where the spectra exhibit expansion of the semi-circle as the temperature decreases. The expansion of the semi-circle at low temperatures indicates that the impedance and time constants are increasing as the temperature drops. Similarly, the measured EIS results for the $LiFePO_4$ cell shown in Figure 5.62 also demonstrate an enlarged semi-circle at low temperatures.

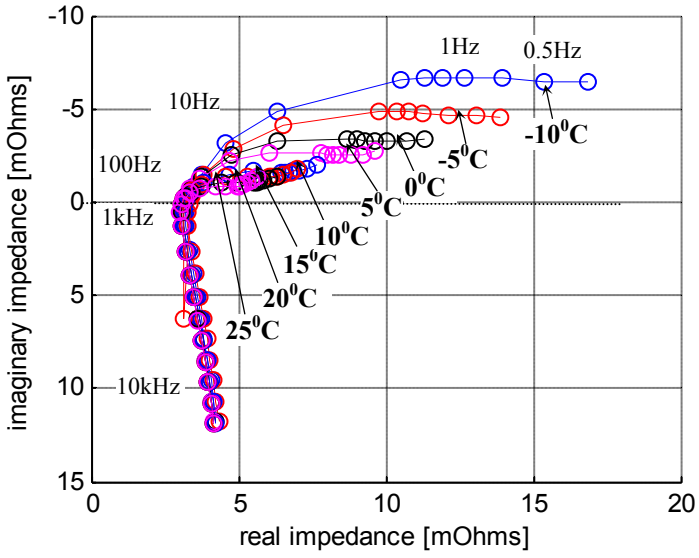

Figure 5.61 Measured Optima lead-acid battery EIS results, -10^0 to 25^0C

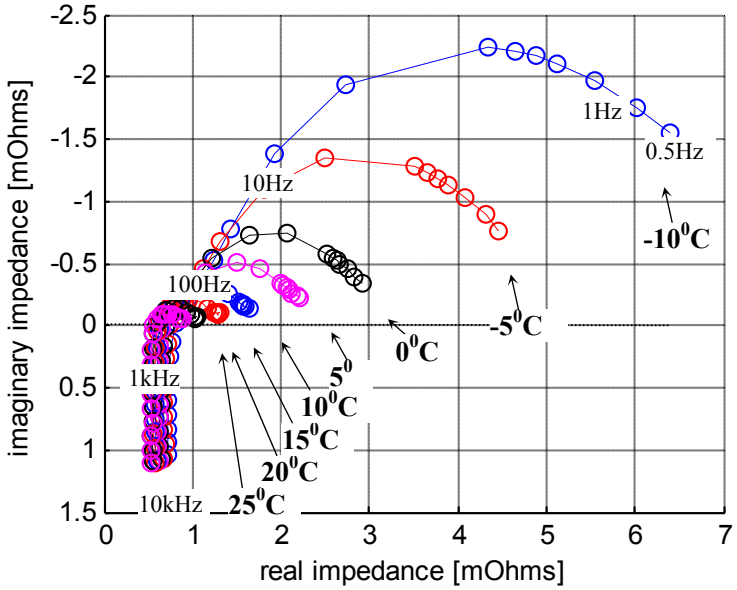

Figure 5.62 Measured CALB $LiFePO_4$ 60 Ah battery EIS results, -10^0C to 25^0C

Although not easily observed from Figure 5.61 and Figure 5.62, lowering the temperature also results in shifting of the whole spectrum to the right due to increases in the series resistance R_0. The increase in R_0 at lower temperatures is shown more clearly in Figure 5.63 for the CALB $LiFePO_4$ cell, where the resistance values at the point where the impedance curves cross the real impedance zero axis are plotted for different temperatures. The results in Figure 5.63 are consistent with the Arrhenius equation modeling approach.

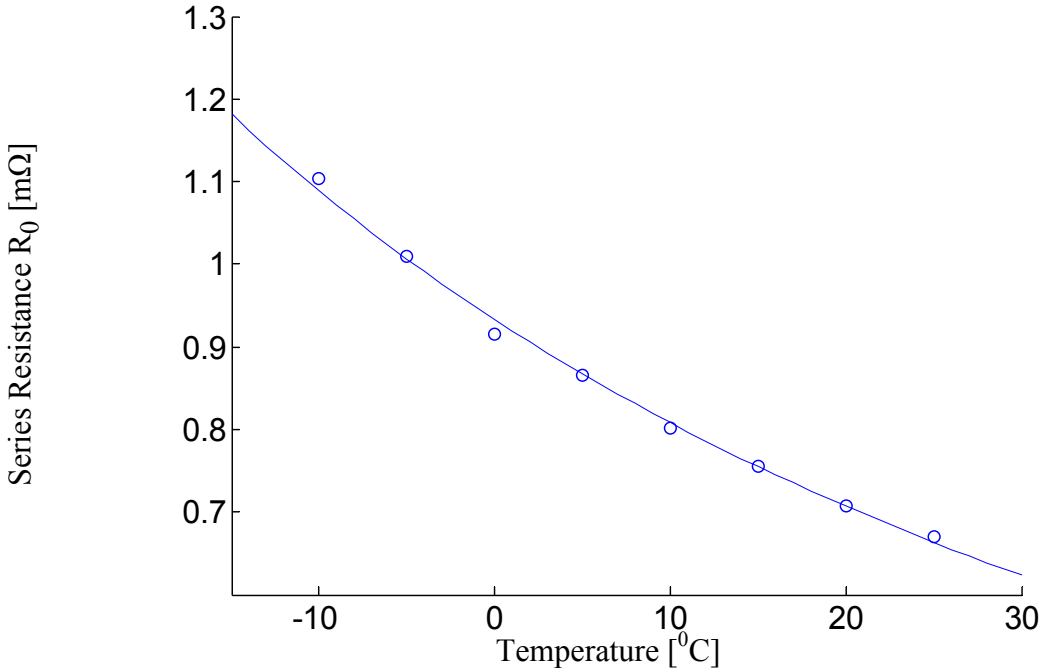

Figure 5.63 Measured CALB LiFePO4 series resistances R_0 at different temperatures and fitted with the Arrhenius equation using (5.9.1)

Both batteries were next subjected to EIS with a dc bias current at two temperatures. The dc bias current is applied to the cell continuously while the ac excitation steps through a range of frequencies for the impedance measurements. This method has the disadvantage of changing the SOC during the measurement resulting in v_{ocv} dropping slightly because of the discharging dc bias current. Due to this constraint, impedance spectroscopy was not performed for frequencies below 1 Hz where the SOC changes too much during the time required to take the measurement.

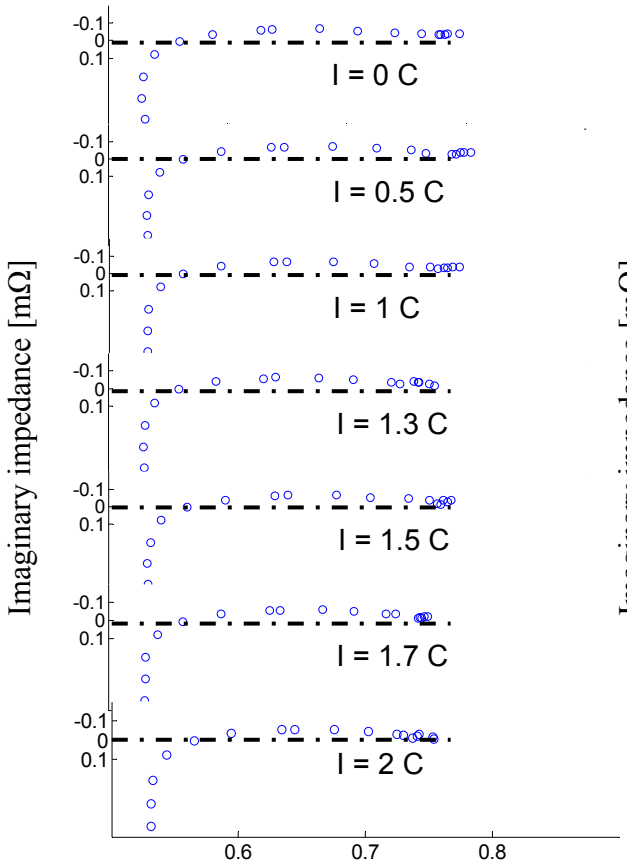

Figure 5.64 Measured CALB $LiFePO_4$ cell EIS results for 7 dc bias currents at 25^0C

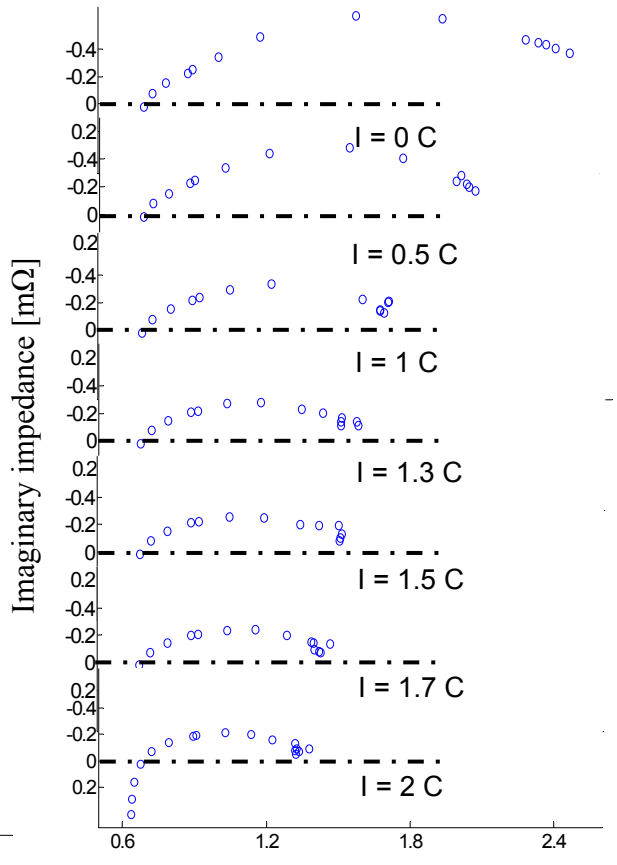

Figure 5.65 Measured CALB $LiFePO_4$ cell EIS results for 7 dc bias currents at 0^0C

For the $LiFePO_4$ cell, Figure 5.64 shows the EIS results for different dc bias current magnitudes, indicated as a C rate, at 25°C. It can be observed that the spectra are similar to one another, and the semi-circle retains much of its size and shape as the dc bias current increases. In contrast, Figure 5.65 demonstrates that, for the 0°C condition, the semi-circle clearly shrinks as the dc bias current increases. This is significant since it can be shown that the diameter of the semi-circle ideally equals the charge transfer resistance R_{ct}.

Closer examination reveals that the shrinking of the semi-circle can be attributed to the Butler-Volmer and Arrhenius equations that give rise to (5.9.3) and (5.9.4). More specifically, lower temperature decreases the value of i_0 calculated using (5.9.3) and causes the dependence of R_{ct} in (5.9.4) on dc bias current to be more prominent. Since the right-side terminus points of the EIS trajectories in Figure 5.64 and Figure 5.65 (corresponding to 1 Hz) approach the *x*-axis (i.e., zero reactive impedance) for the majority of the test results appearing in these two figures, the value of R_{ct} can be approximately estimated by subtracting R_0 (the *x*-axis intercept of each EIS trajectory) from the value of real impedance measured at 1 Hz.

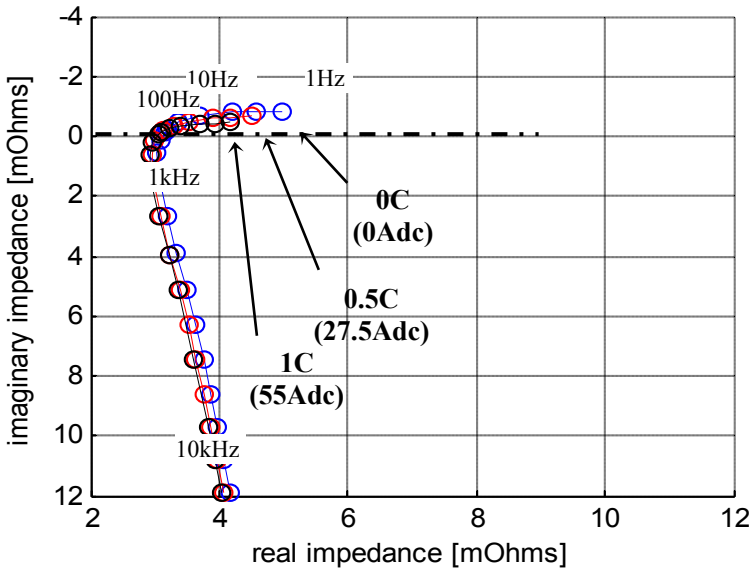

Figure 5.66 Measured Optima D34M lead-acid battery EIS results for 3 dc bias currents at 25^0C

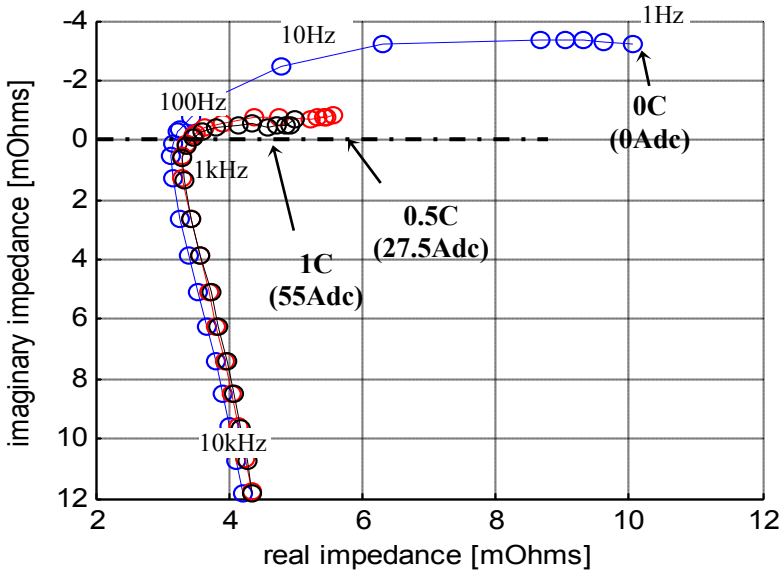

Figure 5.67 Measured Optima D34M lead-acid battery EIS results for 3 dc bias currents at 0^0C

For the lead-acid battery, Figure 5.66 and Figure 5.67 also show the EIS results with different dc bias currents at two temperatures. It is observed that, at both temperatures, the dc bias influence on the semi-circle's shape is prominent. It can also be noted that the EIS results for 0^oC show an increase in R_0, similar to the results for $LiFePO_4$ cell. Overall both types of chemistries exhibit results expected.

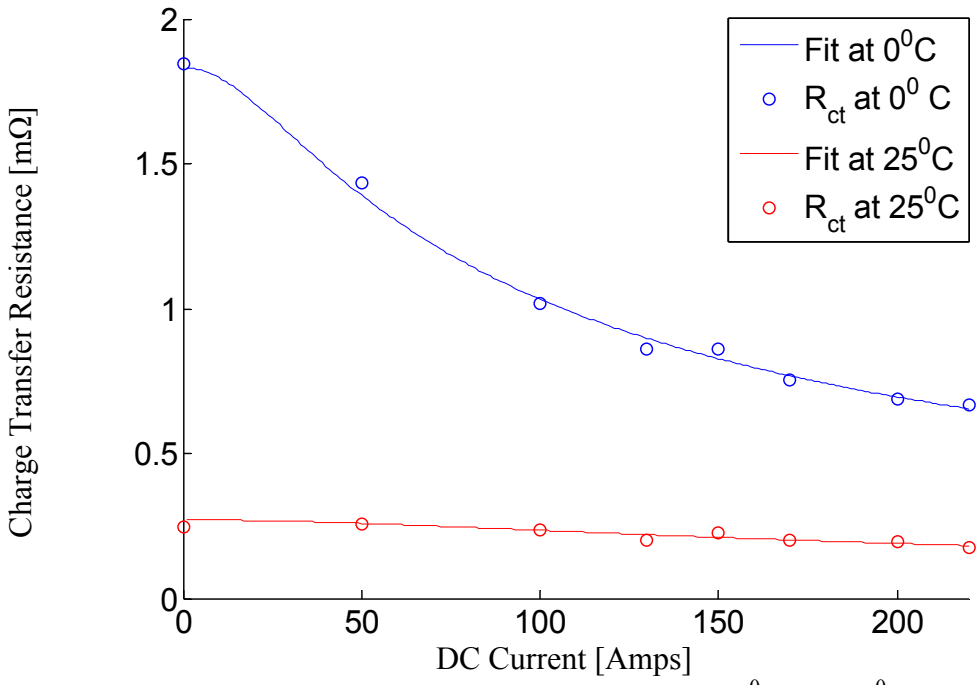

Figure 5.68 CALB $LiFePO_4$ charge transfer resistance R_{ct} for 0^0C and 25^0C and their respective fitted curves with (5.9.4)

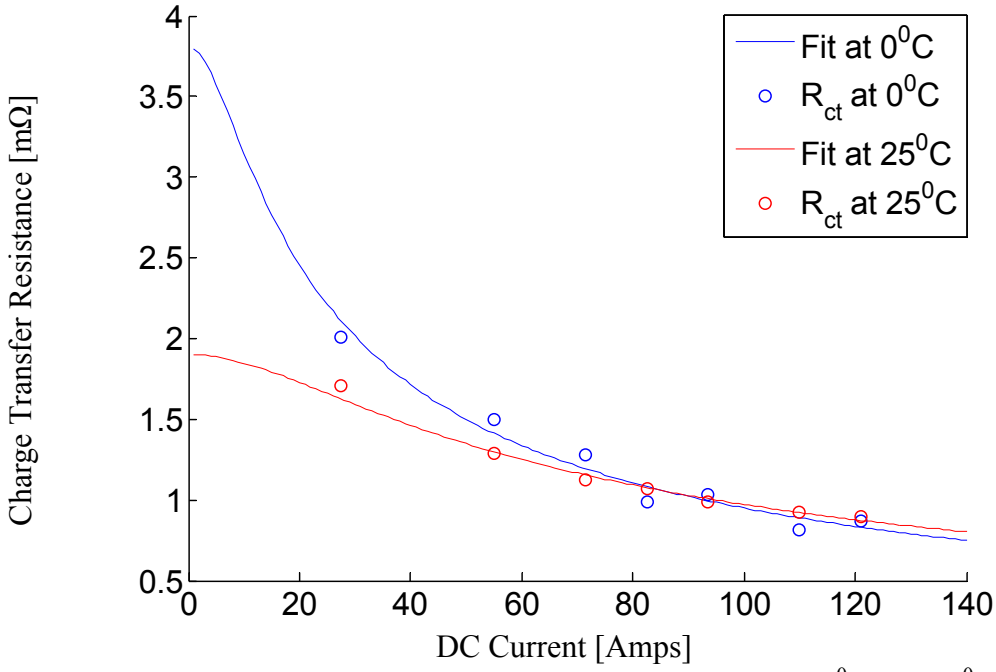

Figure 5.69 Optima lead-acid D34M charge transfer resistance R_{ct} for 0^0C and 25^0C and fitted curves using solid lines based on (5.9.4)

In Figure 5.68, the R_{ct} values extracted from the measured EIS trajectories for the $LiFePO_4$ cell are plotted for the different temperatures and dc bias currents. As expected,

the significant drop in the value of R_{ct} as the dc bias current increases for the 0°C condition is clearly visible, while the corresponding curve for 25°C exhibits a nearly constant value of R_{ct}. Again, this behavior is predicted by the Butler-Volmer relationship in (5.9.2) and (5.9.4).

Using the same techniques as used for the $LiFePO_4$ cell, the measured value of R_{ct} as a function of the dc bias current for the lead-acid battery can also be plotted. Figure 5.69 shows the resulting plot of R_{ct} vs. dc bias current. The plotted curves exhibit similarities to the corresponding R_{ct} curves for $LiFePO_4$ cells in Figure 5.68, although the value of R_{ct} varies more at 25^0C for the lead-acid battery than for the $LiFePO_4$ counterpart. The two curves in Figure 5.69 show that the impact of the nonlinear Butler-Volmer equation is significant at both 25^0C and 0^oC for the lead-acid battery, consistent with the findings in chapter three.

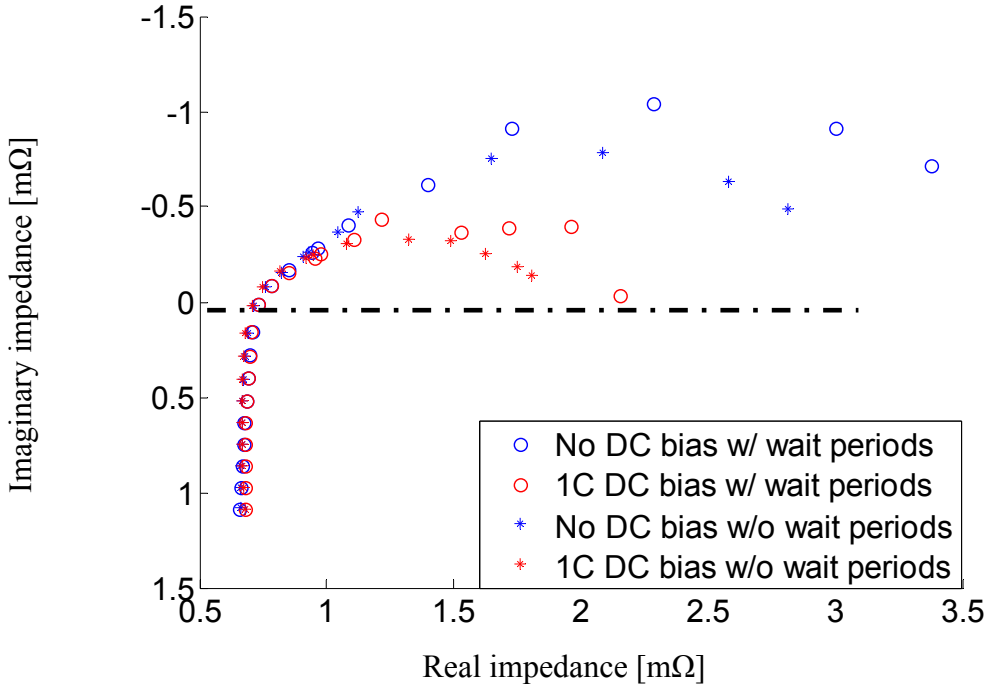

Figure 5.70 Measured CALB LiFePO4 EIS results with and without a wait period between frequency data points for no dc bias current and 1 C dc bias current conditions

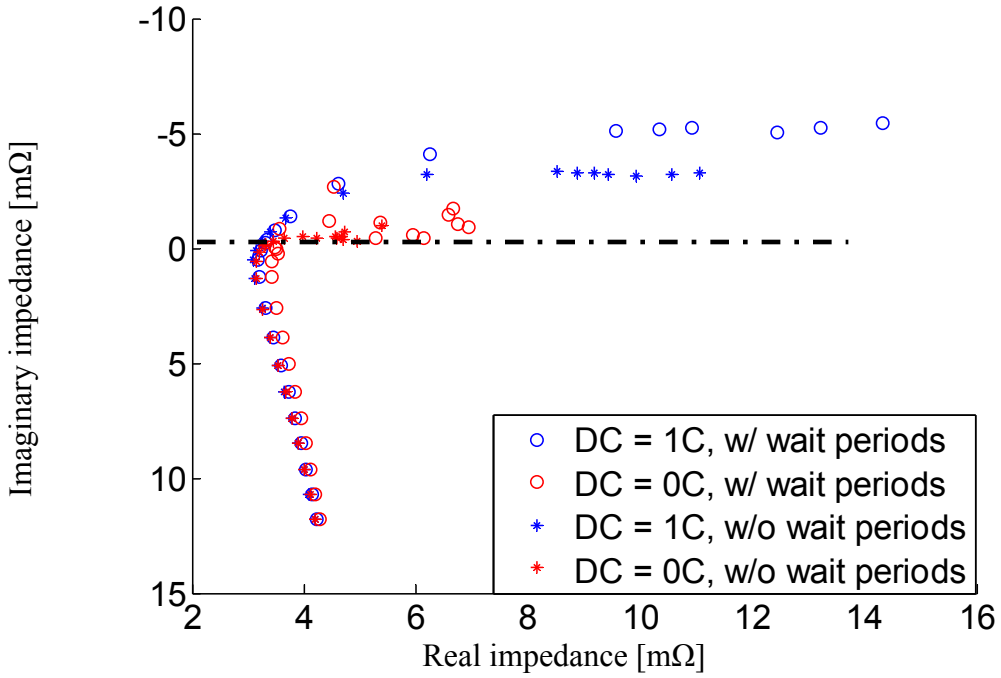

Figure 5.71 Measured Optima lead-acid D34M EIS results with and without a wait period between frequency data points for no dc bias current and 1 C dc bias current conditions

In [28], it was discovered that the amplitude of the ac current excitation used can have an impact on the EIS results at low temperature, with a higher RMS value leading to a smaller semicircle. This effect was attributed to higher internal losses leading to a higher internal temperature. In order to investigate whether the shifting of the spectra in Figure 5.65 can be attributed solely to internal heating, the $LiFePO_4$ cell has been subjected to EIS testing, at 0^0C ambient, with and without a 10-minute wait period between frequency data points for no dc bias current and 1C dc bias current conditions. Figure 5.70 shows that the impedance is higher with wait periods between data points, demonstrating that internal cell heating does influence the cell impedance. However, Figure 5.70 also shows that, even with the wait periods, the effect of dc bias current on the impedance characteristics is clearly visible, indicating that internal heating is not sufficient to explain the battery impedance changes that are observed. The same

phenomena are also observed for the lead-acid battery in Figure 5.71, where both the impact of cooling by waiting and the dc bias current effects can be observed.

In this section, the Butler-Volmer behavior and its temperature dependence have been explored using EIS with dc current biases. EIS's emphasis on the frequency domain makes it possible to observe that, in addition to temperature's influence on the steady-state Butler-Volmer behavior, temperature also changes the size of the double-layer capacitance semi-circle. This means that the transient behavior, i.e., time constant, of the battery is influenced by temperature and the current magnitude. This phenomenon remains to be modeled in the time domain, and a suitable approach has not yet been reported in the literature.

5.10 Summary

This chapter presents a unifying battery modeling approach that varies the cell resistance and electrode overpotential as functions of temperature. Experimental results are used to build confidence in the model, demonstrating that use of the Butler-Volmer relationship yields more accurate voltage predictions than the linear model for $LiFePO_4$ cells at lower temperatures (0^0C and below).

Using nonlinear regression, a method has been proposed to construct a generic cell model that explicitly uses temperature as an input for resistance and overpotential. This temperature-dependent model is better suited for predicting the lithium battery cell behavior at low temperatures than the baseline linear model. In addition, this generic cell model also makes it possible to carry out offline simulations that can achieve accurate battery behavior modeling under various temperatures.

The generic cell model has also been adopted for Kalman filtering in order to monitor battery performance online, i.e., SOF and SOC. An SOC estimation method based on the generic cell model has been proposed that exhibits strong promise with its 3.8% standard error performance. This sophisticated SOC estimation takes into account aging, temperature, and current dyanimics. For a lead-acid battery, it was shown that this same modeling approach is successful for drive cycles without regenerate braking.

Finally, a frequency-domain approach using EIS has been adopted to verify the findings on battery temperature-dependent behavior, and the results corroborate the data collected using time-domain methods such as HPPC and drive cycle tests. It has been pointed out that this generic cell approach serves as a good starting point for modeling different battery chemistries, but care must be taken to observe any discrepancy between model and data, e.g., the charging behavior of the lead-acid battery. Furthermore, the location at which the temperature is measured will influence the results of the modeling approach introduced in this chapter.

Chapter 6
Design of Experiment for Superimposed AC Waveform's Influence on Battery Aging Based on Resistance Growth

This chapter investigates the aging influence of a superimposed AC waveform on discharge current for lithium-ion batteries. Based on the results of two experiments, the discharge current RMS value is determined to be a significant aging factor, while evidence does not support the importance of the DC current value, waveform shape, or frequency on the battery aging characteristics. The practical significance of this result lies in recognizing its importance for properly choosing capacitor values for filtering the battery pack terminal current, perhaps making an argument for implementing the filter using an electrochemical ultracapacitor.

Furthermore, a quantitative analysis is provided for numerically determining the aging effect of the RMS factor. Such a methodology can provide a useful filter design guideline for power electronics engineers. The design of experiment and associated analyses proposed in this chapter can also be adopted for the investigation of other battery aging factors of interest.

6.1 Interest in Superimposed AC Waveform's Influence on Aging

Due to the limitations in cycling life and the associated vehicle warranty issue, understanding of lithium-ion battery's aging process has become an important research

topic. As discussed in 2.7.1 mechanisms cited for aging include the following: electrolyte decomposition leading to solid-electrolyte interface (SEI) layer buildup, solvent co-intercalation and subsequent cracking of formation in electrode, change in electrode volume and surface area due to SEI layer growth, and current collector corrosion. The consensus in the literature suggests the growth of SEI layer can lead to an increase in resistance, resulting in cell power fade and a decrease in capacity due to the loss of active materials. The capacity and resistance of a lithium battery throughout its aging thus have a negative correlation. Due to their measurability and direct influence on battery performance, both resistance and capacity have been used as metrics for battery aging.

In the literature, some efforts are made to discern if certain factors are influential on battery aging rate. In [98], several factors and their joint cross coupling effect were studied; it is claimed that effects including temperature, end of discharge voltage, and charging voltage are significant, as well as their cross-coupling effects. The temperature influence on aging is indeed well documented throughout the literature.

One interesting factor in battery aging is the superimposed AC waveform. The literature has many examples of indirect proof for superimposed AC waveform being important for battery aging rate, see the discussion in 2.7.4. If superimposed AC waveforms are irrelevant to aging, the sizing of the capacitor may be reduced for cost benefits. If these AC waveforms are significant to aging, a quantitative metric for balancing between the right amount of filtering and cost would be important.

In this chapter an experiment is conducted focusing on determining if a superimposed AC waveform in the discharge current leads to more aging. If so, is the

additional aging resulting from the higher root mean square (RMS) value in the discharge current or simply from the swinging of the waveform? Having found in the experiment that the higher RMS value leads to higher aging, we conducted a second experiment to determine if different waveforms and frequencies have an impact on aging besides the RMS value. Finally, the data of the first and second experiments are used together to statistically determine the growth of resistance as a function of RMS and show that the DC value of the discharge waveform is far less important than the RMS value in influencing aging.

6.2 Experimental Details for the First Experiment

The experiment was conducted using ICR14500NM cells rated at 760 [mAh] from HYB Battery. These cells use lithium cobalt oxide as their cathode material according to the vendor. The test stand specification is briefly discussed here, and the interested reader is referred to [26] for more details. The test stand consists of 16 channels housed in two enclosures, eight channels each. A LabVIEW® program running on two National Instruments PXI units controls the two enclosures. Figure 6.1 shows the test stand system level diagram [26].

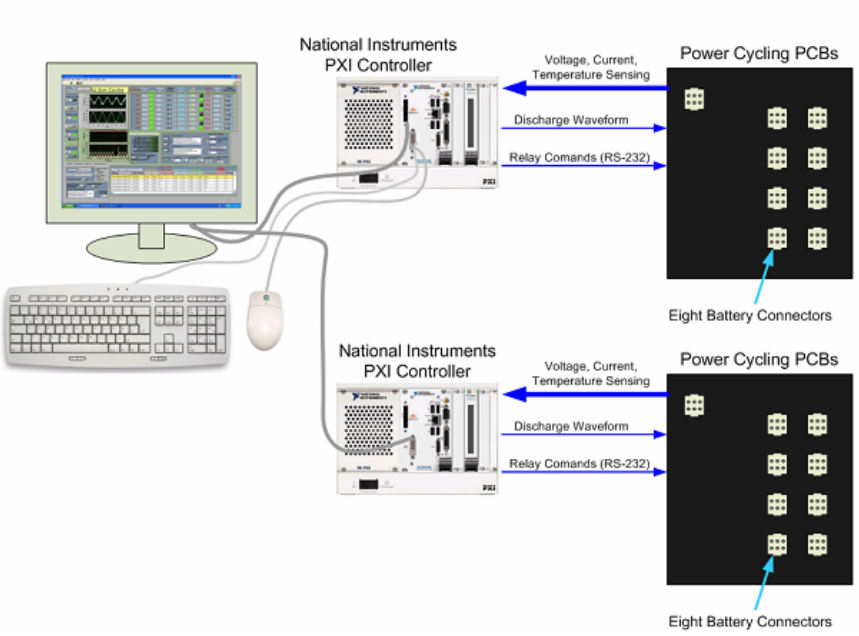

Figure 6.1 Test stand system level diagram [26]

A wire harness connects a cell to each channel, providing pathways for the main current loop and sensing for voltage, current, and temperature. The charging of the cell is performed by a circuit that implements the constant current, constant voltage algorithm. The cell discharge is performed by another separate feedback circuit made of a BJT and an Op-Amp, able to scale arbitrary discharge current commands given by the PXI unit. The discharge circuit allows various discharge waveforms and electrochemical impedance spectroscopy (EIS) at a DC current offset. Additionally, a heat chamber is available, and throughout testing the cells were maintained at 30^0C.

In the first experiment, the goal is to determine whether a superimposed AC component on a DC discharge current will have a significant difference in aging. If so, does the effect come from the additional RMS value or the AC swing itself? Three discharging waveforms were designed for answering these questions. They are listed in Table 6.1. The units are all in milliamps [mA].

Table 6.1 Treatments summary for the first experiment

	Waveform [mA]	RMS	DC	AC
AC-905	$i = 600*\sin(2*\pi*20*t) + 800$	905	800	$600*\sin(2*\pi*20*t)$
DC-800	$i = 800$	800	800	0
DC-905	$i = 905$	905	905	0

For the treatment AC-905, the 800 [mA] discharge waveform is superimposed by a 20 Hz, 600 [mA] peak sinusoidal waveform. The resulting RMS value of the waveform is 905 [mA]. The selection of 20 Hz was due to this frequency's proximity to the location of the peak of the EIS semicircle for this particular cell, which might enhance aging effect. However, our later results suggest frequency is largely irrelevant for aging. As seen in Table 6.1, for each of the three attributes, RMS, DC, and AC, two treatments have the same value and one is different. Thus if RMS value is an important aging factor, we would expect to see treatments AC-905 and DC-905 show the same aging characteristic while DC-800 differs from the other two. The same logic applies to the other two attributes, DC offset and the presence of AC signal. In this experiment, 8 cells were assigned to the superimposed AC waveform, while treatments DC-800 and DC-905 were assigned 4 cells each. The reason behind this distribution was that the experiment focused on the superimposed AC waveform, and the statistical resolution is better with more cells assigned.

The reference performance tests (RPT's) designed to extract aging information were conducted in the following fashion. The RPT consists of both EIS and capacity test. The EIS was performed twice: once at fully charge condition (100% SOC) and once at fully discharged (0% SOC) condition as determined by a cut-off voltage. The capacity test was performed with an 800 [mA] discharge from the fully charge condition. We found that the capacity test did not yield statistically significant results and this paper will

focus on the aging results as determined by the resistance value. The resistance value is the real impedance of the point where the imaginary impedance is zero. This value can be linearly extrapolated from the EIS results using the two data points straddling zero imaginary impedance, as shown in Figure 6.2.

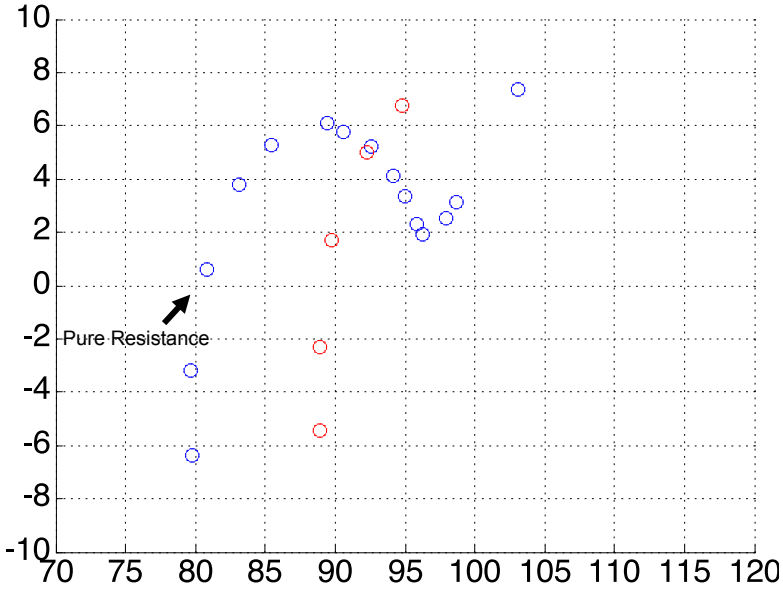

Figure 6.2 EIS results for one cell at 100% SOC and 0% SOC conditions

The cycling procedure was conducted in the following fashion. The RPT's were performed before any cycling. Each cell was then cycled 30 times with a discharge of the prescribed waveform for 3000 seconds and a full charge. The RPT's were repeated at the end of the 30th cycle, and the sequence repeats until 300 cycles were performed. The test sequence is illustrated in Figure 6.3.

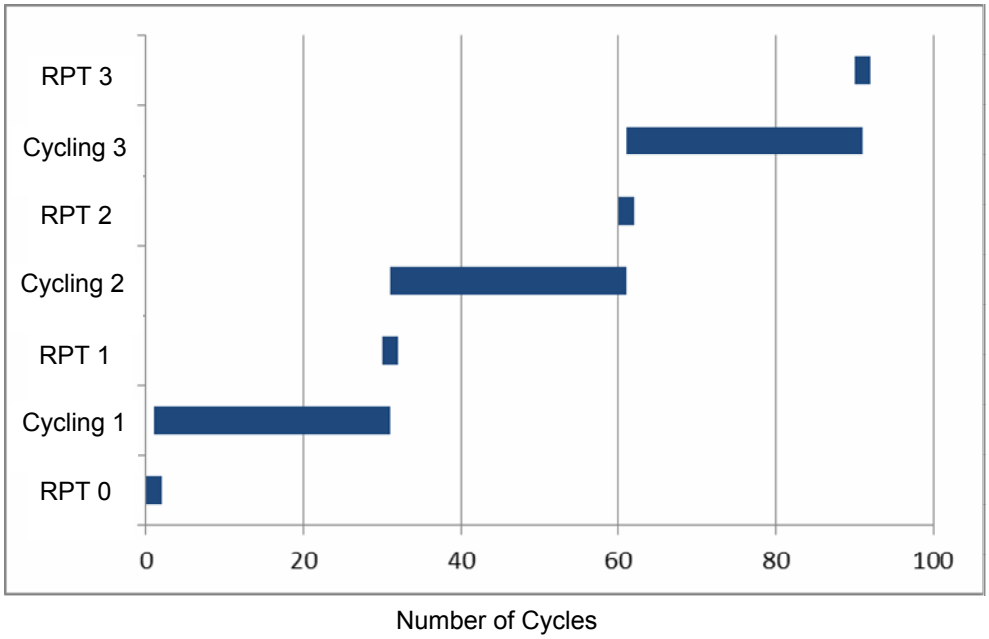

Figure 6.3 Test sequence schedule

6.3 Analyses and Results for the First Experiment

In this section the statistical analyses are introduced to discern if the differences between the three test groups are significant statistically. The results are used to make inferences about which aging attribute in Table 6.1 is the most important. The raw data from the first experiment are shown in Figure 6.4 and Figure 6.5, for 0% SOC and 100% SOC conditions respectively. The aging metric on the y-axis is the resistance value, R, defined in the previous section. In Figure 6.4 and Figure 6.5, the normalized cycle Z is defined as (6.3.1).

$$Z = \frac{C - \overline{C}}{\Delta C} \tag{6.3.1}$$

In (6.3.1), C is the cycle numbers i.e. 30, 60, …, 300, $\overline{C}$ is the average of the cycle numbers, i.e. 165, and ΔC is the interval cycles 30.

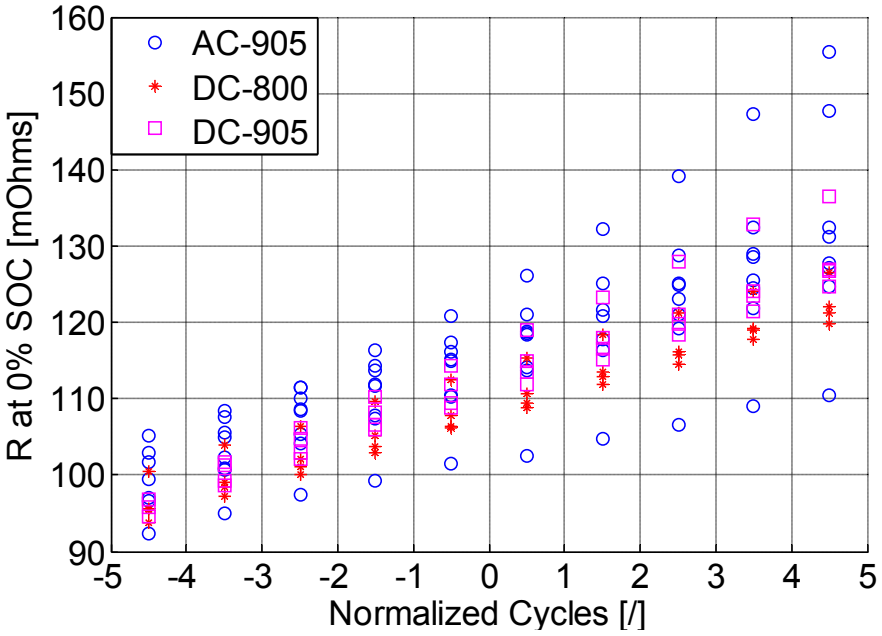

Figure 6.4 R value progression for cells in the first experiment at 0% SOC

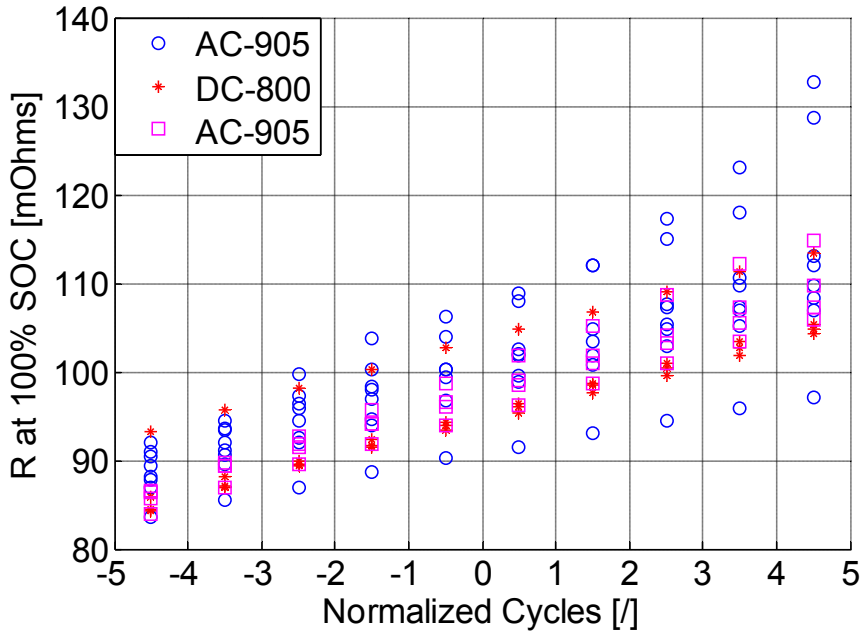

Figure 6.5 R value progression for cells in the first experiment at 100% SOC

The statistical model adopted for the analysis is written from (6.3.3) to (6.3.4).

$$R_{ij} = \hat{\beta}_0 + \hat{\beta}_1 R_{i0} + \hat{\beta}_2 X_{1j} + \ldots + \hat{\beta}_{17} X_{16j} + \varepsilon_{ij} \quad (6.3.2)$$

$$X_{kj} = Z_j \delta(i - k) \quad (6.3.3)$$

$$Z_j = \frac{C_j - \bar{C}}{\Delta C} \tag{6.3.4}$$

In (6.3.2), R_{ij} is the resistance of i^{th} battery and j^{th} EIS measurement. R_{i0} is the initial resistance measurement for the i^{th} battery. In (6.3.3), X_{kj} is defined as the predictor value for k^{th} battery and j^{th} measurement, and δ is the Kronecker delta function. Thus X_{kj} has a value of zero when $i \neq k$, and takes the value of the normalized cycle Z_j when $i = k$. This statistical model assumes an offset term, $\hat{\beta}_0$, shared by all cells. Contrary to the popular approach of normalizing aging metrics against cell manufacturing differences by dividing by initial values, this model adopts the analysis of covariance (ANCOVA) approach by including the initial values as one of the predictor terms. Interested reader can find a complete treatment for ANCOVA in [133]. One benefit of this approach compared with the normalizing method is the retention of the physical unit. The rest of the 16 predictor terms correspond to the normalized cycles for each of the cells, and their coefficients, $\hat{\beta}_2$ to $\hat{\beta}_{17}$, are the cells' estimated rates of resistance increase in $\left[\frac{\text{Ohms}}{30 \text{ cycles}}\right]$. The coefficients in (6.3.2) are estimated using least square error method. It is noted here that due to the transformation of the cycles in (6.3.4), the covariance matrix resulting from the estimation has no covariance terms between any of the estimated coefficients from $\hat{\beta}_2$ to $\hat{\beta}_{17}$ and these estimated coefficients have the same variance. Thus the rates of resistance increase are estimated with the smallest variance possible, i.e. optimal for statistical inference.

Since the coefficients are estimated with data with random error, the estimated coefficients can be considered as random variables themselves. As each battery has its estimated slope, each treatment group's average estimated slope and its variance can be found as (6.3.5) and (6.3.6) respectively. In (6.3.5) and (6.3.6), it is assumed that there are n cells in this group.

$$\hat{\beta}_{avg} = \frac{\sum \hat{\beta}_i}{n} \tag{6.3.5}$$

$$\mathrm{Var}\left(\hat{\beta}_{avg}\right) = \frac{\mathrm{Var}\left(\hat{\beta}_i\right)}{n} \tag{6.3.6}$$

Our objective here is to determine whether two groups' mean estimated slopes are statistically the same; or equivalently whether the difference between the two groups can be attributed to noise alone. The null hypothesis that there is no difference between two groups' mean estimated slopes can be tested with Student's t-statistic, which is given in (6.3.7). If there is no difference between two groups, the t-statistic in (6.3.7) will tend towards zero.

$$t = \frac{\hat{\beta}_{avg1} - \hat{\beta}_{avg2}}{\sqrt{\mathrm{Var}\left(\hat{\beta}_{avg1}\right) + \mathrm{Var}\left(\hat{\beta}_{avg2}\right)}} \tag{6.3.7}$$

In the analysis of our first experiment, the degrees of freedom for the error are 142 since there are 160 data points and 18 terms in the regression model. The t-statistic is therefore distributed with a t-distribution of 142 degrees of freedom under the null hypothesis, and the probability for observing a value equal or greater in magnitude than the calculated t-statistic under null hypothesis (p-value) can be found using the t-distribution.

Table 6.2 Average estimated slope of each group for the 0% SOC condition in the first experiment

	$\hat{\beta}_{avg}$	Std. Dev.
AC-905	3.5e-3	1.7e-4
DC-800	2.9e-3	2.5e-4
DC-905	3.6e-3	2.5e-4

Table 6.3 Average estimated slope of each group for the 100% SOC condition in the first experiment

	$\hat{\beta}_{avg}$	Std. Dev.
AC-905	2.7e-3	1.4e-4
DC-800	2.2e-3	2.0e-4
DC-905	2.6e-3	2.0e-4

In Table 6.2 and Table 6.3, the groups' average estimated slopes and their standard deviations are provided. It is noted that the standard deviation of the AC-905 group is smaller because 8 cells were assigned to it instead of the 4 for the other two groups. The t-statistics for the group comparisons are listed in Table 6.4 and Table 6.5.

Table 6.4 t-statistics and p-values for the 0% SOC condition in the first experiment

	t-statistic	p-value
AC-905 vs. DC-800	1.91	5.81 %
DC-905 vs. DC-800	2.01	4.63 %
AC-905 vs. DC-905	0.41	68.24 %

Table 6.5 t-statistics and p-values for the 100% SOC condition in the first experiment

	t-statistic	p-value
AC-905 vs. DC-800	1.84	6.79 %
DC-905 vs. DC-800	1.44	15.21 %
AC-905 vs. DC-905	0.17	86.53 %

From Table 6.4 and Table 6.5, it is observed that the AC-905 group and DC-905 group seem to have about the same aging rate while the DC-800 group has a noticeably slower aging rate as reflected by the t-statistics that compare the DC-800 group to the others.

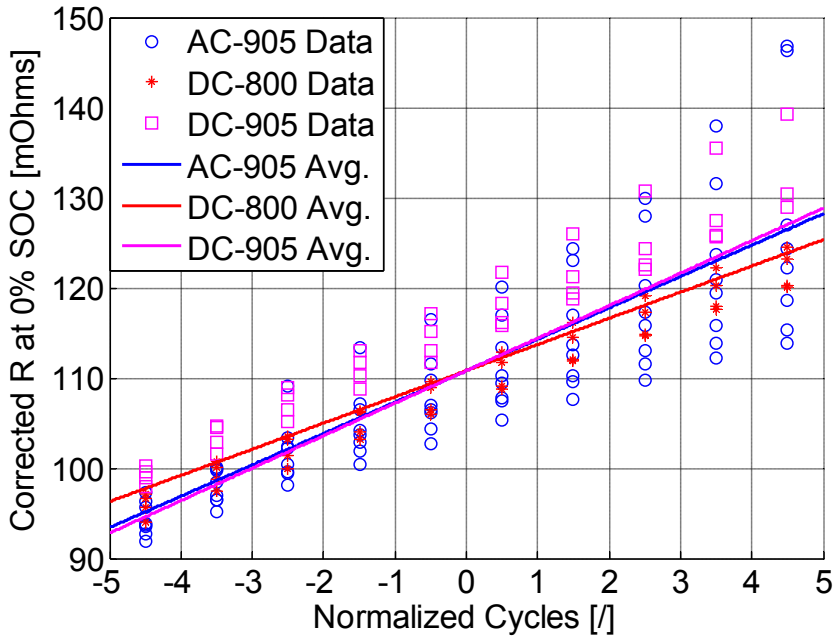

Figure 6.6 Corrected R value progression for every cell and group averaged fitted model at 0% SOC in the first experiment

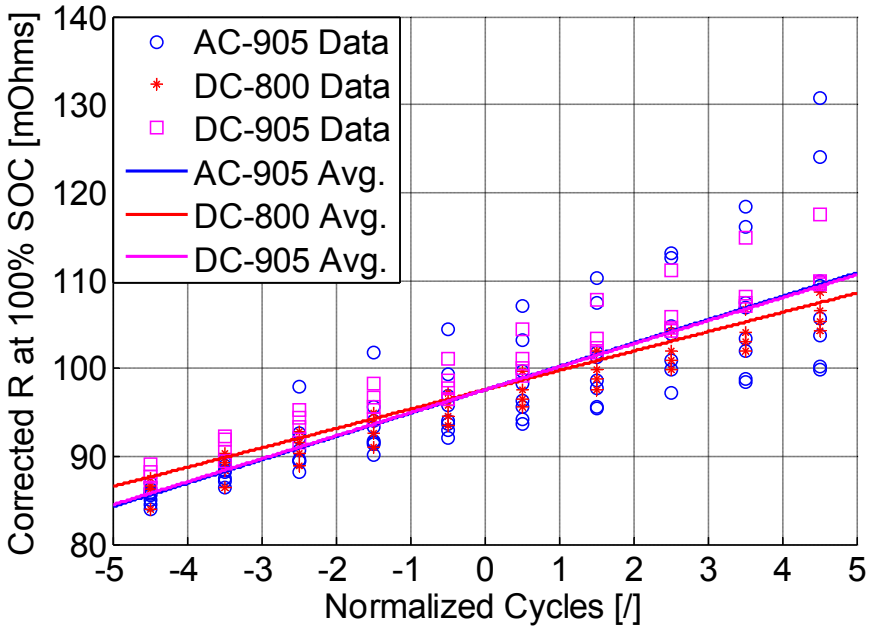

Figure 6.7 Corrected R value progression for every cell and group averaged fitted model at 100% SOC in the first experiment

In Figure 6.6 and Figure 6.7, the R values corrected for the initial conditions are plotted on the y-axis, i.e. $R_{ij} - \hat{\beta}_1 R_{i0}$. Additionally, each group's average model was also

plotted for a visual comparison, i.e. $\hat{\beta}_0 + \hat{\beta}_{avg}Z$. In both the 0% and 100% SOC cases, the graphs demonstrate visually the difference in slopes between the groups with 905 [mA] RMS waveforms and the group with 800 [mA] RMS. Instead of visually inferring differences/similarities between regressed lines, the probabilistic approach provides a guideline for determining whether the null hypothesis of no difference is significantly in doubt, leading to the alternative hypothesis that there exists a difference.

With the results demonstrated so far, a few remarks can be made. The first is that battery aging seems to be related to RMS value of the discharge waveform instead of the DC value. Since each waveform lasts exactly 3000 seconds per cycle, the AC-905 group discharges the same amount of Ah as DC-800 every cycle while suffers the same aging rate as DC-905. This result shows the importance of adequate filtering to reduce unnecessary battery aging in operation. It is also pointed out here that the usual 5% rule for statistical inference, i.e. rejecting the null hypothesis when p-value is below 5%, has been used with considerations. If we were to follow the rule with strictness, paradoxes would develop. For example with a strict interpretation of the rule, in Table 6.4 AC-905 vs. DC-800 and AC-905 vs. DC-905 would not have been considered as statistically different but DC-905 vs. DC-800 would have been. Additionally, the two sets of data at different SOC's provide some assurance due to their qualitative agreement to the conclusion drawn above. Noting the relative high p-values, a second experiment was proposed to confirm the conclusion as well as answering a couple additional questions.

6.4 Experimental Details and Results for the Second Experiment

The objectives of the second experiment are the following: 1) Confirmation of the influence of RMS value on battery aging, 2) Investigation on possible influence of

waveform shape on aging, 3) Investigation on possible influence of frequency on aging, 4) Quantitative analysis of RMS influence for battery aging, and 5) The incorporation of data from the first experiment.

The second experiment involved sixteen cells with the same cycling schedule as in Figure 6.3, lasting 300 cycles exactly like the first experiment. This experiment is separated into four treatment groups, as seen in Table 6.6.

Table 6.6 Treatments summary for the second experiment

	Waveform [mA]	RMS	DC	AC
S-807-20Hz	800 + 105*square(20Hz)	807	800	105*square(20Hz)
S-807-1000Hz	800 + 105*square(1000Hz)	807	800	105*square(1000Hz)
S-703-20Hz	695 + 105*square(20Hz)	703	695	105*square(20Hz)
S-703-1000Hz	695 + 105*square(1000Hz)	703	695	105*square(1000Hz)

Each treatment had four cells assigned to it. However, due to hardware difficulty one channel assigned to the group S-703-20Hz was terminated right after the experiment had begun.

Due to the structure of the statistical model in (6.3.2), the data collected during the second experiment can be combined with that of the first. The new model is rewritten as (6.4.1). The number of data points is now 310 instead of 160, and the number of coefficients involved is 33 instead of 18.

$$R_{ij} = \hat{\beta}_0 + \hat{\beta}_1 R_{i0} + \hat{\beta}_2 X_{1j} + \ldots + \hat{\beta}_{32} X_{31j} + \varepsilon_{ij} \qquad (6.4.1)$$

It is noted here that with the combined data and the additional 15 terms, the estimated slopes for the first experiment's 16 cells, $\hat{\beta}_2$ to $\hat{\beta}_{17}$, take the same numerical values in (6.4.1) as in (6.3.2). The estimated slopes for the last 15 cells, $\hat{\beta}_{18}$ to $\hat{\beta}_{32}$, along with other coefficients can also be found through linear regression.

To determine if frequency is an important factor in influencing aging, the estimated slopes for the second experiment are grouped into those at 20 Hz and those with at 1000 Hz. The statistical inference procedure as specified from (5) to (7) is applied to the data. The average slopes and standard deviations for the two frequency groups are shown in Table 6.7 and Table 6.8.

Table 6.7 Average estimated slopes of two frequency groups for the 0% SOC condition in the second experiment

	t-statistic	p-value
20 Hz (7 cells)	2.7e-3	2.0e-4
1000 Hz (8 cells)	2.5e-3	1.8e-4

Table 6.8 Average estimated slopes of two frequency groups for the 100% SOC condition in the second experiment

	t-statistic	p-value
20 Hz (7 cells)	2.1e-3	1.5e-4
1000 Hz (8 cells)	1.9e-3	1.4e-4

Table 6.9 and Table 6.10 show the t-statistics and p-values for the frequency comparison for 0% and 100% SOC conditions respectively. Neither SOC condition data indicate any evidence for frequency being an important aging factor. Additionally, when considering the results for AC-905 vs. DC-905 in the first experiment, the DC waveform can also be considered as an AC signal with a zero frequency. Thus between 0 Hz and 20 Hz sine waves, a significant difference is also not observed. The analysis for the rest of the paper will drop the distinction in frequency. Figure 6.8 and Figure 6.9 show the graphical results for the frequency comparison.

Table 6.9 t-statistic and p-value for the frequency groups' comparison at 0% SOC condition in the second experiment

	t-statistic	p-value
20 Hz vs. 1000 Hz	0.96	33.59 %

Table 6.10 t-statistic and p-value for the frequency groups' comparison at 100% SOC condition in the second experiment

	t-statistic	p-value
20 Hz vs. 1000 Hz	0.99	26.90 %

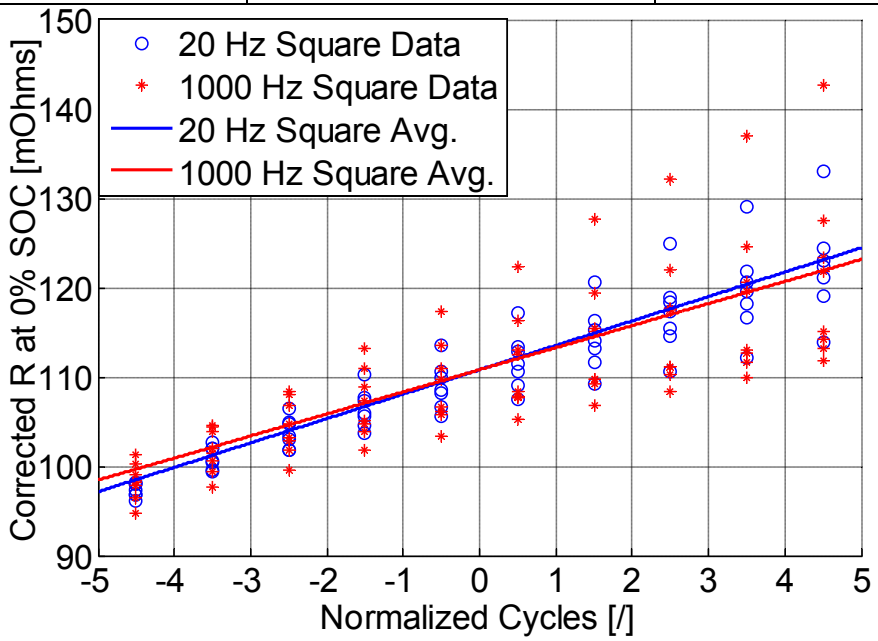

Figure 6.8 Frequency groups' corrected R value progression and averaged fitted models at 0% SOC for the second experiment

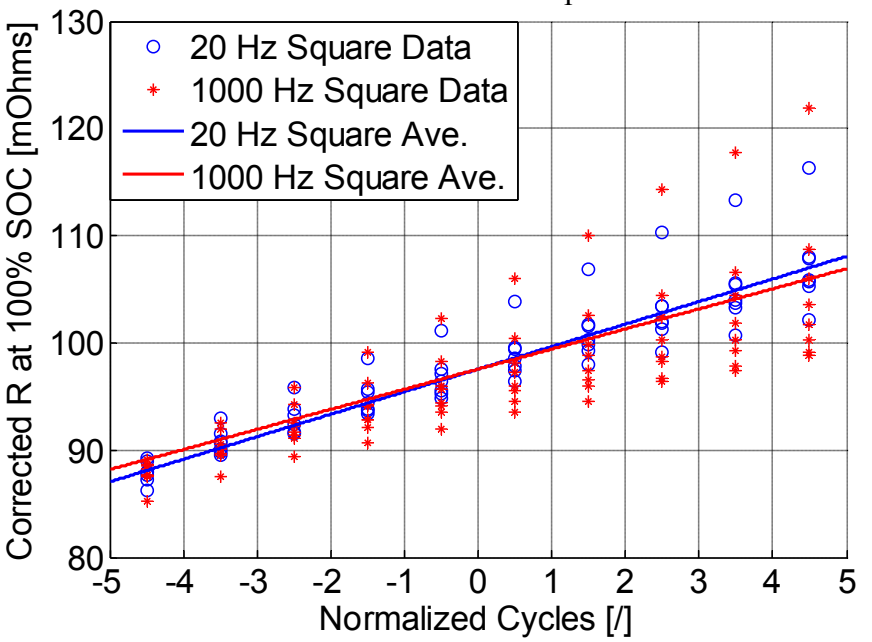

Figure 6.9 Frequency groups' corrected R value progression and averaged fitted models at 100% SOC for the second experiment

It is noted that by the hypothesis obtained through the first experiment, one should expect the aging rate obtained in S-807 should be very similar to DC-800 while these two should have a higher aging rate against S-703. The results from regressing (6.4.1) allows for the confirmation of this hypothesis. Table 6.11 and Table 6.12 show the average estimated slopes for the three groups in discussion, and Table 6.13 and Table 6.14 show the t-statistics and p-values for the three groups' comparisons.

Table 6.11 Average estimated slopes of S-807, DC-800, S-703 for the 0% SOC condition

	$\hat{\beta}_{avg}$	Std. Dev.
S-807	3.1e-3	1.8e-4
DC-800	2.9e-3	2.6e-4
S-703	2.0e-3	2.0e-4

Table 6.12 Average estimated slopes of S-807, DC-800, S-703 for the 100% SOC condition

	$\hat{\beta}_{avg}$	Std. Dev.
S-807	2.3e-3	1.4e-4
DC-800	2.2e-3	2.0e-4
S-703	1.6e-3	1.5e-4

Table 6.13 t-statistics and p-values for S-807, DC-800, S-703 comparisons at the 0% SOC condition

	t-statistic	p-value
S-807 vs. DC-800	0.65	51.62 %
S-807 vs. S-703	4.09	< 0.01 %
DC-800 vs. S-703	2.75	0.64 %

Table 6.14 t-statistics and p-values for S-807, DC-800, S-703 comparisons at the 100% SOC condition

	t-statistic	p-value
S-807 vs. DC-800	0.47	63.87 %
S-807 vs. S-703	3.47	0.06 %
DC-800 vs. S-703	2.41	1.66 %

It is seen in Table 6.13 and Table 6.14 that the hypothesis from the first experiment holds quite well. Namely, RMS value noticeably influences the aging rate. By virtue of having the second experiment reproducing similar results, the strength of the hypothesis is more assured. It is also observed that despite the difference in waveform shape S-807 and DC-800 are considered statistically similar in aging rate. This observation, along with the previous observation that DC-905 and AC-905 had a similar aging rate, suggest waveform shape is not an important aging factor. Figures 7a and 7b show the graphical results of the three groups' comparisons.

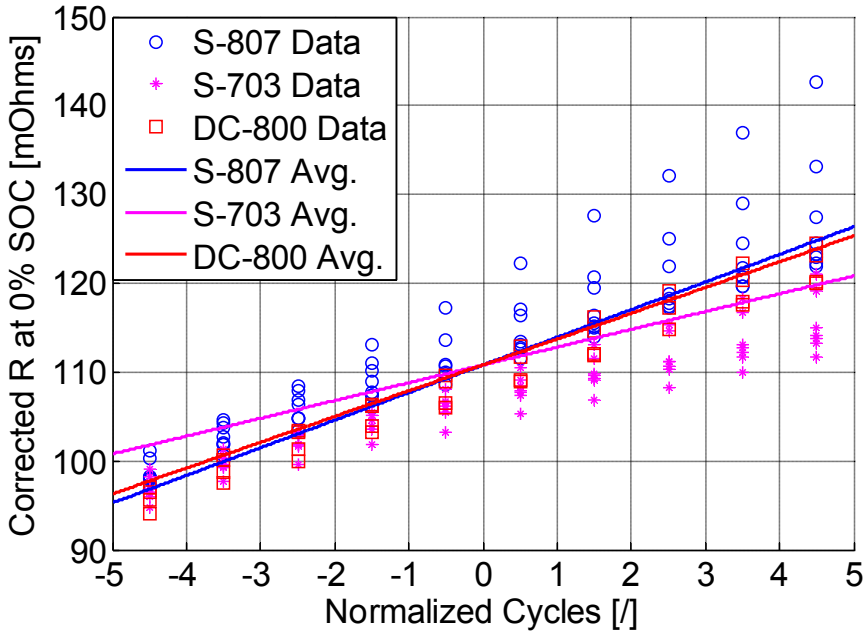

Figure 6.10 S-807, DC-800, S-703's corrected R value progression and averaged fitted models at 0% SOC

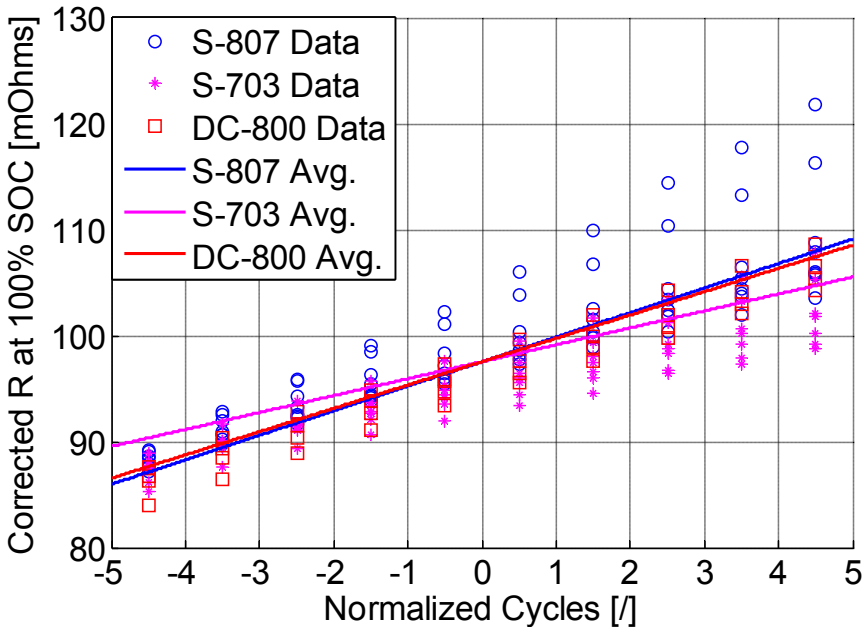

Figure 6.11 S-807, DC-800, S-703's corrected R value progression and averaged fitted models at 100% SOC

6.5 Analysis for Quantification of RMS Effect on Battery Aging

So far the analyses for the second experiment data show that frequency and waveform differences are secondary in aging influence compared with the RMS value of the waveform. The attention is now turned to constructing a quantitative aging model for resistance growth using RMS as an input. This quantitative analysis is performed using a different model than (6.4.1). The statistical model is adopted as in (6.5.1) and (6.5.2).

$$dR_{ij} = R_{ij} - R_{ij-1} \tag{6.5.1}$$

$$dR_{ij} = \hat{b}_0 + \hat{b}_1 RMS_i + \hat{b}_2 QRMS_i + \hat{b}_3 DC_i + \varepsilon_{ij} \tag{6.5.2}$$

In (6.5.1), the j^{th} resistance growth for the i^{th} battery, dR_{ij}, is the difference between j^{th} and $j\text{-}1^{th}$ resistance measurement. These 310 values are used as the output for the regression model in (6.5.2). Notice that from Tables 1 and 6 that the prescribed

discharged waveforms are roughly divided into three levels, 700, 800, and 900 [mA]. Taking advantage of the consistent intervals, the predictors in (6.5.2) are transformed into polynomials. Specifically, for the DC and RMS predictors, the values are coded with -1 for 700, 0 for 800, and 1 for 900 [mA]. For the QRMS predictor that represents the quadratic component of the RMS influence, the values are coded with 1 for 700, -2 for 800, and 1 for 900 [mA]. The regression summaries for both 0% SOC and 100% SOC data are shown in Table 6.15 and Table 6.16.

Table 6.15 Regression summary table for (6.5.2) with 0% SOC data

	Estimate	Std. dev.	t-statistic	p-value
$\hat{b}_0$	3.2 e-3	1.1 e-4	30.52	< 0.01 %
$\hat{b}_1$	6.1 e-4	2.2 e-4	2.81	0.53 %
$\hat{b}_2$	-9.4 e-5	6.6 e-5	-1.44	15.13 %
$\hat{b}_3$	2.1 e-4	2.8 e-4	0.75	45.35 %

Table 6.16 Regression summary table for (6.5.2) with 100% SOC data

	Estimate	Std. dev.	t-statistic	p-value
$\hat{b}_0$	2.5e-3	9.7e-5	25.71	< 0.01 %
$\hat{b}_1$	5.1e-4	2.0e-4	2.53	1.2 %
$\hat{b}_2$	-7.0e-5	6.0e-5	-1.17	24.3 %
$\hat{b}_3$	-3.1e-5	2.6e-4	-0.12	90.4 %

The model in (6.5.2) provides a direct comparison between the explanatory powers of DC and RMS predictor. From Table 6.15 and Table 6.16, it can be observed that the explanatory power of the DC predictor is weak in the presence of the RMS predictor, as reflected by the low t-statistics and high p-values, which indicates a high probability of being the estimated parameter being zero under the null hypothesis. To complete the

quantitative analysis of the RMS influence, the DC term is now dropped from the model in (6.5.3).

$$dR_{ij} = \hat{b}_0 + \hat{b}_1 RMS_i + \hat{b}_2 QRMS_i + \varepsilon_{ij} \quad (6.5.3)$$

The resultant regression summary tables from (6.5.3) are shown in Table 6.17 and Table 6.18.

Table 6.17 Regression summary table for equation (6.5.3) with 0% SOC data

	Estimate	Std. dev.	t-statistic	p-value
$\hat{b}_0$	3.2e-3	8.6e-5	37.34	< 0.01 %
$\hat{b}_1$	7.6e-4	1.1e-4	6.87	< 0.01 %
$\hat{b}_2$	-1.2e-4	5.8e-5	-2.05	4.12 %

Table 6.18 Regression summary table for equation (6.5.3) with 100% SOC data

	Estimate	Std. dev.	t-statistic	p-value
$\hat{b}_0$	2.5e-3	7.8e-5	32.03	< 0.01 %
$\hat{b}_1$	4.8e-4	1.0e-4	4.83	< 0.01 %
$\hat{b}_2$	-6.7e-5	5.3e-5	-1.27	20.50 %

It is noted that the aging influence of the RMS quadratic component is not as strong as the linear component, but there is some evidence supporting its existence as seen in the relatively low p-value 4.12% for the $\hat{b}_2$ in Table 6.17. In addition to the summary tables, the fitted values and the 95% prediction intervals for (6.5.3) with both sets of data are plotted in Figure 6.12 and Figure 6.13.

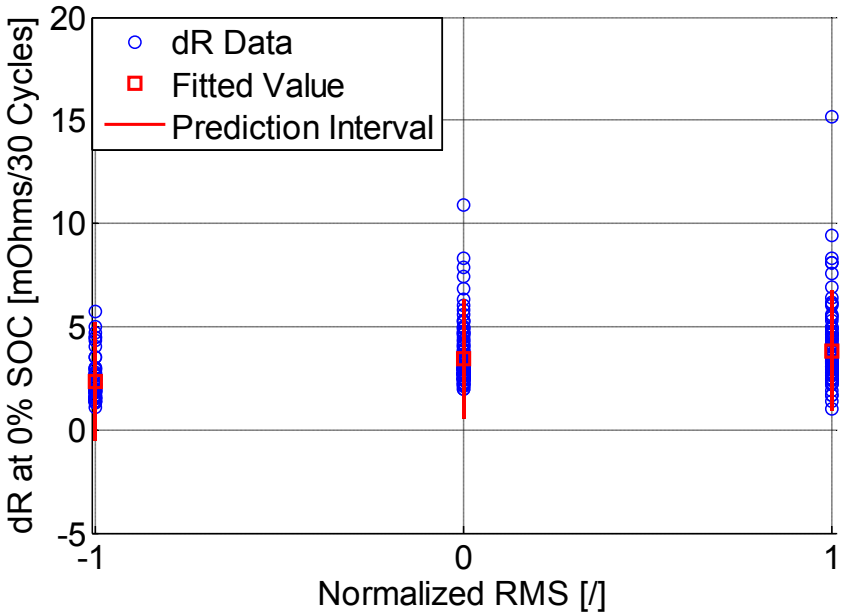

Figure 6.12 dR data and fitted model (6.5.3) with the 95% prediction interval for 0% SOC

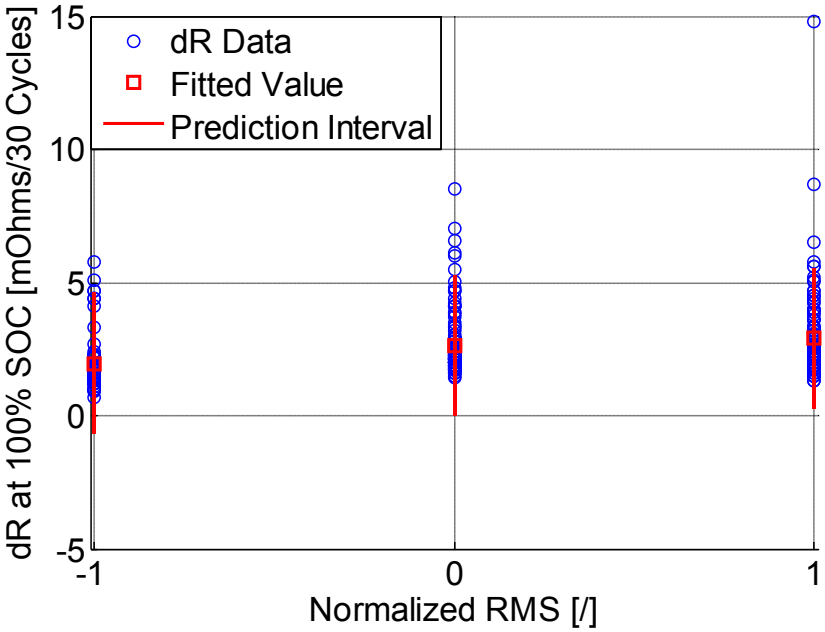

Figure 6.13 dR data and fitted model (6.5.3) with the 95% prediction interval for 100% SOC

From Figure 6.12 and Figure 6.13, it is noted that some values are quite off from the fitted value and the prediction interval, suggesting other mechanisms not taken into account in (6.5.3). For example, when examining the data, it was found that the growth

of resistances from the RPT before cycling to the RPT after the first 30 cycles is much higher than the rest. This phenomenon may suggest an activation mechanism not modeled in (6.5.3).

The practical significance of the difference in aging caused by different RMS values can be illustrated in the following example. Three hypothetical cells with 80 [mΩ] resistance at 0% SOC each undergoes 300 cycles of 700, 800, and 900 [mA] RMS with the length of 3000 seconds. Based on the fitted results in Table 6.17, their expected values for 0% SOC resistance are 103, 114, 118 [mΩ], respectively. If the cell open circuit voltage is assumed to be stable during aging, then the power capability of these three hypothetically aged cells at the end of the 300 cycles are 77.7%, 70.2%, and 67.8% of the original, respectively. Thus by implementing proper filtering to lower the RMS value of the discharge cycle, the battery power capability can be better maintained.

One emphasis for the statistical methods employed in this study is the rigorous inference on the significance of aging factors. Instead of regressing with all possible predictor terms, this methodology takes the effort to investigate if the factor of interest is actually significant in the statistical sense. This feature allows investigators to avoid confusion between a small regression coefficient of a significant factor and the random noise of a non-significant factor included in the model. In order to achieve such rigor in inference, the design of experiment and analyses are complementary parts to the same whole. The design allows the analyses, while only analyses that adhere to statistical principles can achieve rigorous inference. An example of the design permitting analyses is the employment of the waveforms with RMS value of 700 mA in the second

experiment. It is possible to conduct the quantitative analysis only with the data from these waveforms, expanding the available data in terms of range of RMS value.

Another critical issue is that sometimes a number of equally valid models can be applied, given a set of data various. It is therefore preferable to determine the statistical model before the data become available, in order to avoid choosing a model for the sake of obtaining favorable results. Employing the same statistical model as the first experiment, the second experiment's data are incorporated with those of the first and provide results consistent with the first experiment's conclusion. This fact strengthens the main conclusion made in the study, namely that RMS value influences battery aging.

6.6 Planned Aging Experiment for the New Wisconsin Energy Institute Battery Test Equipment

The Wisconsin Energy Institute (WEI) received a $500,000 worth of battery test equipment donation from Johson Controls Inc in 2014. The battery test equipment includes a suite of Diagtron cyclers, three thermal chambers, and other supporting tools such as a thermal camera and a resistance welder. As of October 15, 2014, the equipment suite is pending on Madison Fire Department's approval for its safety requirements. During the preliminary exam, a few ideas were proposed to continue the battery aging study using the new battery test equipment. Since the equipment has not been commissioned in its final form, this work will not include the experimental results and only contain a detailed discussion on one planned experiment.

Figure 6.14 The Diagtron Cyclers in WEI

The planned experiment seeks to address the following two issues: 1) investigate whether the regen operation will influence aging rate, 2) the interaction of RMS and temperature aging influences, and 3) confirmation of the RMS influence on aging. The battery used in this experiment will be the Panasonic NCR18650PF nickel-manganese-oxide, rated at 2.9 Ah and 3.6 V.

The Digatron suite includes twelve channels rated at 18 V and 25 A. These channels can be used to perform cell level experiments. In addition, the 18 V rating allows the testing of three cells in series. However, such a series connection represents an additional layer of complexity in statistical analysis.

The particular experiment planned on the new equipment seeks to understand the influence of the regenerative braking on aging. Specifically, three driving profiles have been selected as shown in Table 6.19.

Table 6.19 The proposed driving profiles for experiments aiming at understanding regenerative braking on aging

Time	DC Discharge	Drive w/o Regen	Drive w/ Regen
1 s	2.9 A	3.69 A	4.26 A
2 s	2.9 A	5.75 A	2.50 A
3 s	2.9 A	0.41 A	-1.26 A
4 s	2.9 A	0 A	3.50 A
5 s	2.9 A	4.65 A	5.50 A

In Table 6.19, the three driving profiles have the same DC value while the two non-DC discharge drive cycles have the same RMS value, 3.7 A. One of the drive cycles has a regenerative break component, while the other does not. A summary of the proposed drive cycles' properties is shown in Table 6.20.

Table 6.20 Summary for the proposed driving profiles in Table 6.19

	DC	RMS	Ripples	Regenerative braking
DC Discharge	2.9 A	2.9 A	-	-
Drive w/o Regen	2.9 A	3.7 A	+	-
Drive w/ Regen	2.9 A	3.7 A	+	+

It is observed in Table 6.20 that the comparison of cells' aging performance under the three driving cycles can answer whether regenerative braking and RMS value are influential in battery aging. Figure 6.15 illustrates the proposed three driving cycles.

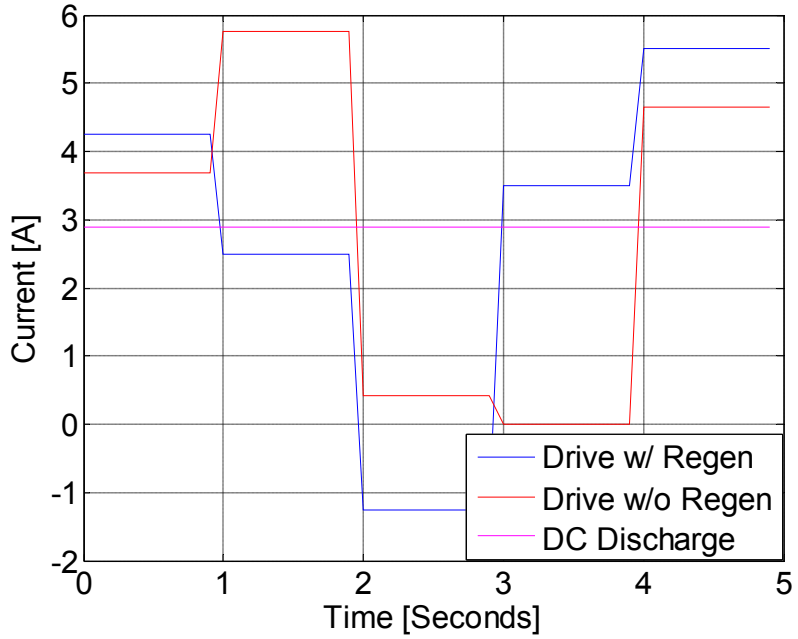

Figure 6.15 The proposed driving profiles for experiments aiming at understanding regenerative braking on aging

In addition to the three driving cycles, two temperature conditions, 0^0C and 25^0C, are deployed in the experiment. The twelve circuits can be split equally between two temperature conditions. In the following analysis, it is assumed that the experiment is repeated once for added resolution, and the resulted number for cells tested is 72 (12 circuits, 3 cells in series, and two experiments). The circuits are equally distributed among the three discharge waveforms.

As discussed earlier in this chapter, two aging characteristics can be obtained at RPT's, the capacity and resistance. The capacity for a single cell is impossible to obtain for the cells in series connection. On the other hand, the resistance of a single cell can be found by applying a HPPC type pulse current and the measurement of individual cell voltage. EIS is also an option for evaluating resistance at RPT's. However, the WEI equipment suite only has twelve channels of EIS, and frequency connection/disconnection of EIS on the cells is adverse for the consistency of resistance

data. The following analysis assumes the resistances of the cells connected in series have been obtained in the two repeated sets of experiment.

In 6.3, the experiment with one cell per circuit was analyzed with the following empirical model.

$$R_{ij} = \hat{\beta}_0 + \hat{\beta}_1 R_{i0} + \hat{\beta}_2 X_{1j} + \ldots + \hat{\beta}_{17} X_{16j} + \varepsilon_{ij} \tag{6.6.1}$$

$$X_{kj} = Z_j \delta(i - k) \tag{6.6.2}$$

$$Z_j = \frac{C_j - \bar{C}}{\Delta C} \tag{6.6.3}$$

As explained in 6.3, R_{ij} is the resistance of i^{th} battery and j^{th} EIS measurement. R_{i0} is the initial resistance measurement for the i^{th} battery, and X_{kj} is defined as the predictor value for k^{th} battery/circuit and j^{th} measurement, and δ is the Kronecker delta function. In this modeling approach, perculiar features unique to the circuit, as reflected on resistance measurements, are lumped together with the tested cell. In the series connection setup, it is necessary to provide additional terms to take the circuits' contribution to resistance measurements into account. One possible scenario where this additional modeling is necessary could be biased error on the current control, which would cause all three cells in series to have an erroneous HPPC resistance. Taking the circuits' contribution to resistance measurement can be accomplished by the following equation.

$$R_{ijk} = \hat{\beta}_0 + \hat{\beta}_1 R_{i0} + \hat{\beta}_2 X_{1jk} + \ldots + \hat{\beta}_{73} X_{72jk} + \hat{U}_k + \varepsilon_{ijk}, \sum \hat{U}_k = 0 \tag{6.6.4}$$

In (6.6.4), the subscript k now represents the k^{th} circuit and $\hat{U}_k$ is the constant term modeling the effect of the circuit on the resistance measurement. In order to ensure the

matrix $(X^TX)^{-1}$ exists, i.e. predictor matrix X is full rank, the constraint $\sum \hat{U}_k = 0$ is specified and implemented [133]. As in the previous model (6.6.1), $\hat{\beta}_2$ to $\hat{\beta}_{73}$ represent the estimated resistance growth slopes for individual cells. These $\hat{\beta}$'s are then grouped into their treatment groups to find the groups' mean growth rates and variances for statistical inferences, as shown again in (6.6.5), (6.6.6), and (6.6.7).

$$\hat{\beta}_{avg} = \frac{\sum \hat{\beta}_i}{n} \tag{6.6.5}$$

$$Var\left(\hat{\beta}_{avg}\right) = \frac{Var\left(\hat{\beta}_i\right)}{n} \tag{6.6.6}$$

$$t = \frac{\hat{\beta}_{avg1} - \hat{\beta}_{avg2}}{\sqrt{Var\left(\hat{\beta}_{avg1}\right) + Var\left(\hat{\beta}_{avg2}\right)}} \tag{6.6.7}$$

Additionally, the temperature and RMS influences' interactions can be quantitatively examined by the following [133].

$$t = \frac{\left(\hat{\beta}_{avg1} - \hat{\beta}_{avg2}|T_+\right) - \left(\hat{\beta}_{avg1} - \hat{\beta}_{avg2}|T_-\right)}{\sqrt{Var\left(\hat{\beta}_{avg1} - \hat{\beta}_{avg2}|T_+\right) + Var\left(\hat{\beta}_{avg1} - \hat{\beta}_{avg2}|T_-\right)}} \tag{6.6.8}$$

In addition to the comparison between cycles with and without regenerative braking, the planned experiment accommodates the series connection of the cells, thus increasing the resolution of the experiment. It also allows a quantitative study on the interaction between two aging factors, temperature and RMS value. It is hoped that the experiment can be implemented soon and its methodology examined with real data.

6.7 Summary

This chapter proposes an experiment procedure and its associated analyses to determine if a superimposed AC waveform on the discharge current will cause an accelerated aging rate. The experimental results confirm the accelerated aging rate exists and this accelerated aging rate is due to the additional RMS value from the superimposed AC waveform during discharge. Furthermore, three other possible aging factors are found to be insignificant compared with the discharge RMS value, namely the DC value during discharge, discharge waveform shape, and waveform frequency. The practical significance for maintaining battery power capability by proper filtering is also pointed out. The proposed methodology can help guide the design of power electronics in terms of filter sizing. On the other hand, the general methodology can be further extended to study any other aging factors deemed interesting, e.g. charging voltage. The statistical rigor employed provides confidence in the inferences made with data analyses, instead of relying on visual differences/similarities. The experiment design facilitates the reasoning process and allows for statistical analyses. The contribution of this work lies both in its practical conclusion and its promotion for more careful experimental reasoning within the field of battery testing.

Chapter 7
Contributions and Future Work

This thesis focuses on the evaluation and estimation of battery resistance and overpotential for the purpose of battery modeling, monitoring, and aging study. The state-of-the-art review covers basic electrochemistry, battery modeling, battery SOC, SOH, and SOF estimation, as well as basic statistical methods and concepts.

A study of Optima D34M lead-acid batteries in a Corbin Sparrow EV has determined the necessity of introducing the Butler-Volmer relationship into the modeling for lead-acid batteries and provides a methodology for performing online recursive estimation using the improved nonlinear model. The issue of providing SOF and SOP estimates using recursive estimation method is also discussed, where the traditional SOP estimate's inherent variability is pointed out and a SOF estimate with a confidence interval provided by the Kalman filter is introduced. The temperature's influence on battery resistance and overpotential for lithium batteries has also been presented. It has been found that, under lower temperatures, the battery resistance increases rapidly, and the overpotential demonstrates Butler-Volmer behavior that is absent at room temperature.

A generic cell modeling methodology that uses temperature as an explicit input has also also provided. The generic cell model is also adapted to a recursive form for online power prognostics and temperature dependent SOC estimation. In Chapter 6, a

statistical aging study using resistance as the aging metric also shows the importance of proper DC bus filtering to extend battery life.

This chapter summarizes the major contributions made in this thesis and provides a list of future work.

7.1 Contributions

Key contributions of this thesis are summarized in this section including battery nonlinear modeling, SOF monitoring, battery temperature-dependent modeling and associated battery SOC, SOF monitoring techniques, and battery aging factor study.

7.1.1 Butler-Volmer Equation Based Battery System Identification

The necessity of introducing the Butler-Volmer equation into lead-acid battery modeling has been demonstrated. Both test bench impulse current tests and experimental EV tests provide experimental justification for adopting the Butler-Volmer equation-based model over the traditional linear circuit model for the lead-acid battery. While the Butler-Volmer equation and its inverse hyperbolic sine approximation have been discussed in the literature, a new contribution of the thesis is a methodology to adapt the equation for linear filtering technique for battery online monitoring. The following summarizes the key components of the major contributions in this area.

- **Derivation of discrete time battery model incorporating the Butler-Volmer equation**

  The qualitative difference between the linear circuit model and the Butler-Volmer model has been pointed out. Under a high-current load, the effective resistance of the overpotential described by Bulter-Volmer equation decreases. This phenomenon is incorporated into a discrete battery model by the use of the

inverse hyperbolic sine approximation for the Butler-Volmer equation. It has also been observed that the inverse hyperbolic sine approximation is necessary from a model prediction perspective. While the original Butler-Volmer equation has overpotential as the input and current as the output, the inverse hyperbolic sine form has current as the input and overpotential as the output. This makes inverse hyperbolic sine form suitable for modeling prediction, since the current is measurable while the electrode overpotential is not.

- **Numerical study for combining two electrodes' responses into one Butler-Volmer relationship**

  The necessity of combining two electrodes into one when modeling the Butler-Volmer relationship arises from the inability to distinguish the two electrodes without a reference electrode in the middle. A numerical study has been conducted to identify any errors introduced by this assumption. It was found that even

  when the two electrodes have up to 20 times difference in exchange current for the Butler-Volmer equation, the combination of the two electrodes does not introduce much numerical error.

- **Application of the discrete model that includes the Butler-Volmer relationship for a lead-acid battery powered EV**

  Application of the discrete model that includes the Butler-Volmer relationship to online recursive estimation has been carried out and investigated. It has been found that, by providing prior knowledge for the double-layer time constant and exchange current, the discrete model can be written in a linear form. The Kalman

filter can be directly applied to this linear form, achieving online estimation. A corresponding recursive estimation form for the linear circuit model has also been derived for performance comparison.

- **Methodology for estimating the time constant and exchange current using only step current responses**

  A methodology for estimating the time constant and exchange current using only step current responses has been presented. By providing a current pulse of duration longer than the time constant and segmenting the voltage response into resistive and overpotential parts, estimation of both the time constant and exchange current is achieved. It is noted, however, that while this step current response method requires only low-end test equipment with limited current command options, it requires the battery to have a relatively small time constant. The methodology introduced in Chapter 5 for estimating parameters offline does not have the same restriction.

- **Demonstration of the necessity of adopting the Butler-Volmer nonlinearity in the lead-acid battery model using Corbin Sparrow drive cycle experimental results**

  The experimental results provided by Corbin Sparrow drive cycles demonstrate that, while both the Butler-Volmer and linear circuit models can recursively track the output voltage of the battery thanks to the feedback mechanism, their internal parameters behave differently due to different model structures. It has been shown that the linear circuit model adapts the model parameters constantly to mimic the nonlinear behavior of the battery, causing unstable and erroneous

power prediction. Statistical analysis confirms that the Butler-Volmer model performs better than the linear circuit model. When used for prediction, which excludes the influence of the feedback mechanism, the Butler-Volmer model's advantage is clear in least-square-error performance, whereas the linear circuit model has a difficult time predicting voltage correctly if the data used to fit the parameter has adifferent current magnitude than the data used for prediction.

7.1.2 Battery Power Prognostics

The battery's power delivery capability is a significant topic for BMS research. Working with operating voltage upper and lower limits provided by manufacturers, the chapter focuses on methods and their evaluations for power prediction in the context of recursive estimation. Because the commonly seen SOP metric is shown to have a strong volatility within the context of recursive estimation, the second contribution of the thesis is an equivalent SOF metric that takes advantage of the Kalman filter probabilities for power prognostics with confidence. This power prognostic with confidence provides a margin of safety based on Kalman filter probabilities. The recursively-estimated power prognostics results are experimentally compared with the results from the standard HPPC offline test, and they are also directly verified using a drive cycle that is injected with high load current pulses. The following summarizes the key steps towards the contribution of that chapter.

- **Study on the volatility of SOP under recursive estimation**

  The derivation of the SOP definition is reexamined and it is found that SOP is inherently volatile using the recursive estimation scheme. This volatility comes

from the correlation between the estimates of $\hat{v}_{ocv}$ and $\hat{R}$, and the small value of $\hat{R}$. A sensitivity study has been carried out to quantify this volatility.

- **Proposal of an SOF metric with a confidence interval from Kalman filter probabilities that is suitable for nonlinear battery model forms**

  A definition of SOF is presented, and its confidence interval using Kalman filter probabilities has been derived. The SOF is equivalent to SOP with respect to determining if battery power delivery capability is above a set threshold. However, given the confidence interval, the SOF estimate can be better utilized with assurance against unexpected failures in battery power delivery. A detailed argument has been presented about the suitability of adopting SOF in place of SOP based on the inherent volatility of SOP and the fact that motor drive control usually only needs to know if battery power exceeds the minimum requirement. In addition, the SOF form is suitable for use with the nonlinear battery model forms.

- **Experimental results using a lithium-iron-phosphate battery for the UDDS drive cycle to demonstrate SOP volatility and SOF confidence interval**

  The CALB lithium-iron-phosphate 60AHA battery has been subjected to a UDDS-based simulated drive cycle using the test equipment. The drive cycle data has been used to estimate both SOP and SOF. It has been demonstrated that SOP indeed exhibits a substantial volatility. The use of the confidence interval has also been demonstrated.

- **A direct comparison between HPPC and recursively estimated SOP**

The recursively estimated SOP has been directly compared with results from the HPPC test. The HPPC test applies a pulsed current of a fixed duration and estimates the battery total resistance based on the voltage drop. The $\hat{v}_{ocv}$ at an SOC level has also been estimated by the rest voltage. It has been found that, given suitable assumptions, the recursively estimated SOP can approximate the HPPC results, thus strengthening the confidence in the recursive estimation method. The discrepancy between SOP and HPPC results are attributed to the difference between the time constant, less than 5 seconds, used in the recursive battery model and the one-hour rest time period in the HPPC procedure. This difference in time causes a discrepancy in $\hat{v}_{ocv}$ estimation, with the HPPC-based $\hat{v}_{ocv}$ substantially higher due to its longer relaxation time.

- **Evaluation of power capability prediction using an UDDS drive cycle interjected with high current pulses**

  The UDDS drive cycle has been combined with the injection of high current pulses to directly evaluate the recursive method's power prediction capability. The results show that, with the injection of 250 [A] current pulses, the minimum voltage prediction was only off by approx. 20 [mV], strengthening confidence in the method.

7.1.3 Lithium-Ion Battery Resistance and Overpotential Behavior under Various Temperatures

The temperature-dependent behavior of the resistance and overpotential of the CALB 60AHA lithium-iron-phosphate battery cell is explored in that chapter. The

significance of the work lies in its confirmation of the inadequacy of the baseline linear circuit model for lithium batteries at low temperatures and its presentation of a modeling approach that provides better agreement with measured battery characteristics by taking into account the temperature effect explicitly. The temperature explicit model can serve as a simulation tool for system studies that use battery as a component. The third contribution of the thesis is to demonstrate an estimation methodology for a battery model that has temperature as an explict input for resistance and overpotential, as well as the evaluations for the effectiveness of the temperature dependent model against the simple linear circuit approach and the development of SOC, SOF algorithms based on the new model form. It is important to note that while the linear model can adapt somewhat to temperature variation by using appropriate parameters, that approach cannot model the nonlinear behavior of battery overpotential at lower temperatures. The key supporting elements for this contribution are summarized as follows.

- **Derivation of battery resistance and overpotential temperature dependence and experimental verification**

  The theory of battery resistance and overpotential temperature dependence is discussed. By using the Arrhenius equation, both resistance and overpotential dependence on temperature are derived qualitatively. For a CALB lithium-iron-phospoate 60AHA battery, the HPPC and EIS tests are employed to experimentally confirm the temperature dependence of the resistance and overpotential. It is found that battery pure resistance rises rapidly as temperature decreases, as predicted by the Arrhenius equation. Using the HPPC test results, it is observed that at lower temperature the battery effective resistance is

significantly influenced by current pulse magnitude, confirming the temperature influence on the exchange current in the Butler-Volmer relationship.

- **Offline parameter fitting procedure using short term drive cycle data for both Butler-Volmer and linear circuit models.**

  An offline parameter fitting procedure is proposed for both linear circuit and Bulter-Volmer models without temperature as an explicit input to the models. By using a short term drive cycle data at a fixed temperature, both models are fitted to compare their least squares error performance in prediction. It is found that while at room temperature the two models perform equally well, the Butler-Volmer model has an edge over the linear circuit model at a lower temperature. The qualitative difference of the battery behavior at different temperatures is illustrated by showing the fitted battery voltage drop as a function of current using the Butler-Volmer based model. At room temperature, the fitted battery voltage drop appears to be a linear function of current, i.e. resistive behavior, while the same fitted voltage drop shows a distinct nonlinear Butler-Volmer behavior at a lower temperature. While the fitting procedure is good for one temperature condition, this procedure is limited when expanding to multiple temperature operating points.

- **Generic cell model with temperature as an explicit input and its parameter fitting procedure**

  A generic cell model with temperature as an explicit input is proposed. The model structure incorporates the resistance and overpotential temperature dependence into the simple discrete time Bulter-Volmer battery form. The data

used for fitting the model parameters need to come from various drive cycles of different temperatures. This is performed with concatenation of data to form a single matrix. The combined matrix is then used for parameter estimation.

- **Experimental prediction comparison between generic cell, simple Butler-Volmer, and linear circuit models**

  The prediction performances of the generic cell model, simple Butler-Volmer, and linear circuit model are compared. It is found that at lower temperature where the Butler-Volmer behavior is more prominent, the generic cell and simple Bulter-Volmer models have an edge over the linear circuit model. Otherwise, the linear circuit model performs well compared with its more complicated counterparts.

- **Adaptation of temperature dependent generic cell model for recursive estimation and experimental verification on generic cell model's power prognostics capability**

  The generic cell model is adopted for recursive estimation. The simplified recursive form relies on both prior knowledge obtained via offline tests and online recursive fitting. The inputs to the recursive form are the measured voltage, current, and temperature. The recursive generic cell model is shown to have good real-time power prognostics capability in a wide range of temperatures. This recursive form is also robust against aging effects, as it keeps track of the growth of resistance and change in overpotential.

- **Offline Li-ion battery modeling based on the generic cell model impedance structure and the OCV modeled as a polynomial of temperature and discharged Ah**

The generic cell's advantage over the recursive methodology proposed in [139] has been discussed in 5.6. In short, the recursive methodology in [139] is robust against aging and temperature effect since it allows the model parameters be guided by the measured voltage and current. However, its implicit temperature dependence on the measured data, instead of having temperature as an explicit input as the approach proposed in this work, makes it inadequate for the task of offline simulation. For the offline simulation model, the impedance relies directly on the generic cell model offline parameter estimation, while the v_{ocv} is obtained through polynomical fitting of the estimated v_{ocv} using the adapted recursive form and measured temperature. The offline model can be used in an overall system simulation, and it can help guide the tuning of Kalman filter used for the recursive form.

- **The investigation of resistance and overpotential behavior under various temperatures for Li-ion and lead-acid batteries using EIS**

  The Butler-Volmer behavior is a major component to this investigation. The time domain nature of the Butler-Volmer equation means most of the investigation is conducted with time-domain analysis such as driving cycles or the HPPC test. In this chapter, EIS and DC bias current are applied to study the Butler-Volmer behavior through the shrinking of the EIS semi-circle. It was shown that Li-ion batteries tend to have significant Butler-Volmer response at low temperature, while such a response is prominent for lead-acid battery even at room temperature. The results from the frequency domain analysis are consistent with those from the time domain techniques.

- **The power prognostics derived SOC estimation evaluated using both bench experimental results and the WEMPEC truck data**

  Using the adopted recursive generic cell model form and its power prognostics, the arrival of the "turtle" mode is estimated for an accurate and practical SOC estimation. It was shown that this SOC estimation method is robust against temperature and driving cycle dynamics. The use of the recursive generic cell model and of the adaptive Ah vs. Temperature polynomial also provides robustness against aging effects. The SOC estimates' standard deviation is shown to be within 3.3% across a wide range of temperatures. The truck's drive data were also used to evaluate the performance of the proposed SOC method.

- **The application of the generic cell model to lead-acid battery for discharge only driving profiles**

  This work attempts to apply the generic cell methodology to a lead-acid battery, OPTIMA D34M. It was observed that the electrochemical phenomona included in the generic cell model do not take into account the additional reactions during the charging of a lead-acid battery. As a result, the generic cell model is only applicable to a lead-acid battey under discharge-only driving profile. For discharge only cycles, the power prognostics performance of the generic cell model is excellent, comparable to that achieved in Chapter three which uses a simpler Butler-Volmer form without temperature explicit dependence.

7.1.4 Design of Experiment for Superimposed AC Waveform's Influence on Battery Aging Based on Resistance Growth

Two statistical experiments are designed, conducted, and analyzed in that chapter in order to examine whether a superimposed AC waveform on discharging current has an impact on lithium-ion battery aging. It was found that by raising the RMS value of the discharge waveform, the superimposed AC waveform increases the aging rate of a lithium-ion battery. Other factors, namely frequency, waveform shape, and DC value, were studied as well but were not found to be statistically significant. The practical significance of the finding includes the sizing of the DC bus capacitor as a filter for the battery pack on an EV. A numerical model is thus provided for the purpose of demonstrating the methodology for quantitatively linking aging rate and waveform RMS. The main contribution of the chapter is the use of statistical thinking throughout the investigation for experiment design, data analysis, and quantitative modeling. The rigor of the study gives more confidence to the results compared with some other works in the literature. The key elements of this chapter's contribution are summarized as follows.

- **Statistical design of experiment and analysis that determine a superimposed AC waveform on the discharge current causes accelerated aging due to the increased RMS value**

  A statistical design of experiment is conducted in order to discover whether battery aging is influenced by a superimposed AC waveform on the discharge current. The design allows for determining whether RMS value, DC value, or the existence of AC waveform causes significant difference in aging. Statistical

analysis is performed, and results suggest the importance of RMS value in influencing aging rate.

- **Statistical design of experiment and analysis that reaffirm the importance of discharge waveform RMS in aging and show the lack of evidence for waveform shape and frequency in aging influence**

  A second statistical design of experiment is conducted, following the first experiment. In this second experiment, the discharge waveforms are chosen so that, in conjunction with the first experiment's data, a comparison in aging rate between waveform shapes, RMS value, and frequency can be made. The results reaffirm the importance of RMS value in determining aging rate, while evidence does not support waveform shape and frequency being important aging factors.

- **A numerical model to quantify RMS influence on resistance growth and reaffirm the dominance of RMS discharge waveform value against DC value**

  Using data from both experiments, a numerical model for battery resistance growth as a function of discharge waveform RMS value is constructed. Additionally, using linear regression the battery resistance growth data reaffirms the dominance of discharge waveform RMS value over DC value in terms of aging influence. The numerical model provides the power electronics designer a tool for quantitatively design the battery pack filter through DC bus capacitor sizing with battery aging effect taken into account.

- **The general statistical methodology in design of experiment and analysis in the field of battery aging testing**

The statistical methodology used in this chapter emphasizes the importance of rigorous inference from experimental data. Only by designing appropriate experiments and performing analyses adhering to statistical principles can the conclusions be safeguarded against criticism. The method used also avoids the confusion between a small regression coefficient of a significant factor and the random noise of a non-significant factor included in the model. This same approach can be adopted to study other likely aging factors for the same standard of rigor in inference.

- **A planned experiment and its analyses, which allows for series connection of cells, for looking into whether regenerative braking has an impact on aging and a quantitative study on temperature and RMS aging influence interaction**

  This planned experiment could not be carried out due to equipment commissioning issues. However, contributions are made in the design of the discharge waveforms for studying regenerative braking aging influence, temperature and RMS aging interactions, and proper statistical modeling for series connection of cells.

7.2 Future Work

Based on the work presented in this document, the following is a list of the work that I recommend for further investigation.

1) **Implementing the temperature-dependent SOC and SOF algorithm on the WEMPEC truck and study the user experience for improvement**

The SOC and SOF algorithms proposed in Chapter five have been thoroughly evaluated with the data gather from the WEMPEC truck. An onboard implementation with more drive cycles under various climate conditions can be expected to provide a deeper insight on how the algorithms can be improved.

2) **Execution of the planned experiment to evaluate the aging impact of regenerative braking on Li-ion batteries**

   The planned experiment in Section 6.6 should be able to answer whether regenerative braking has a quantifiable impact on battery aging. Its analysis should also improve the understanding of the interactions between temperature and RMS aging influences in Li-ion batteries.

3) **Investigation of lead-acid battery modeling for regenerative braking**

   Lead-acid batteries can be used in start-stop mild hybrid vehicles. Given the strong nonlinearity of the lead-acid battery demonstrated in this thesis, it is possible that further advances can be made by paying closer attention to temperature effects on lead-acid battery behavior in the start-stop vehicle application. HPPC, EIS, and engine-start load cycles can be used to characterize and learn from the lead-acid battery operating at various temperatures. However, the generic cell modeling approach is still insufficient for lead-acid batteries under driving profiles with regenerative braking. A deeper understanding of the electrochemical processes, e.g. gassing, could help lead to more satisfactory mathematical models.

4) **An investigation into the influence of battery charging voltage on aging through a statistical experiment**

Battery charging voltage has been reported to have an influence on battery aging. Selecting an appropriate charging voltage is fundamental to the design of cell chargers and balancing circuits. The statistical experiment concept used in this work for the superimposed AC waveform's aging influence can be adapted to study the charging voltage's influence on aging as well.

5) **An investigation of the influence of battery SOC range on aging through a statistical experiment**

   In a hybrid vehicle application, the battery pack usage is usually restricted to a band of SOC, e.g. 60% to 90%. The width of the band is related to the sizing of the battery pack, but the location of the band may have an impact on the battery's aging performance. A statistical experiment can be conducted to investigate whether the location of the band has an impact on the battery aging performance.

6) **Dynamic modeling for online battery aging control**

   The statistical approach for understanding aging adopted in this work can lead to quantification of battery aging factors and improved solutions in system design. Another approach would be a physics-based, Newman-type model that can yield aging predictions based on the temperature and current profile. Such an aging model would allow for more real-time battery aging control, as opposed to system design solutions, e.g., sizing of capacitors. The difficulty with such an approach is the estimation of the necessary parameters through designed experiments. Further investigation is required to explore this alternative approach.

7) **Implementation of observer for internal states such as the electrode overpotential for the purpose of aging control**

The Butler-Volmer model structure in this research program lumps the two electrodes' overpotential together. While this approach is unavoidable due to the lack of information to differentiate the electrodes in series, it is possible to build an observer based on offline information that separates the two electrodes' overpotential. Since the overpotential is critical to inducing aging reactions, developments in this research area may lead to advances in aging control.

8) **Evaluation of different numerical methods other than the Kalman filter**

In this thesis, the Kalman filters have been adopted for their simplicity and flexibility. The possibility of using other recursive estimation techniques such as the least-mean-square (LMS) method and other variants of the Kalman filter can be further explored, including a detailed comparison of their benefits and drawbacks.

9) **Detailed investigation on Li-ion battery capacitance value and its associated diffusion processes**

The discrete-time models used in this work assume a simple time constant representing the complex process of ion diffusion. With the help of EIS and the ability to vary temperature and the charging/discharging processes, it should be possible to more deeply explore the capacitive diffusion behavior of the cell. This work may lead to further insights into modeling the transient behavior of the cell.

Bibliography

[1] Idaho National Engineering & Environmental Laboratory, "Battery Test Manual for Plug-In Hybrid Electric Vehicles", INL/EXT-07-12536, March 2008

[2] C. G. Hochgraf, J. K. Basco, T. P. Bohn, I. Bloom, "Effect of Ultracapacitor-Modified PHEV Protocol on Performance Degradation in Lithium-Ion Cells," Journal of Power Sources (2012), http://dx.doi.org/10.1016/j.jpowsour.2012.09.038

[3] H. J. Bergveld, W. S. Kruijt, and P. H. L. Notten, "Battery Management Systems, Design by Modeling", Kluwer Academic Publishers, 2002

[4] The Electromagnetic Telegraph: A technical history of the 19th-century electromagnetic telegraph, with special reference to the origin and variety of the alphabets, or codes, that were used, as of 10/12/2012 Website: http://mysite.du.edu/~jcalvert/tel/morse/morse.htm

[5] Battery Facts: All you need to know about batteries, as of 10/12/12 Website: http://www.batteryfacts.co.uk/index.html

[6] Voltaic Pile – Wikipedia: the Free Encyclopedia, as of 10/12/12 Website: http://en.wikipedia.org/wiki/Volta_pile

[7] Leclanché Cell – Wikipedia: the Free Encyclopedia, as of 10/12/12 Website: http://en.wikipedia.org/wiki/Volta_pile

[8] W. Feng, O. J. Kwon, and C-Y Wang, "Electrochemical-thermal modeling of automotive Li-ion Batteries and Experimental Validation Using a Three-Electrode Cell", International Journal of Energy Research, vol. 34, pp. 107-115, 2010.

[9] Lead-Acid Batteries, as of 10/12/12 Website: http://hyperphysics.phy-astr.gsu.edu/Hbase/electric/leadacid.html#c2

[10] Battery Types: Flooded vs. AGM and Gel, as of 10/12/12 Website: http://www.vonwentzel.net/Battery/01.Type/index.html

[11] Nickel Cells-How they work, as of 10/12/12 Website: http://www.batterieswholesale.com/nickel_cell_how_it_works.htm

[12] Lithium Ion Batteries – Panasonic Industrial Devices Global as of 10/12/12 Website: http://industrial.panasonic.com/wwwdata/pdf/ACA4000/ACA4000PE3.pdf

[13] D. Aurbach, "Review of selected electrode-solution interactions which determine the performance of Li and Li ion batteries", Journal of Power Sources 89 (2000) 206-218

[14] A. J. Bard and L. R. Faulkner, "Electrochemical Methods, Fundamentals and Applications", 2nd ed., John Wiley & Sons, Inc., New York, 2001

[15] John Alfred Valentine Butler– Wikipedia: the Free Encyclopedia, as of 10/12/12 Website: http://en.wikipedia.org/wiki/John_Alfred_Valentine_Butler

[16] Max Volmer– Wikipedia: the Free Encyclopedia, as of 10/12/12 Website: http://en.wikipedia.org/wiki/Max_Volmer

[17] D. A. Noren and M. A. Hoffman, “Clarifying the Butler-Volmer equation and related approximations for calculating activation losses in solid oxide fuel cell models”, Journal of Power Sources 152 (2005) 175-181

[18] Z. M. Salameh, M. A. Casacca, and W. A. Lynch, “A Mathematical Model for Lead-Acid Batteries”, IEEE Transactions on Energy Conversion, Vol. 7, No. 1, pp. 93-97, March 1992

[19] M. Chen and G. A. Rincon-Mora, “Accurate Electrical Battery Model Capable of Predicting Runtime and I-V Performance”, IEEE Transactions on Energy Conversion, Vol. 21, No. 2, pp. 504-511, June 2006

[20] H.L.N. Wiegman, “Battery State Estimation and Control for Power Buffering Applications”, Ph.D. dissertation, University of Wisconsin-Madison, 1999.

[21] L.W. Juang, P.J. Kollmeyer, T.M. Jahns, and R.D. Lorenz, ”System identification-based lead-acid battery online monitoring system for electric vehicles,” in Proc of 2010 IEEE Energy Conversion Congress and Exposition (ECCE), pp. 3903-3910, Sept. 2010.

[22] J, Li, M. S. Mazzola, J. Gafford, B. Jia, and M. Xin, “Bandwidth based electrical-analogue battery modeling for battery modules”, Journal of Power Sources 218 (2012) 331-340

[23] G. L. Plett, “Extended Kalman filtering for battery management systems of LiPB-based HEV battery packs Part 2. Modeling and identification”, Journal of Power Sources 134 (2004) 262-276

[24] E. Barsoukov and J. R. MacDonald, “Impedance Spectroscopy: Theory, Experiment, and Applications”, 2nd ed., John Wiley and Sons, Inc.Hoboken, New Jersey, 2005

[25] E. Karden, “Using low-frequency impedance spectroscopy for characterization, monitoring, and modeling of industrial batteries”, Ph.D. dissertation, RWTH Aachen University, 2001.

[26] A. Anders, “Effect of Current Dynamics on Li-ion Cell Capacity and Impedance”, Master’s thesis, University of Wisconsin-Madison, 2010

[27] U. Troltzsche, O. Kanoun, and H. Trankler, “Characterizing ageing effects of lithium ion batteries by impedance spectroscopy”, Electrochimica Acta 51 (2006) 1664-1672

[28] D. Andre, M. Meiler, K. Steiner, H. Walz, T. Soczka-Guyh, and D. U. Sauer, “Characterization of high-power lithium-ion batteries by electrochemical impedance spectroscopy. I: Experimental investigation”, Journal of Power Sources 196 (2011) 5334-5341

[29] D. Andre, M. Meiler, K. Steiner, H. Walz, T. Soczka-Guyh, and D. U. Sauer, “Characterization of high-power lithium-ion batteries by electrochemical impedance spectroscopy. II: Modeling”, Journal of Power Sources 196 (2011) 5349-5356

[30] M. D. Ortigueira, “An introduction to the fractional continuous-time linear systems: the 21st century systems”, IEEE Circuits and Systems Magazine Vol. 8 Issue 3, third quarter 2008.

[31] J. Sabatier, M. Aoun, A. Oustaloup, G. Gregoire, F. Ragot, and P. Roy, “Fractional system identification for lead acid battery state of charge estimation”, Signal Processing 86 (2006) 2645-2657

[32] G. L. Plett, “Extended Kalman filtering for battery management systems of LiPB-based HEV battery packs Part 1. Background”, Journal of Power Sources 134 (2004) 256-261

[33] G. L. Plett, “Extended Kalman filtering for battery management systems of LiPB-based HEV battery packs Part 3. State and parameter estimation”, Journal of Power Sources 134 (2004) 277-292

[34] X. Hu, F. Sun, Y. Zou, and H, Peng, “Online Estimation of an Electric Vehicle Lithium-Ion Battery Using Recursive Least Squares with Forgetting”, in Proc. of 2011 American Control Conference (ACC), June 29 – July 01, 2011

[35] E. Manla, A. Nasiri, C. H. Rentel, and M. Hughes, “Modeling of Zinc Bromide Energy Storage for Vehicular Applications”, IEEE Transactions on Industrial Electronics, Vol. 57, No. 2, pp. 624-632, February 2010

[36] G. Plett, “Sigma-point Kalman filtering for battery management systems of LiPB-based HEV battery packs Part 1: Introduction and state estimation”, Journal of Power Sources 161 (2006) 1356-1368

[37] G. Plett, “Sigma-point Kalman filtering for battery management systems of LiPB-based HEV battery packs Part 2: Simultaneous state and parameter estimation”, Journal of Power Sources 161 (2006) 1369-1384

[38] Y. Hu and S. Yukovich, “Battery cell state-of-charge estimation using linear parameter varying system techniques”, Journal of Power Sources 198 (2012) 338-350

[39] S. Wang, M. Verbrugge, J. S. Wang, and P. Liu, “Multi-parameter battery state estimator based on the adaptive and direct solution of the governing differential equations”, Journal of Power Sources 196 (2011) 8735-8741

[40] J. Lee, O. Nam, and B. H. Cho, “Li-ion battery SOC estimation method based on the reduced order extended Kalman filtering”, Journal of Power Sources 174 (2007) 9-15

[41] J. Lee, J. Lee, O. Nam, J. Kim, B. H. Cho, H. Yun, S. Choi, K. Kim, J. H. Kim, and S. Jun, “Modeling and Real Time Estimation of Lumped Equivalent Circuit Model of a Lithium Ion Battery”, in Proc. Of 10th International Power Electronics and Motion Control Conference (EPE-PEMC 2006), 2006

[42] B. S. Bhangu, P. Bentley, D. A. Stone, and C. M. Bingham, “Nonlinear Observers for Predicting State-of-Charge and State-of-Health of Lead-Acid Batteries for Hybrid-Electric Vehicles”, IEEE Transactions on Vehicular Technology, Vol. 54, No. 3, pp. 783-794, May 2005

[43] S. Lee, J. Kim, J. Lee, and B. H. Cho, “State-of-charge and capacity estimation of lithium-ion battery using a new open-circuit voltage versus state-of-charge”, Journal of Power Sources 185 (2008) 1367-1373

[44] J. Han, D. Kim, and M. Sunwoo, “State-of-charge estimation of lead-acid batteries using an adaptive extended Kalman filter”, Journal of Power Sources 188 (2009) 606-612

[45] M. Verbrugge and B. Koch, “Generalized Recursive Algorithm for Adaptive Multiparameter Regression: Application to Lead Acid, Nickel Metal Hydride, and Lithium-Ion Batteries”, Journal of the Electrochemical Society 153 (1) A187-A201 (2006)

[46] Y. Li, R. D. Anderson, J. Song, A. M. Philips, and X. Wang, "A Nonlinear Adaptive Observer Approach for State of Charge Estimation of Lithium-Ion Batteries", in Proc. of 2011 American Control Conference (ACC), June 29 – July 01, 2011

[47] W. Peukert, "Über die Abhängigkeit der Kapazität von der Entladestromstärke bei Bleiakkumulatoren", Electrotech. Z., ETZ V. 18, 1897, pp 287-288

[48] H. Lin, T. Liang, S. Chen, and K. Li, "Forecasting the State-of-Charge of Li-Ion Batteries using Fuzzy Inference and Fuzzy Identification", in Proc of 2012 IEEE Energy Conversion Congress and Exposition (ECCE), Sept. 2012

[49] C. C. Hua, T. Y. Tasi, C. W. Chuang, and W. B. Shr, "Design and Implementation of a Residual Capacity Estimator for Lead-Acid Batteries," in Proc. of Second IEEE Conference of Industrial Electronics and Applications, 2007

[50] D. T. Lee, S. J. Shian, C. M. Lee, and Y. C. Wang, "State-of-Charge Estimation for Electric Scooters by Using Learning Mechanisms," IEEE transactions on Vehicular Technology, Vol. 56, No. 2, March 2007

[51] D. Doerffel and S. Abu Sharkh, "A critical review of using Peukert equation for determining the remaining capacity of lead-acid and lithium-ion batteries", Journal of Power Sources 155 (2006) 395-400

[52] T. Hansen and C. Wang, "Support vector based battery state of charge estimator", Journal of Power Sources 141 (2005) 351-358

[53] K. Kutluay, Y. Çadırcı, Y. S. Özkazanç, and I. Çadırcı, "A New Online State-of-Charge Estimation and Monitoring System for Sealed-Acid Batteries in Telecommunication Power Supplies", IEEE transactions on Industrial Electronics, Vol. 52, No. 5, October 2005

[54] O. Caumount, P. Le Moigne, C. Rombaut, X. Muneret, and P. Lenain, "Energy Gauge for Lead-Acid Batteries in Electric Vehicles", IEEE transactions on Energy Conversion, Vol. 15, No. 3, September 2000

[55] M. Doyle, T. F. Fuller, and J. Newman, "Modeling of Galvanostatic Chargen and Discharge of the Lithium/Polymer/Insertion Cell", Journal of Electrochemical Society, Vol. 140, No. 6, June 1993

[56] T. F. Fuller, M. Doyle, and J. Newman, "Simulation and Optimization of the Dual Lithium Ion Insertion Cell", Journal of Electrochemical Society, Vol. 141, No. 1, January 1993

[57] R. Klein, J. Christensen, J. Ahmed, and A. Kojic, "Algorithms for Advanced Battery Management Systems", IEEE Control Systems Magazine, Vol. 30, Issue 3, 49-68

[58] J. Marcicki, G. Rizzoni, A. T. Conlisk, and M. Canova, "A reduced-order electrochemical model of lithium-ion cells for system identification of battery aging", in Proc. of 2011 ASME Dynamic Systems and Control Conference (DSCC 2011), October 31 – November 02, 2011

[59] A. Tenno, R. Tenno, and T. Suntio, "Charge-discharge behavior of VRLA batteries: model calibration and application for state estimation and failure detection", Journal of Power Sources 103 (2001) 42-53

[60] R. D. Perkins, A. V. Randall, X. Zhang, and G. L. Plett, "Controls oriented reduced order modeling of lithium deposition on overcharge", Journal of Power Sources 209 (2012) 318-325

[61] A. V. Randall, R. D. Perkins, X. Zhang, and G. L. Plett, "Controls oriented reduced order modeling of solid-electrolyte interphase layer growth", Journal of Power Sources 209 (2012) 282-288

[62] W. Lai, "Electrochemical modeling of single particle intercalation battery materials with different thermodynamics", Journal of Power Sources 196 (2011) 6534-6553

[63] J. C. Forman, S. J. Moura, J. L. Stein, and H. K. Fathy, "Genetic identification and fisher identifiability analysis of the Doyle-Fuller-Newman model from experimental cycling of a LiFePO4 cell", Journal of Power Sources 210 (2012) 263-275

[64] A. P. Schimdt, M. Bitzer, A. W. Imre, and L. Guzzella, "Experiment-drive electrochemical modeling and systematic parameterization for a lithium-ion battery cell", Journal of Power Sources 195 (2010) 5071-5080

[65] T. Yang, L. Cai, and R. E. White, "Mathematical modeling of the LiAl/FeS2 high temperature battery system", Journal of Power Sources 201 (2012) 322-331

[66] K. A. Smith, C. D. Rahn, and C. Wang, "Model-Based Electrochemical Estimation and Constraint Management of Pulse Operation of Lithium Ion Battery", IEEE transactions on Control Systems Technology, Vol. 18, No. 3, May 2010

[67] D. Eroglu and A. C. West, "Modeling of reaction kinetics and transport in the positive porous electrode in a sodium-iron chloride battery", Journal of Power Sources 203 (2012) 211-221

[68] S. Santhanagopalan, Q. Guo, P. Ramadass, and R. E. White, "Review of models for predicting the cycling performance of lithium ion batteries", Journal of Power Sources 156 (2006) 620-628

[69] X. Hu, S. Stanton, L. Cai, and R. White, "A linear time-invariant model for solid-phase diffusion in physics-based lithium ion cell models", Journal of Power Sources 214 (2012) 40-50

[70] S. Renganathan, G. Sikha, S. Santhanagopalan, and R. E. White, "Theoretical Analysis of Stresses in a Lithium Ion Cell", Journal of Electrochemical Society, Vol. 157, No. 2, 2010

[71] Hydrometer – Wikipedia: the Free Encyclopedia, as of 10/12/12 Website: http://en.wikipedia.org/wiki/Hydrometer

[72] T. Torikai, T. Takesue, Y. Toyota, and K. Nakano, "Research and Development of the Model-Based Battery State of Charge Indicator," in Proc. of 1992 International Conference on Power Electronics and Motion Control, p.p. 996-1001, November, 1992

[73] Shriram Santhanagopalan, Ralph E. White, "Online Estimate of the State of Charge of a Lithium Ion Cell", Journal of Power Sources 161 (2006) 1346-1355

[74] Sabine Piller, Marion Perrin, and Andreas Jossen, "Methods for State of Charge Determination and Their Applications", Journal of Power Sources 96 (2001) 113-120

[75] X. Lin, A. Stefanopoulou, P. Laskowsky, J. Freudenberg, Y. Li, and R. D. Anderson, "State of Charge Estimation Error due to Parameter Mismach in a Generalized Explicit Lithium Ion Battery Model", in Proc. of ASME 2011 Dynamic Systems and Control Conference and Bath/ASME Symposium on Fluid Power and Motion Control (DSCC2011), pp. 393-400, October 31-November 2, 2011

[76] F. Huet, R.P. Nogueira, L. Torcheuz, P. Lailler, "Simultaneous real-time measurements of potential and high frequency resistance of a lab cell", Journal of Power Sources 113 (2003) 414-421

[77] H. Blanke, O Bohlen, S Buller, R W. De Doncker, B. Fricke, A. Hammouche, D. Linzen, M. Thele, and D. U. Sauer, "Impedance measurements of lead-acid batteries for state-of-charge, state-of-health and cranking capability prognosis in electric and hybrid electric vehicles" Journal of Power Sources 144 (2005) 418-425

[78] A. Hammouche, E. Karden, and R W. De Doncker, "Monitoring state-of-charge of Ni-MH and Ni-Cd batteries using impedance spectroscopy," Journal of Power Sources 127 (2004) 105-111

[79] M. Hughes, R.T. Barton, S.A.G.R. Karunathilaka, N. A. Hampson, and R. Leek, "The Residual Capacity Estimation of Fully Sealed 25 Ah Lead/Acid Cells," Journal of Power Sources, 17 (1986) 305-329

[80] F. Huet, "A review of impedance measurements for determination of the state-of-charge or state-of-health of secondary batteries," Journal of Power Sources 70 (1998) 59-69

[81] M. Coleman, C. K. Lee, C. Zhu, and W. G. Hurley, "State-of-Charge Determination from EMF Voltage Estimation: Using Impedance, Terminal Voltage, and Current for Lead-Acid and Lithium-Ion Batteries," IEEE Transactions on Industrial Electronics, Vol. 54, No. 5, October 2007

[82] J. Zhang and J. Lee, "A review on prognostics and health monitoring of Li-ion battery", Journal of Power Sources 196 (2011) 6007-6014

[83] I. Kim, "A Technique for Estimation the State of Health of Lithium Batteries through a Dual-Sliding-Mode Observer", IEEE transactions on Power Electronics, Vol. 25, No. 4, April 2010

[84] Y. Sun, H-L Jou, and J-C Wu, "Aging Estimation Method for Lead-Acid Battery", IEEE transactions on Energy Conversion, Vol. 26, No. 1, March 2011

[85] M. Broussely, S. Herreyre, P. Biensan, P. Kasztejna, K. Nechev, R.J. Staniewicz, "Aging mechanism in Li ion cells and calendar life prediction", Journal of Power Sources 97-98 (2001) 13-21

[86] M. Wohlfahrt-Mehrens, C. Vogler, and J. Garche, "Aging mechanisms of lithium cathode materials", Journal of Power Sources 127 (2004) 58-64

[87] U. Troltzsch, O. Kanoun, and H-R Trankler, "Characterizing aging effects of lithium ion batteries by impedance spectroscopy", Electrochimica Acta 51 (2006) 1664-1672

[88] D. U. Sauer and H. Wenzl, "Comparison of different approaches for lifetime prediction of electrochemical systems-Using lead-acid batteries as example", Journal of Power Sources 176 (2008) 534-546

[89] Y. Jojima, S. Muto, K. Tatsumi, H. Kondo, H. Oka, K. Horibuchi, and Y. Ukyo, "Degradation analysis of a Ni-based layered positive-electrode active material cycled at elevated temperatures studied by scanning transmission electron microscopy and electro energy-loss spectroscopy", Journal of Power Sources 196 (2001) 7721-7727

[90] M. Ecker, J. B. Gerschler, J. Vogel. S. Kabitz. F. Hust, P. Dechent, and D. U. Sauer, "Development of a lifetime prediction model for lithium-ion batteries based on extended accelerated aging test data", Journal of Power Sources 215 (2012) 248-257

[91] M. Dubarry, C. Truchot, M. Cugnet, B. Y. Liaw, K. Gering, S. Sazhin, D. Jamison, and C. Michelbacher, "Evaluation of commercial lithium-ion cells based on composite positive electrode for plug-in hybrid electric vehicle applications Part I: Initial characterizations", Journal of Power Sources 196 (2011) 10328-10335

[92] M. Dubarry, C. Truchot, M. Cugnet, B. Y. Liaw, K. Gering, S. Sazhin, D. Jamison, and C. Michelbacher, "Evaluation of commercial lithium-ion cells based on composite positive electrode for plug-in hybrid electric vehicle applications Part II: Degradation mechanism under 2 C cycling aging", Journal of Power Sources 196 (2011) 10336-10343

[93] M. Wu and P. J. Chiang, "High-rate capability of lithium-ion batteries after storing at elevated temperature", Electrochimica Acta 52 (2007) 3719-3725

[94] S. Buller, M. Thele, E. Karden, and R. W. De Doncker, "Impedance-based on-linear dynamic battery modeling for automotive applications", Journal of Power Sources 113 (2003) 422-430

[95] T. Osaka, S. Nakade, M. Rajamaki, and T. Momma, "Influence of capacity fading on commercial lithium-ion battery impedance", Journal of Power Sources 119-121 (2003) 929-933

[96] K. Takeno, M. Ichimura, K. Takano, and J. Yamaki, "Influence of cycle capacity deterioration and storage capacity deterioration on Li-ion batteries used in mobile phones", Journal of Power Sources 142 (2005) 298-305

[97] S. Eom, M. Kim, I. Kim, S. Moon, Y. Sun, and Y. Kim, "Life prediction and reliability assessment of lithium secondary batteries", Journal of Power Sources 174 (2007) 954-958

[98] Z. Li, L. Lu, M. Ouyang, and Y. Xiao, "Modeling the capacity degradation of LiFePO4/graphite batteries based on stress coupling analysis", Journal of Power Sources 196 (2011) 9757-9766

[99] J. Marcicki, F. Todeschini, S. Onori, and M. Canova, "Nonlinear Parameter Estimation for Capacity Fade in Lithium-Ion Cells Based on a Reduced-Order Electrochemical Model", in Proc. of American Control Conference (ACC2012), June 27-June 29, 2012

[100] B. Saha, K. Goebel, S. Poll, and J. Christophersen, "Prognostics Methods for Battery Health Monitoring Using a Bayesian Framework", IEEE Transactions on Instrumentation and Measurement, Vol. 58, No. 2, pp. 291-296, February 2009

[101] W. He, N. Williard, M. Osterman, and M. Pecht, "Prognostics of lithium-ion batteries based on Dempster-Shafer theory and the Bayesian Monte Carlo method", Journal of Power Sources 196 (2011) 10314-10321

[102] B. Pattipati, C. Sankavaram, and K. R. Pattipati, "System Identification and Estimation Framework for Pivotal Automotive Battery Management System Characteristics", IEEE Transactions on Systems, Man, and Cybernetics Part C: Applications and Reviews, Vol. 41, No. 6, pp. 869-884, November 2011

[103] J. Vetter, P. Novak, M. R. Wagner, C. Veit, K.-C Moller, J. O. Besenhard, M. Winter, M. Wohlfahrt-Mehrens, C. Vogler, and A. Hammouche, "Ageing mechanisms in lithium-ion batteries", Journal of Power Sources 147 (2005) 269-281

[104] D. Aurbach, "Review of selected electrode-solution interactions which determine the performance of Li and Li ion batteries", Journal of Power Sources 89 (2000) 206-218

[105] S. B. Peterson, J. Apt, and J. F. Whitacre, "Lithium-ion battery cell degradation resulting from realistic vehicle and vehicle-to-grid utilization", Journal of Power Sources 195 (2010) 2385-2392

[106] M. Safari, M. Morcrette, A. Teyssot, and C. Delacourt, "Life-Prediction Methods for Lithium-Ion Batteries Derived from Fatigue Approach I. Introduction: Capacity-Loss Prediction Based on Damage Accumulation", Journal of the Electrochemical Society 157 (6) A713-A720 (2010)

[107] L. Serrao, Z. Chehab, Y. Guezennee, and G. Rizzoni, "An aging model of Ni-MH batteries for hybrid electric vehicles", in Proc. of IEEE Conference on Vehicle Power and Propulsion, September 7- September 9, 2005

[108] M. Dubarry and B. Y. Liaw, "Identify capacity fading mechanism in a commercial LiFePO4 cell", Journal of Power Sources 194 (2009) 541-549

[109] J. Zhang, L. Liao, and J. Lee, "Prognostics and Health Monitoring of Li-ion Battery for Hybrid Electric Vehicle", SAE Technical Paper 210-01-0256, 2010

[110] E. V. Thomas, I. Bloom, J. P. Christophersen, and V. S. Battaglia, "Statistical methodology for predicting the life of lithium-ion cells via accelerated degradation testing", Journal of Power Sources 184 (2008) 312-317

[111] J. Wang, P. Liu, J. Hicks-Garner, E. Sherman, S. Soukiazian, M. Verbrugge, H. Tataria, J. Musser, and P. Finamore, "Cycle-life model for graphite-LiFePO4 cells", Journal of Power Sources 196 (2011) 3942-3948

[112] J. P. Christophersen, I. Bloom, E. V. Thomas, K. L. Gering, G. L. Henriksen, V. S. Battaglia, and D. Howell, "Advanced Technology Development Program for Lithium-Ion Batteries: Gen 2 Performance Evaluation Final Report", INL/EXT-05-00913, July 2006

[113] Idaho National Engineering & Environmental Laboratory, "Battery Technology Life Verification Test Manual", INL/EXT-04-01986, February 2005

[114] E.V. Thomas, H. L. Case, D. H. Doughty, R. G. Jungst, G. Nagasubramnaian, and E. P. Roth, "Accelerated power degradation of Li-ion cells", Journal of Power Sources 124 (2003) 254-260

[115] United States Council for Automotive Research LLC, "USABC Electric Vehicle Battery Test Procedures Manual", website: http://uscar.org/guest/article_view.php?articles_id=74, as of 11/25/2012

[116] M. Coleman, C.K. Lee, W.G. Hurley, "State of Health Determination: Two Pulse Load Test for a VRLA Battery", Power Electronics Specialists Conference, 2006. PESC '06. 37th IEEE

[117] B. Kortschak, C. Kurtulus, M. Dhor, U. Wiedemann, and V. Hennige, "Detection Method of Battery Cell Degradation", Vehicle Power and Propulsion Conference (VPPC), 2011 IEEE
[118] G. L. Plett, "Recursive approximate weighted total least squares estimation of battery cell total capacity", Journal of Power Sources 196 (2011) 2319-2331
[119] P. J. van Bree, A. Veltman, W. H. A. Hendrix, and P. R. J. van den Bosch, "Prediction of Battery Behavior Subject to High-Rate Partial State of Charge," IEEE Transactions on Vehicular Technology, Vol. 58, No. 2, February 2009
[120] K. Yamada, Y. Yamada, K. Otsu, Y. Machiyama, A. Emori, and T. Okoshi, "The intelligent automotive battery, "CYBOX"," Journal of Power Sources 185 (2008) 1478-1483
[121] S. Buller, M. Thele, E. Karden, and R.W. De Doncker, "Impedance-based non-linear dynamic battery modeling for automotive applications," Journal of Power Sources 113 (2003) 422-430
[122] B. Saha, C. C. Quach, and K. Goebel, "Optimizing Battery Life for Electric UAVs using a Bayesian Framework", Aerospace Conference, March 3-10, 2012
[123] E. Meissner and G. Richter, "Battery monitoring and electrical energy management precondition for future vehicle electric power systems," Journal of Power Sources 116 (2003), 79-98
[124] G. Plett, "High-performance battery-pack power estimation using a dynamic cell model," IEEE Transactions on Vehicular Technology, vol. 53, no. 5, pp. 1586-1693, September 2004
[125] H. Cho, W. Choi, J. Go, S. Bae, and H. Shin, "A study on time-dependent low temperature power performance of a lithium-ion battery", Journal of Power Sources 198 (2012) 273-280
[126] T. Momma, M. Matsunang, D. Mukoyama, and T. Osaka, "Ac impedance analysis of lithium ion battery under temperature control", Journal of Power Sources 216 (2012) 304-307
[127] W. Waag, S. Kabitz, and D. U. Sauer, "Experimental investigation of the lithium-ion battery impedance characteristic at various conditions and aging states and its influence on the application", Applied Energy 102 (2013) 885-897
[128] S. Bala, T. Tengner, P. Rosenfeld, and F. Delince, "The effect of low frequency current ripple on the performance of a lithium iron phosphate (LFP) battery energy storage system" in Proc of 2012 IEEE Energy Conversion Congress and Exposition (ECCE), Sept. 2012
[129] S. Okazaki, S. Higuchi, O. Nakamura, and S. Takahashi, "Influence of superimposed alternative current on capacity and cycle life for lead-acid batteries", Journal of Applied electrochemistry 16 (1986) 894-898
[130] R. A. Fisher, "Statistical Methods, Experimental Design, and Scientific Inference: A Re-issue of Statistical Methods for Research Workers, the Design of Experiments, and Statistical Methods and Scientific Inference," Oxford University Press Inc., New York, 1991
[131] G. E. P. Box and N. R. Draper, "Empirical Model-Building and Response Surfaces", John Wiley and Sons, Inc., New York, 1987
[132] M. G. Bulmer, "Principles of Statistics," Dover Publications, Inc., New York, 1979

[133] C. F. J. Wu and M. S. Hamada, “Experiments: Planning, Analysis, Optimization”, 2nd edition, John Wiley and Sons Inc., Hoboken, New Jersey, 2009
[134] A. van den Bos, “Parameter Estimation for Scientists and Engineers”, John Wiley and Sons Inc., Hoboken, New Jersey, 2007
[135] S. Haykin, “Adaptive Filter Theory”, Prentice-Hall, 2002
[136] D. Salsburg, “The Lady Tasting Tea”, Henry Holt and Company, LLC, New York, 2002
[137] K. Pearson, “The Grammar of Science” 2nd edition, Adam and Charles Black, London, 1900
[138] P.J. Kollmeyer, W. Lamb, L.W. Juang, J.D. McFarland, T.M. Jahns, and B. Sarlioglu, “Design of an electric powertrain for a Ford F150 crew cab truck utilizing a lithium battery pack and an interior PM synchronous machine drive,” in *Proc of 2012 IEEE Transportation Electrification Conference and Expo (ITEC’12)* , Dearborn, MI, June 2012
[139] W. Waag, C. Fleischer, and D.U. Sauer, “On-line estimation of lithium-ion battery impedance parameters using a novel varied-parameters approach,” *Journal of Power Sources 237 (2013)*, pp. 260-269
[140] P.J. Kollmeyer, “Electromechanical Modeling and Analysis of a Corbin Sparrow Electric Vehicle using on the Road Data”, Master’s thesis, University of Wisconsin-Madison, 2011
[141] E. Karden, S. Buller, R. De Doncker, “A method for measurement and interpretation of impedance spectra for industrial batteries,” *Journal of Power Sources 85 (2000)*, pp. 72-78
[142] M. Itagaki, N. Kobari, S. Yotsuda, K. Watanabe, S. Kinoshita, M. Ue, “LiCoO2 electrode/electrolyte interface of Li-ion rechargeable batteries investigated by in situ electrochemical impedance spectroscopy,” *Journal of Power Sources 148 (2005)*, pp. 78-84
[143] D. Le, and B. Sisk, "Lead-Acid State of Charge Estimation for Start-Stop Applications," *SAE International Journal Alt. Power. 2(1)*:172-178, 2013

Appendix A
Corbin Sparrow

In Chapter three, drive cycle data was collected from a Corbin Sparrow EV modified and operated by WEMPEC. The work on the Corbin Sparrow EV is foremost the work of Phillip Kollmeyer, a colleague of the author. A full account of his work related to the Corbin Sparrow can be found in [21], [140]. In this appendix, a basic account will be presented on the Corbin Sparrow EV used for the drive cycle data collection.

Figure A 1 WEMPEC Corbin Sparrow with Phillip Kollmeyer [140]

Figure A 1 shows a picture of the WEMPEC Corbin Sparrow. The Corbin Sparrow EV is a DOT-certified single passenger vehicle designed for commuting with an electronically limited top speed of 125 [km/hr] and a range of 45 to 60 [km] [21]. The Corbin Sparrow is an EV that utilizes a series DC motor, a buck DC-DC converter, and a

lead-acid battery pack. Regenerative braking is not available for the vehicle. The rear wheel is directly connected to the shaft via a toothed belt, while the DC motor has a toothed gear connected to the shaft. One 1.5 [kW] onboard charger is available for charging the battery pack by connecting to a standard 120V/15 [A] outlet. A National Instruments Compact Rio microcontroller/FPGA system is installed for logging all sensor signals, including battery voltage, current, and temperature. Figure A 2 shows the Corbin Sparrow system diagram.

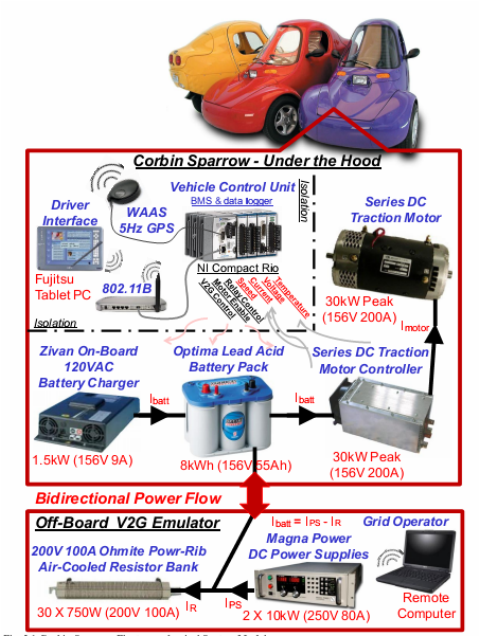

Figure A 2 WEMPEC Corbin Sparrow system diagram [140]

Using the onboard Compact RIO system, a battery management and data-logging system is implemented in the vehicle. The data-logging system creates charging, driving, and idle log files. The following data are logged: individual battery voltages, battery temperatures, pack current and [Ah], accessory current, motor current and voltage, vehicle speed and acceleration, and GPS estimated position and altitude [21].

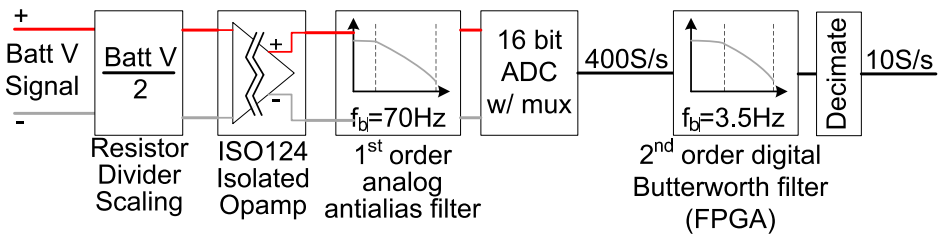

Figure A 3 Corbin Sparrow voltage-sensing configuration [21]

Figure A 3 depicts the voltage sensing, sampling, and filter configuration used in the Corbin Sparrow vehicle. The sensed battery voltage is attenuated by a factor of two with a 0.1% tolerance resistor divider network, buffered with an isolated op-amp circuit, filtered, and sensed with a 16-bit NI 9205 32-channel multiplexed A/D converter. Finally, the voltages are digitally filtered and down-sampled to 10 samples/sec, the same data rate used in the lab test system [21]. Table A 1 summarizes the resulting system performance, resolution, and accuracy specifications.

Table A 1 Corbin Sparrow Test System Specifications [21]

Peak Discharge/Charge Current	225 A/8 A
ADC Voltage Range/Bits	±10V/16 Bits
Voltage & Current Sampling	Multiplexed/400Hz
Voltage & Resolution/Accuracy	670 µV/≈ 25 mV
Current Resolution/Accuracy	10 mA/2.4 A

Appendix B
Battery Test Equipment

Many of the experimental results documented in this thesis are obtained on custom built battery test equipment. This appendix describes the specifications of the said battery test equipment. It is noted here that the design and construction of the system and the diagrams presented here are mostly Phillip Kollmeyer's works.

The lab test system was designed with sufficient capabilities to insure that the resolution and accuracy of the system does not limit the performance of the system identification algorithms. The lab test system consists of a Chroma 63201 electronic load to discharge the battery in parallel with a Chroma 62024P-40-120 power supply to charge the battery, as shown in Figure B 1. A National Instruments Compact dag real-time controller is used to control the electronic load and power supply via serial and analog commands, as well to collect sensor readings for the battery voltage, temperature, and current. The load and source are configured for remote voltage sensing, making it possible to sense the battery voltage directly at the battery terminals in order to minimize the degrading effects of resistive voltage drop in the cables. The controller also provides a user interface via Ethernet.

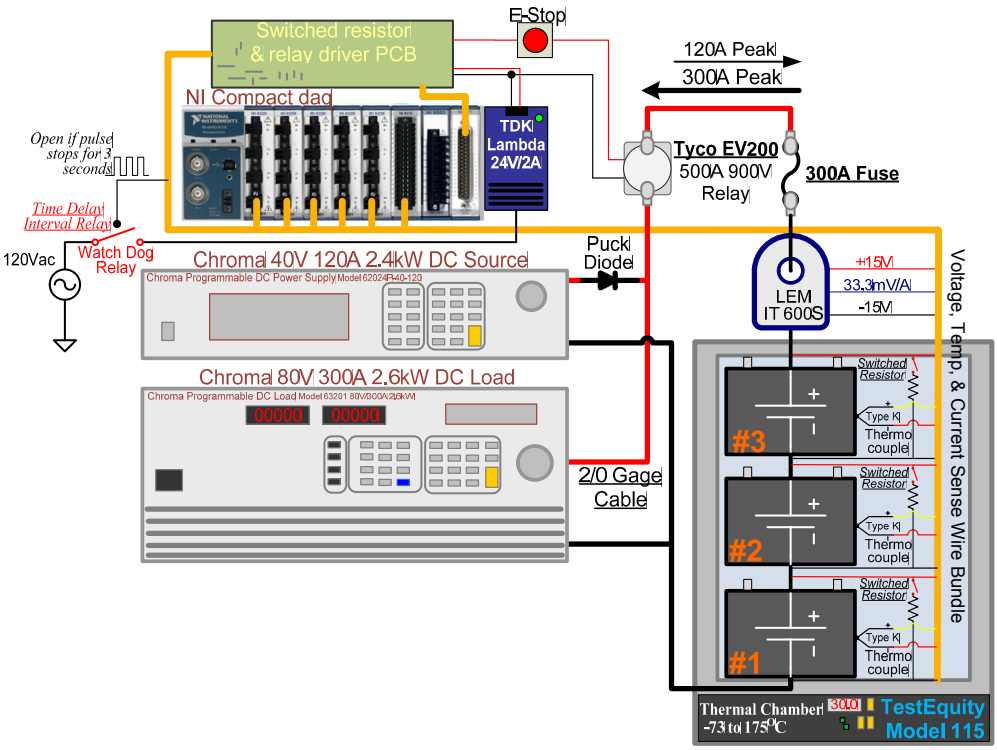

Figure B 1 High accuracy, high bandwidth lab test system

Voltages can sense with up to three channels of an NI 9229 four-channel, +/-60V, 24-bit, simultaneous sampling, isolated channel-to-channel voltage sensing module. The fourth channel is used to sense the output of a LEM IT 600s current sensor, resulting in the lab system performance specs outlined in Table B 1.

Table B 1 Specifications for the lab test equipment

Control Bandwidth	5 kHz
Voltage Res/Acc.	1.25 µV/2.09 mV
Current Res/Acc.	39.3 µA/0.03% (of reading)
V/I Measurement Bandwidth	11.3 kHz
Max Battery Pack Voltage	40 V
Max Charge Current/Power	120 A/2.4 kW
Max Discharge Current/Power	300 A/ 2.6 kW

Additionally, it is noted that a temperature chamber is available for the control of battery external temperature. The temperature chamber is the TestEquity Model 115 and

has an operation range of -73 to 175 ^{0}C. Finally, the anti-aliasing filtering configuration of the channels is shown in Figure B 2.

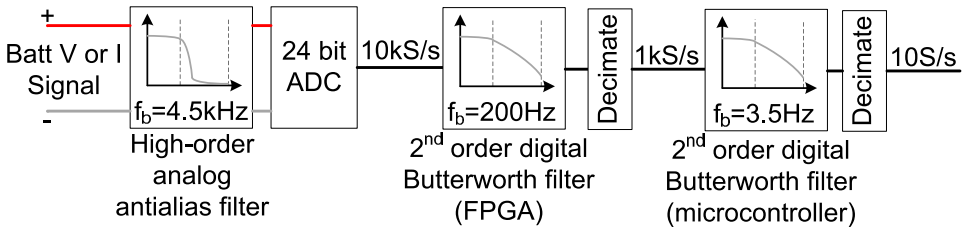

Figure B 2 Lab test system filtering configuration [21]